UNIVERSITÉ DE
NEUCHÂTEL

Institut de chimie

A Novel Nano-optical Sensing Approach for Real-time Amyloid Aggregation Monitoring

Thèse soutenue le 11 Avril 2016 à l'Institut de Chimie, Faculté des Sciences de l'Université de Neuchâtel, pour l'obtention du grade de docteur ès Science

par

Sara SANTI

Titulaire d'un master en Chimie et Technologie Pharmaceutique de la Faculté de Pharmacie de l'Università degli Studi di Padova (Italie)

Membres du Jury :
Prof. Reinhard Neier, directeur de thèse, UniNe
Prof. Hans Peter Herzig, co-directeur de thèse, EPF Lausanne
Prof. Thomas Südmeyer, UniNe
Prof. Emiliano Descrovi, Politecnico di Torino, Italie

Université de Neuchâtel

2016

unine
UNIVERSITÉ DE
NEUCHÂTEL

Faculté des sciences
Secrétariat-décanat de Faculté
Rue Emile-Argand 11
2000 Neuchâtel - Suisse
Tél: + 41 (0)32 718 2100
E-mail: secretariat.sciences@unine.ch

IMPRIMATUR POUR THESE DE DOCTORAT

La Faculté des sciences de l'Université de Neuchâtel autorise l'impression de la présente thèse soutenue par

Madame Sara SANTI

Titre:

“A Novel Nano-optical Sensing Approach for Real-time Amyloid Aggregation Monitoring”

sur le rapport des membres du jury composé comme suit:

- Prof. Reinhard Neier, directeur de thèse, Université de Neuchâtel, Suisse
- Prof. Hans-Peter Herzig, co-directeur de thèse, EPF Lausanne, Suisse
- Prof. Thomas Südmeyer, Université de Neuchâtel, Suisse
- Prof. ass. Emiliano Descrovi, Politecnico di Torino, Italie

Neuchâtel, le 22 juillet 2016

Le Doyen, Prof. B. Colbois

B. Colbois.

ACKNOWLEDGMENTS

Having accomplished the incredible journey into science called “PhD Thesis”, I am well aware of the extraordinary support I received during these last four years. Therefore, I take this occasion to thank the people that have been of fundamental importance for the success of this work. Those who are familiar with me might already know that I favor action to speech. For this reason, this paragraph might appear very short compared to the gratitude that has grown inside myself.

I deeply thank Professor Neier, who has the unique ability of being lovely and irritating at the same moment. In science and in the daily life, he is one of the people who taught me to never give up. Never. Thanks to him, I am now a doctor in sharp persistence.

I genuinely thank Professor Herzig for having been an example of freedom. One should always be aware that we can become anything we want and that light cannot be slowed down.

I thank the members of my jury, Professors Südmeyer and Descrovi, for dedicating their precious time to the careful reading of my manuscript. It has been a great honor for me to discuss my work with you. You made every detail valuable.

Finally, I thank my fellow travelers, colleagues from the two laboratories I have been working in, for being friends above all. I hope I have taught you at least half of what I have learned from you.

“Don't fake it baby, lay the real thing on me
The church of man, love
Is such a holy place to be
Make me baby, make me know you really care
Make me jump into the air.”

(David Robert Jones aka Bowie)

ABBREVIATIONS

Å	Armstrong
Abs	Absorbance
ACh	Acetylcholine
AChE	Acetylcholinesterase
AD	Alzheimer's Disease
AFM	Atomic Force Microscopy
APP	Amyloid Precursor Protein
APTES	(3-AminoPropyl)TriEthoxySilane
ATR	Attenuated Total Reflection
Aβ	Amyloid-Beta Peptide
BEDLS	Bloch Surface Wave-Enhanced Dynamic Light Scattering
BILSI	Bloch Surface Wave-Induced Light Scattering
BSA	Bovine Serum Albumin
BSW	Bloch Surface Wave
CD	Circular Dichroism
CMOS	Complementary Metal-Oxide Semiconductor
d.i.	deionized
Da	Dalton
DLS	Dynamic Light Scattering
DMSO	DiMethyl SulfOxide
ELISA	Enzyme-Linked ImmunoSorbent Assay
em	emission
ex	excitation
FTIR	Fourier Transformed InfraRed (spectroscopy)
Gnd	Guanidinium
HFIP	1,1,1,3,3,3-HexaFluoro-2-Propanol
HMW	High Molecular Weight
HPLC	High-Performance Liquid Chromatography
LMW	Low Molecular Weight
m/v	mass/volume
MMF	Multi-Mode Fiber
MW	Molecular Weight
NFT	NeuroFibrillary Tangle
NHS	N-HydroxySuccinimide
NIR	Near InfraRed
NMDA	N-Methyl-D-Aspartic Acid
NMR	Nuclear Magnetic Resonance

ABBREVIATIONS

NP	Nucleated Polymerization
OM	Optical Microscope
PBS	Phosphate Buffer Solution (Chapter 4)
PBS	Polarizing Beam Splitter (Chapter 6)
PDMS	PolyDiMethylSiloxane
PECVD	Plasma-Enhanced Chemical Vapor Deposition
PEG	Polyethylene Glycol
PHF	Paired Helical Filaments
PMF	Polaritation-Mantaining Fiber
PPST	Plasma-Polymerized STyrene
REDLS	Resonance-Enhanced Dynamic Light Scattering
RIU	Refractive Index Unit
SAM	Self-Assembled Monolayer
SDS	Sodium Dodecyl Sulphate
SEC	Size Exclusion Chromatography
SEIRA	Surface-Enhanced Infrared Absorption Spectroscopy
SEM	Scanning Electron Microscopy
SERS	Surface-Enhanced Raman Spectroscopy
SEW	Surface Electromagnetic Wave
SLS	Static Light Scattering
SMF	Single-Mode Fiber
SNR	Signal-to-Noise Ratio
SP	Surface Plasmons
SPR	Surface Plasmon Resonance
TE	Transverse Electric
TEA	TriEthylAmine
TEM	Transmission Electron Microscopy
ThT	Thioflavin T
TIR	Total Internal Reflection
TIRM	Total Internal Reflection Microscopy
TM	Transverse Magnetic
Tris	Tris-(hydroxymethyl)-aminomethane
TROL	D-Tryptophanol
UV	UltraViolet
v/v	volume/volume
WaterLOGSY	Water-Ligand Observation with Gradient SpectroscopY
WEDLS	Waveguide-Enhanced Dynamic Light Scattering
Δn	refractive index variation

International Abbreviations of Amino Acids

Amino Acid	Three letter code	One letter code
Alanine	Ala	A
Arginine	Arg	R
Asparagine	Asn	N
Aspartic Acid	Asp	D
Cysteine	Cys	C
Glutamic Acid	Glu	E
Glutamine	Gln	Q
Glycine	Gly	G
Hystidine	His	H
Isoleucine	Ile	I
Leucine	Leu	L
Lysine	Lys	K
Methionine	Met	M
Phenylalanine	Phe	F
Proline	Pro	P
Serine	Ser	S
Threonine	Thr	T
Tryptophan	Trp	W
Tyrosine	Tyr	Y
Valine	Val	V

ABSTRACT

The misfolding and aggregation of amyloid proteins has been associated with incurable diseases such as Alzheimer's or Parkinson's disease. In the specific case of Alzheimer's disease, insoluble mature fibrils formed of amyloid-beta (Aβ) peptide aggregates are one of the gross features detectable in brain of Alzheimer-disease-affected patients. Insoluble mature fibrils were for long time believed to be the main culprit of the pathology. Recent studies have shown that cell toxicity is caused by soluble oligomeric forms appearing in the early stages of aggregation, rather than by insoluble mature fibrils. Soluble Aβ oligomers are of difficult identification and study, since the classical amyloid detection techniques are not sensitive enough to reveal their formation. Research on new strategies to investigate Aβ oligomerization is imperative for the better understanding of the causes underlying the Alzheimer’s disease, and to set the basis for the diagnosis of the disease prior to the onset of clinical symptoms.

In this work, we exploit the unique properties of an optical label-free refractometric sensing platform to propose a novel approach for investigating the initial and silent–lag–phase of Aβ42 oligomerization. Our sensing approach allows the real-time optical detection of local refraction index changes occurring as aggregation takes place. The method is based on the optical interrogation of a dielectric multilayer (one-dimensional photonic crystal) sustaining an electromagnetic surface wave, called Bloch Surface Wave (BSW). BSWs generated on dielectric multilayers are sensitive to external perturbations of the refractive index close to the surface of the photonic multilayer. In this work, we report on a proof of principle of the BSW-based detection technique for sensing protein aggregation by monitoring in real time the refractive index variation of an aqueous solution containing the Aβ42 peptide during early aggregation and fibril formation. The multilayer surface is directly contacted with the probed aqueous medium and the sensing chamber is positioned vertically. Hence, we exploit BSWs to locally probe the refractive index variations of a solution wherein the Aβ42 peptide is initially injected in a monomeric form and is progressively aggregating to form fibrils. During this process, the Aβ42 peptide tends to precipitate away from the multilayered surface, therefore, the measurements using BSWs monitor a local variation of the refractive index of the solution, which is directly related to the depletion of the concentration of the Aβ42 monomeric form during aggregation.

We demonstrate the efficacy of the BSW approach by monitoring in real-time the first crucial steps of Aβ42 oligomerization. To address a selective sensing of the analyte, we devise a surface chemical functionalization strategy. Furthermore, we provide new insights into the complex mechanism of aggregation of this protein system in the presence of small molecular probes able to interfere with the dynamics of amyloid formation. As a control method, spectroscopic methods, Transmission Electron Microscopy, Thioflavin T binding assay, and NMR-based measurements are used to morphologically characterize the sample during aggregation. Finally, we present a potential improvement of the setup to perform a simultaneous light scattering measurement, with the purpose of real-time monitoring the size change of the Aβ aggregates, throughout fibrillization.

KEYWORDS

Protein aggregation; Alzheimer's disease, amyloid-beta peptide; biosensing; photonic crystals; Bloch surface wave.

TABLE OF CONTENTS

Chapter 1: Introduction

Chapter 2: Objectives and Strategy

Chapter 3: Real-time Amyloid Aggregation Monitoring with a Photonic Crystal-based Approach

Chapter 4: Chemical Surface Modification Strategy to Improve BSW-Based-Sensing Performances

Chapter 5: The BSW-Based Platform as a Tool to Investigate Molecular Probes Interfering with Aβ Aggregation

Chapter 6: Combining BSW-Based Sensing and Light-Scattering Measurement: a Setup Improvement

Chapter 7: Conclusion and Perspectives

Chapter 8: Experimental Materials and Methods

1. INTRODUCTION

1.1 Amyloidosis and conformational diseases

When talking about conformational diseases, one implies the illnesses arising from aggregate deposits of specific peptides or proteins in different human tissues(1). They originate when peptides or proteins fail to adopt, or to maintain, their native functional conformation, and are generally referred to as protein misfolding diseases. Conformational diseases include pathological states in which lack of the folding efficiency of a given protein results in a reduction in the quantity of the protein that is available to play its physiological function(2). Nowadays, more than 40 human diseases are known to be associated with such an impairment(3). Generally, these peptidic or proteic deposits can be of two different natures: amorphous (disordered) or fibrillar (ordered). Examples of amorphous protein aggregates are the “inclusion bodies”: they can be caused, for instance, by a viral infection and consist mostly in viral capsid proteins. On the contrary, fibrillar or ordered aggregates are mostly represented by “amyloid” fibrils. Amyloid fibrils, or their precursors, are polymeric assemblies characterized by high β-sheet secondary structure(4-6). By classical definition(7), amyloid aggregates possess three key-features: a characteristic green birefringence when stained with Congo Red, fibrous morphology observed by transmission electron microscopy (TEM), and a distinctive X-ray diffraction pattern consistent with a high β-sheet content and cross-β-sheet quaternary structure. In contrast to α-helix structure in which hydrogen bonding is formed between residues within the same strand, the hydrogen bonding in β-sheet structures is among strands(8). This structural feature of the β-sheet allows the formation of intermolecular β-pleated sheets, which are most likely stabilized by protein oligomerization and fibrillization(9).

Generally, these aggregated structures are referred to as amyloid fibrils, or plaques, when they accumulate extracellularly, whereas the term "intracellular inclusions" has been suggested as more appropriate when fibrils morphologically and structurally related to extracellular amyloid form inside the cell(10). The intracellular inclusions thus have amyloid-like characteristics, and are not to be confused with the previously described inclusion bodies, which are amorphous.

The formation and deposition of amyloid fibrils in specific organs or tissues are key events in the pathogenesis of many degenerative diseases, which are in general referred to as "amyloidoses". In a further attempt to classify these diseases, one can group them into neurodegenerative conditions, in which aggregation occurs in the brain, non-neuropathic localized amyloidoses, in which aggregation occurs in a single type of tissue excluding the brain, and non-neuropathic systemic amyloidoses, in which aggregation occurs in multiple tissues(3). Accordingly, a selection of amyloidoses is presented in Tab.1.1.1.

Disease	**Aggregating protein or peptide**
Neurodegenerative diseases	
Alzheimer's Disease	Amyloid β peptide
Spongiform Encephalopathies	Prion Protein or fragments of it
Parkinson's Disease	α-Synuclein
Dementia with Lewy bodies	α-Synuclein
Frontotemporal dementia with Parkinsonism	Tau protein
Nonneuropathic Diseases (systemic and localized)	
Lysozyme Amyloidosis	Mutants of Lysozyme
Fibrinogen Amyloidosis	Variants of Fibrinogen α-chain
Type II Diabetes	Amylin, also called Islet Amyloid Polypeptide
Medullary Carcinoma of the Thyroid	Calcitonin
Atrial Amyloidosis	Atrial Natriuretic Factor
Hereditary Cerebral Haemorrhage with Amyloidosis	Mutants of Amyloid β Peptide
Inclusion-body Myositis	Amyloid β Peptide

Tab.1.1.1. Partial list of human amyloidoses. Diseases associated with formation of extracellular amyloid deposits or intracellular inclusions with amyloid-like characteristics are here presented. Table adapted from Chiti & Dobson, 2006(3), with the permission from Annual Reviews.

1.1.1 Protein aggregation

Prior to get into the details of the specific case of amyloid aggregation, it is imperative to provide with an overall view of protein aggregation mechanisms. It is well accepted that any—if not all—protein or peptide, under specific condition, can undergo aggregation process(9). The general fundamental model for protein aggregation is shown in Fig.1.1.1, where the native forms, ordered aggregates (amyloid fibrils), and amorphous aggregates (inclusion bodies) are all formed from the unfolded protein through intermediates. Hence, the intermediate can be considered a building block or a subunit, both in pathologic and in non-pathologic conditions(11). Commonly, aggregates are formed upon an intermolecular hydrophobic interaction between surfaces, and the spreading in three dimensions of these intermediates forms larger aggregates(12). The aggregates precipitate once the solubility limit is exceeded. On the contrary, in the final folding state, which is normally associated with the functional native conformation of the globular protein, the hydrophobic surfaces are relatively sealed within the three dimensional structure, thus becoming inaccessible to intermolecular interactions. Thus, the native conformation is soluble(13).

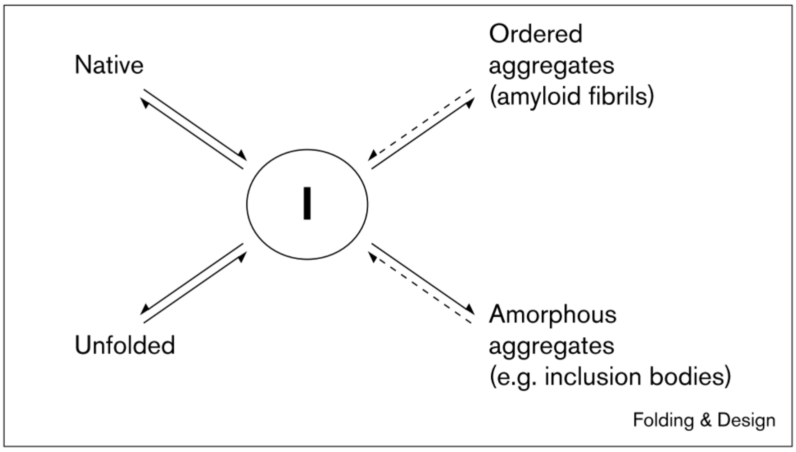

Fig.1.1.1. The basic model for protein aggregation. The central circle represents the intermediate, which is normally un- or partially folded. It can have as origin either the unfolded state (originating from the protein translation process) or the native state. It can itself be the transition state in the normal process of protein folding. Nevertheless, the intermediate has a high propensity to aggregate, leading to either ordered or disordered (amorphous) aggregates according to its amino acid composition. Image reprinted from Fink, 1998(13), with the permission from Elsevier.

1.1.2 Amyloid aggregation: mechanistic models

In the specific case of amyloid aggregation, three prevalent mechanistic models have been proposed depending on a different nature of the intermediate. The first model is known as the “Templated Assembly” (TA), and was first introduced by Griffith in his 1967 Nature article(14). It states that the aggregation is triggered by the formation of a preassembled nucleus, which binds to a soluble state (S) monomeric peptide or protein in a random-coil conformation. The assembly of the fibril is then coincident with the structural change of the peptide, which assumes the conformation of the aggregate (the A state) (Fig.1.1.2, (a)). The second model was first presented by Prusiner in 1982 and published in Science(15). This model is nowadays known as the "Monomer-Directed Conversion" (MDC) model and suggests that, contrary to the TA model, the transition of the monomeric peptide to the conformation called the A state, prone to aggregation, occurs prior to the formation of fibrils. This A-state monomer binds and converts an S state monomer into another A-state monomer prone to rapidly attach to the end of the growing fibril (Fig.1.1.2, (b)). The third model is probably the best known and most often cited: the nucleated polymerization (NP) mechanism, which was fully described by Jarrett & Lansbury in Cell in 1993(16). In the NP model the formation of a nucleus is the result of an equilibrium between monomers that are (A state) and are not (S state) in an aggregation-competent conformation. Thereafter, the aggregation proceeds by the addition of A-state monomers to the growing end of the fibril (Fig.1.1.2, (c)). In this thesis work, we mainly focused on the NP model and made advantage of it to interpret our results.

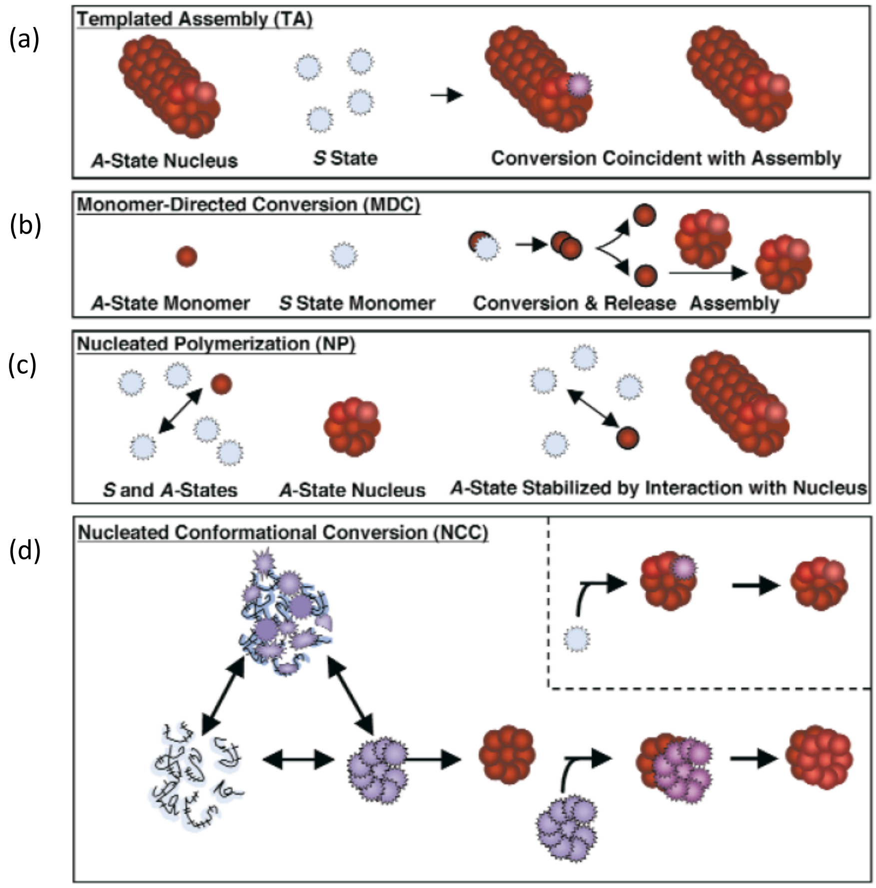

Fig.1.1.2. Putative models for conversion of amyloidogenic polypeptides (monomers) into amyloid fibrils(17). Figure reprinted from Serio *et al*, 2000(17) with modification by Lindquist and Feder, 2002(18), with the permission from Nature Publishing Group.

For the sake of completeness, we here describe a fourth model, which was notably introduced by Serio *et al* in 2000 and published in Science(17). This model was presented to particularly explain yeast prion amyloidogenicity. It is known as the "Nucleated Conformation Conversion" (NCC) model and one can perceive it as a modern and more complete adaptation of the NP model. This model introduces the role of molten oligomeric species as intermediates responsible for triggering the fibrillization. The authors propose that "nuclei form by conformational rearrangements within structurally dynamic oligomers lacking a defined quaternary structure. Once nuclei are formed, they interact with a structurally flexible oligomer with a distribution of subunits, adding a group of subunits to the fibril end simultaneously"(18) (Fig.1.1.2, (d)). The authors speculate that the oligomers have an initial micellar structure and that are in a continuous equilibrium with monomers and aggregates.

1.1.3 Amyloid aggregation: kinetics

As mentioned before, in this project we especially regarded the NP as the fundamental model to describe amyloid aggregation, for kinetic studies strongly support it, thus being the best accepted by many authors(7, 19, 20). The kinetics of amyloid fibril formation explained with the NP model can be represented with a sigmoidal curve, typical of cooperative reactions, related to the extent of formed fibrils(7), as represented in the graphs in Fig.1.1.3 (a). The amyloid aggregation process typically begins with a "lag phase", in which no fibril formation is observed and no variation in the signal is observed. From a thermodynamic point of view, during the lag phase the entropically unfavorable process of nuclei formation occurs. The length of the lag phase, as represented in Fig.1.1.3 (a), strongly depends on the initial concentration of the amyloid monomer(21), in such a way that the higher the concentration, the shorter this silent phase is. Once the nuclei are formed, aggregation proceeds abruptly via fibrillization, and this corresponds to a sudden increase of the signal. A plateau is then reached when the amyloid fibrillization process has ended. This is due to the depletion of the soluble species that are converted into fibrils, thus resulting in a decreased fibrillization rate. The rate of the fibrillization process can be varied, and in general, increased, upon the "seeding" of the system, which corresponds to the introduction of pre-formed nuclei. With this interference, very often a lack of a lag phase has been reported, typical of cooperative assembly(7).

Recently, several authors have reported what is known as "secondary nucleation mechanism"(22, 23), for which the primary nucleation step can also be followed by secondary processes that lead to the spreading and multiplication of amyloid fibrils (see Fig.1.1.3 (b)).

Specifically, these secondary processes involve: the fragmentation of the amyloid fibril, to whose extremities the soluble amyloid proteins can attach; the monomer-dependent secondary nucleation, in which already existing aggregates catalyze the formation of new nuclei(9). The introduction of the monomer-dependent secondary nucleation has helped explaining the, albeit often stochastic(24), length of the lag phase of the NP mechanism. This theory has served more precise and modern mathematical models to fit experimental kinetics of amyloid aggregation, compared to those stemming from the original and classical NP model(25).

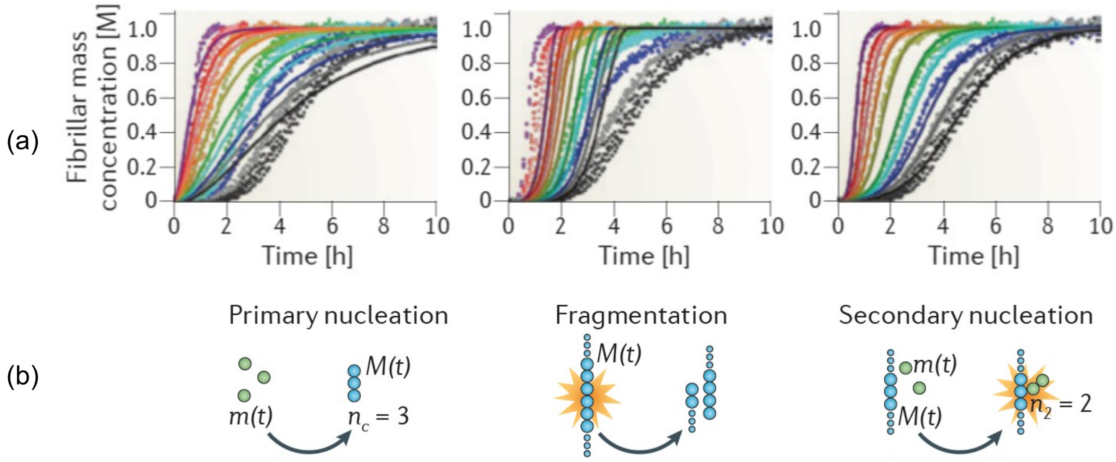

Fig.1.1.3. Kinetics of the aggregation of a protein into amyloid fibrils. (a) Experimental kinetics of amyloid aggregations for different initial monomer concentrations. (b) Schematic representation of the processes of primary nucleation, fibril fragmentation, and secondary nucleation. The fits in (a) use mathematical models where the prevalent mechanisms are primary nucleation, fragmentation, and secondary nucleation, respectively. The agreement between experimental and numerical model for the secondary nucleation mechanism is highlighted. Figure adapted from Knowles *et al*, 2014(9), with the permission from Nature Publishing Group.

1.2 Alzheimer's disease

The Alzheimer's disease (AD) is an aberrant fatal neurodegenerative disease that causes the loss of the neural tissues resulting in disorders regarding memory, ability to communicate, mobility and, finally, with the death of the patient(26). The name "Alzheimer" originates from the German neurologist, Dr. Alois Alzheimer, who, in 1907, first described the case of a 51-year-old female patient that showed severe cognitive disorders pertaining to memory, language, and social interactions. Alzheimer performed an autopsy of the patient and described a dramatic shrinkage of the brain, especially of the cortex, and what he believed to be fatty deposits in small blood vessels, dead and dying brain cells, and abnormal deposits in and around cells(27, 28).

At present, AD has become the most common neurodegenerative disease in the world with more than 25 million patients worldwide, and it is among the ten leading causes of death in the developed countries. AD will become more and more common in the coming decades, especially because of the increased life expectancy and changing population demographics. According to the 2015 World Alzheimer Report, in the United States alone, 5.3 million people are affected by the disease(29). In a study carried out by Hebert *et al* in 2013(30), it has been estimated that, by 2025, the number of people aged 65 and older with AD will reach 7.1 million in the United States. The number of patients is expected to increase to 13.2 million in the United States by 2050 (see Fig.1.2.1), and 114 million worldwide, if new preventive or neuroprotective therapies do not emerge(29).

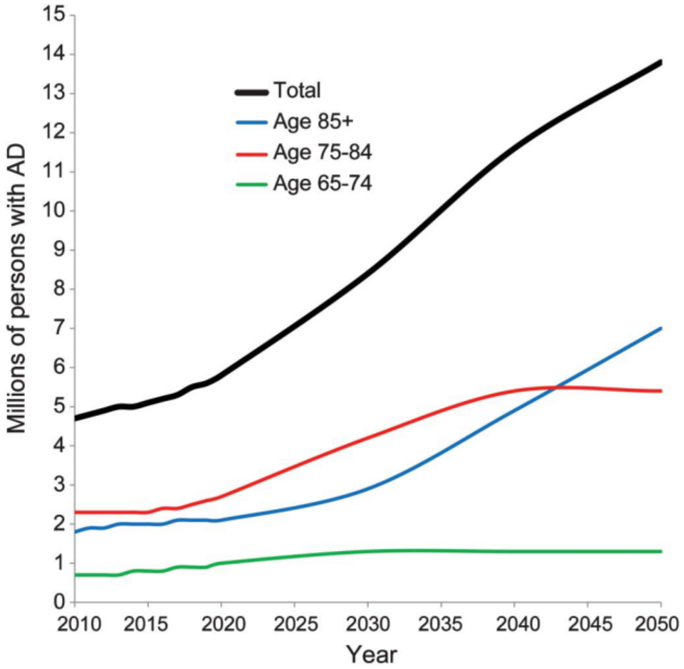

Fig.1.2.1. Projected number of persons in US population with Alzheimer disease. Prospected data are reported by age groups, 65 to 74 years old, 75 to 84 years old, and 85 years and older, using the 2010 US Census Bureau middle-series estimate of population growth. Image reprinted from Hebert *et al*, 2013(30), with the permission from Wolters Kluwer Health, Inc.

Despite a great effort is constantly put on research for preventing and curing AD, leading to the expense of $631 million per year in the USA only(31), AD is a complex disease and the cause for its onset is not yet fully understood. There is no definitive cure to AD(26).

Commonly, AD pathology is characterized by two main abnormal histological features: structures formed by aggregated protein deposits called plaques and neurofibrillary tangles (NFT) are present in neural tissue of AD patients(10). Plaques are found in the extracellular brain matrix, and contain deposits of a protein fragment called beta-amyloid (Aβ), while NFTs are twisted fibers of a protein called Tau, forming intracellularly. Although plaques and NFTs might develop in healthy people as they age(32), AD patients tend to develop massive amounts of these protein deposits, which, notably, tend to form in a predictable pattern, beginning in brain areas involved in learning and memory, and then spreading to other brain regions. Although the gross histological features of AD in the brain are well characterized, a “century-old debate” on the correlation between protein aggregation and neurodegeneration has not been sufficient for researchers to unequivocally identify what role plaques and NFTs play in AD(10, 32, 33). Even the specific mechanisms of cell death occurring during AD is disputed, since it is not fully understood whether it is the result of the activation of apoptotic or necrotic mechanisms(34).

1.2.1 Main theories on Alzheimer's disease etiology

From the histological observations of brain tissues affected by AD, two major misfolding hypotheses have been advanced regarding the primary cause of AD: the "Tau Hypothesis" and the "Amyloid Hypothesis". They suggest that either Tau protein or Aβ peptide misfolding and aggregation trigger the onset of the disease by disrupting the neural signaling or by interfering with normal cell activities(35). Another accepted hypothesis is also the oldest: The so-called "Cholinergic Hypothesis" suggests that deficits in cholinergic neurotransmission prompt the development of the disease(36). While researchers have not identified an unambiguous causative pathway originating from any of the three molecular hypotheses to explain the gross anatomical changes observed in advanced AD, variants of the amyloid hypothesis have become dominant among the three possibilities(2, 32, 37). In this work, we focused our research on the Aβ peptide investigation, thus considering the amyloid hypothesis as the prevailing. Before illustrating it in details, the other hypotheses are briefly presented in the following.

- **Cholinergic hypothesis**

The "cholinergic hypothesis of Alzheimer's disease" was first postulated in the mid-1970s when researchers remarked substantial deficits of the choline acetyltransferase enzyme, responsible for acetylcholine (ACh) synthesis, in subjects affected with AD(36). This observation, together with subsequent studies on another enzyme related to the degradation of ACh, the acetylcholinesterase (AChE), lead to the belief of a strong correlation between ACh signaling in neural tissue and the development of AD. Nowadays, this correlation is considered less as a cause, but mostly as a result or a secondary effect of other complex mechanisms underlying the disease(38). Nevertheless, current approved and administered pharmacological AD treatments are mostly effective on the replacement of presynaptic ACh, having been developed based on the cholinergic hypothesis(39). These are clearly all palliative treatments, used to improve life quality of AD patients and of their families, and consist mainly in AChE-inhibitor medicaments. The first drug of this class to be approved by the FDA for the treatment of mild to severe AD was galantamine (in 2001), followed by donezepil (in 2006), and rivastigmine (in 2006, and in 2007 the rivastigmine transdermal patch became the first patch treatment for dementia). Notably, memantine (approved by FDA in 2003) is the exclusive approved drug acting on the glutamatergic system by reversibly blocking NMDA-glutamate receptor, which is responsible for synaptic plasticity, instead of directly inhibiting AChE, thus being the flagship of a novel class of AD medications(40-42).

- **Tau hypothesis**

Tau protein aggregation must play a more complex and compelling role in the development of AD. Tau protein is a microtubule-associated protein expressed in mainly normal mature neuron, promoting assembly and stability of microtubules in the neural cytoskeleton. This biological function is negatively regulated by the degree of phosphorylation of specific Ser or Thr amino acidic residues of the protein. Hence, pathogenic hyperphosphorylation of Tau is associated with the disintegration of microtubules, resulting in the degradation of the neural cytoskeleton, but also with the aggregation of Tau itself. In AD subjects, hyperphosphorylated Tau has been reported to accumulate as paired helical filaments (PHF) that in turn aggregate into NFT masses inside nerve cell bodies (see Fig.1.2.2) and as dystrophic neurites associated with amyloid plaques(43, 44).

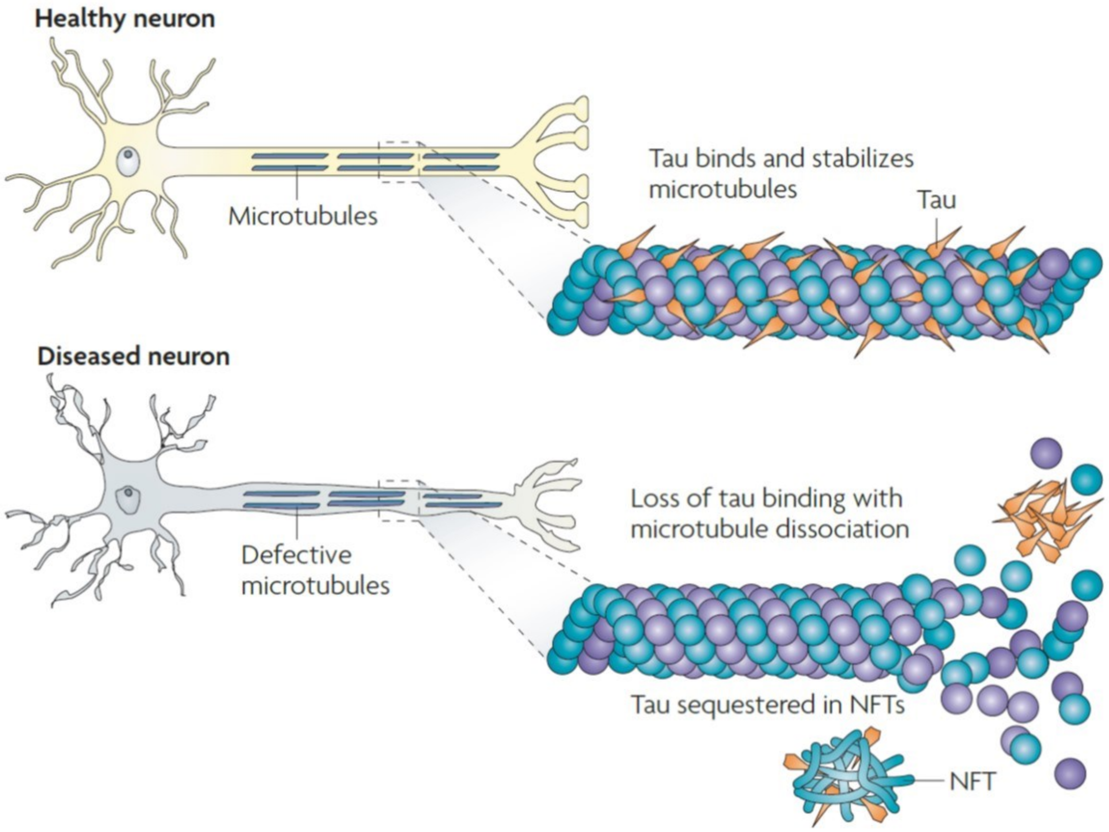

Fig.1.2.2. Schematics of the role of tau-protein as microtubule-associated protein and its aggregation into intracellular NFTs. Image reprinted from Brunden *et al*, 2009(44), with the permission from Nature Publishing Group.

Many neurons in the brain regions typically affected in AD contain large, non-membrane-bound bundles of abnormal NFTs that occupy much of the perinuclear cytoplasm. However, scientific unanimity has not been reached on whether Tau hyperphosphorylation is the cause or the consequence of the formation of the abnormal PHFs(45).

1.2.2 The amyloid hypothesis and the amyloid-β peptide

The well accepted "Amyloid Hypothesis" was first formulated more than 20 years ago by Hardy & Higgins(46), when the correlation between the abnormal deposition of Aβ peptide in amyloid plaques and the development of AD in patients was starting to emerge(37, 47, 48). This unequivocal connection stemmed from the observation that patient with trisomy 21, also known as Down syndrome, inevitably exhibited AD-like disorders. Studies led to the identification of a gene located on chromosome 21 encoding for the amyloid precursor protein (APP)(49). APP is a large type I transmembrane protein expressed, among other tissues, in the synapses of neurons, and subject to a proteolytic cleavage performed by enzymes called α-, β- and γ- secretases. For example, the specific cleavage of APP performed by β- and γ-secretases forms the N- and C- termini, respectively, of the Aβ peptides(50). Among a relatively large pool of products of the APP molecular processing(51), the Aβ peptides were identified as the main components of the senile neuritic plaque of AD patient brain tissue(47). The link between the overexpression of APP in patients with trisomy 21 and the presence of Aβ peptides in neuritic plaques characteristic of AD was then drawn: The amyloid hypothesis was postulated(37). This discovery opened a new and advanced field of research aimed at determining the actual origin and molecular mechanism underlying AD. Especially, this lead to the formulation of the "amyloid cascade" hypothesis, which postulates the role played by the Aβ42 peptide, one of the longest APP double-cleavage product, in dementia. Accordingly, an overproduction and ineffective clearance of Aβ42 peptide in the brain triggers neuronal degeneration and is the initiating event of the disease, as it results in the accumulation and aggregation of Aβ42 in amyloid plaques(37, 46).

As presented in Fig.1.2.3, the amyloid cascade hypothesis has been recently revised in the light of the failure of several therapeutics designed based on it(52), which either targeted the production of Aβ42 by inhibiting γ-secretase(53), or bound soluble Aβ42 to prevent its aggregation into fibrils(54, 55). Moreover, accumulating evidences from human AD studies revealed that amyloid plaque extent poorly correlated with cognitive impairment and severity of dementia(32). Nowadays, a growing body of evidence ascribe the neural cytotoxicity to the first soluble oligomeric aggregated forms of the Aβ42 peptide, rather than to the insoluble amyloid plaques formed by advanced-aggregation-stage fibrils(32, 56-59). Aβ42 oligomers formation, nature and plausible mechanism of toxicity are described in the following sections. For the sake of simplicity, the genetic aspects correlated to the onset of AD are not discussed in this dissertation. They are briefly summarized in Fig.1.2.3, where they are linked to the activation of Aβ42 production. They are specific of particular forms of AD, and have not yet been unequivocally correlated to sporadic AD(32, 50, 60).

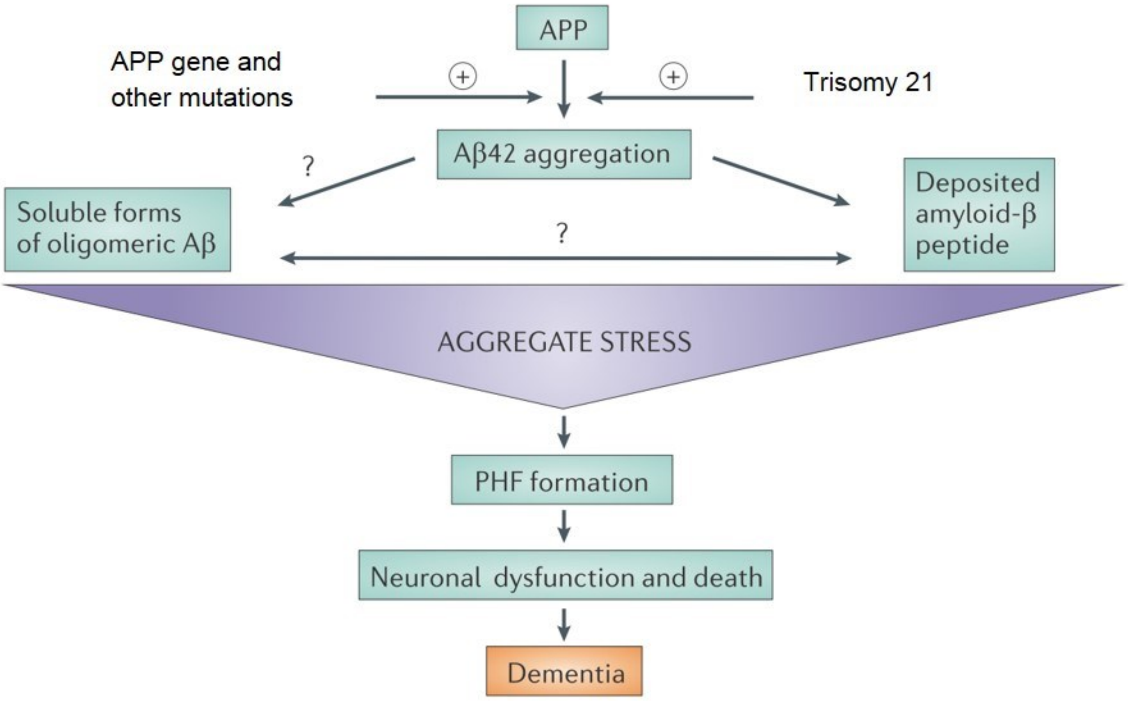

Fig.1.2.3. The sequence of pathogenic events leading to AD proposed by the amyloid cascade hypothesis. The amyloid cascade hypothesis now suggests that synaptotoxicity and neurotoxicity may be mediated by soluble forms of oligomeric amyloid-β peptide species. The dynamic nature of these species and the poorly defined mechanism (or mechanisms) of toxicity make this topic particularly controversial in the field. Given this uncertainty, we prefer to use the term 'aggregate stress' to describe the potential mechanisms that may lead to amyloid-β aggregation, the formation of paired helical filaments (PHFs) of Tau aggregates and, ultimately, result in neuronal loss. Image and caption adapted from Karran *et al*, 2011(52), with permission from Nature Publishing Group.

1.2.3 Aβ aggregation pathway and structure

In the previous sections we described the general mechanism of amyloid aggregation. The NP model supports the explanation of the *in vitro* observed aggregation pathway of many amyloidogenic proteins, including the Aβ peptide. The Aβ peptide is approximately 4kDa and the length varies from 39 to 43 residues, with most of the heterogeneity at the C-terminus. The predominant species that are found in amyloid plaques in brain are the Aβ42 and Aβ40. Both peptides undergo *in vitro* fibrillization with similar mechanism, but different critical concentration and aggregation rates(19, 61, 62). In most of the cases, the research on Aβ peptides encompasses the parallel investigation of both Aβ42 and 40, especially for the latter forms fibrils at lower kinetic rates(63), thus resulting less demanding in studies with "slow-outcome" techniques(64). The sequences of the two peptides are shown in Fig.1.2.4.

Fig.1.2.4. Sequence of human Aβ40 and Aβ42. Colors indicate residues with hydrophobic (green), polar (magenta), positively charged (blue), and negatively charged (red) side chains.

Although Aβ40 is the predominant species produced during APP processing(65), Aβ42, which accounts for only about 10% of total secreted Aβ peptides, is more hydrophobic, more cytotoxic and much more prone to aggregate than Aβ40(23, 65), thus having been commonly accepted as the major culprit of AD(57). As depicted in Fig.1.2.4, the minor differences in the C-terminal cleavage at Val40 or Ala42 have profound consequence on the propensity of aggregation and fibril formation(61), which is schematically represented in Fig.1.2.7.

The Aβ42 peptide is intrinsically disordered or natively unfolded at physiological conditions in its free soluble form, the monomer(66, 67). As the critical concentration of the monomer is exceeded (*in vivo*, in the order of few nM(68), despite dissensus exists among different authors, which have reported values that differ significantly(19)) the monomer undergoes structural transformations for, or driven by, the self-assembly(32). As described by the NP model, monomers assemble to form the first soluble oligomeric nuclei, around which the aggregation proceeds, as represented in Fig.1.2.7. Throughout the elongation phase, mature fibrils are produced(4). They are formed by a bundle of fibrous protofilaments and characterized by typical β-sheet secondary structure(5) (see Fig.1.2.7). As shown in Fig.1.2.5, results from solid state NMR of Aβ40 fibrils(64) have revealed an in-register parallel β-sheet alignment of peptide chains within the cross-β motif. A series of cross-β pleated sheets are oriented parallel to the main (long) axis of the fiber, while the direction of the β-strands constituting the β-sheet is perpendicular to the main axis of the fiber. The hydrogen bonds between strands are thus parallel to the fibril long axis(4, 5).

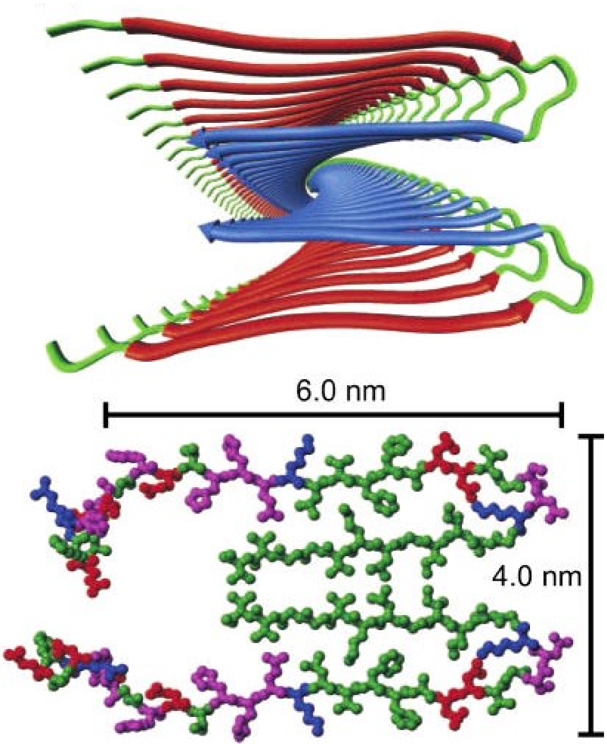

Fig.1.2.5. NMR-derived structural model for Aβ40 protofilaments within fibrils. Top: view of the protofilament through the long axis of the fibril. Parallel in-register β-sheet motifs between separate strands of the peptide (red and blue) form a double-layered cross-β pattern. Bottom: atomic representation of Aβ40 monomers within the fibril structure. Colors are consistent with those used in Fig.1.2.4 to represent hydrophobic (green), polar (magenta), positively charged (blue), and negatively charged (red) side-chains residues. Image reprinted from Tycko, 2003(69), with permission from the American Chemical Society.

While the Aβ fibrils structure model has gained large consensus, interestingly, many types of prefibrillar assembly of Aβ have been isolated and described in the literature, including: Aβ dimers and trimers(70), doughnut-shaped oligomers(71), protofibrils (not to be confused with protofilaments, which are the fibril subunits, as explained before)(72), Aβ derived diffusible ligands (ADDLs), annular Aβ assemblies(58). Generally, they can be defined as high molecular weight (HMW) oligomers when they can be visualized by imaging techniques such as AFM and TEM, being formed by more than 8 monomers, or low molecular weight (LMW) oligomers, when composed of a smaller number of monomers. For example, protofibrils are a heterogeneous mixture of HMW oligomers, metastable, with β-sheet content, revealing curvilinear shape when observed at TEM, and nearly incapable to form fibrils when deprived of free monomers. A robust protocol for the preparation of protofibrils has recently been developed by Jan *et al*(73). Finally, LMW and HMW oligomers are all examples of "soluble oligomers". The term "soluble Aβ oligomers" encompasses any form of Aβ aggregate that is soluble in aqueous buffer and remains in solution after high-speed centrifugation(74). In contrast, mature fibrils are insoluble(10). All the amyloid assemblies here enumerated, regardless of their solubility, reportedly share a common predominant β-sheet secondary structure(57).

1.2.4 On Aβ42 peptide neurotoxicity

At this point, the following questions remain to be addressed: If mature fibrillar Aβ42 assembly are not the main culprit of AD, what is the key-feature that differentiates them from toxic soluble oligomers? What is the mechanism by which soluble Aβ42 oligomers disrupt hippocampal long-term potentiation and thereby cause deficits in learning behavior, as has been reported in *in vivo* studies conducted on rat models(75)? In other studies(76, 77), *in vitro* and *in vivo* treatment of cortical neurons with Aβ42 soluble oligomers led to the downregulation of NMDA receptors and affected the complex system of signaling pathways that are required for synaptic plasticity, thus supporting previous research.

For decades, β-sheet architecture was regarded as the feature for toxicity in fibrils(10, 78). Nowadays, the fibrillar amyloid complex is well accepted as the minimum-energy state of the self-assembly aggregation reaction, thus being the state “biologically conceived” to suppress intermediates toxicity in amyloidoses by capturing them in a more stable complex(9). Minimum-energy-state species are unlikely to take part in reactions whatsoever because they are in a thermodynamic sink. In contrast, soluble Aβ42 oligomers are high-energy-state species, being the metastable first aggregated intermediates(79, 80). As a consequence, soluble Aβ42 oligomers cytotoxicity could originate from the interaction of these highly prone-to-react, and still soluble species with the synaptic membrane of neurons(9). This consideration implies the existence of a specific conformation for soluble Aβ42 oligomers that differs from the typical (β-sheet) arrangement of higher order aggregates(81). The extent of this difference had long been under debate, with studies proposing an antiparallel β-sheet motif for soluble oligomers only, in contrast to the widely accepted parallel β-sheet alignment encountered in fibrils(82, 83). Such a relatively small variation was nevertheless insufficient to compensate for the enormous free-energy difference between soluble Aβ42 oligomers and Aβ42 fibrillar assemblies reported in the literature(84). An elucidation came in 2010 from Ahmed *et al*, which published a work on the isolation of pentameric, disk-shaped Aβ42 oligomers that showed high toxicity when added to neuronal cell cultures(56). These unprecedented Aβ42 oligomer samples revealed homogeneous single size distribution of 24 ± 3 kDa. Structural studies indicated that these neurotoxic LMW Aβ42 oligomers were stabilized in a reportedly non-β-sheet secondary structure by the hydrophobic C-terminal residues (see Fig.1.2.6). The authors described a structural conversion in the transition from pentameric Aβ42 oligomers to β-sheet rich pre-fibrillar assemblies, which did not exhibit *in vitro* toxicity.

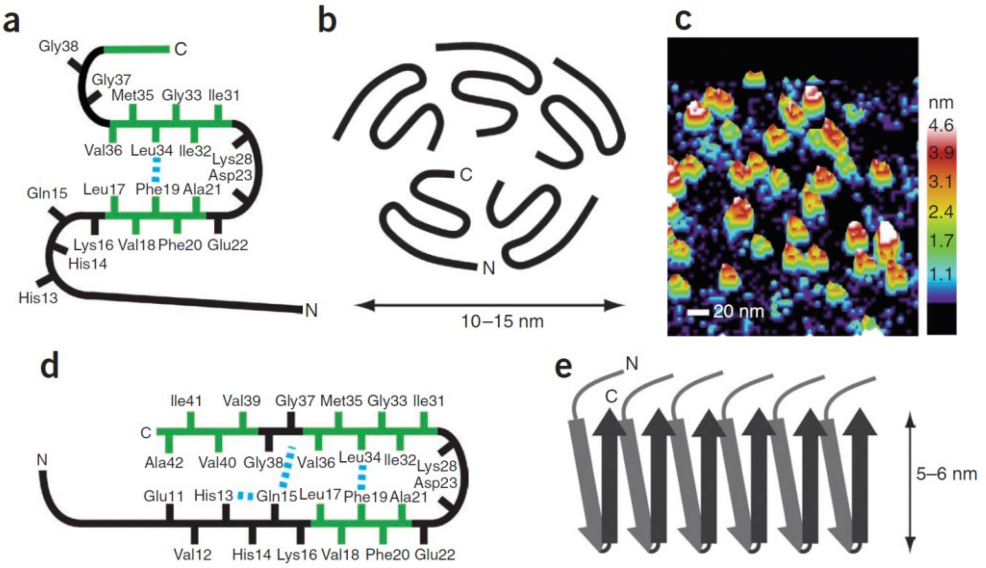

Fig.1.2.6. Molecular models of Aβ42 oligomers and fibrils. (a) Schematic of the monomer within the oligomer complex of Aβ42. (b) Schematic of the Aβ42 pentamer. The orientation of the C terminus is toward the center of the pentamer. (c) Three-dimensional image of single-touch AFM measurements of Aβ42 oligomers. (d) Schematic of the monomer within Aβ42 fibrils. (e) Schematic showing the parallel and in-register packing and staggering of the individual β-strands within Aβ42 fibrils. Image and caption reprinted from Ahmed *et al*, 2010(56), with permission from Nature Publishing Group.

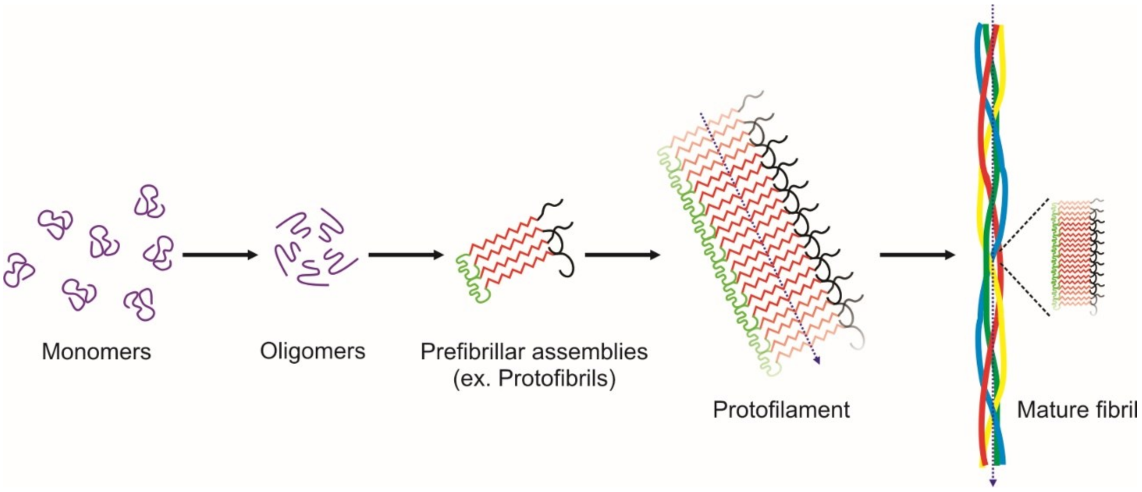

Fig.1.2.7. Simplified schematics of Aβ fibril formation pathway. At a specific concentration and under pathogenic conditions, monomers can misfold and re-organize into soluble aggregates commonly known as oligomers. The oligomeric complex rearranges to the prefibrillar assemblies, characterized by the so-called β-sheets structure (in red), typical of amyloid aggregates. Two such cross-β units comprise the protofilament, here represented in a simplified 2D-single layer. The mature fibrils are made by 2-6 protofilaments. Image and caption adapted from Santi et al, 2014(85), with permission from the Society of Photo Optical Instrumentation Engineers.

1.3 Optical biosensors: state-of-the-art amyloid detection methods

Currently, research is focusing on developing anti-amyloid therapy for future AD treatments aimed at preventing the onset of the disease, rather than curing the symptoms of AD(54, 86, 87). A substantial progress has been made in the understanding of the molecular mechanisms underlying AD. The investigation of the structural transition exhibited by the Aβ42 peptide from its monomeric form, to the soluble oligomer, and, finally, to the β-sheet rich pre- and fibrillar state has been of central importance for the ultimate understanding of toxicity in AD(9, 56). Especially, the notion that a hallmark for toxic oligomers could exist dramatically helps conceiving specific early diagnostic methods, to be applied prior to the onset of AD symptoms(88). In addition, potential molecular treatments begin to be devised based on the precise structure of the Aβ42 oligomer(86). Notably, a great effort is expended on the ongoing development of specific antibodies against Aβ42 peptide epitopes(89), which have hitherto revealed to be mostly ineffective, albeit highly promising(90). To help boosting the advances in the fields devoted to devising specific anti-Aβ42-oligomers treatments and studying oligomerization at a molecular level, a method for the effective and selective detection of soluble toxic Aβ42 oligomeric species is therefore of crucial significance(91). Such a method should provide reliable tools to cover the pathogenic transition occurring during Aβ42 oligomerization. The intimate understanding of this process is directly linked to the possibility of developing therapies. Unfortunately, there is a fundamental lack of valuable techniques capable to cover the early stage of Aβ aggregation process. Classical methods are unresponsive during the lag phase of aggregation, being sensitive to β-sheet structure and, therefore, to high order aggregates. Traditional experimental methods have concentrated on the use of colorimetric assays, in which dyes such as Congo red or Thioflavine T (ThT) exhibit spectral variations upon binding to amyloid fibrils. Other methods, such as TEM, AFM and FTIR, are fundamentally unable to reveal LMW oligomers(73). Very often, not a valid unique technique, but a combination of often poorly selective, expensive and time consuming techniques are exploited(92). Therefore, there is an urgent need of highly sensitive and specific strategies for early Aβ42 oligomers detection that can improve the characterization at the molecular level of these transient intermediates.

New generation optical biosensors should meet up to the challenge of studying biological events as complex as amyloid aggregation. Especially, the non-destructive chemical analysis of biological processes is made possible through optical biosensors. They offer high sensibility, selectivity and robustness(93). A number of sophisticated optical biosensors have been recently applied to biomolecular interaction analysis, delivering kinetic data about biological binding events in real time without labelling. The advantage of the label-free concept, in which biomolecules are unlabelled or unmodified and are detected in their natural forms, is the elimination of detrimental effects from labels that may interfere with fundamental interaction and the absence of a time-consuming pre-treatment. Optical biosensors are also ideal for portable applications that are currently of great interest(91, 94, 95).

An excursus on the most outstanding optical biosensing methods for the detection of amyloid aggregates is presented in the following.

1.3.1 Surface plasmon resonance sensing

Since its first description by Wood in 1902(96), the phenomenon of surface plasmon resonance (SPR) has found countless practical applications in biosensing(97). At specific illumination conditions, surface plasmons (SP) can be excited at the interface between two media, one being a noble metal such as gold or silver. Those conditions are called the resonance ones, and are strongly depending on the refractive index of the outer media, into which the evanescent tail of SP propagates. Once a perturbation of the refractive index of the probed media occurs, new resonance conditions are needed to excite SP. In classical SPR biosensing, the surface of the metallic layer is functionalized with receptors or ligands for the selective recognition of the biomolecule that is under investigation. As the surface immobilization of the specific analyte occurs, an increase of the refractive index is detected as a shift of the resonance conditions or as a variation of the intensity of SP(98).

The most common biosensors used in proteomics are based on SPR(99). Devising SPR-based analytical systems that could be applied to the monitoring of Aβ aggregation has gained enormous attention in the last two decades(92, 100). They offer the possibility to investigate environmental and molecular factors affecting Aβ40(101) or Aβ42(102) monomer tendency to aggregate. In addition, they permit the real-time monitoring of the kinetics of amyloid fibril formation, which can be achieve either by immobilizing pre-formed Aβ40(103, 104) or Aβ42(105) fibrils onto the sensing surface and monitoring their elongation, or by covalently binding the Aβ42 monomer onto the surface for a complete aggregation study(102). SPR has thus become devoted to the discovery of the intimate mechanisms that lead to amyloid aggregation. Even more interestingly, SPR-sensing strategy can also serve as a diagnostic tool for preventive treatments of AD, by the test of antibodies against Aβ42 monomer(106) and oligomers(107, 108).

Unfortunately, SPR-based sensing is also subject to undesiderable factors. Generally, the disadvantages of SPR technique are a deficient sensitivity to a specific signal (due to the relatively small refractive index changes as a result of the binding) and undesirable susceptibilities to non-specific signals, such as detrimental interactions between the analyte and the material composing the metal film of the sensor(91).

1.3.2 Surface-enhanced spectroscopy: Raman and infrared

Raman and FTIR spectroscopy both provide information on the secondary and tertiary structure of proteins in solution, thus having been exploited for multiple biochemical application. Specifically, Raman spectroscopy makes use of several vibrational modes for the analysis of protein structure. Most characteristic bands are associated with the amide group that links the amino acids, referred to as amide I (1700−1600 cm^{-1}) and II bands (1500−1400 cm^{-1}), generated by the scattering of light by the vibrating molecules. Similarly, FTIR spectroscopy provides information about the secondary structure content of proteins. Again, characteristic bands found in the infrared spectra of proteins and polypeptides include the Amide I and Amide II. These arise from the absorption associated with the amide bonds, which is influenced by the protein three-dimensional arrangement and H-bond formation between amino acids(8, 109).

Nevertheless, both these techniques suffer from some tremendous limitations. For example, Raman spectroscopy has a very low sensitivity and is affected by intrinsic fluorescence or absorption of bio-analytes(110), and FTIR performances are hampered by the strong adsorption of water, thus requiring the cumbersome solubilization of protein samples in D_2O(111). Recently, these limitations have been overcome by increasing the output signal via either electromagnetic field enhancement or SP, with the use of metallic surfaces onto which target molecules are adsorbed or to which they are very close to. Therefore, recent years saw the development of surface-enhanced Raman spectroscopy (SERS)(112) and surface-enhanced infrared absorption spectroscopy (SEIRA)(113).

SERS techniques have been extensively employed to the study of amyloid aggregation. In this context, several publications can be found in the literature, spanning from the description of a nanofluidic biosensor to observe Aβ in different conformational states during the self-assembly process(114), to a comparative structural investigation of toxic and non-toxic Aβ42 oligomers(115). In another SERS-based strategy, Beier *et al*(116) envisaged the use of metallic nanoshells to excite SP and improve Aβ detection sensitivity to the pM range. The latter is a complex approach that consisted in monitoring Congo Red signal bound to Aβ peptide. This approach appears as a rather questionable choice if one takes into account that Congo Red binding is reportedly selective to β-sheet architecture only(117), and not to specific conformations of Aβ42 toxic oligomeric assemblies. More recently, Bhowmik *et al*(118) described a sensing scheme in which they made use of gold nanoparticles to excite surface plasmon and, thus, amplify the Raman signal. The authors were able to monitor spontaneous binding of Aβ40 oligomers to the lipid-bilayer-coating of the nanoparticles, which mimicked cell membranes, and to simultaneously provide secondary-structure information on the peptide.

In contrast to SERS, SEIRA techniques are yet to be exploited for the study of amyloid aggregates, but they have delivered highly promising results in real-time monitoring protein interactions in native aqueous environment. In 2013, Adato *et al*(119) reported on what they called “plasmonic internal reflection-SEIRA concept”: making use of plasmonic nanoantennas, they were able to amplify the absorption signal in the infrared region, and to correlate it to the secondary structure of a protein throughout its binding to a specific receptor. In their work, the classical biotin-streptavidin affinity binding was investigated *in situ*, in water and with a monolayer-thickness sample. The eventual application of this sensing technique to the study of amyloid aggregation kinetics and structural transition properties is of extreme interest, especially for experiments could be carried out in the proximity of lipidic membranes coating the nanoantennas, thus mimicking the neural extracellular environment.

1.4 Bibliography

1. Carrell RW & Lomas DA (1997) Conformational disease. *The Lancet* 350(9071):134-138.

2. Dobson CM (2001) The structural basis of protein folding and its links with human disease. *Philos Trans R Soc Lond B Biol Sci* 356(1406):133-145.

3. Chiti F & Dobson CM (2006) Protein misfolding, functional amyloid, and human disease. *Annu Rev Biochem* 75:333-366.

4. Serpell LC (2000) Alzheimer's amyloid fibrils: structure and assembly. *Biochim Biophys Acta* 1502(1):16-30.

5. Makin OS & Serpell LC (2005) Structures for amyloid fibrils. *FEBS J* 272(23):5950-5961.

6. Sunde M, Serpell LC, Bartlam M, Fraser PE, Pepys MB, & Blake CCF (1997) Common core structure of amyloid fibrils by synchrotron X-ray diffraction. *Journal of Molecular Biology* 273(3):729-739.

7. Nilsson MR (2004) Techniques to study amyloid fibril formation in vitro. *Methods* 34(1):151-160.

8. Lehninger AL, Nelson DL, & Cox MM (1999) *Principles of biochemistry* (Worth Publishers).

9. Knowles TPJ, Vendruscolo M, & Dobson CM (2014) The amyloid state and its association with protein misfolding diseases. *Nat Rev Mol Cell Biol* 15(6):384-396.

10. Glenner GG (1980) Amyloid Deposits and Amyloidosis. *New England Journal of Medicine* 302(24):1333-1343.

11. Caughey B & Lansbury PT (2003) Protofibrils, pores, fibrils, and neurodegeneration: separating the responsible protein aggregates from the innocent bystanders. *Annu Rev Neurosci* 26:267-298.

12. Herczenik E & Gebbink MFBG (2008) Molecular and cellular aspects of protein misfolding and disease. *The FASEB Journal* 22(7):2115-2133.

13. Fink AL (1998) Protein aggregation: folding aggregates, inclusion bodies and amyloid. *Folding and Design* 3(1):R9-R23.

14. Griffith JS (1967) Nature of the Scrapie Agent: Self-replication and Scrapie. *Nature* 215(5105):1043-1044.

15. Prusiner S (1982) Novel proteinaceous infectious particles cause scrapie. *Science* 216(4542):136-144.

16. Jarrett JT & Lansbury Jr PT (1993) Seeding “one-dimensional crystallization” of amyloid: A pathogenic mechanism in Alzheimer's disease and scrapie? *Cell* 73(6):1055-1058.

17. Serio TR, Cashikar AG, Kowal AS, Sawicki GJ, Moslehi JJ, Serpell L, Arnsdorf MF, & Lindquist SL (2000) Nucleated Conformational Conversion and the Replication of Conformational Information by a Prion Determinant. *Science* 289(5483):1317-1321.

18. Kelly JW (2000) Mechanisms of amyloidogenesis. *Nat Struct Biol* 7(10):824-826.

19. Harper JD & Lansbury PT (1997) Models Of Amyloid Seeding In Alzheimer's Disease And Scrapie: Mechanistic Truths and Physiological Consequences of the Time-Dependent Solubility of Amyloid Proteins. *Annual Review of Biochemistry* 66(1):385-407.

20. Lansbury PT, Jr. (1999) Evolution of amyloid: what normal protein folding may tell us about fibrillogenesis and disease. *Proc Natl Acad Sci U S A* 96(7):3342-3344.

21. Arosio P, Knowles TPJ, & Linse S (2015) On the lag phase in amyloid fibril formation. *Physical Chemistry Chemical Physics* 17(12):7606-7618.

22. Cohen SIA, Vendruscolo M, Welland ME, Dobson CM, Terentjev EM, & Knowles TPJ (2011) Nucleated polymerization with secondary pathways. I. Time evolution of the principal moments. *The Journal of Chemical Physics* 135(6):065105.

23. Jeong JS, Ansaloni A, Mezzenga R, Lashuel HA, & Dietler G (2013) Novel Mechanistic Insight into the Molecular Basis of Amyloid Polymorphism and Secondary Nucleation during Amyloid Formation. *J Mol Biol* 425(10):1765-1781.

24. Hortschansky P, Schroeckh V, Christopeit T, Zandomeneghi G, & Fändrich M (2005) The aggregation kinetics of Alzheimer's β-amyloid peptide is controlled by stochastic nucleation. *Protein Science* 14(7):1753-1759.

25. Cohen SIA, Linse S, Luheshi LM, Hellstrand E, White DA, Rajah L, Otzen DE, Vendruscolo M, Dobson CM, & Knowles TPJ (2013) Proliferation of amyloid-β42 aggregates occurs through a secondary nucleation mechanism. *Proceedings of the National Academy of Sciences* 110(24):9758-9763.

26. Cummings JL (2004) Alzheimer's Disease. *New England Journal of Medicine* 351(1):56-67.

27. Maurer K & Maurer U (2003) *Alzheimer: The Life of a Physician and Career of a Disease* (Columbia University Press, New York) p 256 p.

28. Alzheimer A (1907) Ueber eine eingenartige Erkrankung der Hirnrinde. *Allgemeine Zeitschrift fur Psychiatrie und psychisch-gerichtliche Medizin* 64:146-148.

29. Prince M, Wimo A, Guerchet M, Ali G-C, Wu Y-T, & Prina M (2015) World Alzheimer Report. eds Rees G & Fletcher S (Alzheimer's Disease International (ADI), London).

30. Hebert LE, Weuve J, Scherr PA, & Evans DA (2013) Alzheimer disease in the United States (2010–2050) estimated using the 2010 census. *Neurology* 80(19):1778-1783.

31. NIH Report (2016) Estimates of Funding for Various Research, Condition and Disease Categories (RCDC). Available at: https://report.nih.gov/categorical_spending.aspx [Accessed February 25, 2016].

32. Lansbury PT & Lashuel HA (2006) A century-old debate on protein aggregation and neurodegeneration enters the clinic. *Nature* 443(7113):774-779.

33. Jellinger KA (2006) Alzheimer 100 – highlights in the history of Alzheimer research. *Journal of Neural Transmission* 113(11):1603-1623.

34. Behl C (2000) Apoptosis and Alzheimer's disease. *Journal of Neural Transmission* 107(11):1325-1344.

35. Selkoe DJ (2004) Cell biology of protein misfolding: The examples of Alzheimer's and Parkinson's diseases. *Nat Cell Biol* 6(11):1054-1061.

36. Davies P & Maloney AJF (1976) Selective loss of central cholinergic neurons in Alzheimer's disease. *The Lancet* 308(8000):1403.

37. Hardy J & Selkoe DJ (2002) The Amyloid Hypothesis of Alzheimer's Disease: Progress and Problems on the Road to Therapeutics. *Science* 297(5580):353-356.

38. Francis PT, Palmer AM, Snape M, & Wilcock GK (1999) The cholinergic hypothesis of Alzheimer's disease: a review of progress. *Journal of Neurology, Neurosurgery & Psychiatry* 66(2):137-147.

39. Musial A, Bajda M, & Malawska B (2007) Recent developments in cholinesterases inhibitors for Alzheimer's disease treatment. *Curr Med Chem* 14(25):2654-2679.

40. Sun X, Jin L, & Ling P (2012) Review of drugs for Alzheimer's disease. *Drug Discov Ther* 6(6):285-290.

41. Anand P & Singh B (2013) A review on cholinesterase inhibitors for Alzheimer's disease. *Archives of pharmacal research* 36(4):375-399.

42. Mount C & Downton C (2006) Alzheimer disease: progress or profit? *Nat Med* 12(7):780-784.

43. Alonso AdC, Zaidi T, Novak M, Grundke-Iqbal I, & Iqbal K (2001) Hyperphosphorylation induces self-assembly of τ into tangles of paired helical filaments/straight filaments. *Proceedings of the National Academy of Sciences of the United States of America* 98(12):6923-6928.

44. Brunden KR, Trojanowski JQ, & Lee VMY (2009) Advances in tau-focused drug discovery for Alzheimer's disease and related tauopathies. *Nat Rev Drug Discov* 8(10):783-793.

45. Avila J, Lucas JJ, Perez M, & Hernandez F (2004) Role of Tau Protein in Both Physiological and Pathological Conditions. *Physiol. Rev.* 84(2):361-384.

46. Hardy J & Higgins G (1992) Alzheimer's disease: the amyloid cascade hypothesis. *Science* 256(5054):184-185.

47. Masters CL, Simms G, Weinman NA, Multhaup G, McDonald BL, & Beyreuther K (1985) Amyloid plaque core protein in Alzheimer disease and Down syndrome. *Proceedings of the National Academy of Sciences of the United States of America* 82(12):4245-4249.

48. Glenner GG & Wong CW (1984) Alzheimer's disease: Initial report of the purification and characterization of a novel cerebrovascular amyloid protein. *Biochemical and Biophysical Research Communications* 120(3):885-890.

49. Kang J, Lemaire H-G, Unterbeck A, Salbaum JM, Masters CL, Grzeschik K-H, Multhaup G, Beyreuther K, & Muller-Hill B (1987) The precursor of Alzheimer's disease amyloid A4 protein resembles a cell-surface receptor. *Nature* 325(6106):733-736.

50. Steiner H, Capell A, Leimer U, & Haass C (1999) Genes and mechanisms involved in β-amyloid generation and Alzheimer’s disease. *European Archives of Psychiatry and Clinical Neuroscience* 249(6):266-270.

51. Esler WP & Wolfe MS (2001) A portrait of Alzheimer secretases--new features and familiar faces. *Science* 293(5534):1449-1454.

52. Karran E, Mercken M, & Strooper BD (2011) The amyloid cascade hypothesis for Alzheimer's disease: an appraisal for the development of therapeutics. *Nat Rev Drug Discov* 10(9):698-712.

53. Blennow K, Zetterberg H, Haass C, & Finucane T (2013) Semagacestat's fall: where next for AD therapies? *Nat Med* 19(10):1214-1215.

54. Jacobson SA & Sabbagh MN (2011) Investigational drugs for the treatment of AD: what can we learn from negative trials? *Alzheimer's research & therapy* 3(2):1-8.

55. Imbimbo BP (2009) Why did tarenflurbil fail in Alzheimer's disease? *J Alzheimers Dis* 17(4):757-760.

56. Ahmed M, Davis J, Aucoin D, Sato T, Ahuja S, Aimoto S, Elliott JI, Van Nostrand WE, & Smith SO (2010) Structural conversion of neurotoxic amyloid-beta1-42 oligomers to fibrils. *Nat Struct Mol Biol* 17(5):561-567.

57. Haass C & Selkoe DJ (2007) Soluble protein oligomers in neurodegeneration: lessons from the Alzheimer's amyloid β-peptide. *Nat Rev Mol Cell Biol* 8(2):101-112.

58. Lashuel HA, Hartley D, Petre BM, Walz T, & Lansbury PT (2002) Neurodegenerative disease: Amyloid pores from pathogenic mutations. *Nature* 418(6895):291-291.

59. Lambert MP, Barlow AK, Chromy BA, Edwards C, Freed R, Liosatos M, Morgan TE, Rozovsky I, Trommer B, Viola KL, Wals P, Zhang C, Finch CE, Krafft GA, & Klein WL (1998) Diffusible, nonfibrillar ligands derived from Aβ1–42 are potent central nervous system neurotoxins. *Proceedings of the National Academy of Sciences of the United States of America* 95(11):6448-6453.

60. Tanzi RE (2012) The Genetics of Alzheimer Disease. *Cold Spring Harbor Perspectives in Medicine* 2(10).

61. Jan A, Gokce O, Luthi-Carter R, & Lashuel HA (2008) The Ratio of Monomeric to Aggregated Forms of Aβ40 and Aβ42 Is an Important Determinant of Amyloid-β Aggregation, Fibrillogenesis, and Toxicity. *Journal of Biological Chemistry* 283(42):28176-28189.

62. Schmidt M, Sachse C, Richter W, Xu C, Fändrich M, & Grigorieff N (2009) Comparison of Alzheimer Aβ(1–40) and Aβ(1–42) amyloid fibrils reveals similar protofilament structures. *Proceedings of the National Academy of Sciences* 106(47):19813-19818.

63. Jarrett JT, Berger EP, & Lansbury PT (1993) The carboxy terminus of the beta amyloid protein is critical for the seeding of amyloid formation: Implications for the pathogenesis of Alzheimer's disease. *Biochemistry* 32(18):4693-4697.

64. Petkova AT, Ishii Y, Balbach JJ, Antzutkin ON, Leapman RD, Delaglio F, & Tycko R (2002) A structural model for Alzheimer's β-amyloid fibrils based on experimental constraints from solid state NMR. *Proceedings of the National Academy of Sciences of the United States of America* 99(26):16742-16747.

65. Iwatsubo T, Odaka A, Suzuki N, Mizusawa H, Nukina N, & Ihara Y (1994) Visualization of Aβ42(43) and Aβ40 in senile plaques with end-specific Aβ monoclonals: Evidence that an initially deposited species is Aβ42(43). *Neuron* 13(1):45-53.

66. Bernstein SL, Wyttenbach T, Baumketner A, Shea J-E, Bitan G, Teplow DB, & Bowers MT (2005) Amyloid β-Protein: Monomer Structure and Early Aggregation States of Aβ42 and Its Pro19 Alloform. *Journal of the American Chemical Society* 127(7):2075-2084.

67. Bitan G, Vollers SS, & Teplow DB (2003) Elucidation of Primary Structure Elements Controlling Early Amyloid β-Protein Oligomerization. *Journal of Biological Chemistry* 278(37):34882-34889.

68. Hu X, Crick SL, Bu G, Frieden C, Pappu RV, & Lee J-M (2009) Amyloid seeds formed by cellular uptake, concentration, and aggregation of the amyloid-beta peptide. *Proceedings of the National Academy of Sciences* 106(48):20324-20329.

69. Tycko R (2003) Insights into the Amyloid Folding Problem from Solid-State NMR. *Biochemistry* 42(11):3151-3159.

70. Walsh DM, Klyubin I, Fadeeva JV, Rowan MJ, & Selkoe DJ (2002) Amyloid-beta oligomers: their production, toxicity and therapeutic inhibition. *Biochem Soc T* 30(4):552-557.

71. Lashuel HA, Hartley DM, Petre BM, Wall JS, Simon MN, Walz T, & Lansbury Jr PT (2003) Mixtures of Wild-type and a Pathogenic (E22G) Form of Aβ40 in Vitro Accumulate Protofibrils, Including Amyloid Pores. *Journal of Molecular Biology* 332(4):795-808.

72. Harper JD, Wong SS, Lieber CM, & Lansbury PT (1997) Observation of metastable A[beta] amyloid protofibrils by atomic force microscopy. *Chemistry & Biology* 4(2):119-125.

73. Jan A, Hartley DM, & Lashuel HA (2010) Preparation and characterization of toxic A beta aggregates for structural and functional studies in Alzheimer's disease research. *Nat Protoc* 5(6):1186-1209.

74. Glabe CG (2008) Structural classification of toxic amyloid oligomers. *J Biol Chem* 283(44):29639-29643.

75. Walsh DM, Klyubin I, Fadeeva JV, Cullen WK, Anwyl R, Wolfe MS, Rowan MJ, & Selkoe DJ (2002) Naturally secreted oligomers of amyloid β protein potently inhibit hippocampal long-term potentiation in vivo. *Nature* 416(6880):535-539.

76. Ye C, Walsh DM, Selkoe DJ, & Hartley DM (2004) Amyloid β-protein induced electrophysiological changes are dependent on aggregation state: N-methyl-d-aspartate (NMDA) versus non-NMDA receptor/channel activation. *Neuroscience Letters* 366(3):320-325.

77. Cirrito JR, Yamada KA, Finn MB, Sloviter RS, Bales KR, May PC, Schoepp DD, Paul SM, Mennerick S, & Holtzman DM (2005) Synaptic Activity Regulates Interstitial Fluid Amyloid-[beta] Levels In Vivo. *Neuron* 48(6):913-922.

78. Pike CJ, Walencewicz AJ, Glabe CG, & Cotman CW (1991) In vitro aging of ß-amyloid protein causes peptide aggregation and neurotoxicity. *Brain Research* 563(1-2):311-314.

79. Gazit E (2002) The "Correctly Folded" State of Proteins: Is It a Metastable State? *Angewandte Chemie International Edition* 41(2):257-259.

80. Knowles TPJ, Shu W, Devlin GL, Meehan S, Auer S, Dobson CM, & Welland ME (2007) Kinetics and thermodynamics of amyloid formation from direct measurements of fluctuations in fibril mass. *Proceedings of the National Academy of Sciences* 104(24):10016-10021.

81. Kayed R, Head E, Thompson JL, McIntire TM, Milton SC, Cotman CW, & Glabe CG (2003) Common Structure of Soluble Amyloid Oligomers Implies Common Mechanism of Pathogenesis. *Science* 300(5618):486-489.

82. Cerf E, Sarroukh R, Tamamizu-Kato S, Breydo L, Derclaye S, Dufrene YF, Narayanaswami V, Goormaghtigh E, Ruysschaert JM, & Raussens V (2009) Antiparallel beta-sheet: a signature structure of the oligomeric amyloid beta-peptide. *Biochem J* 421(3):415-423.

83. Gu L, Liu C, Stroud JC, Ngo S, Jiang L, & Guo Z (2014) Antiparallel Triple-strand Architecture for Prefibrillar Aβ42 Oligomers. *Journal of Biological Chemistry* 289(39):27300-27313.

84. Baldwin AJ, Knowles TPJ, Tartaglia GG, Fitzpatrick AW, Devlin GL, Shammas SL, Waudby CA, Mossuto MF, Meehan S, Gras SL, Christodoulou J, Anthony-Cahill SJ, Barker PD, Vendruscolo M, & Dobson CM (2011) Metastability of Native Proteins and the Phenomenon of Amyloid Formation. *Journal of the American Chemical Society* 133(36):14160-14163.

85. Santi S, Barakat E, Descrovi E, Neier R, & Herzig HP (2014) Real-time protein aggregation monitoring with a Bloch surface wave-based approach. pp 912918-912918-912919.

86. Yiannopoulou KG & Papageorgiou SG (2013) Current and future treatments for Alzheimer's disease. *Therapeutic Advances in Neurological Disorders* 6(1):19-33.

87. Blennow K, de Leon MJ, & Zetterberg H (2006) Alzheimer's disease. *The Lancet* 368(9533):387-403.

88. Laske C, Sohrabi HR, Frost SM, López-de-Ipiña K, Garrard P, Buscema M, Dauwels J, Soekadar SR, Mueller S, Linnemann C, Bridenbaugh SA, Kanagasingam Y, Martins RN, & O'Bryant SE (2015) Innovative diagnostic tools for early detection of Alzheimer's disease. *Alzheimer's & Dementia* 11(5):561-578.

89. Nitsch RM & Hock C (2008) Targeting beta-amyloid pathology in Alzheimer's disease with Abeta immunotherapy. *Neurotherapeutics* 5(3):415-420.

90. Toyn J (2015) What lessons can be learned from failed Alzheimer's disease trials? *Expert Review of Clinical Pharmacology* 8(3):267-269.

91. White DA, Buell AK, Dobson CM, Welland ME, & Knowles TPJ (2009) Biosensor-based label-free assays of amyloid growth. *FEBS Letters* 583(16):2587-2592.

92. Xing Y & Xia N (2015) Biosensors for the Determination of Amyloid-Beta Peptides and their Aggregates with Application to Alzheimer's Disease. *Analytical Letters* 48(6):879-893.

93. Goode JA, Rushworth JVH, & Millner PA (2015) Biosensor Regeneration: A Review of Common Techniques and Outcomes. *Langmuir* 31(23):6267-6276.

94. Cooper MA (2006) Optical biosensors: where next and how soon? *Drug Discovery Today* 11(23-24):1061-1067.

95. Konopsky VN, Karakouz T, Alieva E, Vicario C, & Sekatskii SK (2013) Photonic crystal biosensor based on optical surface waves. *Sensors (Basel)* 13:2566-2578.

96. Wood RW (1912) Diffraction gratings with controlled groove form and abnormal distribution of intensity. *Philosophical Magazine Series 6* 23(134):310-317.

97. Homola J, Yee SS, & Gauglitz G (1999) Surface plasmon resonance sensors: review. *Sensors and Actuators B: Chemical* 54(1–2):3-15.

98. Schasfoort RBM & Tudos AJ (2008) *Handbook of Surface Plasmon Resonance* (The Royal Society of Chemistry, Cambridge) p 403.

99. Cooper MA (2002) Optical biosensors in drug discovery. *Nat Rev Drug Discov* 1(7):515-528.

100. Tjernberg LO, Näslund J, Lindqvist F, Johansson J, Karlström AR, Thyberg J, Terenius L, & Nordstedt C (1996) Arrest of -Amyloid Fibril Formation by a Pentapeptide Ligand. *Journal of Biological Chemistry* 271(15):8545-8548.

101. Kraziński BE, Radecki J, & Radecka H (2011) Surface Plasmon Resonance Based Biosensors for Exploring the Influence of Alkaloids on Aggregation of Amyloid-β Peptide. *Sensors* 11(4):4030.

102. Ryu J, Joung H-A, Kim M-G, & Park CB (2008) Surface Plasmon Resonance Analysis of Alzheimer's β-Amyloid Aggregation on a Solid Surface: From Monomers to Fully-Grown Fibrils. *Analytical Chemistry* 80(7):2400-2407.

103. Cannon MJ, Williams AD, Wetzel R, & Myszka DG (2004) Kinetic analysis of beta-amyloid fibril elongation. *Analytical Biochemistry* 328(1):67-75.

104. Hasegawa K, Ono K, Yamada M, & Naiki H (2002) Kinetic Modeling and Determination of Reaction Constants of Alzheimer's β-Amyloid Fibril Extension and Dissociation Using Surface Plasmon Resonance. *Biochemistry* 41(46):13489-13498.

105. Stravalaci M, Beeg M, Salmona M, & Gobbi M (2011) Use of surface plasmon resonance to study the elongation kinetics and the binding properties of the highly amyloidogenic Aβ1–42 peptide, synthesized by depsi-peptide technique. *Biosensors and Bioelectronics* 26(5):2772-2775.

106. Ramakrishnan M, Kandimalla KK, Wengenack TM, Howell KG, & Poduslo JF (2009) Surface Plasmon Resonance Binding Kinetics of Alzheimer’s Disease Amyloid β Peptide-Capturing and Plaque-Binding Monoclonal Antibodies. *Biochemistry* 48(43):10405-10415.

107. Stravalaci M, Bastone A, Beeg M, Cagnotto A, Colombo L, Di Fede G, Tagliavini F, Cantù L, Del Favero E, Mazzanti M, Chiesa R, Salmona M, Diomede L, & Gobbi M (2012) Specific Recognition of Biologically Active Amyloid-β Oligomers by a New Surface Plasmon Resonance-based Immunoassay and an in Vivo Assay in Caenorhabditis elegans. *Journal of Biological Chemistry* 287(33):27796-27805.

108. Stravalaci M, Canovi M, Romeo M, Tapella L, Beeg M, Cagnotto A, Salmona M, Chiesa R, Diomede L, & Gobbi M (2011) A new immunoassay based on surface plasmon resonance for detection of beta-amyloid oligomers. *Alzheimer's & Dementia: The Journal of the Alzheimer's Association* 7(4):S398.

109. Rygula A, Majzner K, Marzec KM, Kaczor A, Pilarczyk M, & Baranska M (2013) Raman spectroscopy of proteins: a review. *Journal of Raman Spectroscopy* 44(8):1061-1076.

110. Eberhardt K, Stiebing C, Matthaus C, Schmitt M, & Popp J (2015) Advantages and limitations of Raman spectroscopy for molecular diagnostics: an update. *Expert Rev Mol Diagn* 15(6):773-787.

111. Barth A (2007) Infrared spectroscopy of proteins. *Biochim Biophys Acta* 1767(9):1073-1101.

112. Fleischmann M, Hendra PJ, & McQuillan AJ (1974) Raman spectra of pyridine adsorbed at a silver electrode. *Chemical Physics Letters* 26(2):163-166.

113. Ataka K, Kottke T, & Heberle J (2010) Thinner, Smaller, Faster: IR Techniques To Probe the Functionality of Biological and Biomimetic Systems. *Angewandte Chemie International Edition* 49(32):5416-5424.

114. Chou IH, Benford M, Beier HT, Cote GL, Wang M, Jing N, Kameoka J, & Good TA (2008) Nanofluidic biosensing for beta-amyloid detection using surface enhanced Raman spectroscopy. *Nano Lett* 8(6):1729-1735.

115. Voiciuk V, Valincius G, Budvytytė R, Matijoška A, Matulaitienė I, & Niaura G (2012) Surface-enhanced Raman spectroscopy for detection of toxic amyloid β oligomers adsorbed on self-assembled monolayers. *Spectrochimica Acta Part A: Molecular and Biomolecular Spectroscopy* 95:526-532.

116. Beier HT, Cowan CB, Chou I-H, Pallikal J, Henry JE, Benford ME, Jackson JB, Good TA, & Coté GL (2007) Application of Surface-Enhanced Raman Spectroscopy for Detection of Beta Amyloid Using Nanoshells. *Plasmonics* 2(2):55-64.

117. LeVine Iii H & Walker LC (2010) Molecular polymorphism of Aβ in Alzheimer's disease. *Neurobiology of Aging* 31(4):542-548.

118. Bhowmik D, Mote KR, MacLaughlin CM, Biswas N, Chandra B, Basu JK, Walker GC, Madhu PK, & Maiti S (2015) Cell-Membrane-Mimicking Lipid-Coated Nanoparticles Confer Raman Enhancement to Membrane Proteins and Reveal Membrane-Attached Amyloid-β Conformation. *ACS nano* 9(9):9070-9077.

119. Adato R & Altug H (2013) In-situ ultra-sensitive infrared absorption spectroscopy of biomolecule interactions in real time with plasmonic nanoantennas. *Nat Commun* 4:2154.

2. OBJECTIVES AND STRATEGY

This chapter is a partial adaptation of the conference proceeding:

Santi, S., Barakat, E., Descrovi, E., Neier, R. and Herzig, H. P., "Real-time protein aggregation monitoring with a Bloch surface wave-based approach," Biophotonics: Photonic Solutions for Better Health Care IV, Jürgen Popp; Valery V. Tuchin; Dennis L. Matthews; Francesco Saverio Pavone; Paul Garside, Editors, Proc. SPIE 9129, 912918 (2014).

2.1 Aim of the project

Predicting the three-dimensional configuration of a protein, the so-called protein-folding problem, is one of the most challenging topics of structural biology especially since an increasing number of degenerative pathologies results from an incorrect protein folding (or misfolding). Very often, the protein misfolding is associated with the formation of large insoluble proteic aggregates(1-3). Disorders such as Alzheimer and Parkinson diseases, Huntington's chorea, Creutzfeldt-Jacob disease, cystic fibrosis, Gaucher's disease, type II diabetes mellitus and the wide group of systemic amyloidosis are associated with aggregation of misfolded polypeptide chains, commonly referred to as amyloid fibrils. As introduced in Chapter 1, amyloid fibrils, particularly in their prefibrillar forms (oligomeric precursors), can be highly toxic to cells, suggesting their key role in disease pathogenesis. In the specific case of the Alzheimer's disease (AD), the amyloidogenic peptide is known to be the Amyloid-β (Aβ) peptide, which is naturally formed by the cleavage of a neural transmembrane protein(4). Its aggregation pathway has been extensively studied(5-7). It is schematically represented in Fig.2.1.1 and it is believed to proceed as follows: the monomeric Aβ peptide, under pathogenic conditions, self-assembles to form the first small soluble aggregate, the oligomers. The oligomeric complexes rearrange to the prefibrillar assemblies, which are formed by the so-called β-sheets structures, typical of amyloid aggregates. Prefibrillar assemblies are hence the building block, via monomer addition, to the formation of protofilaments, which, as the strings of a rope, are the fibrillar subunit of the mature and insoluble amyloid fibril. A range of experiments, indicates that the fibrils have extensive β-sheet character, and that these sheets run perpendicular to the fibril axis to generate what is described as a cross-β structure(8). Nevertheless, for many years the only structural information about amyloid fibrils came from imaging techniques (TEM, AFM) and from X-ray fiber diffraction(9). Thus far, the real-time monitoring of the Aβ aggregation process is very difficult, if not impossible, with the standard amyloid detection techniques(10). This problem arises from the fact that those valuable techniques are sensitive to the extent of the mature fibril formation, and mainly silent during the first steps of the oligomerization process. This limitation becomes even more significant if one factors in that oligomers are thought to be the main toxic species, leading to the onset of the AD. In fact, it has been shown(11) that Aβ oligomers interact with the membrane of neurons, causing the disruption of ion homeostasis and oxidative stress.

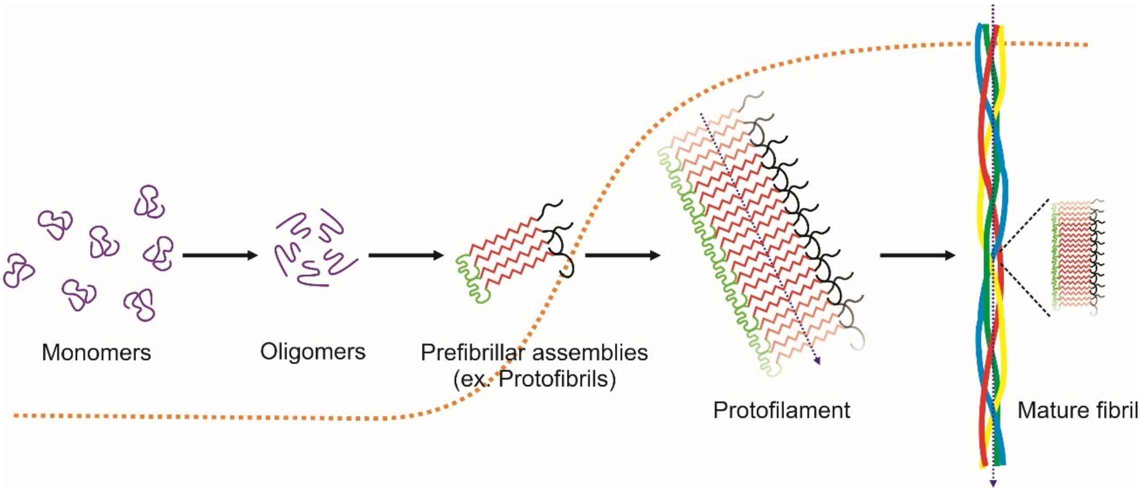

Fig.2.1.1. Schematic and simplified amyloid-beta peptide aggregation pathway. The dotted orange sigmoidal curve represents the signal obtained while monitoring the time-depending aggregation via the use of a standard amyloid detection technique (ThT binding essay, Congo Red staining, FTIR, etc.). Hence, those are not sensitive to the formation of the small, soluble and toxic oligomers, and the first part of the sigmoidal curve is commonly known as "lag-phase"(7, 9). Image reprinted and caption adapted from Herzig *et al*, 2014(12), with the permission from the Swiss Physical Society.

In vitro studies on these soluble cytotoxic oligomeric Aβ aggregates should provide a description of the fibril formation mechanism at the very early stages of aggregation(13). Understanding why and how the peptide may adopt a non-native fold is essential for designing therapeutic approaches(14). In view of these arguments, we chose to study Aβ42 peptide aggregation. This peptide is the longest of the family of Aβ peptides (42 amino acids) and the most fibrillogenic(15).

This work aimed at developing an innovative label-free optical biosensing platform based on a Bloch Surface Waves (BSW) resonator, which is highly sensitive to variations of optical properties due to the conformational changes in proteins. The sensor was applied to the detection of the early dynamic events of fibrillogenesis of the Aβ42 peptide linked to the

Alzheimer’s disease in an effort to overcome the limitation imposed by classical amyloid detection techniques, unable to cover the first aggregation phase during which the formation of soluble toxic Aβ oligomers occurs. We exploited the potential of our innovative label-free optical sensing approach based on BSWs to monitor in real time the refractive index changes (Δn) of a solution containing an initially monomeric Aβ42 peptide. Throughout aggregation, the refractive index properties of the peptidic solution change and it is possible to correlate them to the different steps of Aβ42 peptide fibrillation.

A number of sophisticated optical biosensors have been recently applied to biomolecular interaction analysis, providing kinetic data about biological binding events in real time without labelling. The advantage of the label-free concept, in which biomolecules are unlabelled or unmodified and are detected in their natural forms, is the elimination of detrimental effects from labels that may interfere with fundamental interaction and the absence of a time-consuming pre-treatment. They are also ideal for portable applications that are currently gaining great interest(16-18). Recent progresses on optical sensing for protein interactions permit the construction of biosensors that utilize the refractive index change as the sensing transduction signal. A number of bio-detection schemes were proposed, using different strategies for enhancing the performances of the SPR mechanism, which remains one of the most simple and widespread used configuration in sensors(19). SPR, interferometers, waveguides, fiber gratings, ring resonators, and photonic crystals are optical label-free biosensing platforms that represent the majority of research activities in optical label-free sensor development(20, 21).

In the specific, BSW-based sensing has been validated as a sensitive and reliable approach for label-free and real-time biosensing(18, 22-24). BSWs are Surface Electromagnetic Waves (SEWs)(25, 26). SEWs are non-radiative waves confined at the interface between two media. The optical characteristics of the two media determine the kind of SEW that can be sustained. For example, Surface Plasmon Polaritons (SPP) can be coupled at metal/dielectric interfaces, while Surface Phonon Polaritons can propagate on polar crystals such as SiC mid-infrared wavelengths. One way to create such a kind of SEW is to use a dielectric multilayer. Since the surface confinement obtained on dielectric multilayers is intimately related to the layers periodicity, this SEW is called Bloch Surface Wave(27, 28). The advantages of BSW, compared to SPP, is the high energy that can be confined at the surface of the multilayer and the larger spectral tunability allowed by the low dispersion of refractive index (n) in the dielectric material (instead of metal for SPP). A very high intensity can be produced at the surface of the multilayer used for the BSW generation(29). This property, characteristic of BSW, allows the creation of very sensitive sensors and avoids some of the disadvantages existing with SPR sensors such as the thick sensing region that can decrease the sensitivity. In the case of a BSW-based sensor, the active part is the last layer of the 1D photonic crystal which generates the surface wave. In particular, the surface wave can be guided in order to enhance the sensitivity of the sensor(30). The sensing scheme adopted in this work is described in details in the following section.

2.2 The BSW-based sensing principle and platform

This section is a partial adaptation of the journal article:

Santi, S., Musi, V., Descrovi, E., Paeder, V., Di Francesco, J., Hvozdara, L., van der Wal, P., Lashuel, H. A., Pastore, A., Neier, R. and Herzig, H. P. (2013), Real-time Amyloid Aggregation Monitoring with a Photonic Crystal-based Approach. ChemPhysChem, 14: 3476–3482.

Periodic stacks of dielectric materials (known as Bragg gratings, one-dimensional (1D) photonic crystals, or, simply, multilayers) with different refractive index constants can sustain optical surface modes(28) with either transverse electric (TE) or transverse magnetic (TM) polarization. Such modes are called Bloch surface waves (BSWs) and have a significant amount of their overall power confined close to the truncation interface of the photonic crystal(25). Optical surface waves are solutions of Maxwell's equations. The energy flow is confined on a region that is localized at or near the surface(31). They propagate along the interface and the ambient medium leading to a high field enhancement. The amplitude of these waves decay exponentially in the directions both parallel and perpendicular to the boundary with different decay constants. Operating in Kretschmann configuration, the incident light is coupled under total internal reflection (TIR). The coupling occurs when the projection of the incoming wave vector $\vec{k}_{in}$ onto the multilayer interface matches the wave vector of the BSW $\vec{k}_p$ (28, 32), according to Eq.(2.1):

$$\frac{2\pi}{\lambda} n_o \sin\theta_{in} = k_p \qquad (2.1)$$

where n_o is the refractive index of the prism, and k_p the propagation constant of the BSW, and λ and θ the resonance wavelength and angle, respectively. In our experiment we work at a fixed wavelength λ (632.8 nm), hence the coupling is achievable only at the specific incident angle θ, as depicted in Fig.2.2.1.

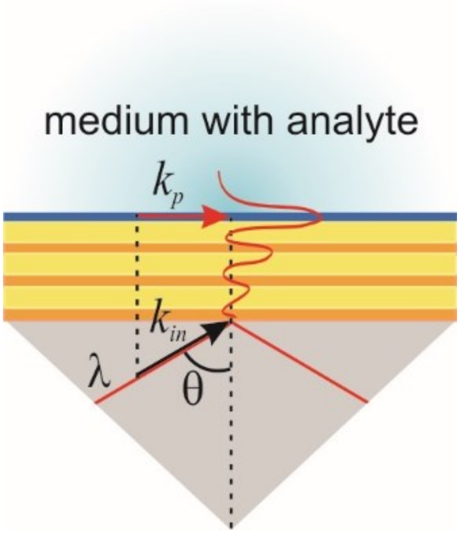

Fig.2.2.1. Sensing scheme in Kretschmann configuration. The coupling of light into the BSW is here represented with a geometric model, where the electromagnetic wave is represented by its wave vector $\vec{k}_{in}$. The projection of the incoming wave matches the BSW propagation constant vector $\vec{k}_p$ under the coupling condition (Eq.(2.1)). Thus, θ and λ become the resonance angle and wavelength, the coupling is achieved, and the BSW is excited in TIR(16). Hence, the outcoming wave leaves the surface with the same angle of the incident light, deprived of the BSW resonance energy.

An intensity dip in the reflected beam is produced when the light is coupled into the BSW(33). As the multilayer consists of dielectric materials, the associated losses can be made very low leading to a narrower reflectance dip as compared to SPs. Another advantage in using BSWs is the possibility of operating within a broad range of wavelengths, by properly designing a suitable multilayered structure. This tunable localized field confinement is particularly attractive for sensing applications(22, 34, 35).

The experimental apparatus developed in-house in collaboration with Dr. Descrovi and Dr. Ballarini from the Politecnico di Torino, Italy, consists of a prism-based goniometric setup, as depicted in Fig.2.2.2.

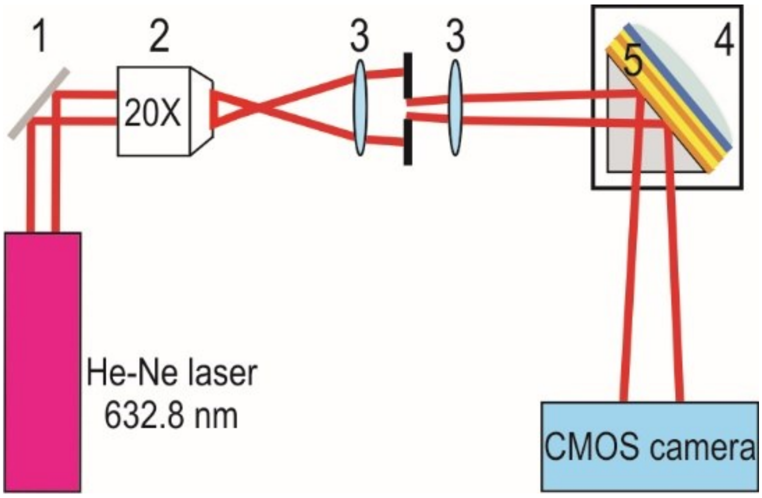

Fig.2.2.2. Schematic top-view of the optical setup. A He-Ne laser (1) is used to illuminate the photonic crystal contacted to a prism (4). The beam is conditioned by using an objective (2) and two subsequent lenses (3) in order to obtain the divergent incident beam whose optical rays are incident on the multilayer at a small range of different angles. The light is then reflected by the multilayer (5) towards the CMOS camera.

A proper silicon-based multilayer is used as a photonic structure sustaining BSWs (see section 2.2.1). In the optical setup, a He-Ne laser illuminates the photonic crystal (λ = 632.8 nm). The TE-polarized laser source is first focused and then expanded on the multilayer through the side facet of a prism (see Chapter 8 for details). The angle of incidence of the beam on the prism can be varied in a controlled way. The incident beam is slightly divergent, thus multiple optical rays are incident on the multilayer at different angles. Since the BSW is excited in a Kretschmann configuration, the glass substrate hosting the photonic crystal is optically contacted to the prism by means of an index-matching oil. The light is then reflected by the multilayer towards the detector, which is a CMOS camera. The truncation interface of the photonic multilayer is sealed to a fluidic cell, in which a thermocouple and a Peltier element in closed feedback loop can maintain a constant temperature. As the laser impinges on the multilayer at the specific BSW resonant angle, part of the laser power is transferred to the BSW mode, resulting in an evanescent field extended in the external (aqueous) medium for a distance of about 0.5µm. As a result, the coupling is observed as an intensity dip in the reflected angular distribution. The reflected spot containing the BSW resonance dip is leaving the prism with a given angular divergence, and is imaged on the linear camera. The position of the dip on the linear camera is indicative of the angular position of the BSW resonance dip and hence of the refractive index as sensed by the BSW. The response will therefore be reported in numbers of pixels The sensing approach is similar to the well-known SPR scheme(36).

In the present work, we exploit BSWs to locally probe the refractive index variations (Δn) of a solution wherein the Aβ42 peptide is initially injected in a monomeric form and is progressively aggregating to form fibrils (Fig.2.2.3).

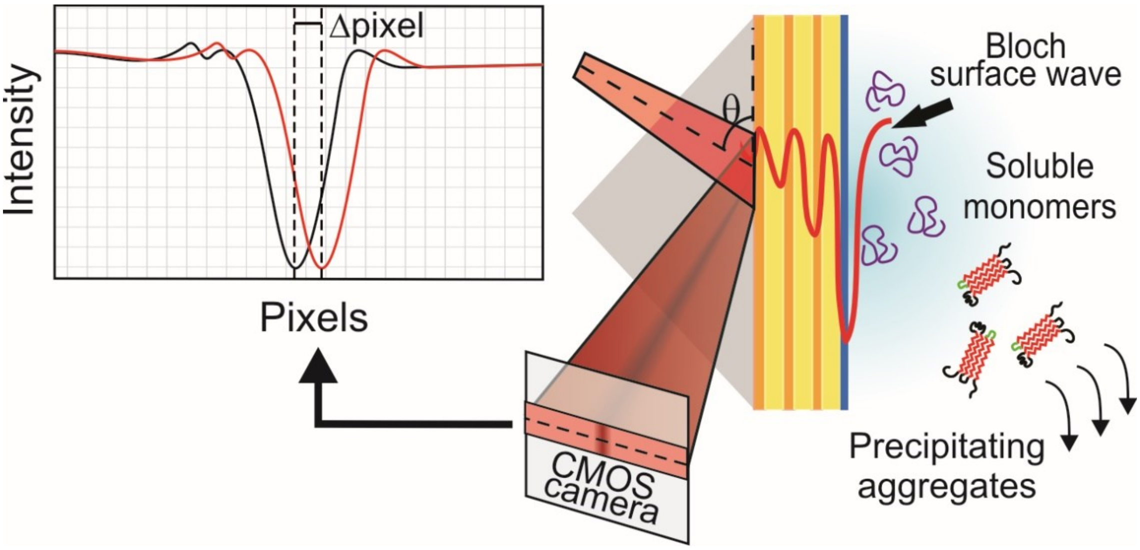

Fig.2.2.3. Lateral enlargement of the sensing chamber. The microfluidic cell is positioned vertically. The laser beam generates the BSW, which is probing the protein solution via an evanescent tail of its associated electromagnetic field distribution. As for SPR, the coupling is observed as an intensity dip in the reflected angular distribution (represented in dark). Any variation in the refractive index of the liquid is resulting in a shift of the reflection minimum (in pixel).

The sensing fluidic chamber is positioned vertically. This specific optical arrangement has never been reported before by others. The vertical position allows for accomplishing our specific biosensing goal. The evanescent tail of the BSW probes the Aβ42 solution. During Aβ42 aggregation, the insoluble fibrils precipitate away from the surface sensed by the BSW, thus causing a variation in the refractive index of the solution. As refractive index perturbations occur within the fluidic cell, the position of the BSW dip shifts (see Fig.2.2.3). The angular position of the dip moves toward smaller output angles as the refractive index decreases. Thus, the detectable signal is the angular shift of the reflection minimum, that is the resonance dip, (in pixel) as the Δn occurs throughout the aggregation process.

As previously mentioned, in our experiments, the photonic structure is a multilayer made of alternating layers of silicon oxi-nitride and silica. The detailed description of the photonic multilayer and its properties is reported in the following. Moreover, to calibrate the response of the BSW dip shift upon refractive index perturbations in the solution(24), control experiments were performed using solutions with different known refractive indices.

2.2.1 1D photonic crystal design and fabrication

The design and fabrication of the multilayer was performed by several internal and external collaborators. For the sake of completeness, I here report a short description of the methods used and of the accomplished simulation results.

The dielectric multilayer was designed by Dr. Descrovi from the Politecnico di Torino, Italy, to work in water (n = 1.33) and to couple the BSW with a TE-polarized laser working at $\lambda = 632.8$ nm. The structure is composed of 4 alternating periods constituted by high (H) and low (L) refractive index dielectric materials, according to the scheme: glass-(H-L)x4-H'-water, depicted in Fig.2.2.4. Thicknesses and refractive indices of the materials are reported in Tab.2.2.1. The dielectric layers were deposited on a glass substrate via plasma-enhanced chemical vapor deposition (PECVD) by Mr. Di Francesco from the Optics & Photonics Technology Laboratory, EPFL.

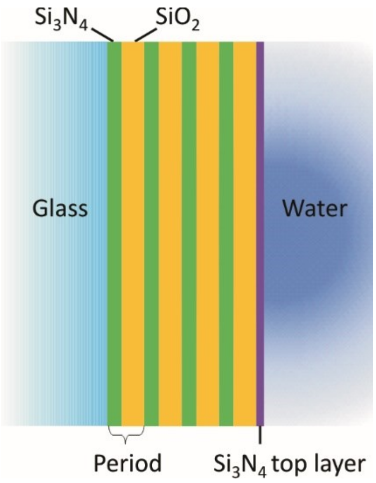

Fig.2.2.4. Multilayer design representation, according to the scheme: glass-(H-L)x4-H'-water, where H is silicon nitride, Si_3N_4, L is silicon oxide, SiO_2, and H' is the silicon nitride top layer, which is in contact with the aqueous analyte.

Material	Layer Thickness	Refractive Index (n)
Silicon Nitride (H)	130 nm	1.95
Silicon Oxide (L)	175 nm	1.46
Silicon Nitride (H')	30 nm	1.95

Tab.2.2.1. Thicknesses and refractive indices of the materials used in the deposition of the 1D photonic crystal multilayer. We thank J. Di Francesco and Dr. E. Barakat from the Optics & Photonics Technology Laboratory, EPFL, for the multilayers fabrication, and Dr. E. Descrovi from the Politecnico di Torino, Italy, for the multilayer design.

To predict the sensitivity of the BSW supported by the one-dimensional photonic crystal described above, Dr. Barakat from the Optics & Photonics Technology Laboratory (EPFL) performed the simulation of the BSW response upon a precise refractive index variation of the aqueous medium. For our simulations, the transfer matrix method was used. It is based on dividing the grating into N sections so that each section can be approximately treated as uniform. By applying the appropriate boundary conditions and solving the coupled-mode equations, the transfer matrix gives the relation between the fields at z and at z + L where L is the total length of the grating(28). Specifically, the BSW intensity dip is resulting from the satisfaction of the coupling conditions (see Eq.(2.1)), which in our case are $\lambda = 632.8$ nm and $\theta = 64.075$. When perturbing the medium of a $\Delta n = 1 \cdot 10^{-3}$, the BSW dip is shifted towards a larger θ, equal to 64.125. This is shown in Fig.2.2.5. Hence, it is possible to theoretically determine the sensitivity: $S_{th} = 50° / \text{RIU}$. This value is consistent with others reported in the literature(37, 38).

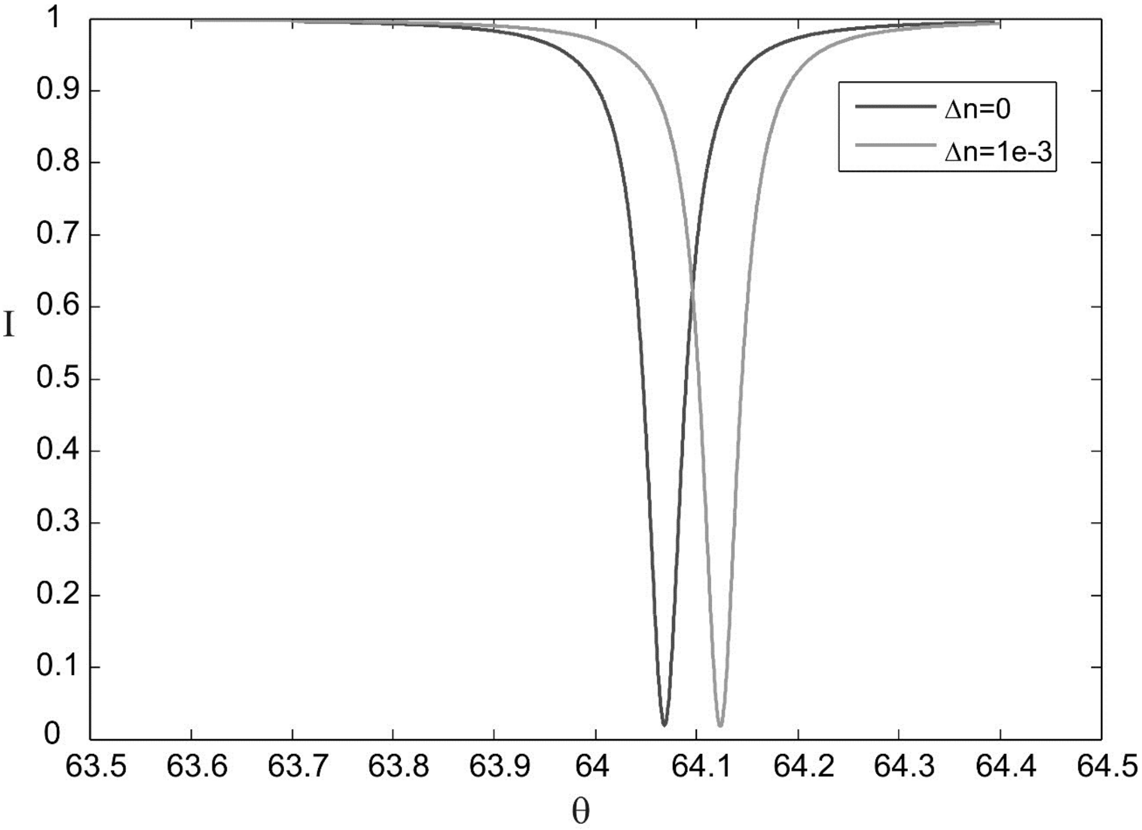

Fig.2.2.5. Simulated angular shift of the BSW intensity dip upon a perturbation of the aqueous medium refractive index Δn of $1 \cdot 10^{-3}$. We thank Dr. E. Barakat from the Optics & Photonics Technology Laboratory, EPFL, for the simulation.

2.2.2 Experimental correlation between angular and pixel shift

With the aim of correlating the angular shift of the BSW intensity dip with the corresponding pixel shift, as imaged onto the CMOS camera(38), we performed an experimental determination of the conversion factor Δθ / pixel shift. Prior to this, we had to take into account that, in our measurements, the illumination angle θ is the angle at which the laser impinges the surface of the multilayer through the BK7 glass prism contacted with the multilayer itself. A θ value of 64.075° is theoretically calculated according to the simulation described above, and is determined by the design of the multilayer. To determine the illumination angle onto the prism γ (see Fig.2.2.6) a simple trigonometric relation was used, which considers the refractive index of the material of the prism, as reported in Eq.(2.2):

$$\gamma = \sin^{-1}\left(n_p \sin(45° - \theta)\right) \qquad (2.2)$$

where n_p is the prism refractive index, which at the laser wavelength $\lambda = 632.8$ nm is equal to 1.51509. If we solve Eq.(2.2) for θ, the resulting relation is expressed by Eq.(2.3):

$$\theta = 45° - \sin^{-1}\frac{\sin\gamma}{n_p} \qquad (2.3)$$

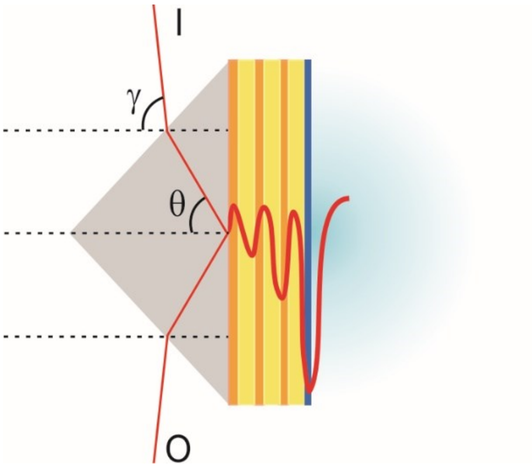

Fig.2.2.6. Schematics of the illumination angle. θ is the illumination angle onto the multilayer surface, and γ is the illumination angle onto the prism surface.

Therefore, to experimentally determine the conversion factor degrees/pixels we manually rotated only the CMOS camera at precise angles γ_n, while incubating d.i. water at constant conditions. We thus recorded the pixel shift of the BSW dip position as imaged onto the camera. Then, with Eq.(2.3) we determined θ_n for each γ_n. We performed this experiment with two multilayers from the same production batch to test the reproducibility of the result. The result is shown in Fig.2.2.7, where the two independent sets of data are presented. The fit shows a linear correlation between angular and pixel shift for both data sets.

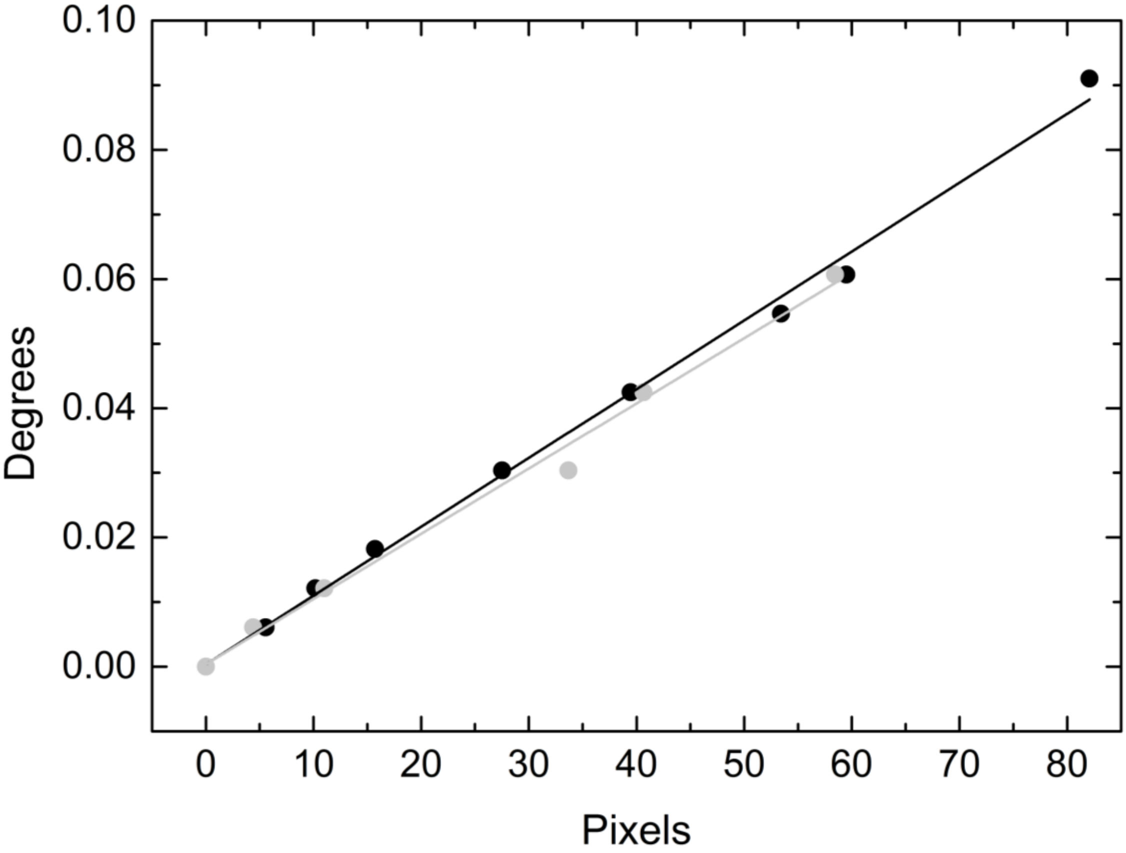

Fig.2.2.7. Experimental correlation between angular and pixel shift. Two sets of data are reported, in black and in grey, respectively. The experiment was performed rotating the CMOS camera only, within an angular range of ± 0.05°.

From the linear fits of data in Fig.2.2.7, an averaged slope of 0.00104° / pixels was determined, which is the conversion factor between angular and pixel shift, as imaged onto the CMOS camera. This factor allows determining the experimental sensitivity of the multilayer, as explained in the following.

2.2.3 1D photonic crystal experimental characterization and BSW response calibration

For our experimental refractive index range, a BSW response calibration was carried out according to two different procedures. The main goal was to prove the linear relationship between the observed shift and the refractive index of the solution, as predicted by known formulas(37), and to determine the experimental multilayer sensitivity.

At first, the angular shift of the BSW resonance dip was obtained varying the temperature of a d.i. water sample directly in the sensing chamber, and hence its refractive index, and to follow the shift of the BSW dip position over the pixels of the detector. Refractive indices of d.i. water at different temperature and at λ = 632.8 nm were chosen as reported elsewhere(39) (see Appendix 1 for details). The temperature of the d.i. water sample was varied from 40 to 60 °C. This temperature-range choice allows for a linear-regime relationship between the variation of the temperature and Δn of water at 632.8 nm. In the second method, glucose solutions at different concentration (% m/v) were used. This method is fully described by Giorgis *et al*(37), where the refractive indices of different glucose solutions are reported (see Appendix 1 for details). To calculate the sensitivity of the multilayer, the experimentally determined conversion factor of 0.00104° / pixels was used, as explained in the previous section.

For the first method, the result is presented in Fig.2.2.8. The relationship is linear, as predicted by known formulas(37).

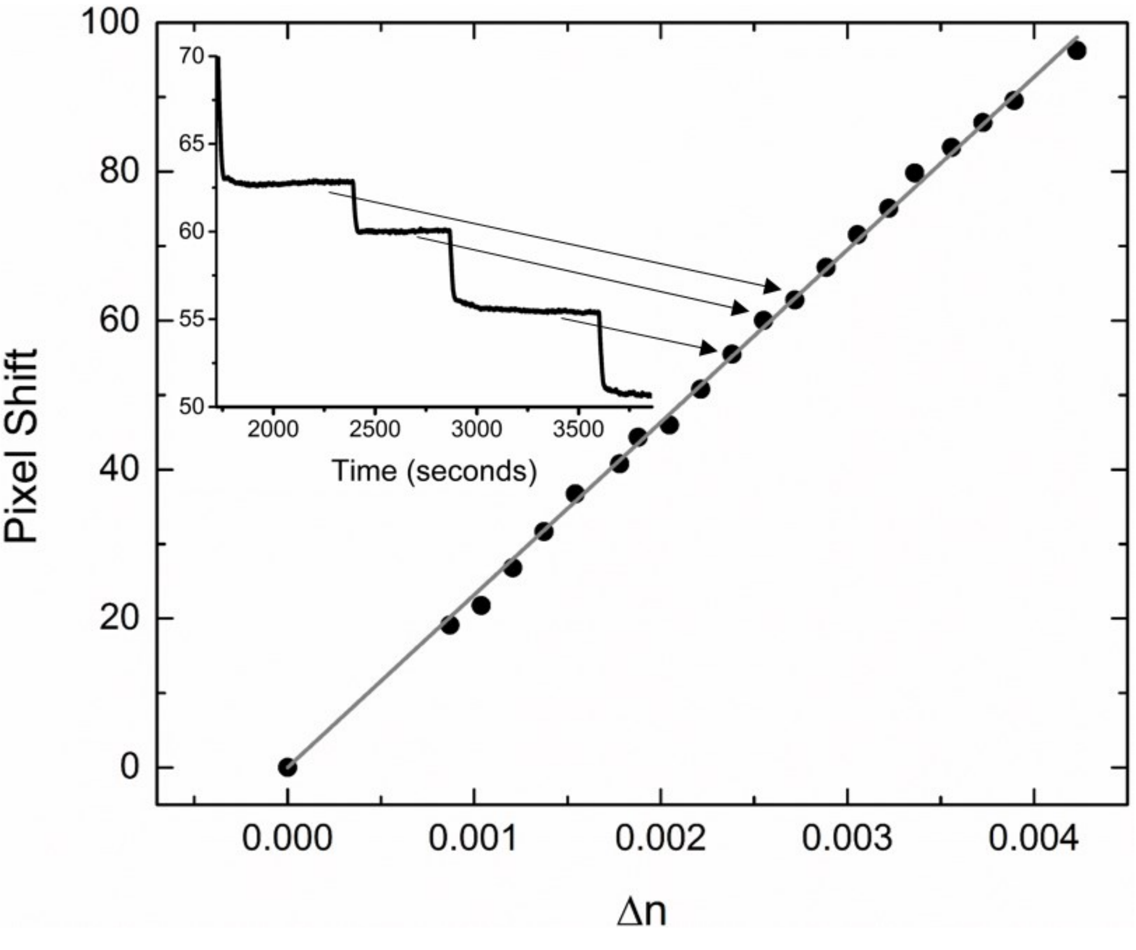

Fig.2.2.8. Linear relationship between the module of Δn of d.i. water (upon change of temperature) and the shift of the BSW dip position along the pixels of the detector, a CMOS camera. Data were interpolated with a linear fit and the slope of the line represents the sensitivity of the multilayer in pixel / RIU. Inset: sensogram obtained upon the temperature variation of the d.i. water sample, corresponding to the indicated experimental points.

From the slopes of the linear fit, it is possible to estimate a sensitivity of 23174 pixel / RIU.

The same calibration experiment was conducted using solutions at different % in m/v of glucose in water at 25 °C(38). The displacement of the BSW dip over the pixels of the camera was recorded, and the result is presented in Fig.2.2.9. As expected, also in this case the relationship between Δn and the pixel shift is linear.

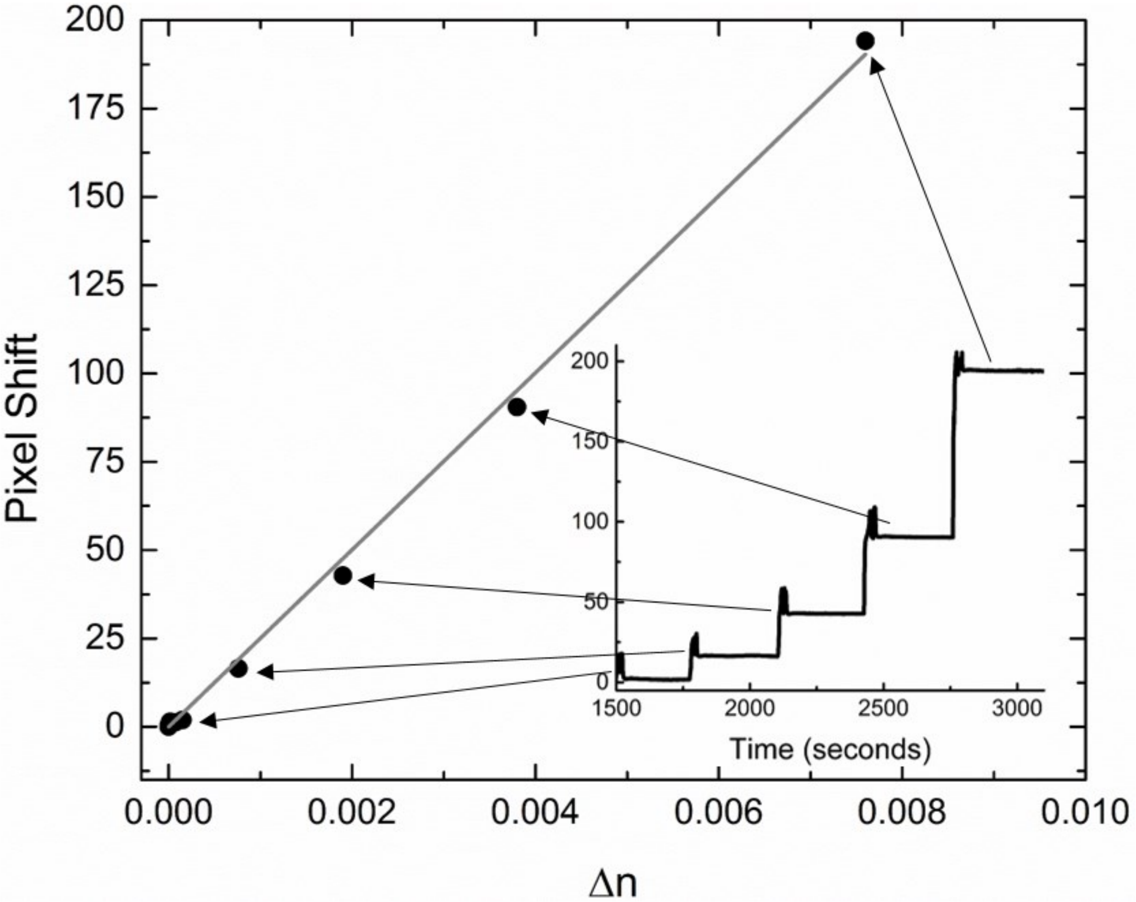

Fig.2.2.9. Linear relationship between the module of Δn of glucose solutions at different concentration (% m/v) in d.i. water and the shift of the BSW dip position along the pixels of the camera. Data were interpolated with a linear fit and the slope of the line represents the sensitivity of the multilayer in pixel / RIU. Inset: sensogram obtained upon the injection of 5 different glucose solutions corresponding to the indicated experimental points.

The slope of the fit allows the estimation of a sensitivity of 25044 pixel / RIU.

If we consider the experimentally determined conversion factor 0.00104° / pixel, the sensitivity can be written as: $S_{exp} = 24.10°$ / RIU and $S_{exp} = 26.05°$ / RIU for the temperature-based calibration and for the glucose-based calibration, respectively. Those experimental sensitivity values are about the half of the theoretically calculated value, estimated through the simulations presented at the beginning of this section. The main reason for such a difference lies in the fabrication inhomogeneities of the layers in the stack.

A further calibration experiment was devised to correlate the response of the BSW-based sensor to the Aβ42 peptide concentration. We prepared samples of Aβ42 monomers at different and known concentrations, and we registered the pixel shift of the BSW dip, as imaged onto the CMOS camera. The test was carried out with the same concept as for the previously reported BSW response calibrations, but it was for us impossible to extract valuable data from it. The main reason for the failure of the attempted tests was related to problems of bubbles and foam formation while emptying the chamber, followed by Aβ42 sample injection difficulties. The BSW resonance position was then difficult to estimate with small uncertainty and without a rough pixel shift approximation, and reasonable results were impossible to obtain.

The experimentally observed sensor resolution was determined using glucose solutions at different concentrations (% m/v), similarly to the experimental system calibration reported in the previous. The result of this investigation is shown in Fig.2.2.10.

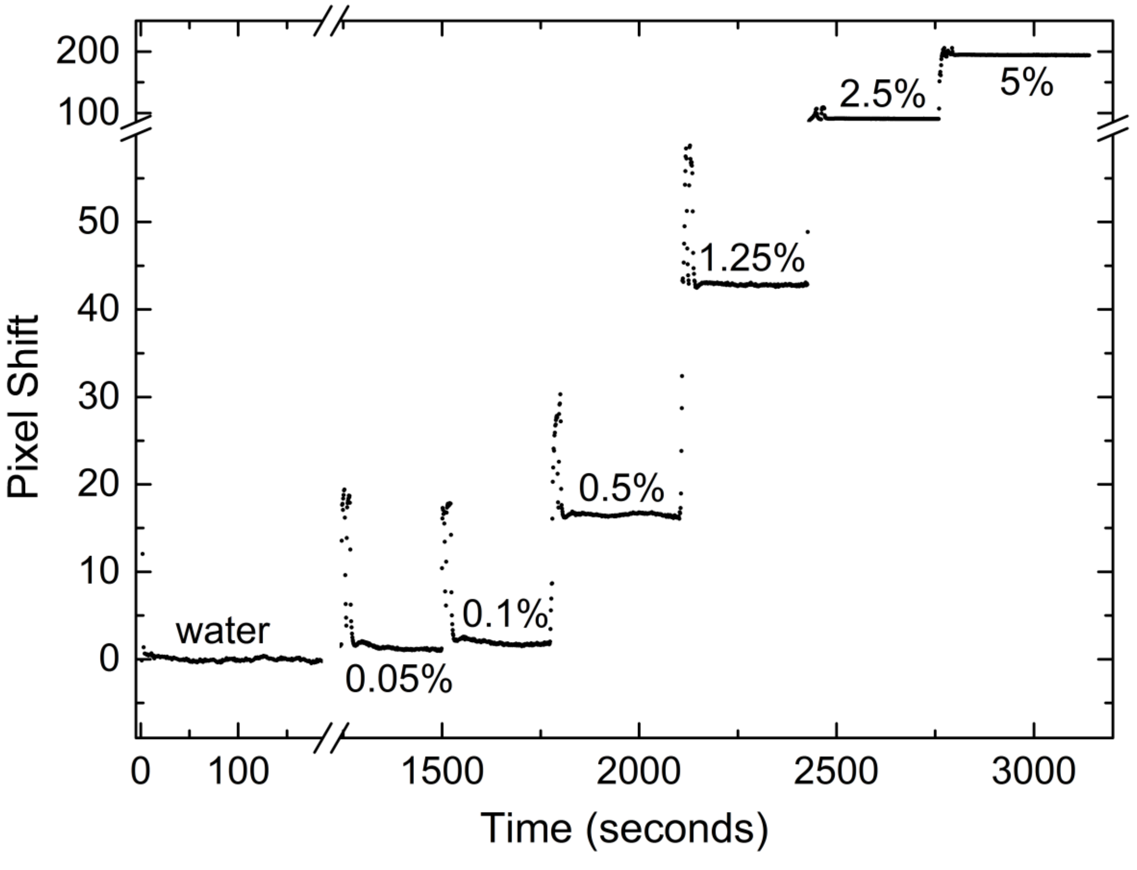

Fig.2.2.10. Experimental sensor resolution determination. Sensogram obtained upon the injection of glucose solutions in different concentrations (% m/v) corresponding to the indicated experimental points (see Appendix 1 for details). Glucose solutions at concentration lower than 0.05% m/v were tested. The corresponding signals are not shown in the sensogram since it was adapted to better appreciate the BSW shift at higher concentrations, as imaged onto the camera pixels.

The smallest Δn variation detected by the system, compared to the signal obtained upon d.i. water injection, was $\Delta n_r = 7.6 \cdot 10^{-5}$ RIU, and it corresponded to the injection of a glucose solution at a concentration of 0.05% m/v(37). This experimental system resolution is thus lower than others reported in the literature(38), but it is sufficient to our purpose.

2.3 Bibliography

1. Kelly JW (2002) Towards an understanding of amyloidogenesis. *Nat Struct Biol* 9(5):323-325.
2. Dobson CM (2001) The structural basis of protein folding and its links with human disease. *Philos Trans R Soc Lond B Biol Sci* 356(1406):133-145.
3. Chiti F & Dobson CM (2006) Protein misfolding, functional amyloid, and human disease. *Annu Rev Biochem* 75:333-366.
4. Walsh DM, Hartley DM, Kusumoto Y, Fezoui Y, Condron MM, Lomakin A, Benedek GB, Selkoe DJ, & Teplow DB (1999) Amyloid β-Protein Fibrillogenesis. *Journal of Biological Chemistry* 274(36):25945-25952.
5. Harper JD & Lansbury PT (1997) Models Of Amyloid Seeding In Alzheimer's Disease And Scrapie: Mechanistic Truths and Physiological Consequences of the Time-Dependent Solubility of Amyloid Proteins. *Annual Review of Biochemistry* 66(1):385-407.
6. Kelly JW (2000) Mechanisms of amyloidogenesis. *Nat Struct Biol* 7(10):824-826.
7. Nilsson MR (2004) Techniques to study amyloid fibril formation in vitro. *Methods* 34(1):151-160.
8. Makin OS & Serpell LC (2005) Structures for amyloid fibrils. *FEBS J* 272(23):5950-5961.
9. Petkova AT, Yau WM, & Tycko R (2006) Experimental constraints on quaternary structure in Alzheimer's beta-amyloid fibrils. *Biochemistry* 45(2):498-512.
10. Nilsson KPR, Ikenberg K, Åslund A, Fransson S, Konradsson P, Röcken C, Moch H, & Aguzzi A (2010) Structural Typing of Systemic Amyloidoses by Luminescent-Conjugated Polymer Spectroscopy. *The American Journal of Pathology* 176(2):563-574.
11. Baglioni S, Casamenti F, Bucciantini M, Luheshi LM, Taddei N, Chiti F, Dobson CM, & Stefani M (2006) Prefibrillar amyloid aggregates could be generic toxins in higher organisms. *J Neurosci* 26(31):8160-8167.
12. Herzig HP, Neier R, Santi S, & Barakat E (2014) Bloch meets Alzheimer. *SPG Mitteilungen* Januar 2014(42):11-14.
13. Jan A & Lashuel H (2012) Establishing the Links Between Aβ Aggregation and Cytotoxicity In Vitro Using Biophysical Approaches. *Amyloid Proteins,* Methods in Molecular Biology, eds Sigurdsson EM, Calero M, & Gasset M (Humana Press), Vol 849, pp 227-243.
14. Kroth H, Ansaloni A, Varisco Y, Jan A, Sreenivasachary N, Rezaei-Ghaleh N, Giriens V, Lohmann S, López-Deber MP, Adolfsson O, Pihlgren M, Paganetti P, Froestl W, Nagel-Steger L, Willbold D, Schrader T, Zweckstetter M, Pfeifer A, Lashuel HA, & Muhs A (2012) Discovery and Structure Activity Relationship of Small Molecule Inhibitors of Toxic β-Amyloid-42 Fibril Formation. *Journal of Biological Chemistry* 287(41):34786-34800.

15. Ahmed M, Davis J, Aucoin D, Sato T, Ahuja S, Aimoto S, Elliott JI, Van Nostrand WE, & Smith SO (2010) Structural conversion of neurotoxic amyloid-beta1-42 oligomers to fibrils. *Nat Struct Mol Biol* 17(5):561-567.

16. Konopsky VN & Alieva EV (2007) Photonic Crystal Surface Waves for Optical Biosensors. *Analytical Chemistry* 79(12):4729-4735.

17. Fan X, White IM, Shopova SI, Zhu H, Suter JD, & Sun Y (2008) Sensitive optical biosensors for unlabeled targets: A review. *Analytica Chimica Acta* 620(1–2):8-26.

18. Rivolo P, Michelotti F, Frascella F, Digregorio G, Mandracci P, Dominici L, Giorgis F, & Descrovi E (2012) Real time secondary antibody detection by means of silicon-based multilayers sustaining Bloch surface waves. *Sensors and Actuators B: Chemical* 161(1):1046-1052.

19. Brolo AG (2012) Plasmonics for future biosensors. *Nat Photon* 6(11):709-713.

20. Altug H, Englund D, & Vuckovic J (2006) Ultrafast photonic crystal nanocavity laser. *Nat Phys* 2(7):484-488.

21. Fan X, White IM, Shopova SI, Zhu H, Suter JD, & Sun Y (2008) Sensitive optical biosensors for unlabeled targets: a review. *Anal Chim Acta* 620(1-2):8-26.

22. Santi S, Musi V, Descrovi E, Paeder V, Di Francesco J, Hvozdara L, van der Wal P, Lashuel HA, Pastore A, Neier R, & Herzig HP (2013) Real-time Amyloid Aggregation Monitoring with a Photonic Crystal-based Approach. *Chemphyschem* 14(15):3476-3482.

23. Paeder V, Musi V, Hvozdara L, Herminjard S, & Herzig HP (2011) Detection of protein aggregation with a Bloch surface wave based sensor. *Sensors and Actuators B: Chemical* 157(1):260-264.

24. Descrovi E, Frascella F, Ballarini M, Moi V, Lamberti A, Michelotti F, Giorgis F, & Pirri CF (2012) Surface label-free sensing by means of a fluorescent multilayered photonic structure. *Applied Physics Letters* 101(13):131105-131104.

25. Meade RD, Brommer KD, Rappe AM, & Joannopoulos JD (1991) Electromagnetic Bloch waves at the surface of a photonic crystal. *Physical Review B* 44(19):10961-10964.

26. Shinn M & Robertson WM (2005) Surface plasmon-like sensor based on surface electromagnetic waves in a photonic band-gap material. *Sensors and Actuators B: Chemical* 105(2):360-364.

27. Robertson WM (1999) Experimental Measurement of the Effect of Termination on Surface Electromagnetic Waves in One-Dimensional Photonic Bandgap Arrays. *J. Lightwave Technol.* 17(11):2013.

28. Yeh P, Yariv A, & Cho AY (1978) Optical surface waves in periodic layered media. *Applied Physics Letters* 32(2):104-105.

29. Sfez T, Descrovi E, Yu L, Quaglio M, Dominici L, Nakagawa W, Michelotti F, Giorgis F, & Herzig HP (2010) Two-dimensional optics on silicon nitride multilayer: Refraction of Bloch surface waves. *Applied Physics Letters* 96(15):151101-151103.

30. Descrovi E, Sfez T, Dominici L, Nakagawa W, Michelotti F, Giorgis F, & Herzig H-P (2008) Near-field imaging of Bloch surface waves on silicon nitride one-dimensional photonic crystals. *Opt. Express* 16(8):5453-5464.

31. Barnes WL, Preist TW, Kitson SC, & Sambles JR (1996) Physical origin of photonic energy gaps in the propagation of surface plasmons on gratings. *Physical Review B* 54(9):6227-6244.

32. Yeh P, Yariv A, & Hong CS (1977) Electromagnetic propagation in periodic stratified media. I. General theory. *J Opt Soc Am* 67:423-438.

33. Descrovi E, Giorgis F, Dominici L, & Michelotti F (2008) Experimental observation of optical bandgaps for surface electromagnetic waves in a periodically corrugated one-dimensional silicon nitride photonic crystal. *Opt Lett* 33(3):243-245.

34. Jamois C, Li C, Orobtchouk R, & Benyattou T (2010) Slow Bloch surface wave devices on porous silicon for sensing applications. *Photonics and Nanostructures - Fundamentals and Applications* 8(2):72-77.

35. Qiao H, Guan B, Gooding JJ, & Reece PJ (2010) Protease detection using a porous silicon based Bloch surface wave optical biosensor. *Opt. Express* 18(14):15174-15182.

36. Barnes WL, Dereux A, & Ebbesen TW (2003) Surface plasmon subwavelength optics. *Nature* 424(6950):824-830.

37. Giorgis F, Descrovi E, Summonte C, Dominici L, & Michelotti F (2010) Experimental determination of the sensitivity of Bloch surface waves based sensors. *Opt Express* 18(8):8087-8093.

38. Sinibaldi A, Danz N, Descrovi E, Munzert P, Schulz U, Sonntag F, Dominici L, & Michelotti F (2012) Direct comparison of the performance of Bloch surface wave and surface plasmon polariton sensors. *Sensors and Actuators B: Chemical* 174(0):292-298.

39. Bashkatov AN & Genina EA (2003) Water refractive index in dependence on temperature and wavelength: a simple approximation. pp 393-395.

3. REAL-TIME AMYLOID AGGREGATION MONITORING WITH A PHOTONIC CRYSTAL-BASED APPROACH

This chapter is a partial adaptation of the journal article:

Santi, S., Musi, V., Descrovi, E., Paeder, V., Di Francesco, J., Hvozdara, L., van der Wal, P., Lashuel, H. A., Pastore, A., Neier, R. and Herzig, H. P. (2013), Real-time Amyloid Aggregation Monitoring with a Photonic Crystal-based Approach. ChemPhysChem, 14: 3476–3482.

3.1 Introduction

The misfolding and aggregation of specific proteins have been recognized as the cause of widespread degenerative pathologies such as AD and Parkinson's diseases(1). In the specific case of AD, the neuronal and synaptic loss has been commonly identified with the presence of senile plaques of extracellular highly fibrillogenic Aβ peptides. These peptides, one of the longest being Aβ42, are produced as soluble monomers. As already explained in Chapter 1, the prevailing hypothesis is that cell toxicity, associated to neuronal death, is triggered by intermediate soluble oligomeric forms of Aβ peptide developing at a very early stage of aggregation, rather than by the final insoluble plaques composed of Aβ fibrils(2, 3). Aβ aggregation is thought to proceed through the NP model(4-6). This model consists of a first rate-limiting nuclei formation, described as "lag-phase", corresponding to the formation of toxic oligomeric species at the early stages of Aβ aggregation, followed by an elongation/polymerization phase, which leads to the formation of fibrils. One of the major challenges for AD research is to detect the early events of aggregation since the classical detection methods, such as Congo red and ThT staining, TEM, X-ray diffraction and classical NMR are all too insensitive to detect the minute soluble species formed during the lag-phase(7, 8). A prompt and sensitive detection would also be crucial to allow AD early diagnosis and design of powerful therapeutic treatments.

In this chapter, we present the unique properties of an optical label-free refractometric sensing platform as a novel approach for investigating the initial lag-phase of Aβ42 aggregation. Our sensing approach allows the real-time optical detection of local refraction index changes occurring as aggregation takes place. The method is based on the optical interrogation of a dielectric multilayer (1D photonic crystal) sustaining an electromagnetic surface wave(9, 10). The sensing technique is reminiscent of SPR: Instead of having a SP propagating on a thin metallic film, an evanescent SEW called BSW is coupled on a purely dielectric multilayer structure(11) (see Chapter 2 for details). Depending on the materials used and the layout of the periodic dielectric multilayer, the BSW can be produced in a wide spectral range, from the visible to the near-infrared(12-14). This spectral tunability represents one of the main advantages of BSW-based optical transduction systems, as compared to SPR. In addition, BSWs present very narrow resonances that can increase the resolution and the limit of detection in label-free detection schemes. BSWs generated on dielectric multilayers are sensitive to external perturbations of the refractive index close to the surface of the photonic multilayer(15-17).

In the following, we report on a proof of principle of the BSW-based detection technique for sensing protein aggregation by monitoring in real time the refractive index variation (Δn) of an aqueous solution containing the Aβ42 peptide during early aggregation and fibril formation. The multilayer surface is directly contacted with the probed aqueous medium and the sensing chamber is positioned vertically, as explained in Chapter 2. Hence, the measurements using BSWs monitor a local variation of the refractive index of the solution, which is directly related to the depletion of the concentration of the Aβ42 monomeric form during aggregation.

3.2 BSW-based Aβ42 aggregation sensing

The monomeric Aβ42 peptide was incubated at 37 °C in the fluidic chamber in presence of an initial bare (non-functionalized) multilayer. (For details on sample preparation, see Chapter 8.) The measurement consisted in time-monitoring the angular position of a BSW resonance dip upon a laser illumination through the prism. A selection of aggregation curves obtained during incubation of the Aβ42 peptide is shown in Fig.3.2.1. The variation of the refractive index Δn of the initially monomeric Aβ42 solution is monitored as a function of time by tracking the BSW resonance position on a linear CMOS camera (see Chapter 2). For this reason, in the monitorings presented in Fig.3.2.1, but also in measurements presented in the following Chapters, Δn corresponds to the shift of the BSW resonance position in pixels. For the results presented in this thesis work, it is important to highlight that the zero value in pixel shift corresponds to the BSW resonance position at the beginning of the measurement, and not to the signal of the reference buffer solution (10 mM Tris HCl), unless stated otherwise. All the measurements of the Aβ42 aggregating peptide in Fig.3.2.1 show an initial increase followed by a decrease of Δn of the solution. The Δn decrease is in accordance with the Aβ42 monomer depletion due to aggregation. The BSW-assisted monitoring was compared with TEM imaging data to allow the detection of the Aβ42 species and their corresponding morphologies before and during aggregation(18). TEM imaging was performed on an Aβ42 sample probed at different stages of aggregation, thus revealing the morphological evolution of the peptide from a monomeric (Fig.3.2.2, micrograph (a)), to an oligomeric and pre-fibrillar stage (Fig.3.2.2, micrographs (b), (c) and (d)), and to a non-soluble aggregate fibrillar conformation (Fig.3.2.2, micrographs (e) and (f)).

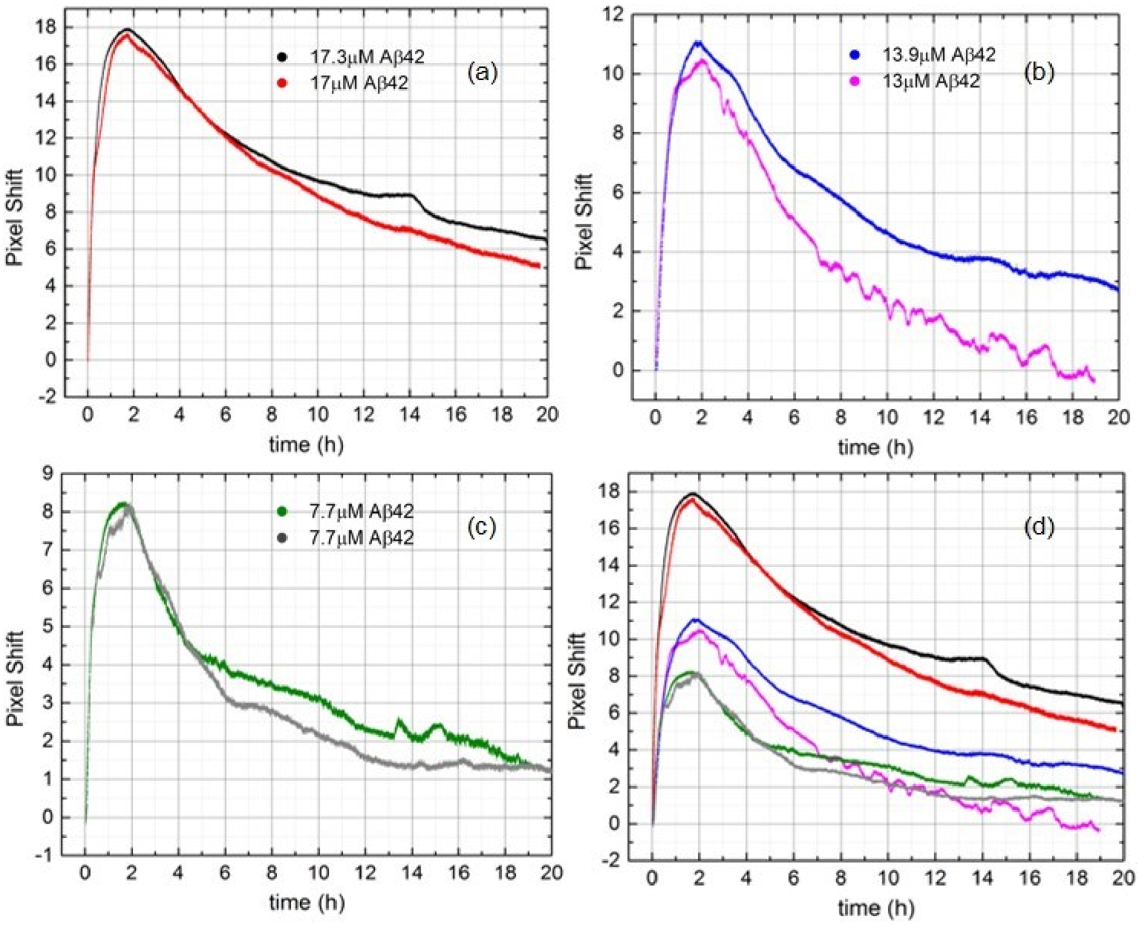

Fig.3.2.1. Real-time monitoring of the refractive index shift of incubating Aβ42 peptide. Refractive index variation Δn, in pixel shift, of Aβ42 peptide solutions incubated at 37 °C. Six distinct Aβ42 samples (in 10 mM Tris HCl buffer, pH 7.4, initial Aβ42 monomer concentrations: (a) 17.3 and 17 µM; (b) 13.9 and 13 µM; (c) 7.7 µM,) were incubated in the BSW sensing cell. The overlap of the three distinct measurements is presented in a close-up view in graph (d), where colors are consistent with those used for the single measurements. In (b), the curve corresponding to the monitoring of the Aβ42 peptide at the initial concentration of 13 µM (in magenta) was perturbed by the probable formation of bubbles in the sensing cell. Nevertheless, the measurement reveals the characteristic evolution of Δn.

The six curves in Fig.3.2.1 show the real-time Δn variation of the initially monomeric Aβ42 solutions at three sets of concentrations: 17.3 and 17 µM (Fig.3.2.1 (a)), 13 and 13.9 µM (Fig.3.2.1 (b)), and 7.7 µM (Fig.3.2.1 (c)). We observed that working in such a small range of low concentrations did not affect the overall evolution trend of the Δn as sensed by the BSW, as shown in the overlap of the measurements presented in Fig.3.2.1 (d). Remarkably, the maximum amplitude of the Δn measurement is attained at approximately 2 hours, regardless of the initial peptide concentration. Differently, the initial sample concentration appears influencing the extent of the refractive index increase in this time frame, being greater for higher, and lower for smaller Aβ42 peptide concentrations. Moreover, a positive correlation is also observed between the subsequent refractive index decrease rate and the peptide concentration.

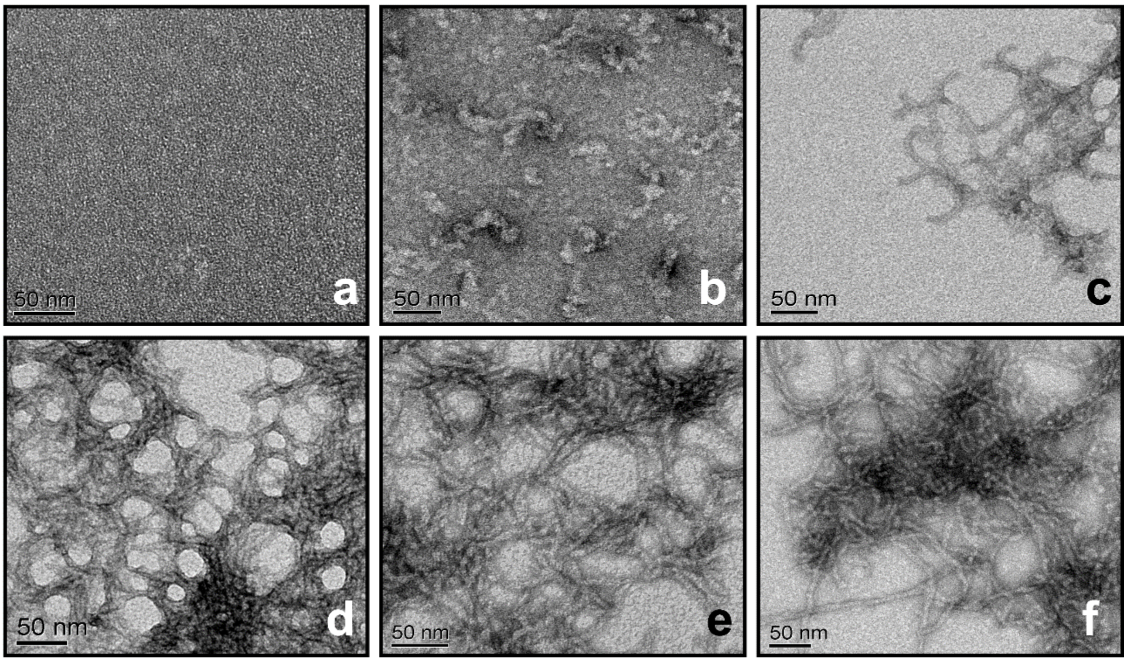

Fig.3.2.2. TEM micrographs of Aβ42 peptide at different stages of aggregation. The initial Aβ42 concentration was 17 µM (in 10 mM Tris HCl, pH 7.4). Micrographs were taken at: (a) t = 0, T = 4 °C; (b) t = 30 minutes, T = 37 °C; (c) t = 2 h, T = 37 °C; (d) t = 10 h, T = 37 °C; (e) t = 24 h, T = 37 °C; (f) t = 48 h, T = 37 °C. The morphological changes of the Aβ42 peptide during incubation are displayed.

In our measurements, the real-time refractive index variation of the aggregating Aβ solution is the result of different contributions, which are difficult to study individually. A simple empirical model describing the variation of Δn as sensed by the BSW involves the contribution from two terms, shown in Eq.(3.1):

$$\Delta n = \Delta n_s + \Delta n_b \qquad (3.1)$$

wherein Δn_s is the refractive index variation due to surface adsorption/desorption processes, and Δn_b is the refractive index variation occurring in the bulk solution, as observed within the evanescent tail of BSWs. (Notably, this model to interpret the BSW-based measurements is a simplified approach, and others might be considered.) Since our multilayer presents a bare silicon oxi-nitride surface, Δn_s is mainly due to the hydrophobic adsorption of the Aβ42 peptide onto the surface. Instead, Δn_b refers mainly to the variation of the Aβ42 monomer concentration in the bulk solution throughout aggregation: The decrease of the monomer concentration reveals the formation of non-soluble aggregates. The final result of the Aβ42 aggregation process, the precipitate of the non-soluble fibers, statistically accumulates at the bottom of the vertically positioned sensing chamber, away from the BSW probe.

The overall time evolution of the refractive index value Δn as shown in Fig.3.2.1, can be divided into three distinct stages, which are labeled with roman numbers in Fig.3.2.3, where the Aβ42 aggregation monitoring in Fig.3.2.1 (a), in black, is displayed as a representative measurement. These stages are discussed in the text following Fig.3.2.3.

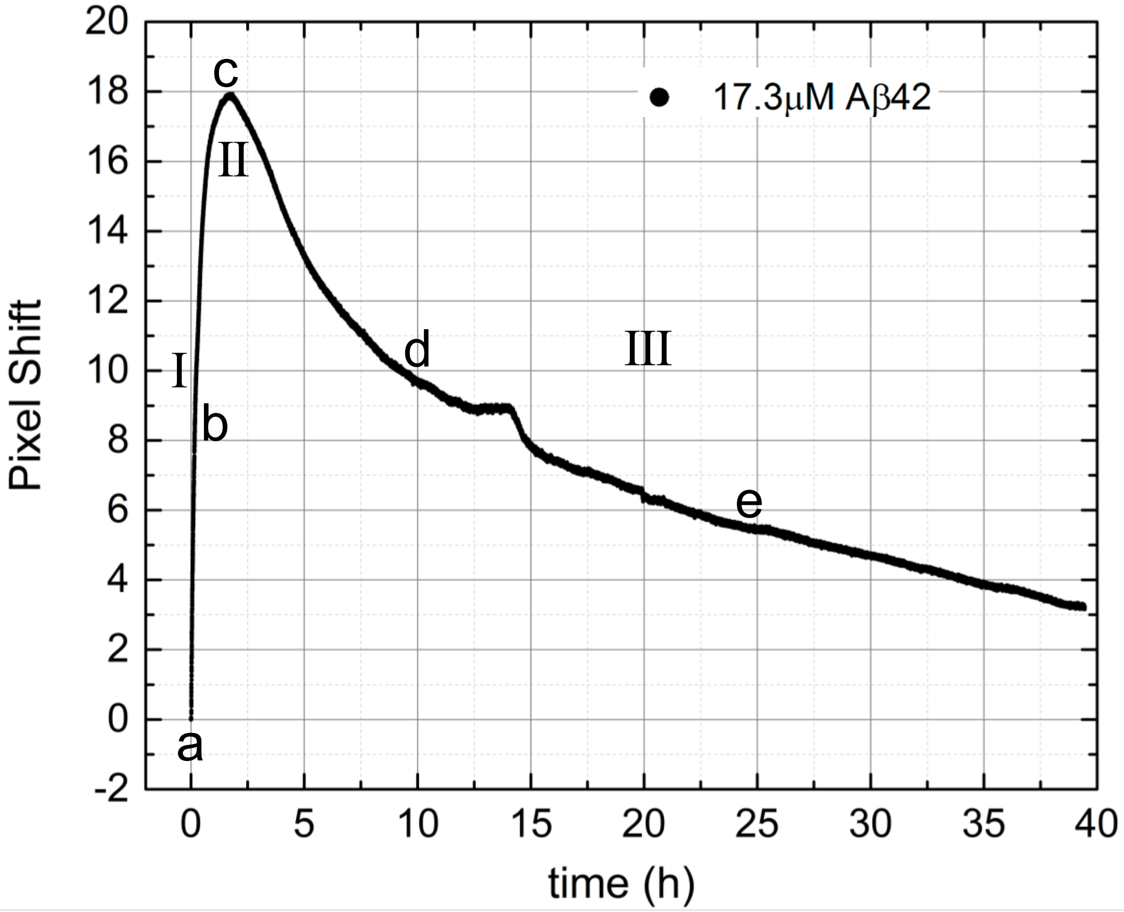

Fig.3.2.3. Real-time monitoring of the refractive index shift of incubating Aβ42 peptide. Refractive index variation Δn, in pixel shift, of an Aβ42 monomer peptide solution incubated at 37 °C at the initial concentration of 17,3 μM in 10 mM Tris HCl, pH 7.4. Roman numbers refer to the three distinct zones of the Δn monitoring, as described in the text. The lowercase letters refer to the TEM micrographs collected at different stages of aggregation, during the Δn monitoring, and reported in Fig.3.2.2.

I. An initial period characterized by a steep increase of Δn during the first approximately 2 hours of the experiment. This is consistent with the adsorption or physisorption of the Aβ42 peptide in an adhesion-competent conformation, onto the silicon oxi-nitride surface. This event produces a local increase of Δn_S. This surface-loading mechanism hampers the direct observation of the Δn_b decrease due to peptide aggregation in this very early stage. Nevertheless, at this specific early stage, the changes of the concentrations in the bulk solution are expected to be negligible.

II. A maximum amplitude of the curve, attained at ~ 2 hours and characterized by the amount of the overall Δn change as measured from the start of the experiment. The reaching of the maximum refractive index value can be associated to an equilibrium condition due, *e.g.* to the saturation of the surface and a decreased availability of free adhesion-competent peptides because of a simultaneous polymerization occurring in the solution.

III. A slow and steady decrease of Δn as observed after passing the maximum. The exponential decrease of the refractive index can be possibly ascribed to two processes: the detachment of the peptide from the surface, and/or the formation of fibrillar structures according to the aggregation mechanism, and thereby depleting the bulk solution. Both of them lead to a decrease of Δn_b.

In the following section we show that different conformational species of Aβ42 exhibit different affinities for the surface.

3.3 BSW-based protofibrillar and fibrillar Aβ42 aggregation sensing

We finally considered Aβ42 samples containing defined populations of Aβ species, including protofibrillar and fibrillar forms of Aβ42. (For sample preparation, see Chapter 8.) The purpose of these measurements was to try identifying the different aggregation states with the sensograms obtained along the amyloid pathway of Aβ42 samples. Protofibril samples are heterogeneous prefibrillar aggregates of different morphologies and sizes(18), reported to be generally unable to assemble into fibrils in the absence of the Aβ42 monomer(19, 20), and showing low induced fluorescence response upon binding ThT. The mature aggregates, the fibrils, filamentous aggregates presenting considerable β-sheet structure, strongly bind ThT. ThT-binding fluorescence assay is used to routinely control the aggregation state of aggregating Aβ42 samples since it is reported to specifically bind amyloid aggregates(6). In this specific case, we performed a control test on Aβ42 peptide samples to assess the extent of fibril formation via ThT fluorescence enhancement under the same conditions as for the BSW-assisted monitoring. Hence, the emission fluorescence intensity of ThT at 482 nm was measured at different times, as shown in Fig.3.3.1. Two types of experiments were performed: a classical ThT binding assay, presented in Fig.3.3.1 (a), and a “seeding” assay, in which at the starting monomeric Aβ42 peptide was added 5% molar ratio of pre-formed Aβ42 fibrils, presented in Fig.3.3.1 (b).

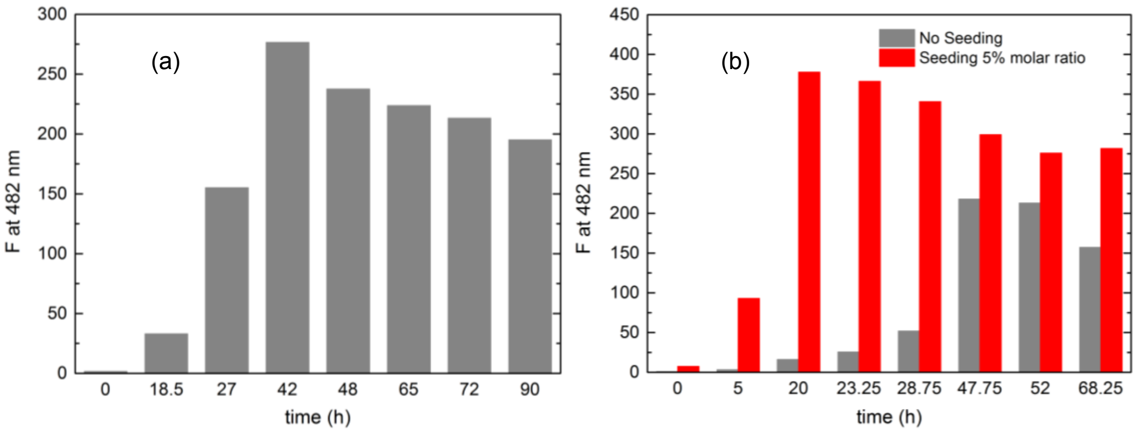

Fig.3.3.1. ThT binding assay. (a) Enhancement in fluorescence at 482 nm given by the binding of ThT to the Aβ42 peptide during the aggregation at 37 °C. The initial concentration of the monomeric peptide was 8 µM in 8 mM Tris HCl, 50 mM gly-NaOH and 10 µM ThT, pH 7.8-8.2. (b) Time course of seeded Aβ42 aggregation at 37 °C monitored by change of ThT fluorescence at 482 nm, and time course of not seeded Aβ42. Experimental concentrations were 8 µM for the peptide, 8 mM for Tris HCl buffer, 50 mM for gly-NaOH, and 10 µM for ThT.

As highlighted by Fig.3.3.1 (a), there is a threshold in the aggregate concentration value at which the ThT fluorescence enhancement is exhibited. After a critical incubation time, the Aβ42 sample self-assembles into β-sheet secondary structures, allowing the insertion of ThT molecules into the channels made by the long axis of this domain(21). Thus, the ThT fluorescence intensity enhances upon binding. This occurs after about 15-20 hours of incubation at 37 °C. This aggregation mode is consistent with the nucleation-elongation model(5), where an initial lag phase is exhibited due to the early formation of small soluble oligomeric aggregates that are unable to incorporate the ThT molecules. After the nucleation, the aggregation proceeds abruptly. This corresponds to the elongation phase, during which Aβ fibrils are formed. After about 50 hours, the aggregate structure becomes too compact to embed the dye molecules, which are therefore excluded from the assembly. This is reflected in a decrease in the fluorescence intensity as demonstrated by many authors(6, 22) and shown by the measurement in Fig.3.3.1. It is possible to overcome the lag phase by adding 5% molar ratio of Aβ42 fibrils to the incubated Aβ42 monomer(4) (see Fig.3.3.1 (b)). In this scenario, the monomeric Aβ peptide is seeded by the presence of these already formed fibers, around which the aggregation proceeds. The ThT binding assays reveal the predicted time evolution of the fibril formation, as reported in the literature(18). Nevertheless, they emphasize the incapability of the ThT binding method to cover the early events of oligomerization.

Finally, protofibrils (PF) and fibrils (F) were incubated at 37 °C in the BSW sensing cell with a bare multilayer, and the resulting profiles are shown in Fig.3.3.2, and compared to the profile of the initially monomeric peptide incubation (M), already presented in Fig.3.2.3.

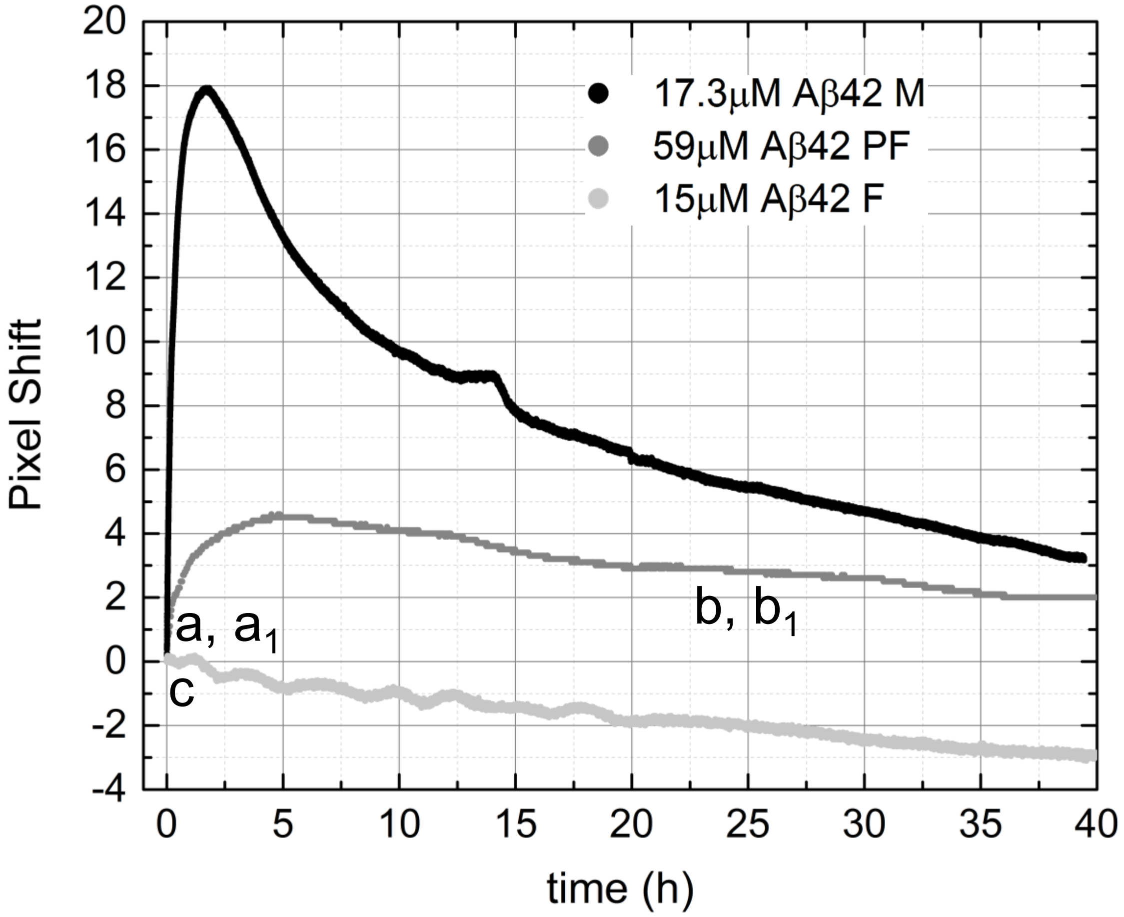

Fig.3.3.2. Real-time monitoring of the refractive index shift of incubating Aβ42 peptides. Real-time refractive index variation Δn, in pixel shift, of Aβ42 peptides, incubated at 37 °C in 10 mM Tris HCl, pH 7.4, at different initial aggregation states and experimental conditions: M, 17.3 μM initially monomeric peptide, PF, 59 μM protofibril, and F, fibril form of the peptide (produced incubating a 15 μM monomeric Aβ42 sample at 37 °C for 48 h). The lower-case letters refer to the TEM micrographs collected at different stages of aggregation of protofibrils and fibrils during the Δn monitoring, and reported in Fig.3.3.3.

Monomeric, protofibrillar and fibrillar forms of Aβ42 peptide present three distinct curves for the evolution of the refractive index over time. Regardless of the starting material used, the overall Δn decreases on the long run. The variation of the refractive index of the incubated protofibrils and fibrils is smoother with respect to the case of monomeric species, during incubation at 37 °C. Previous studies(18, 20) suggest that Aβ42 fibrils and, especially, purified protofibril species present a less pronounced tendency to further assembly, being already embedded in organized aggregation pattern. The TEM micrographs reveal a slow evolution of the Aβ42 protofibril during a 24-hour period of incubation, as shown in micrographs (a), (a_1) and (b), (b_1) of Fig.3.3.3.

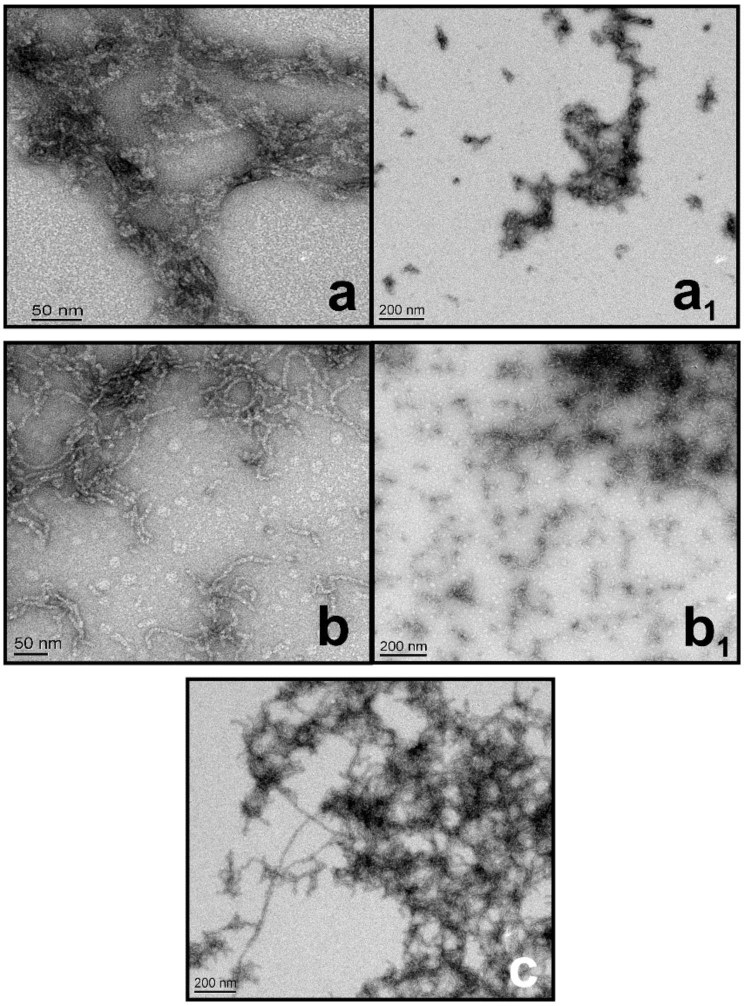

Fig.3.3.3. TEM micrographs of Aβ42 peptides at different stages of aggregation. TEM micrographs of: protofibrils at the initial concentration of 59 µM at: (a&a_1) t = 0 h, T = 4 °C; (b&b1) t = 24 h, T = 37 °C; fibrils at: (c) t = 0 h, T = 4 °C.

Concerning the surface loading effect, we do not report an appreciable Δn increase when mature fibrils, identified by TEM imaging (Fig.3.3.3, micrograph (c)), are incubated in the BSW sensing cell. This evidence allows inferring that surface adsorption of mature fibrils can be safely neglected in this specific case. Since fibrils were obtained incubating a purified monomeric Aβ42 sample at 37 °C for 48 hours, the incubation of these mature aggregates can be even considered as pursuing the measurement of the Aβ42 monomer incubation, after 48 hours, unaffected by any significant interaction with the multilayer. More interestingly, the BSW monitoring of the protofibrillar Aβ42 form shows no substantial surface adsorption. This observation is indicated by a minute increase of the Δn value during the first period of the incubation, as compared to the Δn of the M profile. The observed increase stays small especially if one takes into account that a four times smaller concentration of monomer was used in the experiment. Accordingly, the surface adsorption mechanism onto the unfunctionalized multilayer is found being a process associated with and depending on the Aβ42 peptide in a specific aggregation form. Protofibrils seem to be less prone to be adsorbed onto the surface. The species that are strongly adsorbed onto the multilayer nitride surface have to be in a precise pre-fibrillar conformation, with a lower molecular weight than the average weight attributed to protofibrils.

3.4 Conclusion

This chapter describes how a photonic crystal-based optical platform can be applied to monitor the Aβ42 peptide aggregation during the early events of the fibrillization process that lead to AD. By sensing the refractive index change of the peptide solution, this approach provides unprecedented information covering the transition period from a homogenous dispersion, the monomer solution, to a heterogeneous suspension containing fibrillar amyloids. The presented photonic crystal-based approach provides relevant information on the aggregation of Aβ42 peptides during the nucleation process, the silent lag phase, where other classical amyloid detection methods are limited by their sensitivity.

As reported in the literature(23), the Aβ42 peptide undergoes major morphological changes during the aggregation process. The variation of the Aβ42 secondary structure has been extensively demonstrated(24, 25), especially in the transition from the monomeric form to the soluble oligomeric forms and these changes vary the water-exposed surface of the peptide(26). We suggest that the Aβ42 peptide desorption from the sensing surface should be caused by a variation in the secondary structure of the species initially adsorbed onto the multilayer surface. In the pathway from the oligomeric forms to the mature fibrils the structures become more compact and expose a different and less surface-affine pattern. The TEM micrographs in Fig.3.2.2 are in good agreement with this hypothesis, showing the formation of oligomeric protofibrils from lower to higher molecular weight, in correspondence with the establishment of the maximum amplitude of the Δn signal for the monomeric profile in Fig.3.2.3. The presented results support the hypothesis that the interaction with the unfunctionalized bare surface, and especially the postulated detachment of the peptide from it, may be determined by a specific early molecular structure variation.

An analogous event has been reported by Yagi *et al*(27), whose work suggests the formation of oligomeric Aβ seeds attached to a quartz surface.

Despite the technical restrictions imposed by the prototype system, our approach reveals a high potential that might overcome some of the limitations in other techniques(28). The presented photonic crystal-based approach is a novel promising candidate for direct, label-free and real-time monitoring of the Aβ transitions during oligomerization at early stages(29). In perspective, this innovative amyloid-sensing strategy can be exploited to screen for molecular factors that influence the oligomerization process. Furthermore, the photonic crystal-based sensing can serve as a direct screening tool for new potential inhibitor of Aβ42 toxic oligomers and early nucleation events, as will be explained in Chapter 5.

3.5 Bibliography

1. Hardy J & Selkoe DJ (2002) The Amyloid Hypothesis of Alzheimer's Disease: Progress and Problems on the Road to Therapeutics. *Science* 297(5580):353-356.

2. Lashuel HA, Hartley D, Petre BM, Walz T, & Lansbury PT (2002) Neurodegenerative disease: Amyloid pores from pathogenic mutations. *Nature* 418(6895):291-291.

3. Haass C & Selkoe DJ (2007) Soluble protein oligomers in neurodegeneration: lessons from the Alzheimer's amyloid β-peptide. *Nat Rev Mol Cell Biol* 8(2):101-112.

4. Harper JD & Lansbury PT (1997) Models Of Amyloid Seeding In Alzheimer's Disease And Scrapie: Mechanistic Truths and Physiological Consequences of the Time-Dependent Solubility of Amyloid Proteins. *Annual Review of Biochemistry* 66(1):385-407.

5. Kelly JW (2000) Mechanisms of amyloidogenesis. *Nat Struct Biol* 7(10):824-826.

6. Nilsson MR (2004) Techniques to study amyloid fibril formation in vitro. *Methods* 34(1):151-160.

7. Li H, Rahimi F, Sinha S, Maiti P, Bitan G, & Murakami K (2006) Amyloids and Protein Aggregation—Analytical Methods. *Encyclopedia of Analytical Chemistry*, (John Wiley & Sons, Ltd).

8. Bruggink KA, Müller M, Kuiperij HB, & Verbeek MM (2012) Methods for Analysis of Amyloid-β Aggregates. *Journal of Alzheimer's Disease* 28(4):735-758.

9. Robertson WM (1999) Experimental Measurement of the Effect of Termination on Surface Electromagnetic Waves in One-Dimensional Photonic Bandgap Arrays. *J. Lightwave Technol.* 17(11):2013.

10. Descrovi E, Sfez T, Dominici L, Nakagawa W, Michelotti F, Giorgis F, & Herzig HP (2008) Near-field imaging of Bloch surface waves on silicon nitride one-dimensional photonic crystals. *Opt Express* 16(8):5453-5464.

11. Shinn M & Robertson WM (2005) Surface plasmon-like sensor based on surface electromagnetic waves in a photonic band-gap material. *Sensors and Actuators B: Chemical* 105(2):360-364.

12. Ballarini M, Frascella F, Michelotti F, Digregorio G, Rivolo P, Paeder V, Musi V, Giorgis F, & Descrovi E (2011) Bloch surface waves-controlled emission of organic dyes grafted on a one-dimensional photonic crystal. *Applied Physics Letters* 99(4):043302-043303.

13. Farmer A, Friedli AC, Wright SM, & Robertson WM (2012) Biosensing using surface electromagnetic waves in photonic band gap multilayers. *Sensors and Actuators B: Chemical* 173(0):79-84.

14. Rivolo P, Michelotti F, Frascella F, Digregorio G, Mandracci P, Dominici L, Giorgis F, & Descrovi E (2012) Real time secondary antibody detection by means of silicon-based multilayers sustaining Bloch surface waves. *Sensors and Actuators B: Chemical* 161(1):1046-1052.

15. Konopsky VN & Alieva EV (2007) Photonic Crystal Surface Waves for Optical Biosensors. *Analytical Chemistry* 79(12):4729-4735.

16. Giorgis F, Descrovi E, Summonte C, Dominici L, & Michelotti F (2010) Experimental determination of the sensitivity of Bloch surface waves based sensors. *Opt Express* 18(8):8087-8093.

17. Sinibaldi A, Danz N, Descrovi E, Munzert P, Schulz U, Sonntag F, Dominici L, & Michelotti F (2012) Direct comparison of the performance of Bloch surface wave and surface plasmon polariton sensors. *Sensors and Actuators B: Chemical* 174(0):292-298.

18. Jan A, Hartley DM, & Lashuel HA (2010) Preparation and characterization of toxic A beta aggregates for structural and functional studies in Alzheimer's disease research. *Nat Protoc* 5(6):1186-1209.

19. Jan A, Gokce O, Luthi-Carter R, & Lashuel HA (2008) The Ratio of Monomeric to Aggregated Forms of Aβ40 and Aβ42 Is an Important Determinant of Amyloid-β Aggregation, Fibrillogenesis, and Toxicity. *Journal of Biological Chemistry* 283(42):28176-28189.

20. Jeong JS, Ansaloni A, Mezzenga R, Lashuel HA, & Dietler G (2013) Novel Mechanistic Insight into the Molecular Basis of Amyloid Polymorphism and Secondary Nucleation during Amyloid Formation. *J Mol Biol* 425(10):1765-1781.

21. Krebs MRH, Bromley EHC, & Donald AM (2005) The binding of thioflavin-T to amyloid fibrils: localisation and implications. *Journal of Structural Biology* 149(1):30-37.

22. Levine H (1993) Thioflavine T interaction with synthetic Alzheimer's disease β-amyloid peptides: Detection of amyloid aggregation in solution. *Protein Science* 2(3):404-410.

23. Serpell LC (2000) Alzheimer's amyloid fibrils: structure and assembly. *Biochim Biophys Acta* 1502(1):16-30.

24. Lansbury PT, Costa PR, Griffiths JM, Simon EJ, Auger M, Halverson KJ, Kocisko DA, Hendsch ZS, Ashburn TT, Spencer RGS, Tidor B, & Griffin RG (1995) Structural model for the β-amyloid fibril based on interstrand alignment of an antiparallel-sheet comprising a C-terminal peptide. *Nat Struct Mol Biol* 2(11):990-998.

25. Walsh DM, Klyubin I, Fadeeva JV, Cullen WK, Anwyl R, Wolfe MS, Rowan MJ, & Selkoe DJ (2002) Naturally secreted oligomers of amyloid β protein potently inhibit hippocampal long-term potentiation in vivo. *Nature* 416(6880):535-539.

26. Ahmed M, Davis J, Aucoin D, Sato T, Ahuja S, Aimoto S, Elliott JI, Van Nostrand WE, & Smith SO (2010) Structural conversion of neurotoxic amyloid-beta1-42 oligomers to fibrils. *Nat Struct Mol Biol* 17(5):561-567.

27. Yagi H, Ban T, Morigaki K, Naiki H, & Goto Y (2007) Visualization and Classification of Amyloid β Supramolecular Assemblies. *Biochemistry* 46(51):15009-15017.

28. Hubin E, van Nuland NAJ, Broersen K, & Pauwels K (2014) Transient dynamics of Aβ contribute to toxicity in Alzheimer’s disease. *Cellular and Molecular Life Sciences* 71(18):3507-3521.

29. Nasica-Labouze J, Nguyen PH, Sterpone F, Berthoumieu O, Buchete N-V, Coté S, De Simone A, Doig AJ, Faller P, Garcia A, Laio A, Li MS, Melchionna S, Mousseau N, Mu Y, Paravastu A, Pasquali S, Rosenman DJ, Strodel B, Tarus B, Viles JH, Zhang T, Wang C, & Derreumaux P (2015) Amyloid β Protein and Alzheimer's Disease: When Computer Simulations Complement Experimental Studies. *Chemical Reviews* 115(9):3518-3563.

4. CHEMICAL SURFACE MODIFICATION STRATEGY TO IMPROVE BSW-BASED-SENSING PERFORMANCES

4.1 On the choice of the surface functionalization approach

In label-free biosensing, the main advantage is to perform investigations of analytes without the interference of a probe, the label, interacting with(1), covalently bond to(2, 3), or, in the case of isotopic labelling, being part of the molecule subject to the analysis(4). The label can be seen as a non-natural presence that could affect the behavior of the analyte(5). In the specific case of protein aggregation monitoring, the label could deeply vary the aggregation trend, for the variation of the hydrophobic/hydrophilic balance is essential for determining the predisposition to misfold(6). Moreover, label-based assays require additional sample treatments, which are time consuming and often expensive(7). However, introducing a label is frequently not only necessary to track the investigated protein: The presence of the label plays a fundamental role for specificity and signal amplification. Especially in complex matrices analysis, the label is essential to discriminate between signal and noise, thus providing a direct response even at very low concentrations(8, 9).

In this work, we exploit the potential of a refractive index surface-sensing, which has the advantage of being label-free, but the drawback of monitoring a non-specific property of the Aβ peptide solution. Hence, the BSW-based sensing is non-selective. To overcome this limitation, a method to chemically modify the sensing surface with the aim of selectively probe the aggregation of the Aβ peptide only was developed and it is presented in the following sections. The original idea was to devise a functionalization method for the sensing surface that could serve for different applications, from the surface passivation, to the specific attachments of ligands. Moreover, we aimed at monitoring the aggregation of the Aβ peptide, qualitatively studying the underlying mechanisms for its interaction with the sensing surface, as shown in Chapter 3. The quantitative analysis of the peptide sample was not our main goal, since it requires time-consuming procedures, such as the surface immobilization of monoclonal antibodies, and delivers results easily achievable with commercially available techniques, such as SPR sensing(10) or ELISA immunoassay(11, 12), among others.

Many surface modification strategies have been proposed(13, 14). The general requirement is to guarantee a sufficient degree of freedom to the ligand allowing its unperturbed interaction with the analyte in its free solution conformation. Hence, a proper flexible linker must be designed for this purpose. On the other hand, the ligand should be bond near the surface for sensing purposes. Therefore, the linker length, and not only its flexibility, is of topmost importance. For the interaction with the analyte, correct ligand orientation is also imperative. The choice of a suitable functionalization strategy is thus imperative for the success of a binding experiment, especially in the scenario of surface sensing measurements. It becomes clear that physisorption as a means to devise surface modifications should be avoided. Under physisorption conditions, neither immobilization homogeneity, stability, nor ligand orientation and density can be easily controlled. The reproducibility of the surface modification is also an issue, since one would preferably perform multiple experiments under identical working conditions. Physisorption does not assure reproducibility of the surface treatment. On the contrary, chemical surface modification via covalent attachment strategies is an approach allowing to control many of these parameters(13). As explained in Chapter 2, our sensing surface is made of a stack of dielectric materials, the top layer being silicon nitride. Water and air oxidation of silicon nitride results in the formation of silicon hydroxyl groups at the surface of the multilayers(13). Therefore, silicon nitride surfaces can be, in a general approximation, treated as silica. Exploiting a glass-based surface functionalization chemistry appeared to be the most compelling approach to address the silicon oxi-nitride multilayer surface modification matter. To the best of our knowledge, to date there is no report on the chemical modification of silicon-nitride photonic-crystal surfaces in the literature. In the following sections, the strategy adopted in this project is presented in details.

4.1.1 The glass-based surface functionalization chemistry: a multistep approach

The chemical modification of the multilayer surface was devised in collaboration with Dr. Van der Wal from the Sensors, Actuators and Microsystems Laboratory (EPFL). Our idea was to implement and develop a general strategy widely applicable to the introduction of small ligand molecules as well as to protein or antibodies. Especially, the goal of our work was dual and consisted in: a) generating a reproducible passivated surface that could sense the analyte without non-specific interactions; b) functionalizing the surface with a specific ligand for prefibrillar Aβ amyloids detection, thus increasing the selectivity of our sensing approach. Because of this dual purpose, we conceived a multistep chemical surface functionalization strategy that can be outlined with three main phases: i) treatment of the surface with an established chemical method to generate a suitable functional group, ii) attachment of a versatile bi-functional linker for spacing purposes, to which iii) the ligand could be covalently bond. Such a multistep approach is of great advantage in the context of batch surface modification. Each reaction step can be carried out with several multilayers at the same time. For the final ligand binding, the treated multilayers can be divided in two or more groups and made react with the specific desired molecule.

Therefore, as we aimed at establishing a protocol enabling a wide variety of surface modifications, for the first reaction step i), we decided to employ the highly versatile glass-based surface functionalization chemistry. It is based on the use of organosilanes. Silanization as surface modification method is characterized by high physical and chemical stability of the introduced layer, thus giving access to a wide variety of chemical reactions for further modifications. We selected an amino organosilane ((3-Aminopropyl)triethoxysilane, APTES) that has been extensively used by different research groups(15, 16). APTES introduces an amino group on the treated surface (see Fig.4.1.1). The free -NH2 group can be used as handle to attach probes or linkers using a well-developed and reliable chemistry. APTES has been reported to be a versatile tool for disparate applications(13, 16). Using APTES, good surface homogeneity has been achieved, and, depending on the reaction conditions, the formation of ordered self-assembled monolayers (SAMs) has been demonstrated(17). Moreover, the moderate length of the aliphatic chain connecting the amino group to the silicon atom in APTES brings the ligand close to the surface. This proximity is favorable in our sensing scheme, as the BSW is evanescent and field intensity, hence measurement sensitivity, exponentially decays with distance(18), as explained in Chapter 2. The mechanism by which APTES condensates onto hydrated silica surfaces is shown in Fig.4.1.1(16, 19). With APTES, the presence of water molecules at the surface is fundamental for the silanization process. The condensation reaction between two or more APTES molecules depicted in the top scheme in Fig.4.1.1 is possible both in solution and at the surface, but it is most likely to occur at the surface once the silanization reaction has commenced(16).

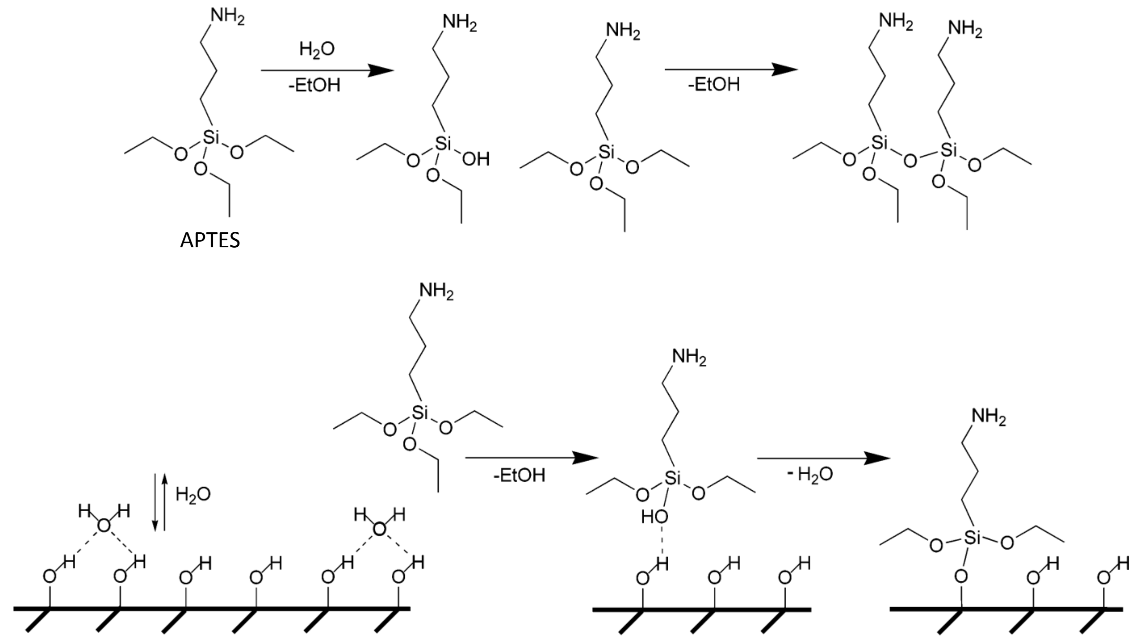

Fig.4.1.1. APTES surface condensation scheme. In the top scheme the hydrolysis of APTES in solution phase is presented to highlight the possible mechanism of initiation of the SAM formation. The following condensation reaction between two or more APTES molecules is also depicted in the top scheme. The presence of water molecules is fundamental for the surface silanization process, as shown in the bottom scheme. Scheme reprinted from J.A. Howarter and J.P. Youngblood, 2006(19) with permission from the American Chemical Society.

For the following step ii), we envisaged using a bi-functional linker devised for antibodies attachment to AFM tips, adapted from a work published by Wildling *et al* in 2011(20). The linker was synthetized in our group by Dr. Kolympadi, and it carries an N-hydroxysuccinimide (NHS) ester function and an aldehyde protected group (see Fig.4.1.2).

Regardless of the nature of the final ligand, all the reactions involved in our multistep surface chemistry strategy are presented in Fig.4.1.2 and discussed in details in the following paragraph.

Finally, depending on the selected ligand, the final binding step iii) is described in details in section 4.2 for the surface passivation procedure (compound 4a in Fig.4.1.2), and in section 4.3, for the selective prefibrillar Aβ recognition experiment (compound 4b in Fig.4.1.2), respectively.

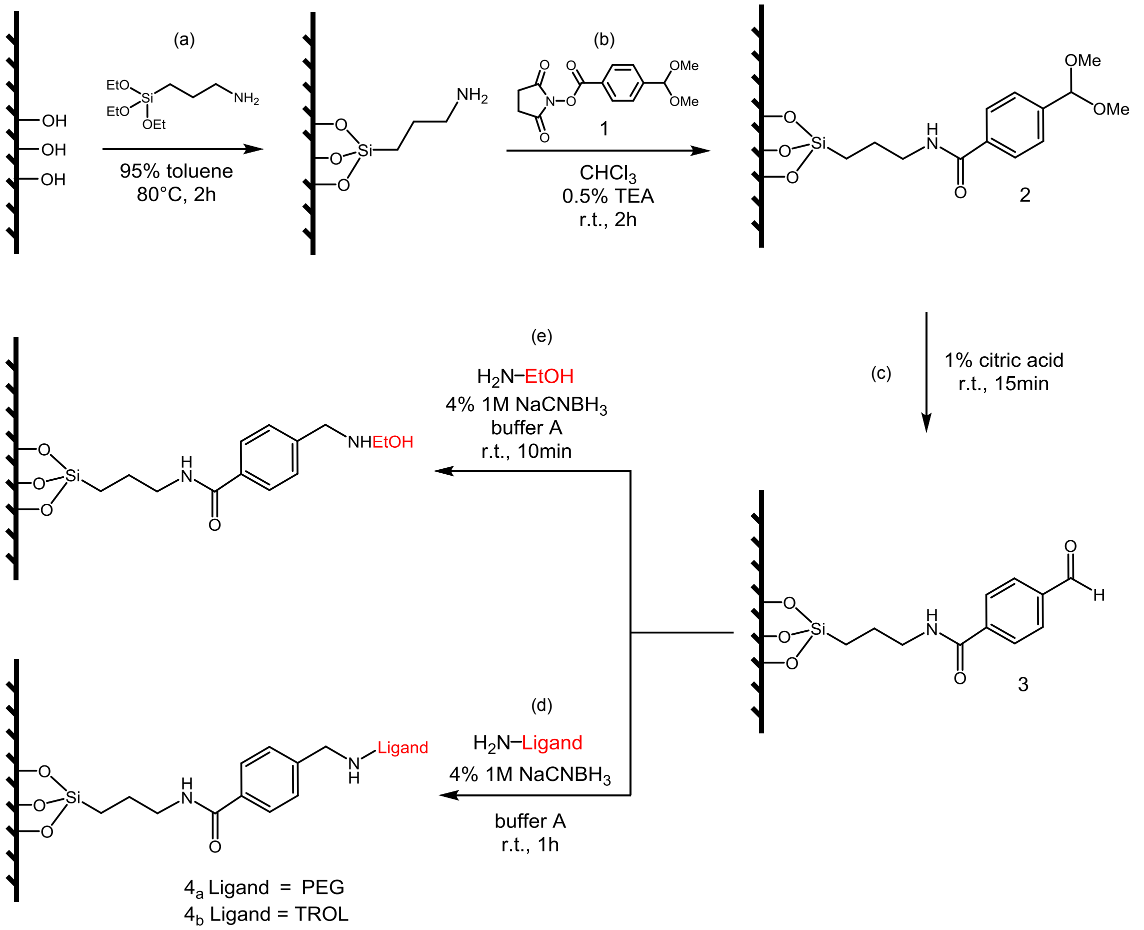

Fig.4.1.2. Surface functionalization chemistry scheme. The silicon nitride surface is represented by hydroxyl functions in the top layer. The sensing surface was treated via subsequent reaction steps: (a) aminosilanization with APTES; (b) attachment of the acetal-NHS linker via amide bond formation; (c) linker deprotection: conversion of the acetal to the aldehyde function; (d) ligand coupling via Schiff-base formation and reduction to stable C-N single bond (see sections 4.2 and 4.3); (e) end-capping of unreacted linker. Buffer A was 100 mM NaCl, 50 mM NaH_2PO_4, pH 7.5. Steps (b), (c), (d), (e) were adapted from the literature(20). See Chapter 8 for details.

All the surface modification reaction steps in Fig.4.1.2 were performed by immersion, either vertically positioning the dielectric multilayers in the reaction bath, or placing them at the bottom of it, with the dielectric layers oriented upwards. After each reaction step, the multilayers were extensively rinsed with water or with the organic solvent used in the reaction bath, and then dried with a gentle N_2 flux. This procedure was essential to avoid the staining of the substrates.

As a preliminary step, the silicon nitride surface was treated with a piranha solution (3:1 H_2SO_4:H_2O_2). Piranha is a potent oxidizing agent, which removes unwanted organic contaminants and generates silanols functions Si-OH able to react with APTES(21). For the aminosilanization with APTES (Fig.4.1.2 (a)), 5% of water was added to the toluene bath to induce APTES surface condensation(16), as previously explained. The following step consisted in binding the bi-functional linker 1 to the free amine groups of the APTES-modified surface, as presented in Fig.4.1.2 (b). The acetal group of 2 was subsequently deprotected with mild acid, thus creating the aldehyde 3 (Fig.4.1.2 (c)). Finally, 3 was connected to the free amino group of the ligand via Schiff-base formation. The consecutive *in situ* reduction resulted in the stable compounds 4a and 4b (Fig.4.1.2 (d)). As a final step(20), we end-capped the unreacted activated linker 3 via the use of ethanol amine (Fig.4.1.2 (e)). For further details on the functionalization strategy, see Chapter 8.

4.2 Polyethylene glycol self-assembled monolayer coating

This section is a partial adaptation of the journal article:

Santi, S., Musi, V., Descrovi, E., Paeder, V., Di Francesco, J., Hvozdara, L., van der Wal, P., Lashuel, H. A., Pastore, A., Neier, R. and Herzig, H. P. (2013), Real-time Amyloid Aggregation Monitoring with a Photonic Crystal-based Approach. ChemPhysChem, 14: 3476–3482.

For a better understanding of the type of process observed during the monitoring of the Aβ42 peptide, as presented in Chapter 3, we explored an approach based on "passivating" the multilayer surface by a chemical coating. The goal of these experiments was to indirectly investigate the Aβ42 surface interaction process throughout its aggregation. Polyethylene glycol (PEG) of a molecular weight of 750 Da, attached to a glassy surface, forms an ordered brush-like SAM(22). The SAM thickness is reported to be 50-70 Å. PEG coated surfaces successfully avoid non-specific protein interaction, independently of the nature of the surfaces(23), and were shown to be almost inert(24, 25). Synthetizing a PEGylated multilayer surface should therefore considerably reduce or even totally suppress the surface influence on the process of Aβ42 aggregation.

As explained in the previous section 4.1, we devised a surface chemistry where a ligand can be bound to the surface if provided with an amino group. Therefore, methoxy polyethylene glycol amine 750, an α- and ω-substituted PEG derivate, was selected to be linked to the silicon nitride top layer of the sensing multilayer. Hence, the amino end-group of the modified PEG molecule 4a was reductively coupled to the linker 3 (see scheme in Fig.4.1.2), as presented in Fig.4.2.1. We thus obtained a PEGylated multilayer surface.

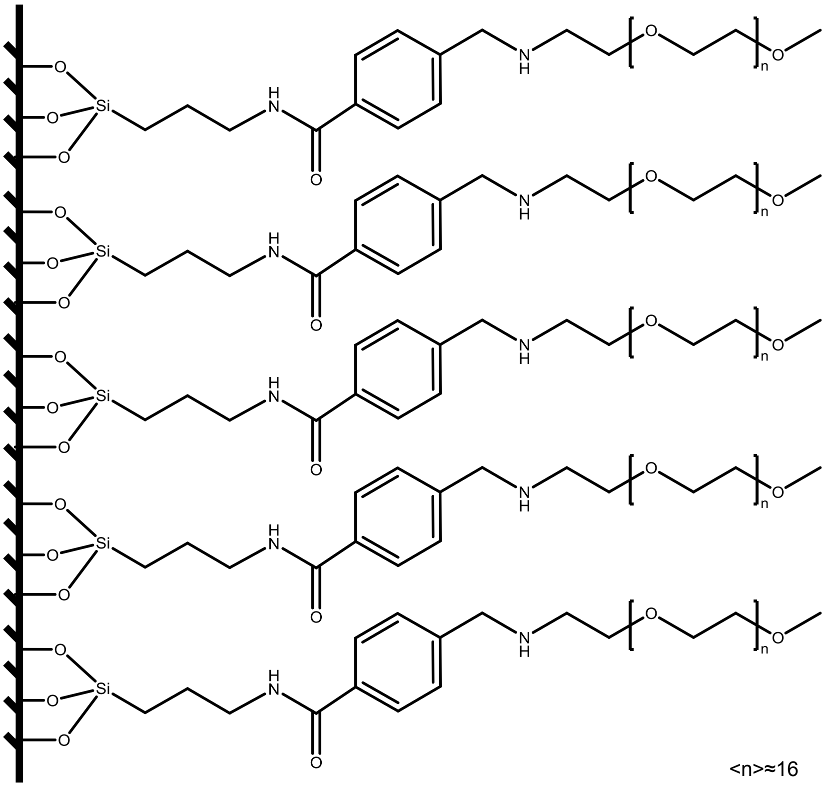

Fig.4.2.1. PEG coating scheme. Methoxy polyethylene glycol amine 750 was reductively coupled to the aldehyde function of the linker. In contrast to higher-molecular-weight PEGs forming bundle-like SAMs, PEG750 forms an ordered brush-like SAM on the multilayer surface(22). The selected PEG derivate was 50-70 Å long and formed by approximately 16 ethylene glycol units.

4.2.1 Bovine Serum Albumin aggregation sensing: efficacy test of the passivation treatment with PEG

Bovine Serum Albumin (BSA) is a model protein widely used for several protein chemistry and biochemistry applications due to its high availability, stability at room temperature and low purchase price(26). For example, BSA is employed in ELISA tests as blocking agent(27), in the Bradford protein assay as reference for protein quantification(28), and in cell cultures as nutrient(26). BSA has frequently been employed as a passivating agent for prosthetic implants, due to its high propensity to adhere to almost any hydrophilic surface because of its overall negative charge at neutral pH(29). Provided the easy access to this protein and its countless applications, many research groups are using BSA as a model to study aggregation *in vitro*. It has been shown that BSA undergoes aggregation at high temperatures forming an amyloid-like pattern. The native structure of BSA is an all-α helix. Upon aggregation, a strong increase of β-sheet content, a typical feature of amyloidogenicity, has been reported(30). A series of investigations lead to the identification of the conditions and mechanism for the BSA amyloid-like self-assembly. Interestingly, thermally induced ordered fibrillization occurs at pH values above the protein isoelectric point (4.8) and at a low concentration regime(31). In the view of these findings, we selected the BSA protein as a suitable candidate to perform a real-time BSW-based monitoring. The purpose of these experiments was dual: Provided the properties of this peptide to be adsorbed onto hydrophilic surfaces and to aggregate in controlled conditions, we employed it as a control test for the PEGylation coating effectiveness, and, in a second series of experiments, as a model for studying the kinetics of aggregation.

To prove the capability of PEG to prevent non-specific protein interactions with the multilayer surface, we separately incubated two identical BSA sample solutions in the presence of a bare and of a PEGylated multilayer. The signal obtained from the real-time monitoring of the refractive index variation of these samples, as sensed by the BSW, is shown in Fig.4.2.2 and in Fig.4.2.3. Note that, for the set of BSW-assisted monitorings presented in this section only, the d.i. water pixel value prior to the BSA incubation was set to zero.

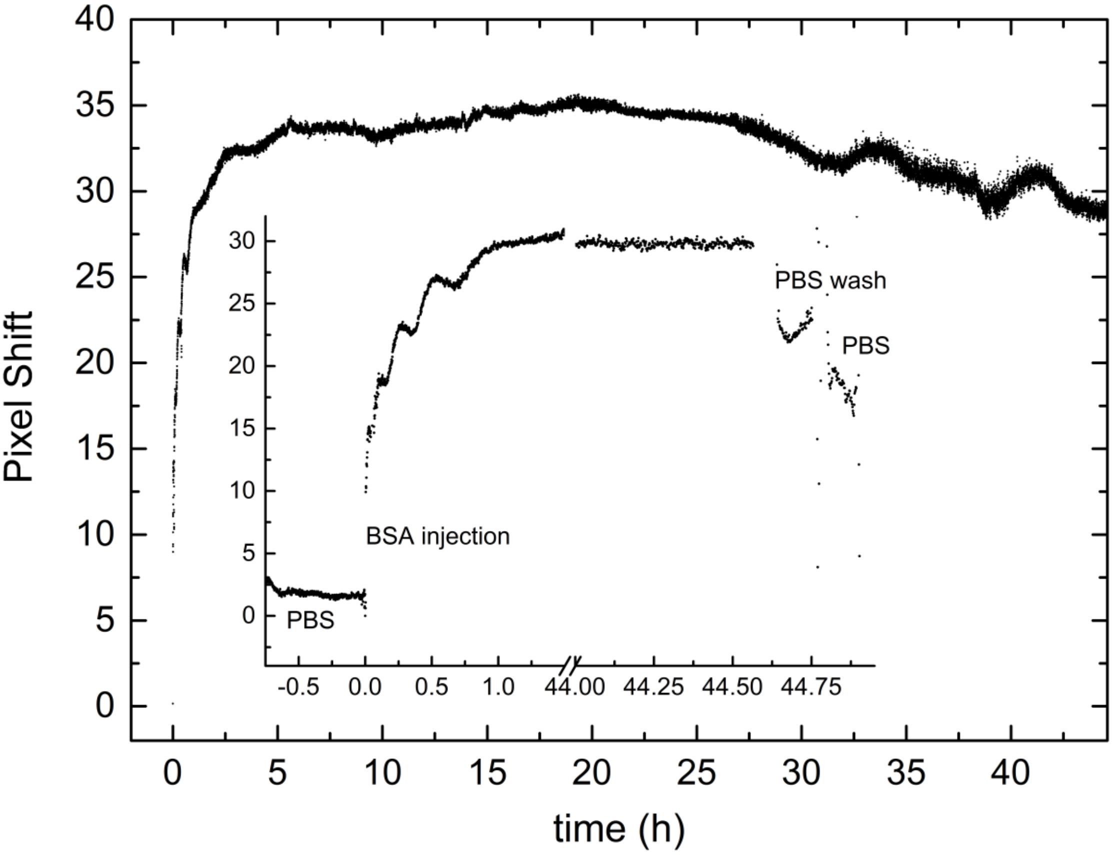

Fig.4.2.2. Real-time monitoring of the refractive index shift of incubating BSA protein with a bare multilayer. The BSA sample (initial monomer concentration 0.56 mg/mL, in 0.1 M PBS, pH 8.9) was incubated at 57 °C in contact with a bare multilayer. Inset: enlargement of the sensogram obtained upon the injection of the BSA sample, following the calibration with PBS at 57 °C. The d.i. water pixel value prior to the BSA aggregation monitoring was arbitrarily set to zero.

As shown in Fig.4.2.2, the incubation of BSA with a bare multilayer was performed with an initial protein concentration of 0.56 mg/mL in PBS at 57 °C. PBS which was also used to calibrate the BSW response before the incubation of the protein, as presented in the inset. BSA concentration, buffer and incubation temperature were chosen according to the literature(31), where they have been reported to promote a steady amyloid-like aggregation process within few hours. After more than 20 hours of incubation, no significant change of the refractive index as sensed by the BSW could be correlated to BSA aggregation or secondary structure variation process. The scattering signal after 30 hours of incubation has to be best regarded as the effect of temperature fluctuations, rather than as the monitoring of BSA aggregation. As expected, the initial monitoring of the BSA sample revealed an abrupt positive pixel shift. As seen in Chapter 3, this signal is related to a strong adsorption of the protein onto the bare surface of the sensor. A significant local increase of the refractive index is therefore observed. Highlighted by the inset in Fig.4.2.2, the signal resulting from the first hour of monitoring was increasing with a steady but intermittent trend. The BSW, at this specific monitoring stage, was reasonably sensing both the BSA aggregation occurring in the bulk and the unspecific BSA protein adhesion onto the surface. We propose that the undulating trend of the refractive index, as sensed by the BSW, was the result of those two concomitant processes.

Finally, PBS was employed to extensively wash the fluidic cell and then incubated without varying the temperature of the system, as presented in the inset of Fig.4.2.2. The signal resulting from the monitoring of PBS in this condition was not constant and did not reach the initial pixel value exhibited before the BSA incubation. A reasonable explanation can be that the multilayer surface was steadily coated by surface-adsorbed BSA proteins. The consequent shielding of the BSW sensitivity could be the reason for the absence of refractive index variations of the solution, as sensed by the BSW, for long incubation time.

To verify the correlation between the positive pixel shift and the BSA surface adsorption process we performed the same experiment with a PEGylated multilayer, and the result of the monitoring is presented in Fig.4.2.3, where the real-time monitoring of the proteic sample refractive index variation, incubated at 57 °C, is shown. As explained before, the goal of this test was to provide a proof for the effectiveness of the PEG coating, which should avoid any non-specific protein-multilayer interactions throughout a real-time BSW-assisted measurement.

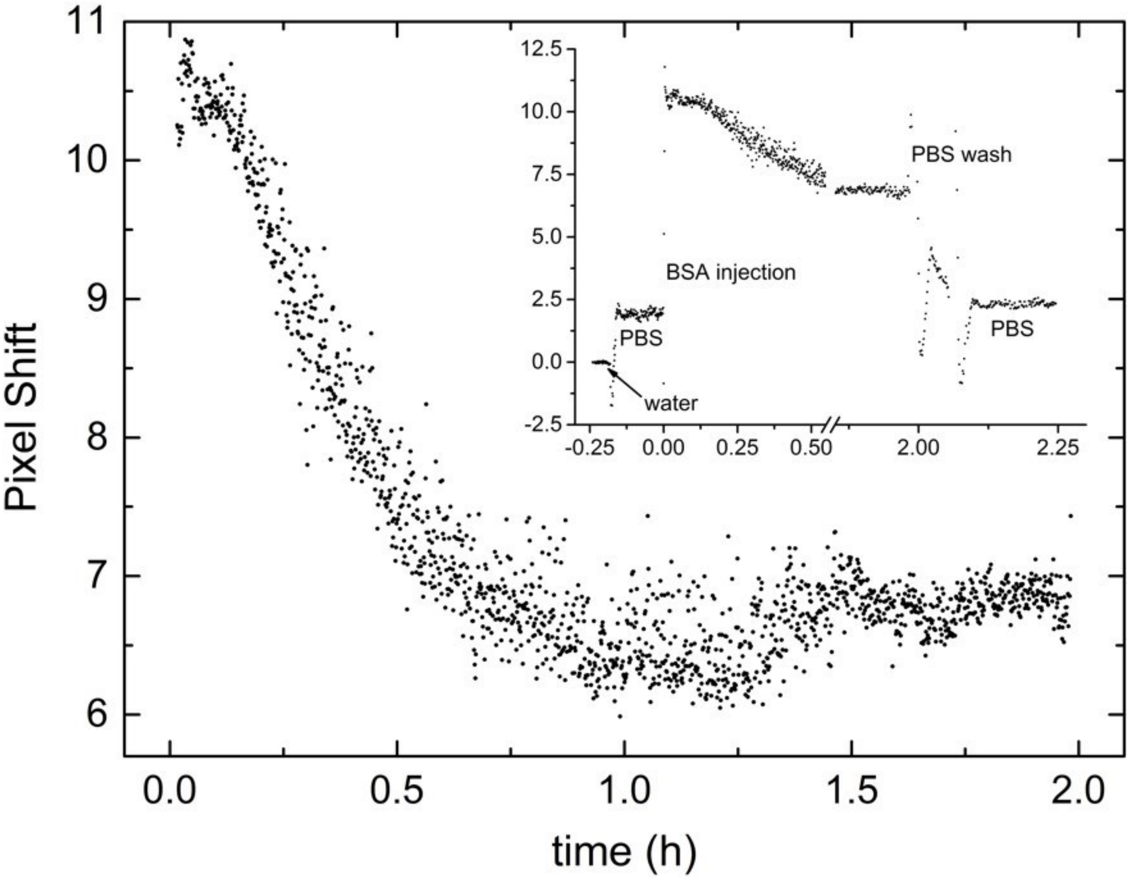

Fig.4.2.3. Real-time monitoring of the refractive index shift of incubating BSA protein with a PEGylated multilayer at 57 °C. The BSA sample (initial monomer concentration: 0.52 mg/mL, in 0.1 M PBS, pH 8.9) was incubated at 57 °C in contact with a PEGylated multilayer surface. Inset: enlargement of the sensogram obtained upon the injection of PBS, before and after the BSA sample incubation, at 57 °C. The d.i. water pixel value prior to the BSA aggregation monitoring was arbitrarily set to zero.

As shown in Fig.4.2.3, with a PEGylated multilayer surface the initial positive pixel shift is almost negligible. This observation is compatible with the hypothesis that the BSA protein non-specific interaction with the multilayer surface is prevented by the PEG coating. The observed decrease of the pixel shift can be attributed to the monitoring of the BSA aggregation occurring in the bulk. Moreover, as presented in the inset of Fig.4.2.3, after washing the fluidic cell with PBS, the signal returns to approximately the same pixel value as exhibited before the incubation of BSA. This behavior is compatible with the proposal that almost no BSA coating was formed, which might have affected the BSW sensitivity. From the result presented in Fig.4.2.3, a steady refractive index decrease throughout incubation can be noticed. This signal variation can be tentatively correlated to the aggregation of the BSA protein. These observations and interpretations are similar to those reported for the monitoring of the Aβ42 peptide presented in Chapter 3.

Hence, we performed a second series of experiments with the purpose of investigating the capability of the BSW-based sensing approach to detect different BSA aggregation dynamics. The result of this study is presented in Fig.4.2.4 and Fig.4.2.5, and it stems from the choice of thermally inducing the BSA protein fibrillization at different temperatures, as suggested by the work published by Vetri *et al*(31). We selected to carry out the BSW-based monitoring at 57 °C, as already presented in Fig.4.2.3, and at 67 °C, as presented in Fig.4.2.4. The aggregation at the higher temperature has been reported to be the most rapid. At this condition, the authors described the BSA aggregation to occur without a lag-phase and to reach an abundant fibril extent within few hours, as confirmed by other studies(30, 32). Within this temperature range and at 632.8 nm, the refractive index of aqueous solutions varies linearly(33), as explained in Chapter 2.

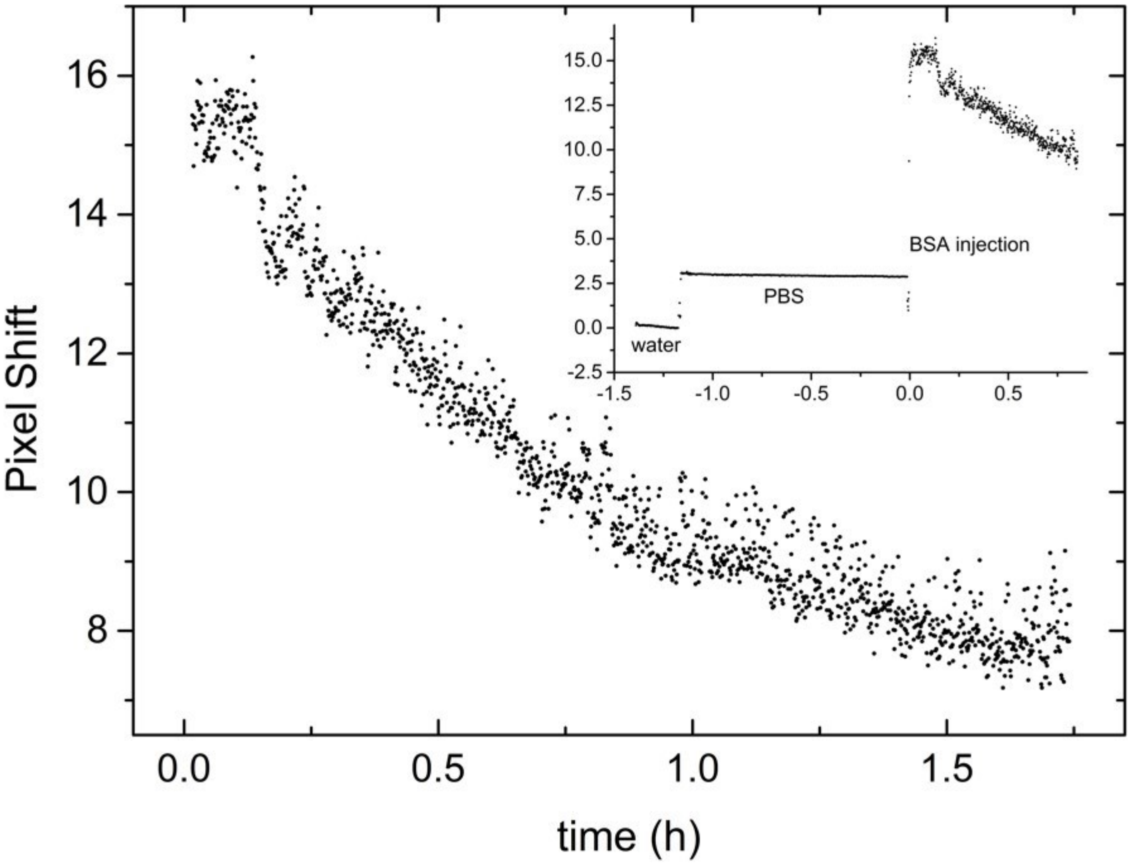

Fig.4.2.4. Real-time monitoring of the refractive index shift of incubating BSA protein with a PEGylated multilayer at 67 °C. The BSA sample (initial monomer concentration: 0.52 mg/mL, in 0.1 M PBS, pH 8.9) was incubated at 67 °C in contact with a PEGylated multilayer surface. Inset: enlargement of the sensogram obtained upon the injection of PBS before the BSA sample incubation, and after the system calibration with d.i. water, at 67 °C. The d.i. water pixel value prior to the BSA aggregation monitoring was arbitrarily set to zero.

As shown in Fig.4.2.4, the BSW-based monitoring was able to detect a decrease of the pixel shift in time, which can be attributed to the BSA protein aggregation at 67 °C. The protein interaction with the sensing surface was negligible based on the absence of an initial refractive index increase. As predicted, the presence of the PEG coating successfully prevented non-specific protein-surface interactions.

To perform a comparison between the monitorings of the BSA protein aggregation dynamics at the two selected temperatures, we had to normalize the signal. To take into account the different Δn response at different temperatures(34), we considered the pixel shift between water and PBS ($\Delta\text{pixel}_{\text{water/PBS}}$) at each experimental temperature as a reference, and used this value to normalize the signal of the monitorings. At 57 °C, $\Delta\text{pixel}_{\text{water/PBS}} = 2$ (see Fig.4.2.3, inset), and, at 67 °C, $\Delta\text{pixel}_{\text{water/PBS}} = 3$ (see Fig.4.2.4, inset). The two normalized experimental curves were shifted to zero to enable their comparison, and are presented in Fig.4.2.5.

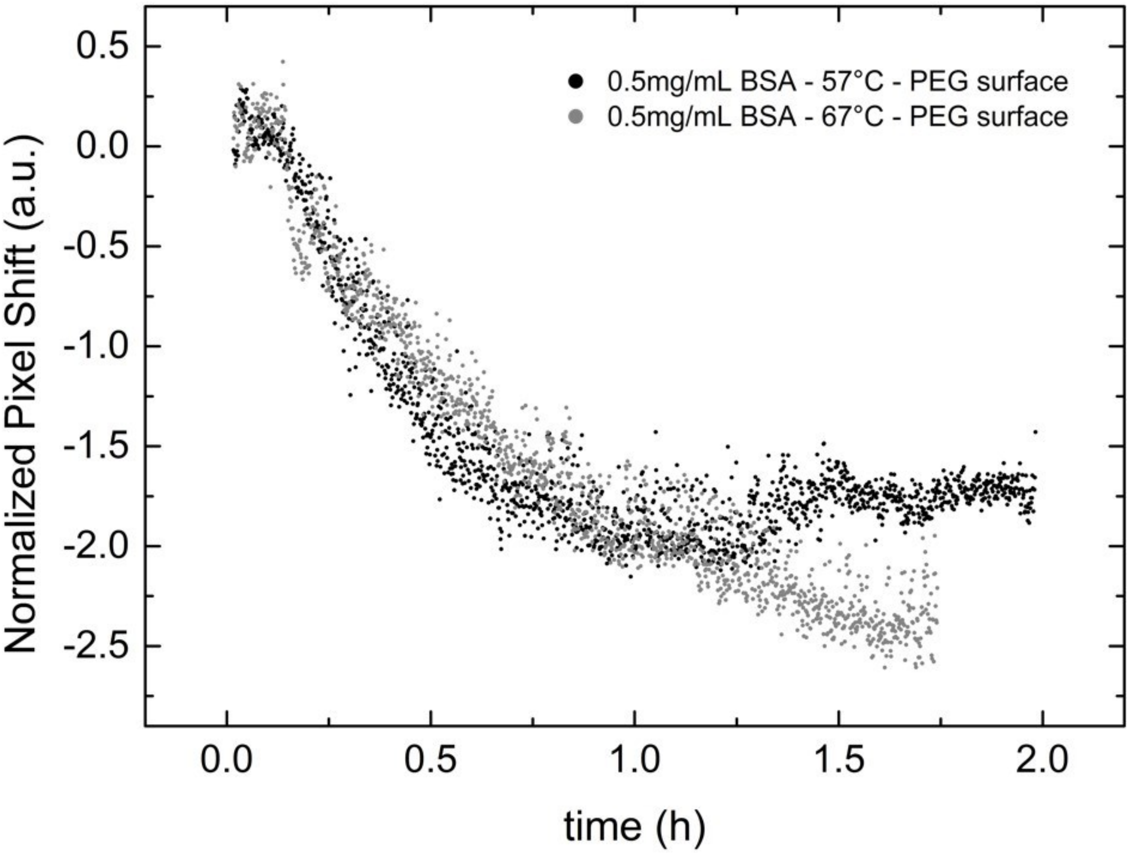

Fig.4.2.5. Comparison of the real-time monitoring of the refractive index shift of incubating BSA protein with a PEGylated multilayer. Two BSA samples (identical initial monomer concentration: 0.52 mg/mL, in 0.1 M PBS, pH 8.9) were incubated at 57 °C and 67 °C, separately, in contact with a PEGylated multilayer surface. The curves were normalized and the initial data points were set to zero for the comparison.

At the two selected working temperatures, the monitorings of the aggregating BSA protein, as sensed by the BSW, resulted in similar signals. For both measurements, the refractive index steadily decreases almost immediately after the beginning of BSA incubation. As expressed before, we attributed the decrease of the refractive index to the extent of the BSA fibril formation. The rate of this refractive index decrease at 57 °C is comparable with, or at least not distinguishable from that of the BSA incubation monitoring at 67 °C. The main difference between the results presented in Fig.4.2.5 is that, after approximately 1.5 hours, the monitoring showed a continuing decrease at 67 °C. At 57 °C, a plateau was instead reached. The signal plateau is likely to be ascribed to the end of the BSA fibrillization process. This hypothesis assumes that no concentration variations of the soluble prefibrillar BSA form is sensed by the BSW once the plateau is reached. Indeed, our measurement relies on the monitoring of the refractive index variation of the solution, which is related to the BSA monomer concentration depletion during aggregation. As explained in the previous chapter, the extent of the fibril formation is therefore indirectly assumed upon refractive index decrease. Therefore, we speculate that a higher extent of BSA fibril was formed at 67 °C, leading to a larger putative plateau. However, at 67 °C, the apparent fibrillation rate was the same as at 57 °C (or maybe even slower than at 57 °C). This result is in disagreement with what reported in the literature, where authors have reported a higher fibrillar extent, but also a faster fibrillization rate, exhibited by the BSA protein when incubated at 67 °C, compared to the same experiment performed at 57 °C(31, 35). Further attempts to duplicate the experiment lead to outcomes that were comparable to those reported in Fig.4.2.5. At present, we are unable to explain the last part of the signal we obtained employing the BSW-assisted approach to cover the BSA protein aggregation at 67 °C. To deduce conclusions on the intimate dynamics of BSA aggregation, supporting biochemical experiments are needed. As the investigation of the aggregation dynamics of the BSA protein was not the prime goal of our research, we therefore concentrated on the study of the Aβ42 peptide, for which complementary studies were performed in parallel to those based on the BSW sensing approach (for further studies on the Aβ42 peptide, see Appendix 2).

4.2.2 Aβ42 aggregation sensing with a PEGylated multilayer surface

Results on the variation of the amyloid aggregation dynamics as sensed by the BSW with a passivated PEGylated multilayer are presented in Fig.4.2.6. We incubated initially monomeric Aβ42 samples at 37 °C in the fluidic chamber of the sensor under the same conditions as with the bare multilayer. The monitoring of the refractive index change throughout the Aβ42 aggregation process revealed a variation in the first part of the measurement compared to the monitoring of the Aβ42 peptide with an unfunctionalized multilayer. This preeminent variation was concerning the amount of peptide interacting with the surface. On the contrary, as explained in the following, the rate and timing of the fibrillization process resulted unaffected by the presence of the PEG coating. A comparison between results obtained monitoring the Aβ42 peptide with a bare and a PEGylated multilayer surface, respectively, is presented in Fig.4.2.7, as revealed by the BSW-based sensing.

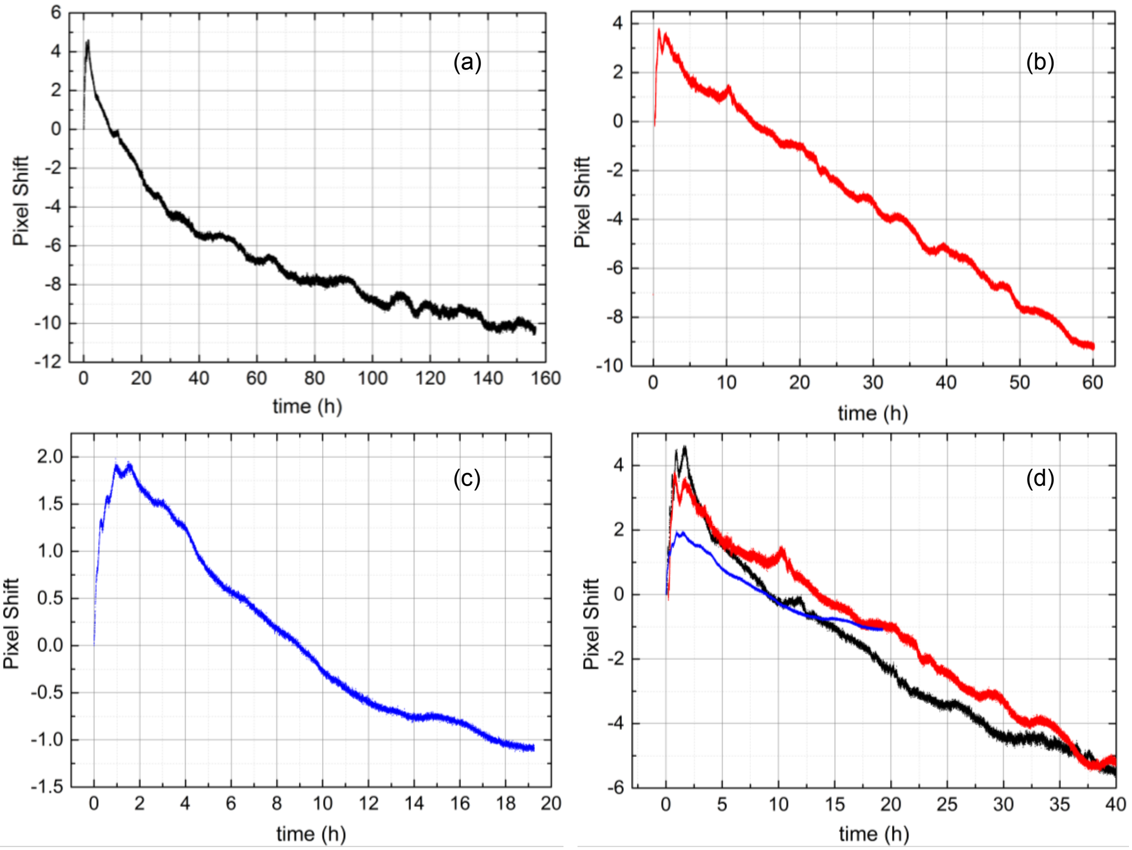

Fig.4.2.6. Real-time monitoring of the refractive index shift of incubating Aβ42 peptide with a PEGylated multilayer surface. Three Aβ42 samples (in 10 mM Tris HCl buffer, pH 7.4, initial Aβ42 monomer concentrations: (a) 17.3 µM; (b) 17.3 µM; (c) 7.7 µM,) were incubated at 37 °C in contact with a PEGylated multilayer. The overlap of the three distinct measurements is presented in a close-up view in graph (d), where colors are the same as those used for the single measurements.

The monitoring of Aβ42 aggregation with a PEGylated multilayer was performed with initial peptide concentration of 17.3 and 7.7 µM (see Fig.4.2.6). The results are reproducible and consistent, as highlighted by the overlap of the three curves presented in Fig.4.2.6 (d). A higher initial monomer concentration led to a larger initial refractive index increase, and to an acceleration of the refractive index decrease rate (consistent with the results presented in Chapter 3). These observations are in accordance with the results reported the literature(36-

38), where a positive correlation between Aβ peptide initial concentration and amyloid aggregation rate has been demonstrated.

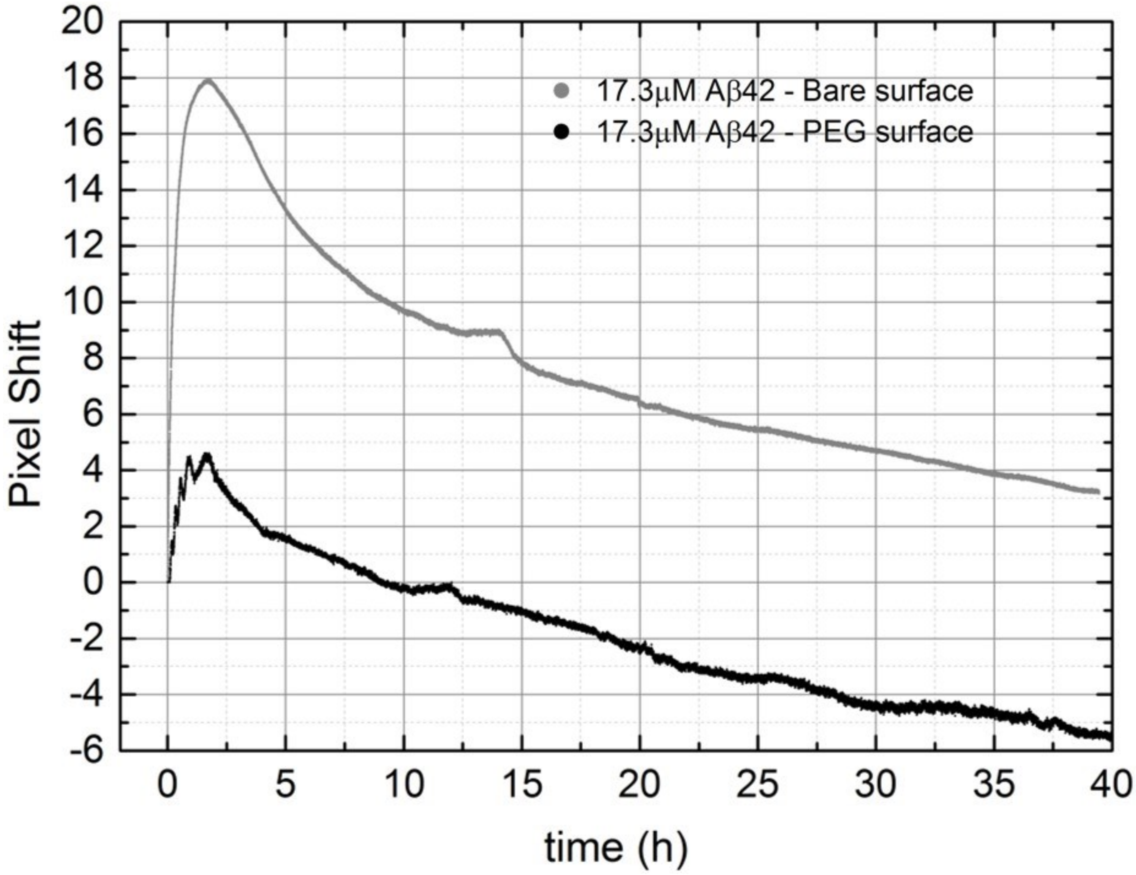

Fig.4.2.7. Selection of real-time monitorings of the refractive index shift of incubating Aβ42 peptide. Comparison of the monitoring presented in Fig.3.2.3, in grey, and in Fig.4.2.6 (a), in black, respectively. They correspond to the results obtained incubating two distinct Aβ42 samples (in 10 mM Tris HCl buffer, pH 7.4, identical initial monomer concentration 17.3 μM, T = 37 °C) with a bare and with a PEGylated multilayer surface, respectively.

To analyze the effect of the surface PEGylation on the monitoring of Aβ42 aggregation one may especially focus on the comparison shown in Fig.4.2.7, where selected real-time monitorings of the Aβ42 peptide aggregation without and with surface coating are presented. In the measurements with a PEGylated multilayer surface, the curve (in black) reveals an initial positive pixel shift that is four times smaller compared to the same experiment with a bare multilayer (in grey). As discussed in Chapter 3, the real-time refractive index variation of the aggregating Aβ solution, as sensed by the BSW, were interpreted as the result of different contributions, which can be described by Eq.(3.1):

$$\Delta n = \Delta n_s + \Delta n_b \qquad (3.1)$$

wherein Δn_s is the refractive index variation due to surface adsorption/desorption processes, and Δn_b is the refractive index variation occurring in the bulk solution, as observed within the evanescent tail of BSWs. On the PEGylated multilayer surface a smaller amount of adhesion-competent peptide is adsorbed, causing a smaller Δn_s increase. After 10 hours of incubation, this curve reaches negative values for the BSW resonance shift. Therefore, the refractive index of the solution, as sensed by the BSW, has become lower than at the initial stage of the incubation. This does not happen when incubating the Aβ42 monomer with a bare surface. In this context, the BSW resonance shift onto the camera pixels remains positive because of the shielding due to the initial mass-loading mechanism. The peptide surface-loading effect is therefore hampering the BSW sensitivity. On the contrary, the presence of the PEG coating effectively decreased the loading effect, thus making the BSW mainly sensitive to bulk fibrillization. After an incubation time between 8 and 12 hours, the two curves presented in Fig.4.2.7 show decreasing slopes that present similar rates. Therefore, for long incubation time (over 8 and 12 hours), the temporal evolution of the refractive index change is in general related to the bulk of the solution only, Δn_b, where the fibrillization of the Aβ42 peptide occurs, regardless of the surface functionalization. We infer that the fibrillization process should not be affected by the surface-adsorption mechanism. With a bare multilayer surface, the surface-loading process only results in a decrease of sensitivity, still allowing estimating the time rate of Δn_b. For an incubation time between approximately 2 and 8 hours, the descending Δn profiles of the monitorings in Fig.4.2.7 present different rates. Especially, with a bare multilayer surface Δn decreases with a faster rate. Having established that the fibrillization with a PEGylated and bare multilayer occurs with similar rates, the contribution of Δn_b to the general Δn decrease should be the same with and without surface PEGylation. Therefore, we suggest that this difference should be ascribed to the desorption of the peptide from the bare multilayer surface, causing a decrease of Δn_s.

4.3 Sensing selectivity enhancement: Tryptophanol surface functionalization

Many dyes specifically recognizing amyloid structures, such as Congo Red and ThT, have been used in the last 60 years(1, 39-41). They all are extrinsically fluorescent, meaning that their association with an amyloid pattern results in a considerable enhancement of their fluorescence quantum yield. Notably, ThT has been extensively used to monitor the aggregation pathway of the Aβ peptide, for its intrinsic fluorescence is reported to increase upon binding to amyloid like structures(42, 43). A great effort to find even more selective molecules has been invested. This has led to the investigation of various fluorescent dyes that could overcome the low sensitivity of ThT towards the first oligomerization stages of amyloid aggregation(44, 45). Among others, a class of indoles has been identified to be selective for the recognition and the binding of prefibrillar Aβ aggregates(46). In this thesis project, we focused on L-Tryptophanol ((S)-2-amino-3-(3-indolyl)-1-propanol, TROL, see Fig.4.3.1) as a representative of this class. TROL selectivity has been reported to be nearly 20-fold greater than that of ThT(47). In an article appeared on ChemBioChem journal in 2010, Reinke *et al*(48) described TROL as capable of binding both Aβ40 and Aβ42 early aggregates, covering the first steps of amyloid aggregation and overcoming the heretofore silent “lag phase”, which corresponds to the early stage oligomerization process. Their experiment consisted in a ThT-like spectroscopic assay, where intrinsic TROL inherent fluorescence was quenched upon binding prefibrillar Aβ aggregates, but not by mature Aβ fibrils. They suggested that TROL specificity towards prefibrillar aggregates is due to the interaction of the indolic moiety (see Fig.4.3.1) with one or more sites, especially charged residues, of the amyloid prefibrillar structure that are buried, or are altered, in the mature amyloid fibrils.

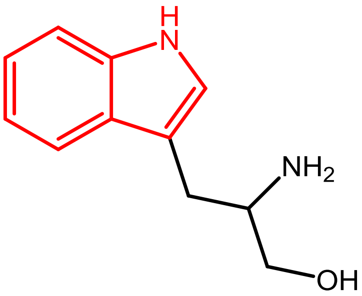

Fig.4.3.1. Structure of TROL. The compound is characterized by an indolic moiety (in red) that grants inherent fluorescence properties.

We chose TROL as a ligand for the surface functionalization strategy presented in the previous sections. We selected this indole molecule to address selective prefibrillar Aβ42 aggregates detection via the BSW-based sensing approach. As presented in Fig.4.3.2, the TROL molecule (corresponding to molecule 4b, see scheme in Fig.4.1.2) could be covalently bond to the linker 3 via its amino group using the functionalization strategy we devised.

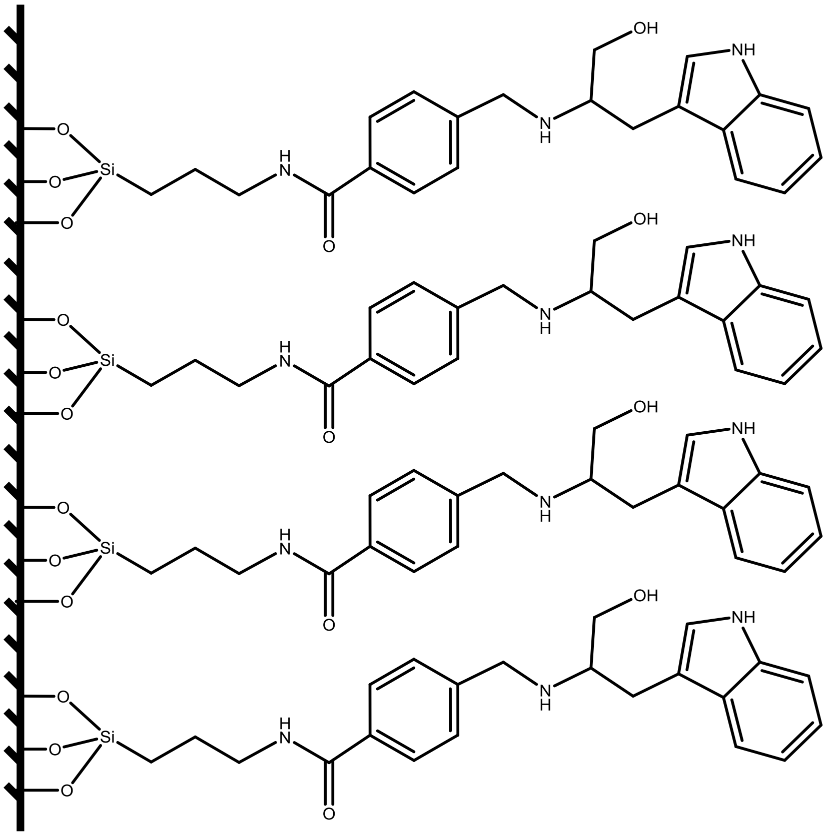

Fig.4.3.2. TROL functionalization scheme. The primary amine group of TROL (Fig.4.3.1) was reductively coupled to the aldehyde function of the linker. The indolic moiety of the compound should still be available for amyloid binding.

4.3.1 On an attempt to perform selective Aβ42 aggregation sensing with a functionalized multilayer surface

We hoped to finally identify the aggregation state of the Aβ42 species interacting with the bare multilayer surface. From the observation of the results we heretofore obtained we inferred that prefibrillar or oligomeric Aβ42 peptides were the species interacting with the surface. In this scenario, the goal of the TROL-functionalization was to capture Aβ42 oligomers near the multilayer surface, and therefore increase the signal during the first part of our monitoring. Enhancing the interaction of the Aβ42 oligomers with the TROL-functionalized multilayer surface should increase the local refractive index, as sensed by the BSW. We expected a larger maximum amplitude of the signal in the time frame of the first 2 hours of the real-time monitoring compared to the monitoring of the Aβ42 peptide with a bare multilayer surface. The interaction of the Aβ42 with TROL was reported to not affect the peptide aggregation dynamics(48). Therefore, for the second part of the measurement (after approximately 2 hours of incubation), where the BSW is mostly sensible to the bulk variation of refractive index Δn_b, we expected a Δn variation similar to the experiment using a bare multilayer. Our predictions are summarized in Fig.4.3.3, where a hypothetic real-time Δn monitoring with a TROL-functionalized surface is compared to an experimental result of the Aβ42 aggregation with a bare multilayer, as sensed by the BSW.

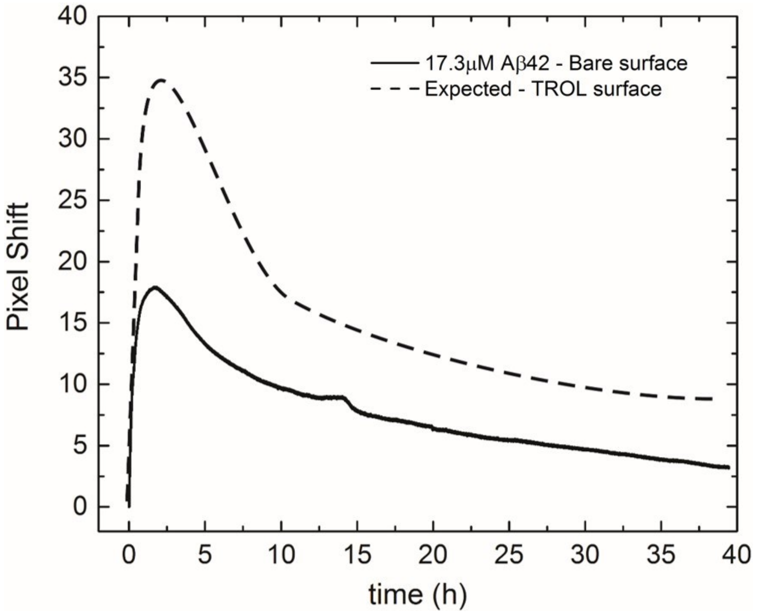

Fig.4.3.3. Prediction of a real-time monitoring of the refractive index shift of incubating Aβ42 peptide with a TROL functionalized multilayer surface. Comparison of the experimental monitoring with a bare surface presented in Fig.3.2.3 (initial Aβ42 monomer concentration 17.3 μM, in 10 mM Tris HCl buffer, pH 7.4), in solid line, and of the predicted monitoring of the same Aβ42 aggregating sample but with a TROL functionalized surface, in dashed line.

However, the experimental results presented in Fig.4.3.4 are distinctively different from our predictions (see Fig.4.3.3). We incubated initially monomeric Aβ42 samples at 37°C in the fluidic chamber of the sensor under the same conditions as the other measurements, regardless of the surface functionalization. With a TROL-functionalized multilayer, the monitoring of the refractive index change throughout the Aβ42 aggregation process revealed a distinct behavior compared to the monitoring of the Aβ42 peptide with an unfunctionalized multilayer.

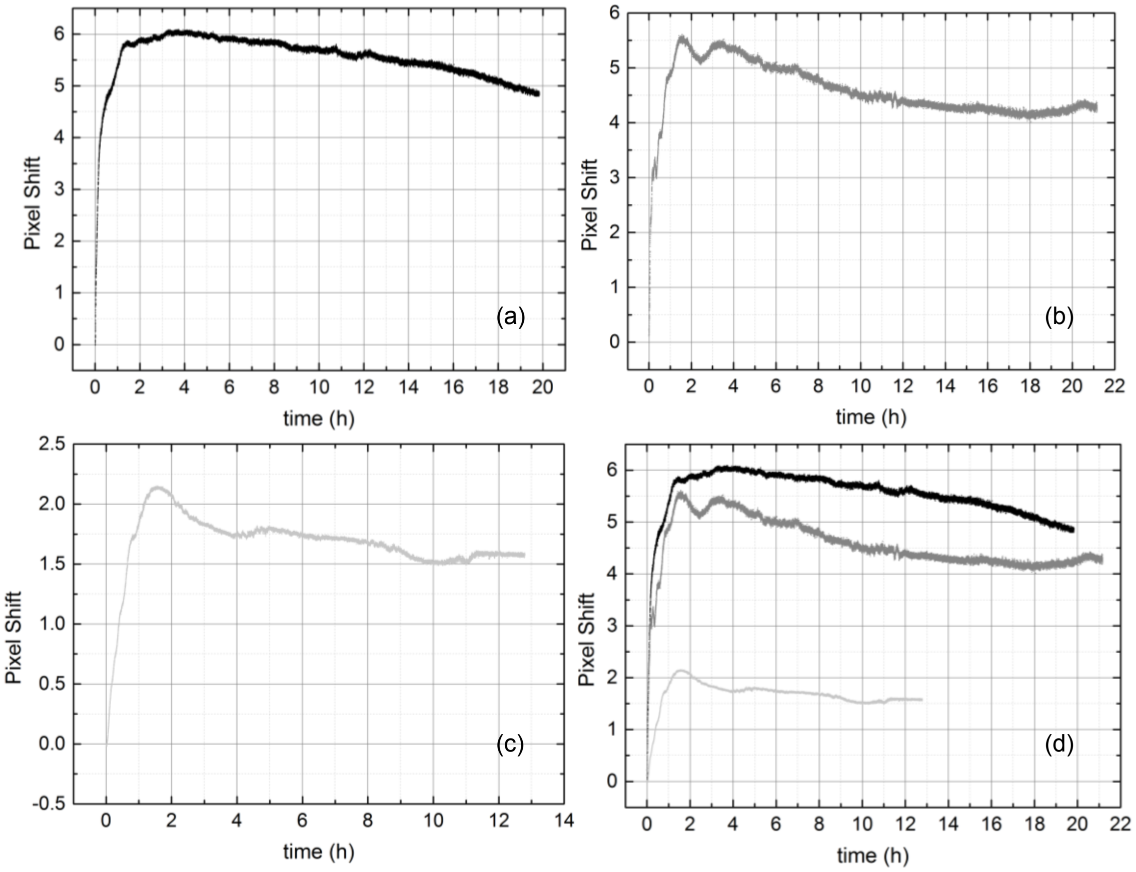

Fig.4.3.4. Real-time monitoring of the refractive index shift of incubating Aβ42 peptide with a TROL functionalized surface. Three Aβ42 samples (in 10 mM Tris HCl buffer, pH 7.4, initial Aβ42 monomer concentrations: (a) 17.3 µM; (b) 17.3 µM; (c) 7.7 µM,) were incubated at 37 °C in contact with a TROL functionalized multilayer. The overlap of the three distinct measurements is presented in graph (d), where colors are consistent with those used for the single measurements results.

As shown in Fig.4.3.4, in the first phase of the real-time monitoring of the refractive index variation of aggregating Aβ42 peptide samples with a selectively TROL-functionalized multilayer we observed a local refractive index increase of the probed solution, as sensed by the BSW. This positive signal was reasonably correlated to the interaction of the peptide with the multilayer surface. As for other real-time measurements obtained with bare or PEGylated multilayer surfaces, the extent of this surface interaction was concentration dependent. As shown by the overlap presented in Fig.4.3.4 (d), the initial monomer concentration of the Aβ42 peptide sample incubating in the sensing chamber was proportional to the amplitude of the increasing signal. For a better understanding of the results in Fig.4.3.4, a comparison between two measurements made under the same experimental conditions, but the first with a bare and the second with a TROL functionalized multilayer surface, is presented in Fig.4.3.5.

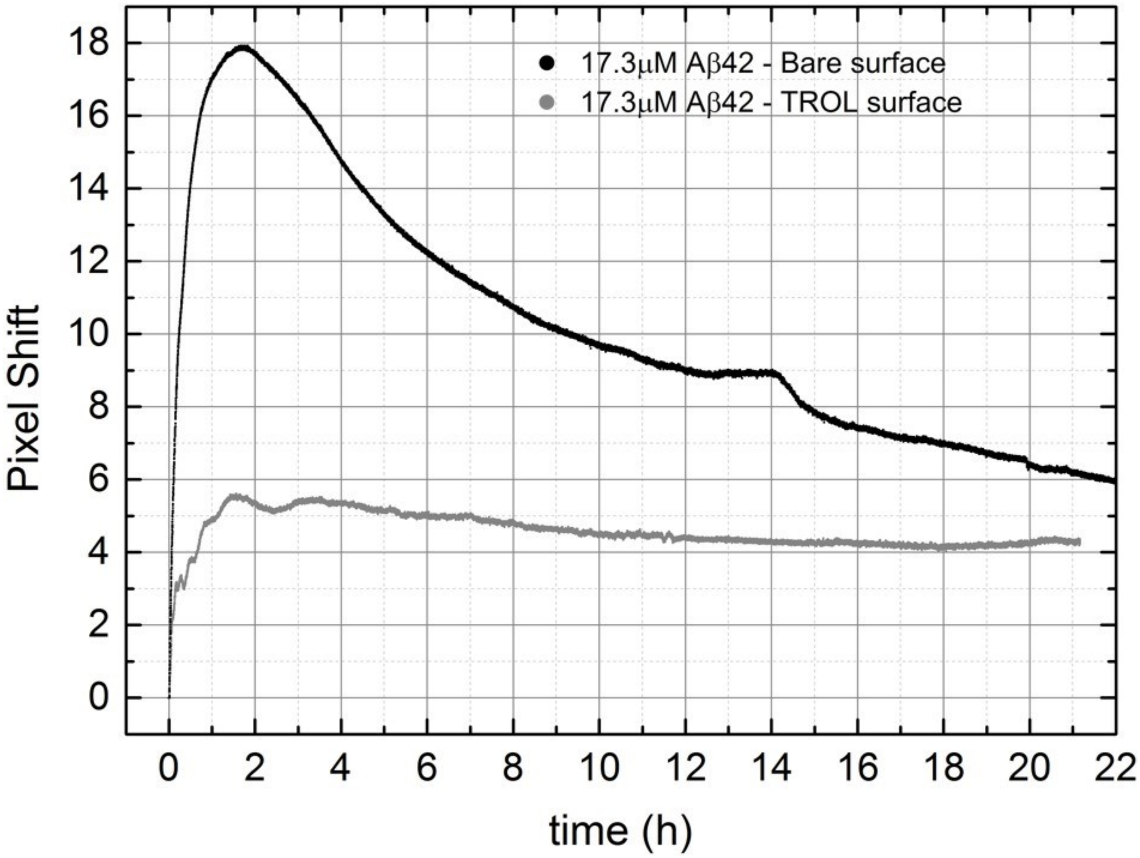

Fig.4.3.5. Selection of real-time monitorings of the refractive index shift of incubating Aβ42 peptide. Comparison of the monitoring presented in Fig.3.2.3, in black, and in Fig.4.3.4 (b), in grey, respectively. They correspond to the results obtained incubating two distinct Aβ42 samples (in 10 mM Tris HCl buffer, pH 7.4, identical initial monomer concentration 17.3 μM, T = 37 °C) with a bare and with a TROL functionalized multilayer surface, respectively.

The comparison in Fig.4.3.5 shows that the surface-loading process of the Aβ42 peptide to the bare or to the TROL-modified surface occurs in the same time frame for both measurements. Nevertheless, in the case of a TROL functionalized multilayer, the amplitude of the induced signal is much smaller.

For long incubation time, no further changes of the signal can be revealed by the BSW-based sensing. Interestingly, we did not observe a similar effect on the BSW sensitivity when measuring the Aβ42 peptide aggregation with a PEGylated multilayer. With a PEG coating, the BSW reveals changes in the refractive index of the solution even over long incubation times. As mentioned in the dedicated section (4.2), with a PEGylated surface the signal reaches negative values (Fig.4.2.7). The BSW thus becomes mostly sensitive to Δn_b, which is correlated to the decrease of the Aβ42 monomer concentration due to fibrillization. The chemical process adopted for the production of PEGylated and TROL-functionalized sensing surfaces was the same (section 4.1). Hence, we assume that an adequate surface modification treatment should not hamper the BSW sensitivity in general. As a consequence, the differences in the measurements presented in Fig.4.3.5 should be correlated to the presence of the surface-bound TROL molecule, which interacts with the Aβ42 peptide. In this context, we therefore assume that the peptide-loading effect should be reasonably ascribed to the presence of the TROL molecule, and not to an aspecific physisorption process, as seen in the case of the monitoring of the Aβ42 peptide aggregating with a bare multilayer. The experiment presented in the next section aimed at testing this working hypothesis.

4.3.2 ThT-like fluorescence assay with Tryptophanol

To further investigate the role played by the TROL molecule in our measurements, we decided to duplicate the ThT-like spectroscopic assay that was reported in the literature by Reinke *et al*(48), who for the first time described this indolic compound as a prefibrillar amyloid ligand. Provided that our purpose was not to study the fluorescence properties of TROL in the context of amyloid detection assays, we anyway decided to verify its effective and selective binding with the prefibrillar Aβ42 peptide.

In view of the results obtained with the BSW-based sensing approach, we especially aimed at investigating the time lapse of the local increase of the refractive index that we attributed to the peptide interaction with the TROL-modified surface (Fig.4.3.4 and 4.3.5).

For the fluorescence quenching experiment with TROL, the Aβ42 peptide was separately incubated, and TROL fluorescence response was measured adding solutions of the indolic molecule to aliquots of the aggregating peptide. As reported in the literature(46, 48), the intrinsic fluorescence of the indolic compound is quenched upon binding to prefibrillar Aβ42 peptide, but not to fibrils. The result of the fluorescence assay is presented in Fig.4.3.6, where the fluorescence response of TROL throughout Aβ42 peptide aggregation at 37 °C is plotted against incubation time. We successfully duplicated the experimental results reported in the literature (Fig.4.3.6), thus confirming the capability of TROL to bind the prefibrillar species of the peptide in our experimental conditions.

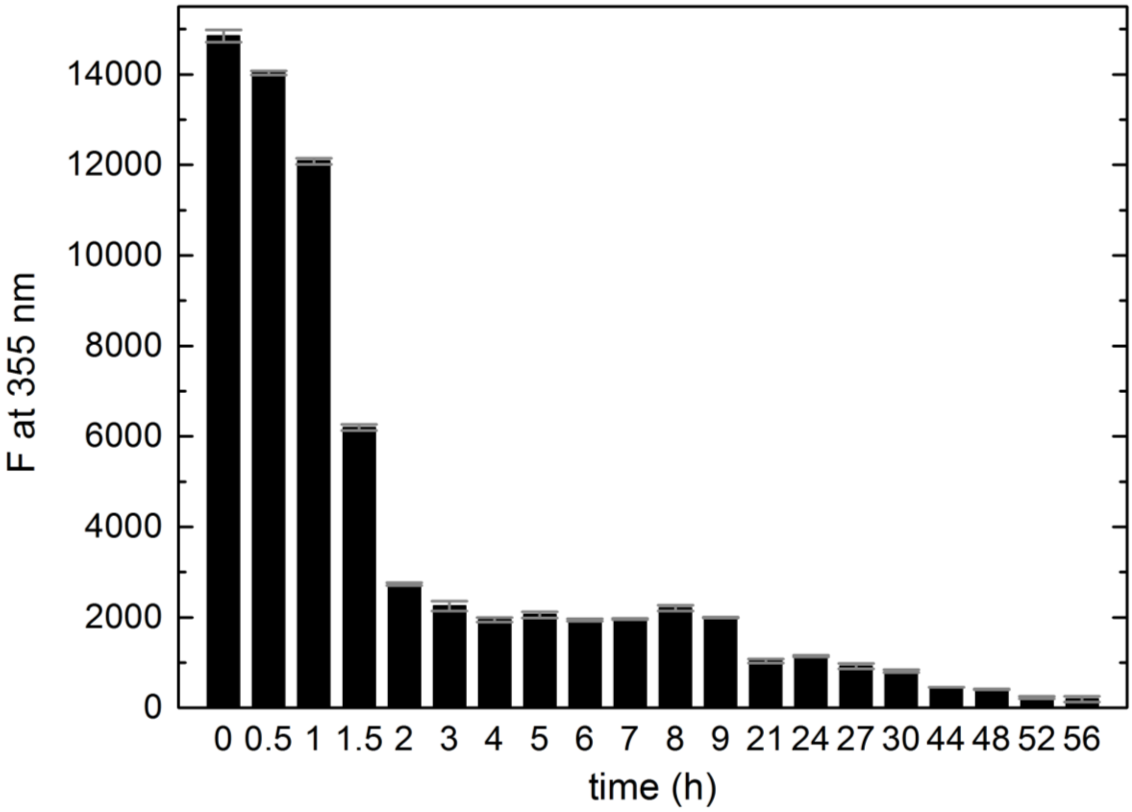

Fig.4.3.6. TROL binding assay. Fluorescence quenching (λ_{ex} = 280 nm, λ_{em} = 355 nm) given by the binding of TROL to the prefibrillar Aβ42 peptide during the Aβ42 aggregation at 37 °C. The initial concentration of the monomeric peptide was 28 μM in 10 mM Tris HCl. For each measurement, 100 μL of 10 μM TROL (in 50 μM Gly-NaOH, pH 8.2, 0.01% DMSO) were added to 10 μL peptide solution. Grey bars represent the standard deviation of each measurement.

Interestingly, TROL fluorescence quenching originating from the Aβ42 peptide binding occurs in a time frame (approximately from 0.5 to 2 hours) that is compatible with the formation of the prefibrillar aggregates(37), as shown in Fig.4.3.6. The Aβ42 peptide surface interaction process revealed by the BSW-based measurements (Fig.4.3.5) occurs in the same time frame. Hence, we can tentatively infer that the local increase of the refractive index revealed by BSW-based monitoring corresponds to the surface binding of the Aβ42 peptide in a prefibrillar conformation, both in the case of a bare and of a TROL-functionalized multilayer surface. This result is in accordance with the general model that we adopted to interpret the signal obtained with our sensing measurements.

TROL fluorescence signal in Fig.4.3.6 remains quenched after many incubation hours. The same behavior was reported in the literature(48). This is remarkable considering that the

Aβ42 peptide has plausibly reached a mature fibrillar state (after 48-hour incubation). The literature(48) claims that TROL fluorescence signal is quenched exclusively upon the binding with prefibrillar Aβ forms. Hence, TROL fluorescence should become more intense as soon as substantial quantities of fibrils are formed. However, as suggested by the literature(48), it is impossible to rule out the presence of prefibrillar Aβ in complex fibrillar mixtures of samples of advanced state of aggregation(49). Therefore, at long incubation time, these prefibrillar assemblies should be the responsible for the high TROL fluorescence quenching, as seen in Fig.4.3.6. With the same logic, the constant signal that we obtained real-time monitoring the aggregation of the Aβ42 peptide with a TROL-functionalized multilayer (Fig.4.3.4) may be the consequence of the persistence of such prefibrillar Aβ42 aggregates on the TROL modified surface. We speculate that, even at long incubation time, those prefibrillar species are bound to the TROL molecule that is chemically attached at the surface, thus generating a local and constant overestimation of the refractive index of the solution, as sensed by the BSW. TROL either irreversibly sequesters the early formed prefibrillar assemblies thus inhibiting the elongation of fibrils, or captures them from the solution as soon as they are formed, in a rapid dynamic on-off binding equilibrium. The experiment presented in the next section aimed at investigating these two alternatives.

4.3.3 BSW-based aggregation monitoring with free, unbound Tryptophanol

The result presented in Fig.4.3.4 are of complex and challenging interpretation. Especially, it is difficult to rationalize the incapability of the measurement using the TROL-functionalized multilayer to cover the further steps of the Aβ42 fibrillization, as minor or negligible refractive index variations are sensed by the BSW for long incubation time (see Fig.4.3.4). Assuming that prefibrillar Aβ42 species are bound to the surface via the interaction with TROL, one would expect to observe signals due to the elongation of fibrils onto the multilayer surface for long incubation time. As amyloid aggregation proceeds, a local increase of the refractive index, as sensed by the BSW, thus corresponding to an increase of the positive pixel shift, would be expected.

Two hypothesis can be suggested to explain the observation that the measured refractive index change was only minor, or almost absent for long incubation time (after approximately 2 hours, Fig.4.3.4): either TROL interferes with the amyloid aggregation by sequestering prefibrillar Aβ42 assemblies, or the TROL-driven surface-loading process creates a peptide overlayer, shielding the BSW and resulting in a lack of sensitivity. The first hypothesis is in disagreement with the literature(46, 48). To test the behavior of TROL, we performed a BSW-based refractive index monitoring incubating a solution containing both TROL and the Aβ42 peptide using a bare multilayer. Here, the assumption is that surface-bound TROL and free TROL exhibit similar behavior towards the Aβ42 peptide. The result of this study is presented in Fig.4.3.7. The comparison with a real-time monitoring of the pure Aβ42 peptide aggregation, under the same experimental conditions, is shown in Fig. 4.3.8.

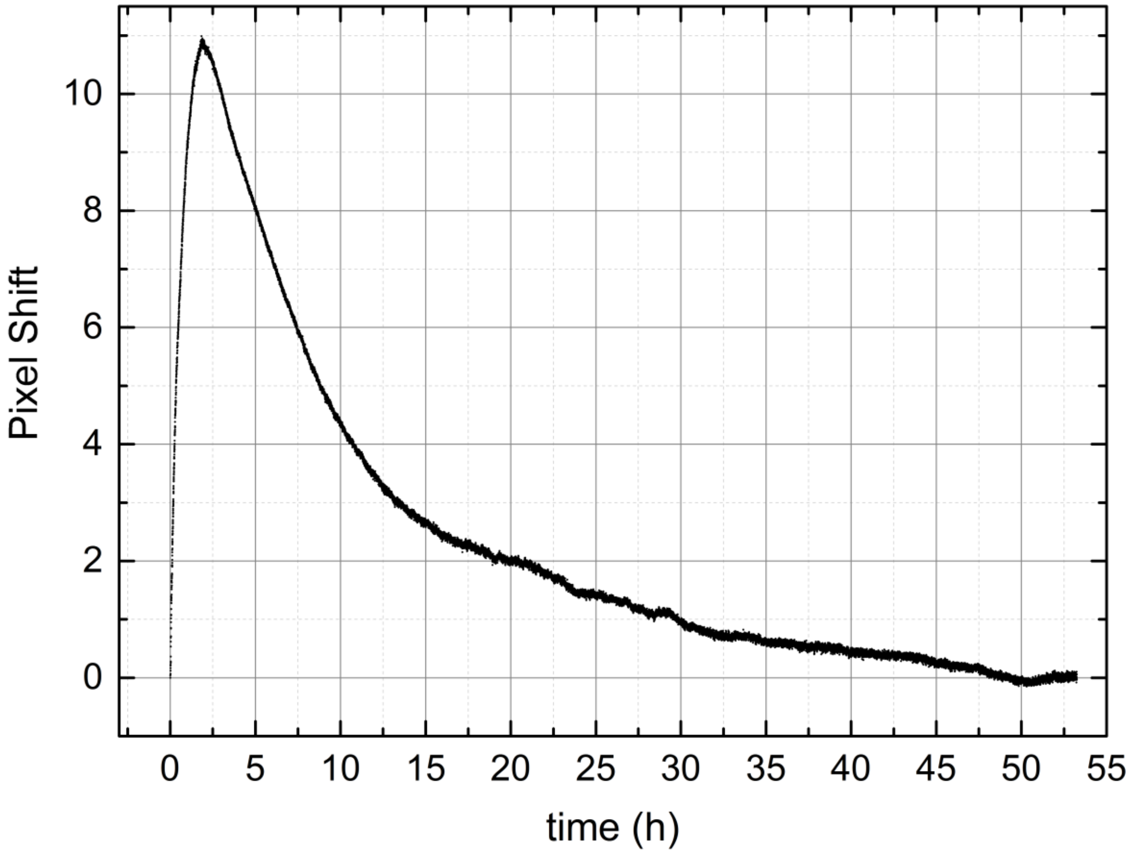

Fig.4.3.7. Real-time monitoring of the refractive index shift of incubating Aβ42 peptide with TROL. The Aβ42 sample (in 10 mM Tris HCl buffer, pH 7.4, initial Aβ42 monomer concentration 13.9 µM) was incubated at 37 °C with TROL in molar ratio of 1:10. The multilayer surface was unfunctionalized.

The real-time monitoring of the Aβ42 aggregation in the presence of TROL with a bare multilayer revealed a refractive index variation of the solution that was qualitatively similar to those of other measurements performed in the absence of TROL (see Chapter 3). As sensed by the BSW, the refractive index evolution of the solution throughout the peptide aggregation is characterized by an initial sharp increase, followed by a slower exponential-like decrease (see Fig.4.3.7).

To better evaluate the potential interference of TROL on Aβ42 aggregation, the monitoring of the Aβ42 peptide aggregation in the presence of TROL (Fig.4.3.7) was compared to the signal obtained in the absence of TROL, under identical experimental conditions. The overlap of the two real-time measurements is shown in Fig.4.3.8.

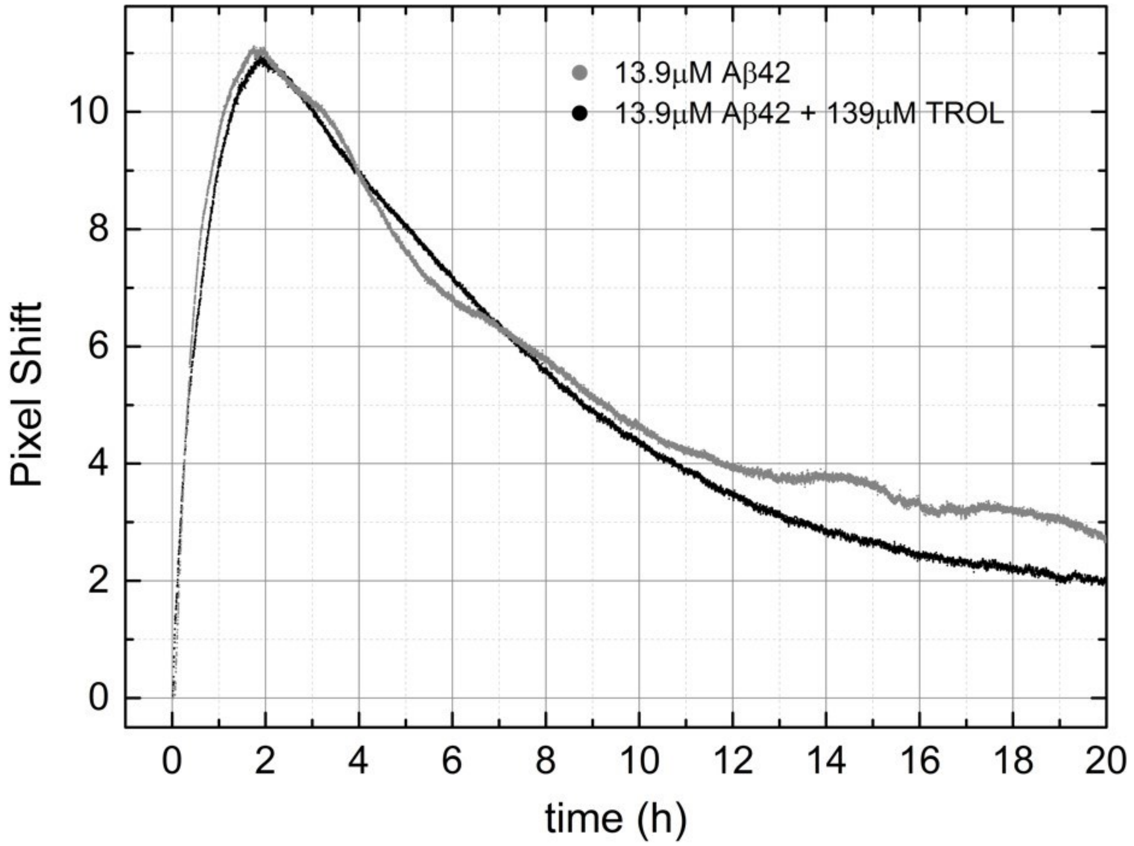

Fig.4.3.8. Comparison of real-time monitorings of the refractive index shift of incubating Aβ42 peptide. Comparison of the monitoring presented in Fig.3.2.1, in grey, and in Fig.4.3.7, in black, respectively. They correspond to the results obtained incubating two distinct Aβ42 samples (in 10 mM Tris HCl buffer, pH 7.4, identical initial monomer concentration: 13.9 μM) without and in the presence of TROL in a molar ratio of 1:10, respectively. Both measurements were carried out with a bare unfunctionalized multilayer surface.

The two curves presented in Fig.4.3.8 show that the overall refractive index variations throughout the measurements are similar. Therefore, our BSW-based sensing measurements detect approximately no influence of TROL on the Aβ42 aggregation process.

As the BSW-based measurements seem independent on the presence or the absence of significant amounts of TROL in the solution, we inferred that TROL does not interfere with the Aβ42 aggregation process, as reported in the literature(46, 48). Reasonably, TROL should not irreversibly sequester prefibrillar assembly nor inhibit the fibrillation process. Hence, we tentatively assume that the presence of surface-bound TROL does not affect the Aβ42 aggregation process neither.

Under these circumstances, we should resort to the second hypothesis: We therefore attributed the invariance of the signal after the initial sharp local refractive index increase (Fig.4.3.4) to a reduced sensitivity of the BSW occurring once the surface is covered by the TROL-Aβ42-aggregate complex. The specific peptide surface-loading effect, driven by the presence of TROL chemically attached to the sensing surface, has as a consequence a rapid and complete saturation of the surface. The multilayer surface is therefore shielded and the BSW becomes insensitive to further refractive index changes induced by the Aβ42 fibrillization process occurring in the bulk.

However, a decreased BSW sensitivity due to surface saturation does not fully justify the overall trend of the refractive index, as sensed by the BSW, in the measurements with a TROL-functionalized multilayer surface (Fig.4.3.4). Especially, we are not yet able to explain the observation that the amplitude of the local refractive index increase, corresponding to the peptide-surface interaction, is much smaller when compared to the same experiment with an unfunctionalized multilayer (see Fig.4.3.5).

4.4 Conclusions

In this chapter, a chemical modification strategy to treat a silicon oxi-nitride photonic-crystal surface was presented. As we aimed high, we developed a versatile step-by-step strategy that could be adopted for the binding of different ligands, from small molecular compounds to antibodies. This initial goal explains the implementation of a rather complex and demanding functionalization strategy, compared to the outcome results.

The development of a surface coating strategy, aimed at preventing non-specific protein interaction onto the surface was accomplished and its effectiveness verified incubating the highly adsorption-prone BSA protein. With a PEGylated multilayer, almost no non-specific interaction was observed. However, the Aβ42 peptide surface-interaction still occurred, contrary to what observed while incubating BSA with a PEGylated multilayer. The results obtained by monitoring the Aβ42 aggregation in the presence of such a passivated surface demonstrated that the interaction with the silicon oxi-nitride multilayer surface is not fundamentally modifying the mechanism of the aggregation. With a bare multilayer surface, for long incubation time, the mass-loading mechanism has definitely reached stationary conditions. As a result, an overlayer of Aβ42 peptide steadily adsorbed on the surface is formed. The presence of such an overlayer produces a shielding effect leading to a general overestimation of the solution refractive index. With PEG, almost no overlayer is formed on the surface and the BSW resonance position should be directly related to the refractive index of the solution. Moreover, the effective despite partial Aβ42 peptide desorption from the sensing surface is supported by the PEG-coating passivation experiment.

The monitoring of the Aβ42 peptide aggregation with a TROL functionalized multilayer surface did not cover the overall fibrillization process. The refractive index of the solution, as sensed by the BSW, was approximately constant after the initial increase due to the peptide surface-loading process. We propose that a steady shielding effect caused by the interaction of the peptide with the indolic ligand reduced the BSW sensitivity. However, the hypotheses we postulated to interpret the results of the monitorings of the Aβ42 peptide aggregation with TROL-functionalized surfaces were not sufficiently confirmed by experimental results. Nevertheless, the latter support the hypothesis that the Aβ42 species interacting with the sensor surface are in a prefibrillar aggregation stage, as suggested by the measurements presented in Chapter 3.

4.5 Bibliography

1. Hawe A, Sutter M, & Jiskoot W (2008) Extrinsic Fluorescent Dyes as Tools for Protein Characterization. *Pharmaceutical Research* 25(7):1487-1499.

2. Bram Y, Lampel A, Shaltiel-Karyo R, Ezer A, Scherzer-Attali R, Segal D, & Gazit E (2015) Monitoring and Targeting the Initial Dimerization Stage of Amyloid Self-Assembly. *Angewandte Chemie International Edition* 54(7):2062-2067.

3. Jungbauer LM, Yu C, Laxton KJ, & LaDu MJ (2009) Preparation of fluorescently-labeled amyloid-beta peptide assemblies: the effect of fluorophore conjugation on structure and function. *J Mol Recognit* 22(5):403-413.

4. Mawuenyega KG, Kasten T, Sigurdson W, & Bateman RJ (2013) Amyloid-beta isoform metabolism quantitation by stable isotope-labeled kinetics. *Analytical Biochemistry* 440(1):56-62.

5. Cooper MA (2006) Optical biosensors: where next and how soon? *Drug Discovery Today* 11(23-24):1061-1067.

6. White DA, Buell AK, Dobson CM, Welland ME, & Knowles TPJ (2009) Biosensor-based label-free assays of amyloid growth. *FEBS Letters* 583(16):2587-2592.

7. Fan X, White IM, Shopova SI, Zhu H, Suter JD, & Sun Y (2008) Sensitive optical biosensors for unlabeled targets: A review. *Analytica Chimica Acta* 620(1–2):8-26.

8. Cooper MA (2002) Optical biosensors in drug discovery. *Nat Rev Drug Discov* 1(7):515-528.

9. Turner APF (2013) Biosensors: sense and sensibility. *Chemical Society reviews* 42(8):3184-3196.

10. Ramakrishnan M, Kandimalla KK, Wengenack TM, Howell KG, & Poduslo JF (2009) Surface Plasmon Resonance Binding Kinetics of Alzheimer’s Disease Amyloid β Peptide-Capturing and Plaque-Binding Monoclonal Antibodies. *Biochemistry* 48(43):10405-10415.

11. Janssen L, Sobott F, De Deyn PP, & Van Dam D (2015) Signal loss due to oligomerization in ELISA analysis of amyloid-beta can be recovered by a novel sample pre-treatment method. *MethodsX* 2:112-123.

12. Schmidt SD, Nixon RA, & Mathews PM (2005) ELISA method for measurement of amyloid-beta levels. *Methods Mol Biol* 299:279-297.

13. Bañuls M-J, Puchades R, & Maquieira Á (2013) Chemical surface modifications for the development of silicon-based label-free integrated optical (IO) biosensors: A review. *Analytica Chimica Acta* 777:1-16.

14. John AA, Subramanian AP, Vellayappan MV, Balaji A, Jaganathan SK, Mohandas H, Paramalinggam T, Supriyanto E, & Yusof M (2015) Review: physico-chemical modification as a versatile strategy for the biocompatibility enhancement of biomaterials. *RSC Advances* 5(49):39232-39244.

15. Flink S, van Veggel FCJM, & Reinhoudt DN (2001) Functionalization of self-assembled monolayers on glass and oxidized silicon wafers by surface reactions. *Journal of Physical Organic Chemistry* 14(7):407-415.

16. Yamaura M, Camilo RL, Sampaio LC, Macêdo MA, Nakamura M, & Toma HE (2004) Preparation and characterization of (3-aminopropyl)triethoxysilane-coated magnetite nanoparticles. *Journal of Magnetism and Magnetic Materials* 279(2–3):210-217.

17. Zeng X, Xu G, Gao Y, & An Y (2011) Surface Wettability of (3-Aminopropyl)triethoxysilane Self-Assembled Monolayers. *The Journal of Physical Chemistry B* 115(3):450-454.

18. Konopsky VN & Alieva EV (2007) Photonic Crystal Surface Waves for Optical Biosensors. *Analytical Chemistry* 79(12):4729-4735.

19. Howarter JA & Youngblood JP (2006) Optimization of Silica Silanization by 3-Aminopropyltriethoxysilane. *Langmuir* 22(26):11142-11147.

20. Wildling L, Unterauer B, Zhu R, Rupprecht A, Haselgrübler T, Rankl C, Ebner A, Vater D, Pollheimer P, Pohl EE, Hinterdorfer P, & Gruber HJ (2011) Linking of Sensor Molecules with Amino Groups to Amino-Functionalized AFM Tips. *Bioconjugate Chemistry* 22(6):1239-1248.

21. Wong I & Ho C-M (2009) Surface molecular property modifications for poly(dimethylsiloxane) (PDMS) based microfluidic devices. *Microfluidics and Nanofluidics* 7(3):291-306.

22. Yang Z, Galloway JA, & Yu H (1999) Protein Interactions with Poly(ethylene glycol) Self-Assembled Monolayers on Glass Substrates: Diffusion and Adsorption. *Langmuir* 15(24):8405-8411.

23. Bell DJ, Brody JP, & Yager P (1998) Using poly(ethylene glycol) silane to prevent protein adsorption in microfabricated silicon channels. ed Gourley PL (SPIE), pp 134-140.

24. Prime KL & Whitesides GM (1993) Adsorption of proteins onto surfaces containing end-attached oligo(ethylene oxide): a model system using self-assembled monolayers. *Journal of the American Chemical Society* 115(23):10714-10721.

25. Prime KL & Whitesides GM (1991) Self-assembled organic monolayers: model systems for studying adsorption of proteins at surfaces. *Science* 252(5009):1164-1167.

26. Francis GL (2010) Albumin and mammalian cell culture: implications for biotechnology applications. *Cytotechnology* 62(1):1-16.

27. Lehninger AL, Nelson DL, & Cox MM (1999) *Principles of biochemistry* (Worth Publishers).

28. Bradford MM (1976) A rapid and sensitive method for the quantitation of microgram quantities of protein utilizing the principle of protein-dye binding. *Analytical Biochemistry* 72(1):248-254.

29. An YH, Bradley J, Powers DL, & Friedman RJ (1997) The prevention of prosthetic infection using a cross-linked albumin coating in a rabbit model. *The Journal of bone and joint surgery. British volume* 79(5):816-819.

30. Holm NK, Jespersen SK, Thomassen LV, Wolff TY, Sehgal P, Thomsen LA, Christiansen G, Andersen CB, Knudsen AD, & Otzen DE (2007) Aggregation and fibrillation of bovine serum albumin. *Biochimica et Biophysica Acta (BBA) - Proteins and Proteomics* 1774(9):1128-1138.

31. Vetri V, D'Amico M, Foderà V, Leone M, Ponzoni A, Sberveglieri G, & Militello V (2011) Bovine Serum Albumin protofibril-like aggregates formation: Solo but not simple mechanism. *Archives of Biochemistry and Biophysics* 508(1):13-24.

32. Bhattacharya M, Jain N, & Mukhopadhyay S (2011) Insights into the Mechanism of Aggregation and Fibril Formation from Bovine Serum Albumin. *The Journal of Physical Chemistry B* 115(14):4195-4205.

33. Bashkatov AN & Genina EA (2003) Water refractive index in dependence on temperature and wavelength: a simple approximation. pp 393-395.

34. Michelotti F & Descrovi E (2011) Temperature stability of Bloch surface wave biosensors. *Applied Physics Letters* 99(23):231107.

35. Militello V, Vetri V, & Leone M (2003) Conformational changes involved in thermal aggregation processes of bovine serum albumin. *Biophysical chemistry* 105(1):133-141.

36. Harper JD & Lansbury PT (1997) Models Of Amyloid Seeding In Alzheimer's Disease And Scrapie: Mechanistic Truths and Physiological Consequences of the Time-Dependent Solubility of Amyloid Proteins. *Annual Review of Biochemistry* 66(1):385-407.

37. Jan A, Hartley DM, & Lashuel HA (2010) Preparation and characterization of toxic A beta aggregates for structural and functional studies in Alzheimer's disease research. *Nat Protoc* 5(6):1186-1209.

38. Hortschansky P, Schroeckh V, Christopeit T, Zandomeneghi G, & Fändrich M (2005) The aggregation kinetics of Alzheimer's β-amyloid peptide is controlled by stochastic nucleation. *Protein Science* 14(7):1753-1759.

39. Nilsson MR (2004) Techniques to study amyloid fibril formation in vitro. *Methods* 34(1):151-160.

40. Vassar PS & Culling CF (1959) Fluorescent stains, with special reference to amyloid and connective tissues. *Arch Pathol* 68:487-498.

41. Puchtler H, Sweat F, & Levine M (1962) On The Binding of Congo Red by Amyloid. *Journal of Histochemistry & Cytochemistry* 10(3):355-364.

42. Levine H (1993) Thioflavine T interaction with synthetic Alzheimer's disease β-amyloid peptides: Detection of amyloid aggregation in solution. *Protein Science* 2(3):404-410.

43. Krebs MRH, Bromley EHC, & Donald AM (2005) The binding of thioflavin-T to amyloid fibrils: localisation and implications. *Journal of Structural Biology* 149(1):30-37.

44. Nilsson KPR, Åslund A, Berg I, Nyström S, Konradsson P, Herland A, Inganäs O, Stabo-Eeg F, Lindgren M, Westermark GT, Lannfelt L, Nilsson LNG, & Hammarström P (2007) Imaging Distinct Conformational States of Amyloid-β Fibrils in Alzheimer's Disease Using Novel Luminescent Probes. *ACS Chemical Biology* 2(8):553-560.

45. Åslund A, Sigurdson CJ, Klingstedt Ts, Grathwohl S, Bolmont T, Dickstein DL, Glimsdal E, Prokop S, Lindgren M, Konradsson P, Holtzman DM, Hof PR, Heppner FL, Gandy S, Jucker M, Aguzzi A, Hammarström P, & Nilsson KPR (2009) Novel Pentameric Thiophene Derivatives for in Vitro and in Vivo Optical Imaging of a Plethora of Protein Aggregates in Cerebral Amyloidoses. *ACS Chemical Biology* 4(8):673-684.

46. Reinke AA, Seh HY, & Gestwicki JE (2009) A chemical screening approach reveals that indole fluorescence is quenched by pre-fibrillar but not fibrillar amyloid-β. *Bioorganic & Medicinal Chemistry Letters* 19(17):4952-4957.

47. Reinke AA & Gestwicki JE (2011) Insight into Amyloid Structure Using Chemical Probes. *Chemical Biology & Drug Design* 77(6):399-411.

48. Reinke AA, Abulwerdi GA, & Gestwicki JE (2010) Quantifying Prefibrillar Amyloids in vitro by Using a “Thioflavin-Like” Spectroscopic Method. *ChemBioChem* 11(13):1889-1895.

49. Jan A, Adolfsson O, Allaman I, Buccarello A-L, Magistretti PJ, Pfeifer A, Muhs A, & Lashuel HA (2010) Aβ42 neurotoxicity is mediated by ongoing nucleated polymerization process rather than by discrete Aβ42 species. *Journal of Biological Chemistry*.

5. THE BSW-BASED PLATFORM AS A TOOL TO INVESTIGATE MOLECULAR PROBES INTERFERING WITH Aβ AGGREGATION

5.1 State of the art of the research on small-molecule inhibitors of toxic Aβ42 fibril formation

AD is currently a major plague of the developed countries and the research on drugs able to stop or slow down the brutal progression of the disease has become more and more significant(1). Currently available therapy simply addresses the enhancement of cholinergic functions, but this clinical effect is not sufficient, since it is treating the symptoms but not the cause of the disease(2, 3). For this reason, many research laboratories aim at developing new potential inhibitors of the Aβ42 fibrillization, not only by testing candidate molecules(4), but also devising new methods for their discovery and *in vitro* validation(5). Moreover, the discovery and development of new compounds interacting with different aggregate species, thus acting as probe molecules, is fundamental for the ultimate understanding of the amyloid aggregation mechanism(6).

Recently, a big effort has been made to qualify compounds, mainly natural products, as potent anti-amyloid-fibrillization agents. The majority of these molecules contain phenolic moieties, and, although they all have very different chemical structures, they share common features presumably required for activity: a second terminal aromatic moiety and a short linker unit connecting the aromatic moieties. The optimal linker has been reported to contain two rotating bonds and to have a length between 8 and 16 Å(7). Among others, apomorphine(8), resveratrol(9), curcumin(10), tolcapone(11), (-)-epigallocatechine gallate (EGCG)(12), bi- and mono-flavonoids(13), tannic acid(14), nordihydroguaiaretic acid(15), RS-0466(16) and RS-0406(17), are well-known examples of polyphenols that have been extensively investigated for their potential to prevent the formation of toxic Aβ42 species(10) (see Tab.5.1.1).

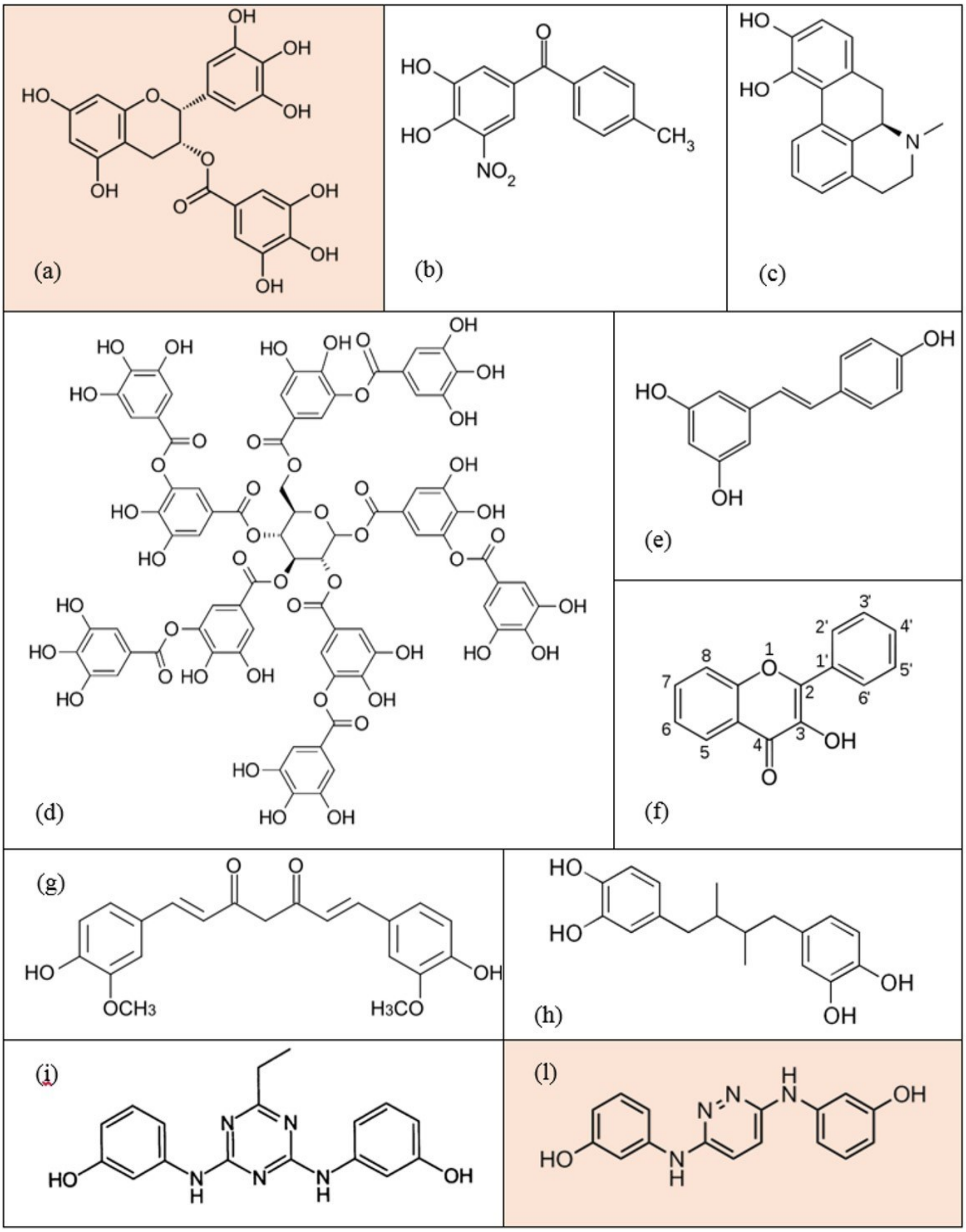

Tab.5.1.1. Selected examples of polyphenolic inhibitors of Aβ aggregation. (a) EGCG; (b) tolcapone; (c) apomorphine; (d) tannic acid; (e) resveratrol; (f) backbone of flavonol, substituents are indicated with numbers, and are mostly -OH or -OCH_3, thus defining a precise flavonol; (g) curcumin, here presented in the keto form, which is the thermodynamically stable tautomer in water. The tautomeric enol form exists too, being thermodynamically preferred in the solid phase; (h) nordihydroguaiaretic acid; (i) RS-0466; (l) RS-0406. In a colored background, the two compounds that have entered clinical trials Phase II: EGCG and RS-0406(18).

Despite the great effort put on the study of these molecules, their presumed efficacy is yet to be fully demonstrated and little is known about their mode of action in the central nervous system. Notably, only few of them have entered clinical trials, with the exception of EGCG and RS-0406, which have entered clinical Phase II of trials(18). The compound RS-0406 has raised great interest since it was reported to inhibit the Aβ42 fibrillogenesis in the ThT binding assay. In their work of 2002, Nakagami *et al*(17) claimed that the compound was also capable of disassembling preformed fibrils. For this reason, RS-0406 is known as a "β-sheet breaker"(18). Further studies have confirmed the efficacy of RS-0406 towards Aβ fibrillation inhibition, suggesting the hydrophobic central region of the Aβ42 peptide as the target for its action. RS-0406 *in vivo* test reported improvements in behavioral deficits seen in the early stages of AD(19). The implications of the investigation of RS-0406 opened new scenarios for the understanding of the mechanism of fibrillogenesis. However, the ThT binding assay performed to test the capability of RS-0406 to inhibit Aβ42 fibrillogenesis is not sufficient to elucidate the mode of action of the drug. The lack of sensitivity of the ThT binding assay during the crucial step of Aβ42 oligomerization(20) precludes a full description of the mechanism of fibrillogenesis inhibition performed by RS-0406.

Therefore, we tested the application of the BSW-based sensing platform to the monitoring of the aggregation dynamics of the Aβ42 peptide in the presence of RS-0406. The goal is to validate the BSW-based sensing strategy as a powerful and direct screening tool for new potential inhibitors of toxic Aβ42 oligomer formation and of early nucleation events. In parallel, NMR studies were carried out in collaboration with Dr. Dalvit from the University of Neuchatel, with the goal of obtaining complementary and independent information on the inhibition mechanism of RS-0406. Dr. Dalvit previously reported on an innovative NMR-based approach for the identification of compounds with binding affinities to proteins, called "WaterLOGSY"(21). Dr. Dalvit applied this method to the study of the interaction between RS-0406 and the Aβ42 peptide during aggregation.

5.2 Test of molecular probes that interfere with the Aβ peptide aggregation dynamics

The BSW-based approach can be applied to provide new insights into the complex mechanism of aggregation in the presence of small molecular probes able to interfere with the dynamics of amyloid formation. For this aim, we selected the two molecules shown in Fig.5.2.1: R548332 as a suitable reference molecule, and RS-0406, a compound reported as an inhibitor of the oligomer formation, and as a molecule capable of breaking-up pre-formed fibrils(17), as mentioned in the previous section.

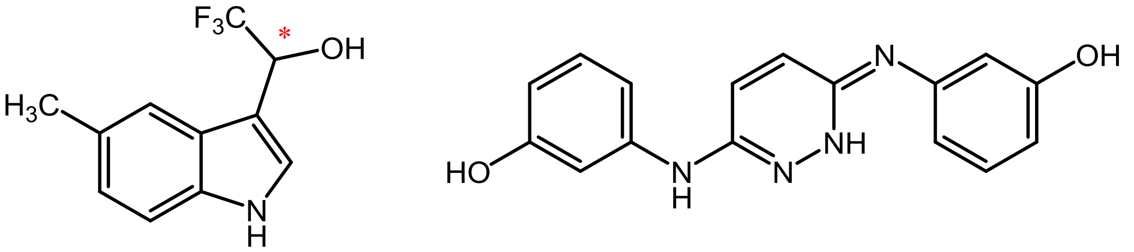

(1) (2)

Fig.5.2.1. Structure of the molecules R548332 (1) and RS-0406 (2). The red asterisk on (1) indicates the position bearing the functionality CF_3-C-OH, crucial for non-specific interaction with the peptide(4).

R548332 was chosen based on a recent publication on screening of potential inhibitors of amyloid aggregation(4). In this work, an impressive series of compounds, mostly indole derivatives, were systematically tested by the authors for their capacity of inhibiting Aβ42 oligomerization and Aβ40 fibrillogenesis, respectively, via ThT binding assay, AFM experiments, and quantitative biotinyl-Aβ42 single-site streptavidin-based assay. In this context, we selected R548332 as a commercially available surrogate for a compound reported in this work, which was bearing an extra -CF_3 substituent in the position marked with * in Fig.5.2.1. In the context of NMR-based ligand-peptide interaction experiments, the compound R548332 was found appropriate for its small size and the presence of a -CH_3 and -CF_3 groups, suitable for WaterLOGSY and ^{19}F T2 filter experiments, respectively(22) (see section 5.2.2).

Finally, concerning RS-0406 our interpretation for the reported interaction with the Aβ peptides is based on the analysis of the structure of the compound. The groups -N=CR-NH- could be seen as analogous and isosteric to amide bonds, thus intervening via H-bond replacements in the β-sheet architecture. Moreover, the phenol groups are a key feature for solubility, since they can be partially deprotonated in water.

5.2.1 BSW-based aggregation monitoring

Results on the variation of the amyloid aggregation dynamics in the presence of R548332 and RS-0406 were obtained separately and are presented in Fig.5.2.2, and Fig.5.2.3. We incubated initially monomeric Aβ42 samples at 37 °C in the fluidic chamber of the sensor with the selected molecules, in a molar concentration ratio of 1:10. For all the measurements presented in this Chapter, a bare unfunctionalized multilayer surface was used. In these conditions, the monitoring of the refractive index change throughout the Aβ42 aggregation process revealed a variation in the dynamics of the aggregation process. This variation was both concerning the timing and the rate of the fibrillization, compared to the monitoring of the aggregation of the pure Aβ42 peptide. Comparisons of the results obtained monitoring the Aβ42 peptide alone with those obtained in the presence of R548332 and RS-0406 are presented in Fig.5.2.4 and Fig.5.2.5, as revealed by the BSW-based sensing approach.

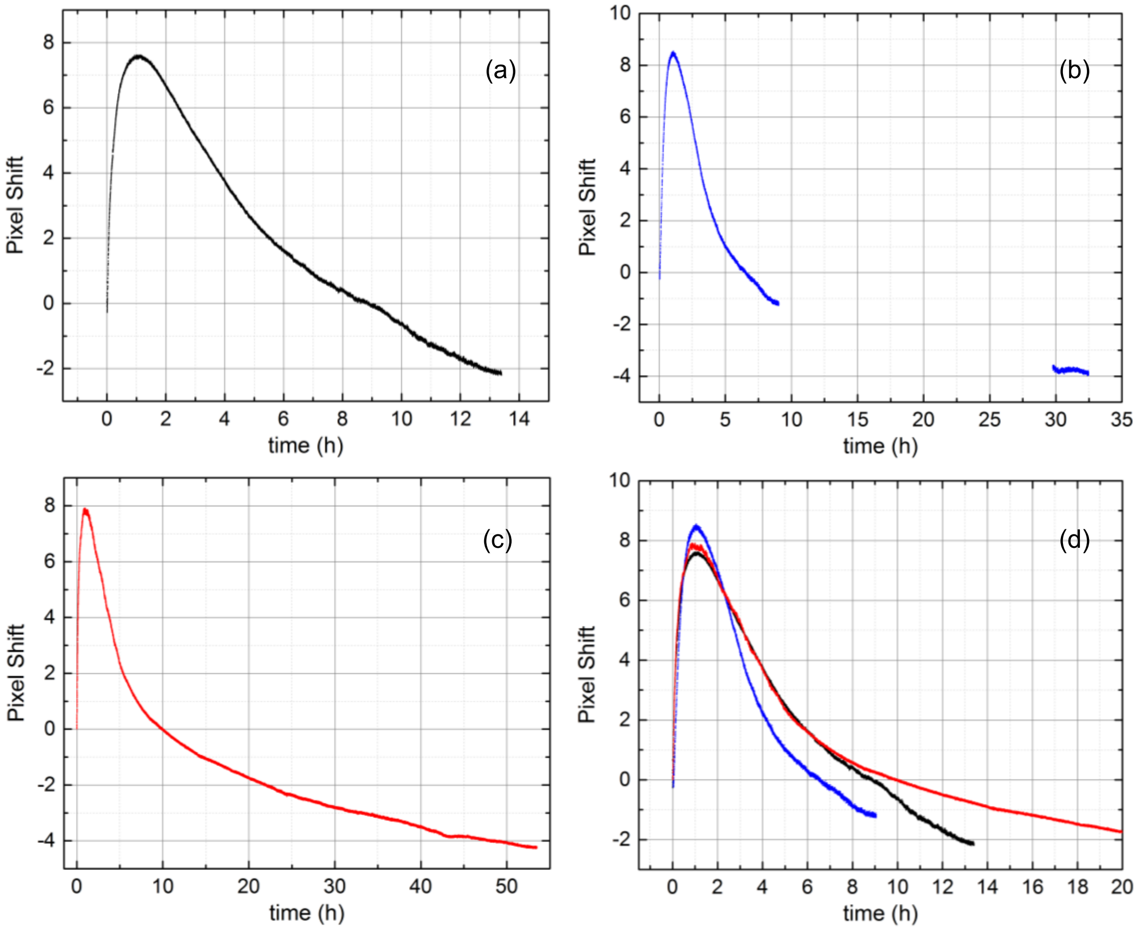

Fig.5.2.2. Real-time monitoring of the refractive index shift of incubating Aβ42 peptide with R548332. Three Aβ42 samples (in 10 mM Tris HCl buffer, pH 7.4, initial Aβ42 monomer concentrations: (a) 13 µM; (b) 13.9 µM; (c) 13 µM,) were incubated at 37 °C with R548332 in molar ratio of 1:10. The overlap of the three distinct measurements is presented in a close-up view in graph (d), where colors are consistent with those used for the single measurements. The central gap in (b) is due to an unexpected interruption of data recording, which, nevertheless, did not affect the experiment.

As shown in Fig.5.2.2, the monitoring of Aβ42 aggregation in the presence of R548332 was performed with initial peptide concentration of 13.9 and 13 µM. Results are reproducible, and the overall refractive index variations throughout the measurements are consistent, as highlighted by the overlap presented in Fig.5.2.2 (d). Furthermore, a higher initial monomer concentration led to a larger initial local refractive index increase, and, in general, accelerated the refractive index decrease rate, as observed in the results presented in Chapter 3. This effect is in accordance with what reported in the literature(23-25), where the positive correlation between Aβ peptide concentration and amyloid aggregation rate, in this work represented by refractive index variations (Chapter 3), has been demonstrated.

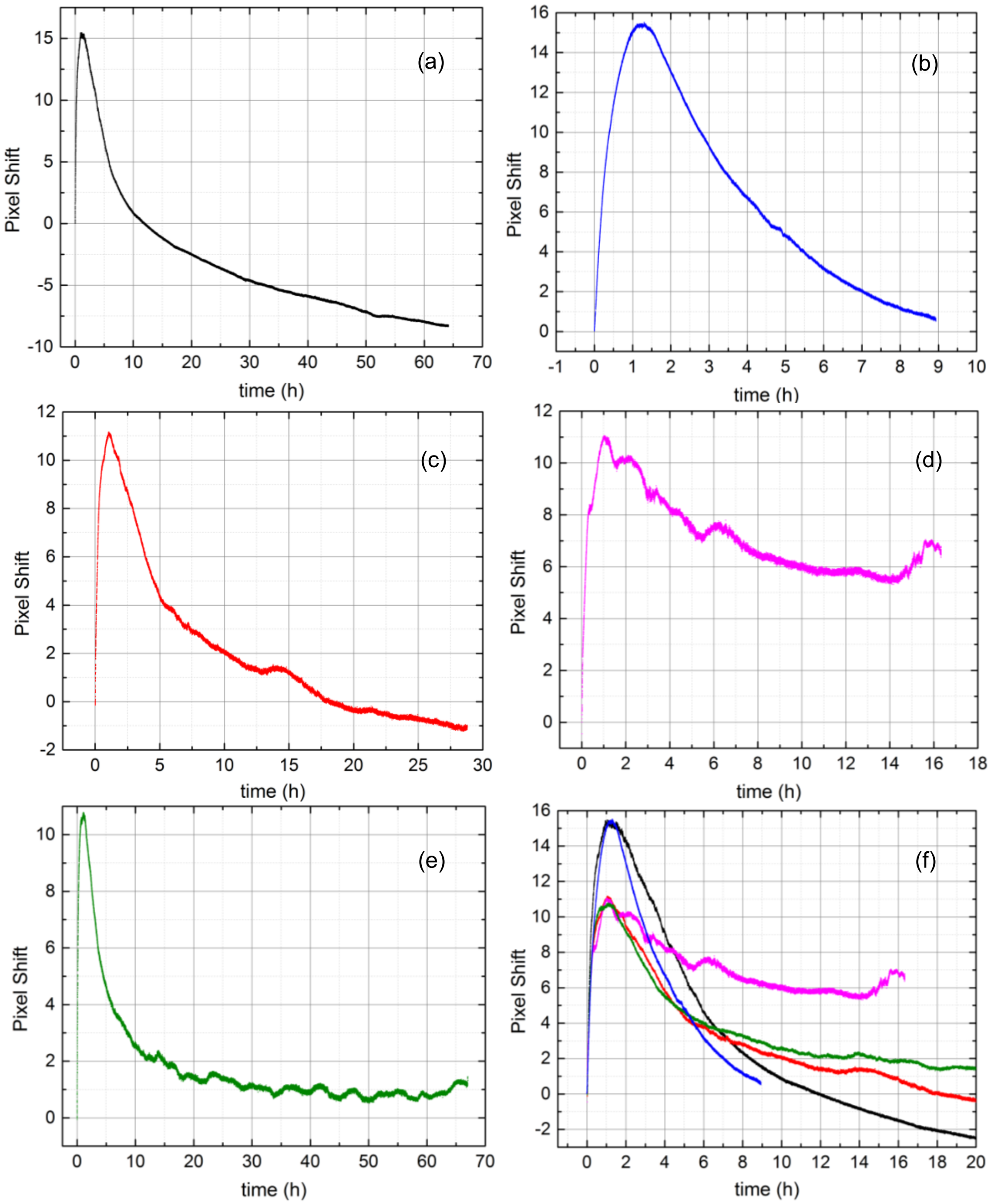

Fig.5.2.3. Real-time monitoring of the refractive index shift of incubating Aβ42 peptide with RS-0406. Five Aβ42 samples (in 10 mM Tris HCl buffer, pH 7.4, initial Aβ42 monomer concentrations: (a) 17 µM; (b) 17 µM; (c) 13.9 µM; (d) 13 µM; (e) 13 µM) were incubated at 37 °C with RS-0406 in molar ratio of 1:10. The overlap of the five distinct measurements is presented in a close-up view in graph (f), where colors are consistent with those used for the single measurements.

The real-time monitoring of the refractive index variation of the Aβ42 peptide aggregating in the presence of RS-0406, as presented in Fig.5.2.3, was carried out with initial peptide concentrations of 17, 13.9 and 13 µM. As for the results presented in Fig.5.2.2, the experiments are reproducible and consistent (Fig.5.2.3 (f)). However, the curve presented in

Fig.5.2.3 (d) deviates from the general evolution characterizing the other refractive index measurements (Fig.5.2.3 (f)). The same applies to the last approximately 55 hours of the experimental signal reported in Fig.5.2.3 (e). Those two specific inconsistencies can be ascribed to background noise caused by the formation of bubbles (air or water vapor) in the sensing chamber, which create discontinuity in the refractive index, as sensed by the BSW. Despite this interference, the essential feature of the monitoring (an initial increase followed by a decrease of the refractive index, as sensed by the BSW) is not affected. Moreover, as reported for the measurements presented in Chapters 3 and 4, we observed a positive correlation between the initial Aβ42 peptide concentration and the rate of the aggregation, as sensed by the BSW and represented by the refractive index variation of the aggregating solution throughout the measurement.

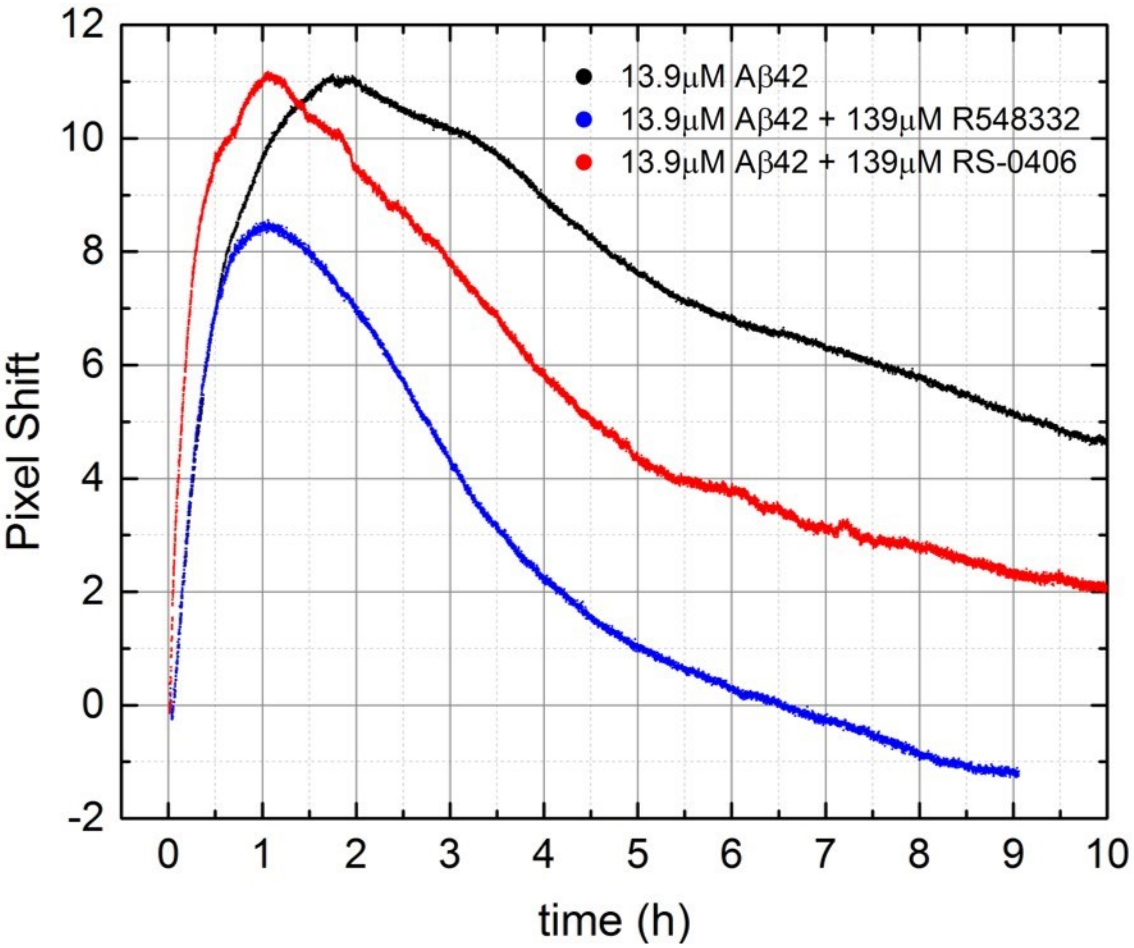

Fig.5.2.4. Selection of real-time monitorings of the refractive index shift of incubating Aβ42 peptide. Close-up view of the first 10 hours of monitoring presented in Fig.3.2.1, in black, Fig.5.2.2 (b), in blue, and in Fig.5.2.3 (c), in red, respectively. They correspond to the results obtained incubating three distinct Aβ42 samples (in 10mM Tris HCl buffer, pH 7.4, identical initial Aβ42 monomer concentration 13.9 μM) without and in the presence of R548332 or RS-0406, respectively.

To analyze the effect of the molecular probes on Aβ42 aggregation, one may especially consider the comparison shown in Fig.5.2.4, where selected real-time monitorings of the Aβ42 peptide aggregation without and with RS-0406 and R548332 are presented. As formerly explained in Chapter 3, one might take into account that the model we propose to interpret the BSW-based measurements is a simplified approach(26). In our measurements, the real-time refractive index variation of the aggregating Aβ solution is the result of different contributions, which are of challenging interpretation. For a preliminary analysis, two aspects of the monitorings have to be considered: i) the point in time of the establishment of a maximum refractive index value, and ii) the rate of the subsequent refractive index decrease. In our interpretation (see Chapter 3), i) is related to an equilibrium condition of the refractive index variation that is due to the saturation of the surface and a decreased availability of free "adhesion-competent" Aβ42 peptides because of a simultaneous fibrillization occurring in the solution, and ii) is associated to the detachment of the Aβ42 peptide from the surface, and/or the formation of fibrillar structures away from the surface, thereby depleting the bulk solution by decreasing the monomer concentration(26). Thus, both i) and ii) are depending on the Aβ42 peptide aggregation rate. For a further analysis of the results, another feature of the measurements that has to be considered is the ascending rate of the refractive index variation before point i). This part of the curve can be regarded as related to the first steps of Aβ42 oligomerization, as fibrillization occurs in a subsequent time frame(24). Throughout the analysis of the results presented in this section, one should consider the distinctive difference between oligomerization, as the early aggregation events leading to pre-fibrillar and toxic soluble aggregates, and fibrillization, as the process of mature and insoluble fibril formation (see Chapter 1). We tentatively attempted to identify these discrete aggregation phases with a temporal portion of our measurements, according to the literature(24).

Both the curves of the refractive index variation of the aggregating Aβ42 peptide in the presence of R548332 (in blue) and RS-0406 (in red) show some noticeable differences if compared with the reference, i.e. the curve corresponding to the monitoring of the pure Aβ42 peptide (in black). As the conditions for the selected experiments were equal (same starting monomer concentration, same buffer and temperature), one can deduce that the reproducible and pronounced differences between the three presented measurements should be due to the interference of the molecular probes with the Aβ42 peptide aggregation.

Specifically, R548332 (in blue) seemingly accelerates the Aβ aggregation. The maximum refractive index value is reached in a shorter time (t ~ 1 hour), and the subsequent decrease of the refractive index, as sensed by the BSW, is faster, reaching negative values in a relatively short period of time (t ~ 6.5 hour). The maximum amplitude of the curve is lower.

We tentatively attributed this observation to a smaller interaction of the peptide with the surface. This is consistent with a faster fibril formation, as mentioned above, which depletes the bulk solution of adhesion-competent Aβ42 peptides. However, R548332 apparently does not interfere with the Aβ42 oligomerization first steps, since the ascending rate of the refractive index change is indistinguishable in the presence or in the absence of the molecular probe.

With the same approach, one can compare the curves of the monitoring of the refractive index of the solution where the Aβ42 peptide aggregates without (in black) and in the presence of the molecular probe RS-0406 (in red). One observes that the initial aggregation rate appears accelerated by the presence of RS-0406, since the maximum refractive index value is reached in a shorter time (t ~ 1 hour). Moreover, the rate of the local refractive index increase, as sensed by the BSW, is higher in the presence of the molecular probe (see Fig.5.2.3 (c)). Interestingly, the maximum amplitude of the refractive index measurement appears for all intents and purposes equal for the measurement without and with RS-0406. Hence, almost the same amount of adhesion-competent Aβ42 peptide is formed in the absence of the molecular probe. We tentatively conclude that RS-0406 does accelerate the Aβ42 early oligomerization, but not the subsequent fibril formation process, producing the adhesion competent peptide with a distinctively faster rate, and thus contrasting the refractive index decrease due to the bulk fibrillization. This speculation is corroborated by the analysis of the second part of the refractive index monitoring, shown in Fig.5.2.5, between 10 and 20 hours of incubation of the Aβ42 peptide alone (in black), and with RS-0406 (in red).

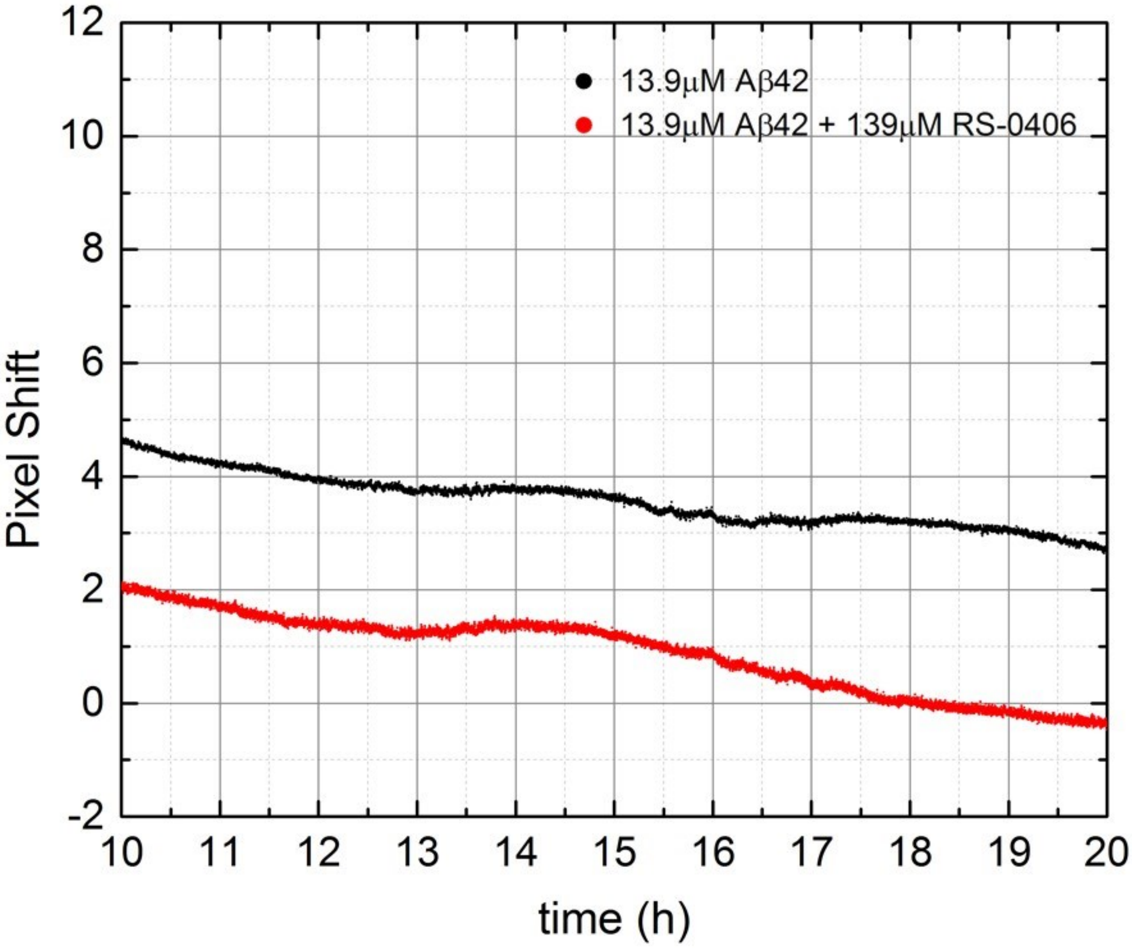

Fig.5.2.5. Selection of real-time monitorings of the refractive index shift of incubating Aβ42 peptide. Close-up view comparison of the monitoring of the Aβ42 peptide alone, presented in Fig.3.2.1, in black, and with RS-0406, presented in Fig.5.2.3 (c), in red, respectively.

In this time frame, the refractive index descending rates of the aggregating Aβ42 peptide solutions without (in black) and with RS-0406 (in red) appear indistinguishable. In the presence of the molecular probe, negative refractive index values are reached at t ~ 17 hours, whereas the monitoring of the refractive index variation of the aggregating Aβ42 peptide alone is never showing negative amplitudes (see discussion in Chapter 4). Our rationale for the observation that the monitoring of pure aggregating Aβ42 never shows negative values is an overloading of the surface, causing a general overestimation of the refractive index of the bulk solution where the fibrillization occurs, as sensed by the BSW(26). This shielding effect becoming constant, the monitoring of the variation of the refractive index of the bulk results unaffected by the surface-loading process, thus allowing the estimation of the time rate of the refractive index variation due to the Aβ42 fibrillization only. Therefore, we can infer that the similar refractive index descending rate of the two measurements (Fig.5.2.5) equals to a similar fibrillization rate. Summarizing our conclusions, we speculate that RS-0406 interferes with the first phase of the amyloid aggregation, accelerating the oligomerization, but not the further fibrillization process. All these interpretations are supported by the NMR-based experiments, for which a short description is reported in the following.

5.2.2 NMR-based WaterLOGSY aggregation monitoring

With the aim of verifying the results obtained applying the BSW-based platform to the monitor the Aβ42 peptide aggregation, the selected molecules, R548332 and RS-0406, were used to carry out parallel NMR studies, in collaboration with Dr. C. Dalvit from the University of Neuchâtel. In previous works(21, 27, 28), Dr. Dalvit reported on an innovative NMR-based approach called "WaterLOGSY" (Water-Ligand Observation with Gradient SpectroscopY) for the identification of compounds with binding affinity to proteins. The method relies on the exploitation of the large reservoir of bulk water magnetization. Hence, via transferring bulk water magnetization to the ligand in several relay pathways it is possible to detect small molecules that interact with a target biomolecule. The NMR WaterLOGSY experiments are recorded as a function of time for studying the kinetics of the Aβ42 peptide aggregation process. Water molecules are trapped into the peptide aggregates and are likely to be involved in the formation of intermolecular hydrogen bonds. Selective excitation of the bulk water signal followed by a mixing period in the WaterLOGSY experiment results in efficient magnetization transfer to the protons of the aggregates via the bound, yet exchangeable, water molecules and via chemical exchange with the numerous -OH and -NH groups of the aggregate species. Non-specific interactions between a selected reporter molecule and the aggregates result in partial transfer of the water magnetization stored by the peptide aggregates to the reporter molecule. This transfer of magnetization is then detected at the chemical shift of the free reporter molecule(27). The main advantage of this technique is the capability of ruling out artifacts and false positives and negatives in binding experiments(28). The method, like all the techniques based on ligand resonance observation, has the disadvantage of not offering information about the ligand binding site. Despite this drawback, the technique represents a powerful and highly reliable means for fast ligand identification, providing binding information freed of false-positives.

NMR studies were performed by Dr. Dalvit using the WaterLOGSY method. The spectra were recorded as a function of time for Aβ42 peptide samples at a concentration of 15 μM in 10 mM Tris HCl, and at 37 °C. These experimental conditions are closely the same as for the BSW-based sensing. R548332 was used as a reporter molecule for its size and the presence of a CF_3 group, which is suitable for complementary ^{19}F transverse relaxation filter experiments, which "*can be used to characterize equilibrium binding of low-affinity ligands* *to proteins without the confounding contributions of chemical shift*"(29). In addition, ^{1}H selective T_1 filter experiments were carried out, as another meaningful tool to detect and study protein binding mechanisms(30). Then, kinetics obtained by monitoring the Aβ42 aggregation in the presence of R548332 were compared with results from the concomitant use of both R548332 and RS-0406 with the peptide. From this comparison, results suggest that the first phase of Aβ42 aggregation is seemingly accelerated by the presence of RS-0406. Dr. Dalvit speculates that the binding of RS-0406 molecule to the Aβ42 monomer, accelerating the self-assembly process of the peptide, would remove the intermediate oligomers via rapidly shifting the self-assembly reaction equilibrium towards the formation of higher order aggregates(31). This explanation would justify RS-0406 toxicity suppression towards Aβ42 aggregation reported in the literature, as discussed in the beginning of the chapter. These unpublished results are highly supportive of the model we used to describe the signal obtained–in the same experimental conditions–by applying the BSW-based sensing platform to the monitoring of Aβ42 aggregation.

5.3 Conclusions

In this chapter, we presented the results obtained applying the BSW-based sensing platform to the investigation of molecular probes interfering with amyloid aggregation. Our sensing approach allows the reliable *in vitro* testing for potential inhibitors of the amyloid fibrillization in real-time, and without the use of detrimental labelling procedures. Studying the aggregation of the Aβ42 peptide in the presence of RS-0406, a molecule whose anti-amyloid-aggregation properties had been reported in the literature(17), we could reveal the plausible mechanism for its presumed activity. Our tentative interpretation of the measurements indicates that RS-0406 should not inhibit the amyloid aggregation. On the contrary, RS-0406 seemingly accelerates Aβ42 peptide aggregation, thus depleting the solution of the soluble toxic oligomers in a shorter time frame. This outcome is strongly corroborated by parallel NMR-based experiments, carried out in collaboration with Dr. Dalvit from the University of Neuchâtel. Moreover, the NMR-based studies helped validating our sensing approach as a powerful and robust screening tool for molecular inhibitor of Aβ early oligomerization process.

5.4 Bibliography

1. Sun X, Jin L, & Ling P (2012) Review of drugs for Alzheimer's disease. *Drug Discov Ther* 6(6):285-290.
2. Yiannopoulou KG & Papageorgiou SG (2013) Current and future treatments for Alzheimer’s disease. *Therapeutic Advances in Neurological Disorders* 6(1):19-33.

3. Casey DA, Antimisiaris D, & O'Brien J (2010) Drugs for Alzheimer's Disease: Are They Effective? *Pharmacy and Therapeutics* 35(4):208-211.

4. Török B, Sood A, Bag S, Kulkarni A, Borkin D, Lawler E, Dasgupta S, Landge S, Abid M, Zhou W, Foster M, LeVine H, & Török M (2012) Structure–Activity Relationships of Organofluorine Inhibitors of β-Amyloid Self-Assembly. *ChemMedChem* 7(5):910-919.

5. Blennow K, Hampel H, & Zetterberg H (2014) Biomarkers in amyloid-beta immunotherapy trials in Alzheimer's disease. *Neuropsychopharmacology : official publication of the American College of Neuropsychopharmacology* 39(1):189-201.

6. Blennow K, de Leon MJ, & Zetterberg H (2006) Alzheimer's disease. *The Lancet* 368(9533):387-403.

7. Kroth H, Ansaloni A, Varisco Y, Jan A, Sreenivasachary N, Rezaei-Ghaleh N, Giriens V, Lohmann S, López-Deber MP, Adolfsson O, Pihlgren M, Paganetti P, Froestl W, Nagel-Steger L, Willbold D, Schrader T, Zweckstetter M, Pfeifer A, Lashuel HA, & Muhs A (2012) Discovery and Structure Activity Relationship of Small Molecule Inhibitors of Toxic β-Amyloid-42 Fibril Formation. *Journal of Biological Chemistry* 287(41):34786-34800.

8. Lashuel HA, Hartley DM, Balakhaneh D, Aggarwal A, Teichberg S, & Callaway DJE (2002) New Class of Inhibitors of Amyloid-β Fibril Formation: Implications for the Mechanism of Pathogenesis in Alzheimer's Disease. *Journal of Biological Chemistry* 277(45):42881-42890.

9. Marambaud P, Zhao H, & Davies P (2005) Resveratrol Promotes Clearance of Alzheimer's Disease Amyloid-β Peptides. *Journal of Biological Chemistry* 280(45):37377-37382.

10. Hawkes CA, Ng V, & McLaurin J (2009) Small molecule inhibitors of Aβ-aggregation and neurotoxicity. *Drug Development Research* 70(2):111-124.

11. Di Giovanni S, Eleuteri S, Paleologou KE, Yin G, Zweckstetter M, Carrupt P-A, & Lashuel HA (2010) Entacapone and Tolcapone, Two Catechol O-Methyltransferase Inhibitors, Block Fibril Formation of α-Synuclein and β-Amyloid and Protect against Amyloid-induced Toxicity. *Journal of Biological Chemistry* 285(20):14941-14954.

12. Ehrnhoefer DE, Bieschke J, Boeddrich A, Herbst M, Masino L, Lurz R, Engemann S, Pastore A, & Wanker EE (2008) EGCG redirects amyloidogenic polypeptides into unstructured, off-pathway oligomers. *Nat Struct Mol Biol* 15(6):558-566.

13. Baptista FI, Henriques AG, Silva AMS, Wiltfang J, & da Cruz e Silva OAB (2014) Flavonoids as Therapeutic Compounds Targeting Key Proteins Involved in Alzheimer's Disease. *ACS Chemical Neuroscience* 5(2):83-92.

14. Ono K, Hasegawa K, Naiki H, & Yamada M (2004) Anti-amyloidogenic activity of tannic acid and its activity to destabilize Alzheimer's beta-amyloid fibrils in vitro. *Biochim Biophys Acta* 1690(3):193-202.

15. Ono K, Hasegawa K, Yoshiike Y, Takashima A, Yamada M, & Naiki H (2002) Nordihydroguaiaretic acid potently breaks down pre-formed Alzheimer's β-amyloid fibrils in vitro. *Journal of Neurochemistry* 81(3):434-440.

16. Nakagami Y, Nishimura S, Murasugi T, Kubo T, Kaneko I, Meguro M, Marumoto S, Kogen H, Koyama K, & Oda T (2002) A novel compound RS-0466 reverses β-amyloid-induced cytotoxicity through the Akt signaling pathway in vitro. *European journal of pharmacology* 457(1):11-17.

17. Nakagami Y, Nishimura S, Murasugi T, Kaneko I, Meguro M, Marumoto S, Kogen H, Koyama K, & Oda T (2002) A novel β-sheet breaker, RS-0406, reverses amyloid β-induced cytotoxicity and impairment of long-term potentiation in vitro. *British Journal of Pharmacology* 137(5):676-682.

18. Nie Q, Du XG, & Geng MY (2011) Small molecule inhibitors of amyloid beta peptide aggregation as a potential therapeutic strategy for Alzheimer's disease. *Acta pharmacologica Sinica* 32(5):545-551.

19. O'Hare E, Scopes DIC, Treherne JM, Norwood K, Spanswick D, & Kim E-M (2010) RS-0406 Arrests Amyloid-β Oligomer-Induced Behavioural Deterioration In Vivo. *Behavioural Brain Research* 210(1):32-37.

20. Nilsson MR (2004) Techniques to study amyloid fibril formation in vitro. *Methods* 34(1):151-160.

21. Dalvit C, Pevarello P, Tatò M, Veronesi M, Vulpetti A, & Sundström M (2000) Identification of compounds with binding affinity to proteins via magnetization transfer from bulk water. *J Biomol NMR* 18(1):65-68.

22. Dalvit C (2009) NMR methods in fragment screening: theory and a comparison with other biophysical techniques. *Drug Discovery Today* 14(21–22):1051-1057.

23. Harper JD & Lansbury PT (1997) Models Of Amyloid Seeding In Alzheimer's Disease And Scrapie: Mechanistic Truths and Physiological Consequences of the Time-Dependent Solubility of Amyloid Proteins. *Annual Review of Biochemistry* 66(1):385-407.

24. Jan A, Hartley DM, & Lashuel HA (2010) Preparation and characterization of toxic A beta aggregates for structural and functional studies in Alzheimer's disease research. *Nat Protoc* 5(6):1186-1209.

25. Hortschansky P, Schroeckh V, Christopeit T, Zandomeneghi G, & Fändrich M (2005) The aggregation kinetics of Alzheimer's β-amyloid peptide is controlled by stochastic nucleation. *Protein Science* 14(7):1753-1759.

26. Santi S, Musi V, Descrovi E, Paeder V, Di Francesco J, Hvozdara L, van der Wal P, Lashuel HA, Pastore A, Neier R, & Herzig HP (2013) Real-time Amyloid Aggregation Monitoring with a Photonic Crystal-based Approach. *Chemphyschem* 14(15):3476-3482.

27. Dalvit C, Fogliatto G, Stewart A, Veronesi M, & Stockman B (2001) WaterLOGSY as a method for primary NMR screening: Practical aspects and range of applicability. *J Biomol NMR* 21(4):349-359.

28. Dalvit C, Caronni D, Mongelli N, Veronesi M, & Vulpetti A (2006) NMR-based quality control approach for the identification of false positives and false negatives in high throughput screening. *Current drug discovery technologies* 3(2):115-124.

29. Dubois BW & Evers AS (1992) 19F-NMR spin-spin relaxation (T2) method for characterizing volatile anesthetic binding to proteins. Analysis of isoflurane binding to serum albumin. *Biochemistry* 31(31):7069-7076.

30. Dalvit C, Gossert AD, Coutant J, & Piotto M (2011) Rapid acquisition of 1H and 19F NMR experiments for direct and competition ligand-based screening. *Magnetic Resonance in Chemistry* 49(4):199-202.

31. Dalvit C, Santi S, Herzig HP, & Neier R (2016) Manuscript in preparation.

6. COMBINING BSW-BASED SENSING AND LIGHT-SCATTERING MEASUREMENT: A SETUP IMPROVEMENT

6.1 Light scattering for particle size characterization

In the previous chapters, we have described the application of a BSW-based sensing platform to the real-time optical investigation of the aggregation dynamics of Aβ42 peptide. The main shortcoming of the proposed approach is that we were unable to fully segregate the bulk and surface contributions to the refractive index variations of the Aβ42 peptide samples, as measured by the BSW throughout aggregation. Therefore, we focused on obtaining complementary information on the mechanisms for the Aβ42 peptide interaction with the multilayer surface and on the precise conformation and size of the peptide during this surface-loading phenomenon. *In vitro* studies of the prefibrillar Aβ42 peptide size evolution throughout pathogenic aggregation have been reported in the literature(1-3), and have revealed a size range of 10 to 15 nm in diameter for the early disc-shaped pentameric aggregates, while protofibrils reportedly reach a length of 200 nm with a diameter of 5 nm. Characterized by the typical filamentous morphology, mature fibrils have revealed a length of more than 1 μm with a diameter of 10 to 12 nm(4). We aimed at discriminating between these three distinct aggregated forms of the Aβ42 peptide throughout a BSW-based real-time monitoring experiment. The information obtained from this study would complement the measurements presented in Chapter 3, where experiments carried out with the peptide at isolated specific aggregation stages were presented.

Light-scattering techniques have widely been used for many applications, spanning from cosmology to polymer science(5). They use the property of a light beam of being deflected upon encountering obstacles or irregularities in the propagation medium. When an incident photon encounters a molecule or a particle, it induces an oscillating dipole in the electron cloud. As a consequence of the dipole variation, energy in the form of scattered light is radiated in all directions. For small particles, whose diameter is approximately less than 1/10 of the light-source wavelength, the so-called “Rayleigh Theory” is applied: It states that the scattering is isotropic and that the intensity of the radiation is proportional to the particle size(6).

In protein chemistry, light-scattering applications are routinely used to characterize the size of a protein in solution, and to monitor, for example, receptor binding and self-assembling processes(7). Protein aggregation can be regarded as a special case of self-assembling, and can be monitored in real-time using commercially available dynamic light-scattering (DLS) tools. Those DLS-based instruments allow estimating the hydrodynamic radius and the translational diffusion coefficient of protein clusters(8). Contrary to static light-scattering (SLS) techniques, where the signal is time averaged, DLS measures real-time intensity fluctuations $I_{(t)}$ of scattered light via a correlation function. DLS has thus become a cardinal technique in protein aggregation investigation(6). Being the result of Brownian motions, the variation of the intensity of the light scattered by proteins in solution is related to their aggregation state. Hence, DLS monitoring can be reliably used for studies of protein aggregation kinetics(9).

Nevertheless, DLS technique suffers from the lack of selectivity and, in general, from a very low signal-to-noise ratio (SNR)(5, 10). For this reason, starting from the late eighties(11), DLS has been combined with evanescent wave generators used as light source. Recent years thus saw the development of the “total internal reflection microscopy” (TIRM)(12), a tool especially suitable for particle tracking and for investigating particle-surface interactions in colloidal solutions. With TIRM, the light confinement achieved with the evanescent wave allows overcoming the low SNR in common DLS techniques. From the notion that light scattering can be induced by evanescent waves in a controlled way(13, 14), several other approaches have emerged, such as waveguide-enhanced DLS (WEDLS)(15) and resonance-enhanced DLS (REDLS)(16),where the evanescent wave is generated by a leaky waveguide or surface plasmons, respectively. They all share the common advantage of an increased SNR, thanks to the field enhancement of the evanescent wave, and the possibility to use different materials instead of only glass substrates, as in the case of TIRM(14). Moreover, a further benefit in employing these techniques in lieu of TIRM is the possibility to *in situ* tailor the penetration depth of the evanescent tail by changing the polarization of the light source, in the case of WEDLS(15), or the wavelength, in the case of REDLS(16). Employing correlation functions for scattering intensity analysis, one can derive information about the dynamics of particle diffusion near the surface and, thus, about the size of the analyte(10).

In this chapter, we present the first original conception of a BSW-enhanced DLS technique (BEDLS), in which the light source for scattering induction is the evanescent tail of the Bloch surface wave. A preliminary and simplified implementation of this technique is also presented. This work stems from the initial attempt of performing a simultaneous BSW-based sensing and a DLS measurement, with the aim of monitoring the size evolution of the Aβ42 aggregates throughout fibrillization. In the following, the two different optical platforms that we developed for scattering analysis are described according to the chronological order of their conception.

6.2 Experimental optical setup modifications

The original idea we conceived was to simultaneously investigate the size variation of the aggregating peptide in solution while performing a BSW-based measurements. We aimed at a non-invasive method that could be implemented in parallel and without fundamentally changing the optical sensing scheme. Combining DLS with our experimental approach was selected as the most appealing strategy. A DLS technique could be implemented in parallel using the existing setup upon making little variations. Commercially available DLS instruments are capable of determining the size of particles in a range of 0.3 to 10 μm, and require very small volume of analytes, in the order of some μL(8). Given the size of the Aβ42 oligomers, protofibrils and fibrils(17), even a low-sensitivity in-house-built DLS platform should be capable of covering the size transition occurring along the fibrillization pathway. This particular setup modification is presented in section 6.2.1.

Afterwards, we recognized the potential of inducing light scattering with the evanescent tail of the BSW, in an effort to increase the SNR and develop a more compact sensing tool. This idea and its development are discussed in section 6.2.2.

6.2.1 Parallel DLS and BSW-based-monitoring setup

The first experimental setup we developed to perform a combined DLS and BSW-based measurement is shown in Fig.6.2.1. It was built to achieve a simultaneous real-time monitoring of the light scattering intensity and of the refractive index, as sensed by the BSW. Two separate and independent illumination sources were used for the BSW excitement and the light scattering induction. The determination of the size evolution of the Aβ42 aggregates during fibrillization would contribute additional information about the size of the aggregates. The results obtained from such a parallel measurement could help clarifying the correlation between the signal revealed by the BSW-based monitoring and the actual aggregation stage of the peptide.

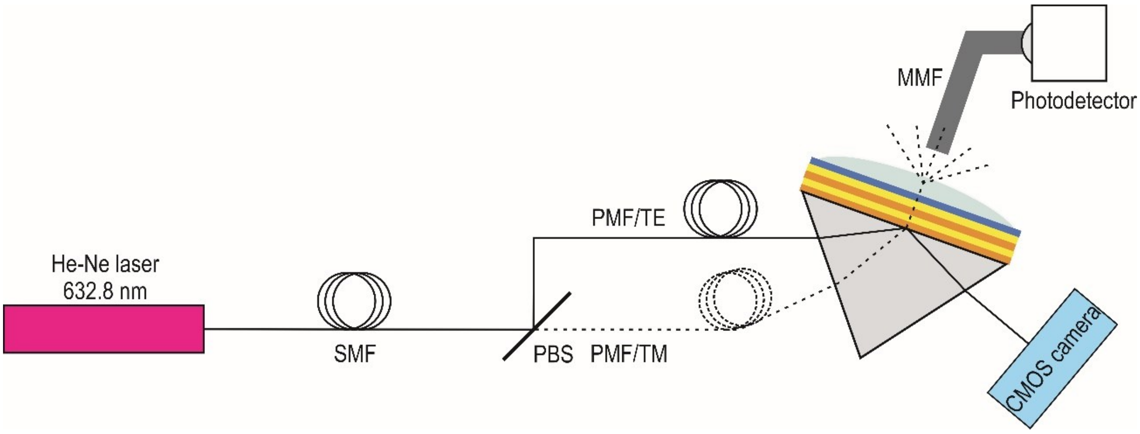

Fig.6.2.1. Top-view simplified schematics of the experimental setup used for the simultaneous light scattering and BSW-based real-time monitoring. SMF: single-mode fiber; PBS: polarizing beam-splitter; PMF: polarization maintaining fiber; MMF: multi-mode fiber. The dashed line symbolizes the light guided through the PMF to induce the light scattering phenomenon, and the light scattered by the analyte. For details on the setup, see Chapter 8.

Compared to the initial BSW-based setup described in Chapter 2, several changes were made to allow the measurement of the light scattered by the Aβ42 aggregates in solution. Light coming from a He-Ne laser is coupled into a single-mode fiber (SMF). A polarizing beam-splitter (PBS) is used for the TE and TM polarization separation. After the PBS, polarization maintaining fibers (PMF) are employed to guide the light to the sensing chamber (see Chapter 8 for details). BSWs are excited with the TE-polarized part, and the Kretschman configured coupling system is the same as in the original setup described in Chapter 2, with the fluidic chamber positioned vertically(18). Additionally, as a source to induce the light scattering, the TM-polarized beam is impinging the multilayer surface above the critical angle for TIR and, thus, above the resonance angle, to avoid interfering with the BSW phenomenon. A circular Peltier element positioned behind the fluidic chamber is used for sample incubation and temperature stabilization. The element central hole allows the collection of the scattered light propagating from the sample, which is performed via a 2 mm-core multimode optical fiber (MMF) connected to a power meter (see Fig.6.2.2).

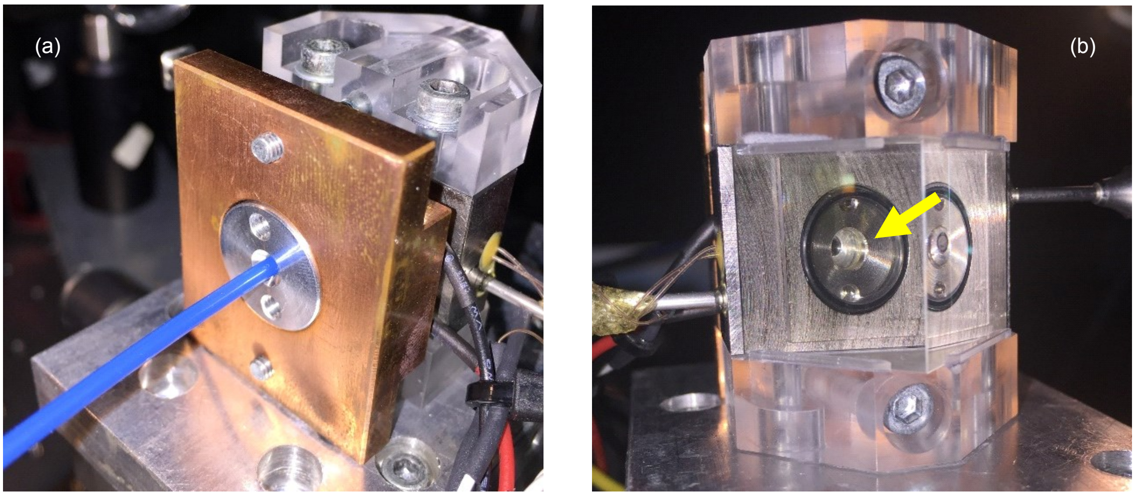

Fig.6.2.2. Pictures of the fluidic chamber adapted for the light scattering collection. (a) the MMF, in blue, is contacted to the back of the fluidic chamber, passing through the Peltier element (not visible), and collects the light scattered by the particles in solution via a back-window in the fluidic chamber, which can be seen in (b), as indicated by the yellow arrow.

To test the performance of the modified setup, we measured the light-scattering response of an aggregating Aβ42 peptide solution at an initial monomer concentration of 5 µM. In parallel, we performed a BSW-based refractive index monitoring of the Aβ42 peptide solution during aggregation using a bare multilayer surface. The result of the BSW-based monitoring of the aggregating peptide was comparable to other measurements performed under the same conditions (Chapter 3). The light-scattering response of the measurement was compared to a reference signal obtained by incubating a sample of d.i. filtered water. Both samples were kept at 37 °C, which is the temperature at which the Aβ42 aggregation occurs. However, we did not observe substantial and rational light intensity fluctuation differences between the DLS monitoring of water and of the aggregating peptide. The signal was mostly characterized by unspecified noise. This was most probably due to the low SNR of the measurements: the MMF was also collecting part of the light used as illumination source for the DLS phenomenon. As a result, the signal from the scattering particles was too low compared to the background light intensity.

6.2.2 BSW induced light scattering imaging

Employing the BSW as the source for inducing the light scattering was the idea we conceived to overcome the low SNR exhibited by the measurement described above. BSWs are evanescent and do not propagate in the far field(19). In a similar sensing scheme as presented before (Fig.6.2.1), where a detector is placed opposite to the light source, with BSW as the source only the light scattered by the analyte should be recovered by the detector. Moreover, with BSW, the strong field enhancement and surface confinement of the evanescent wave should help boosting the signal(20, 21), similarly to what has been described in the literature for REDLS(16). We thus implemented a second experimental setup for scattering measurement, which is shown in Fig.6.2.3. The aim was to study the phenomenon of light scattering induced by BSW prior to modifying the experimental setup for the real-time monitoring. The setup in Fig.6.2.3 is thus a preliminary and simplified implementation of a BEDLS platform. Being a prototype, it does not allow for a time-related signal intensity monitoring, as explained in the following. Therefore, we named this intermediary technique BILSI: BSW Induced Light Scattering Imaging.

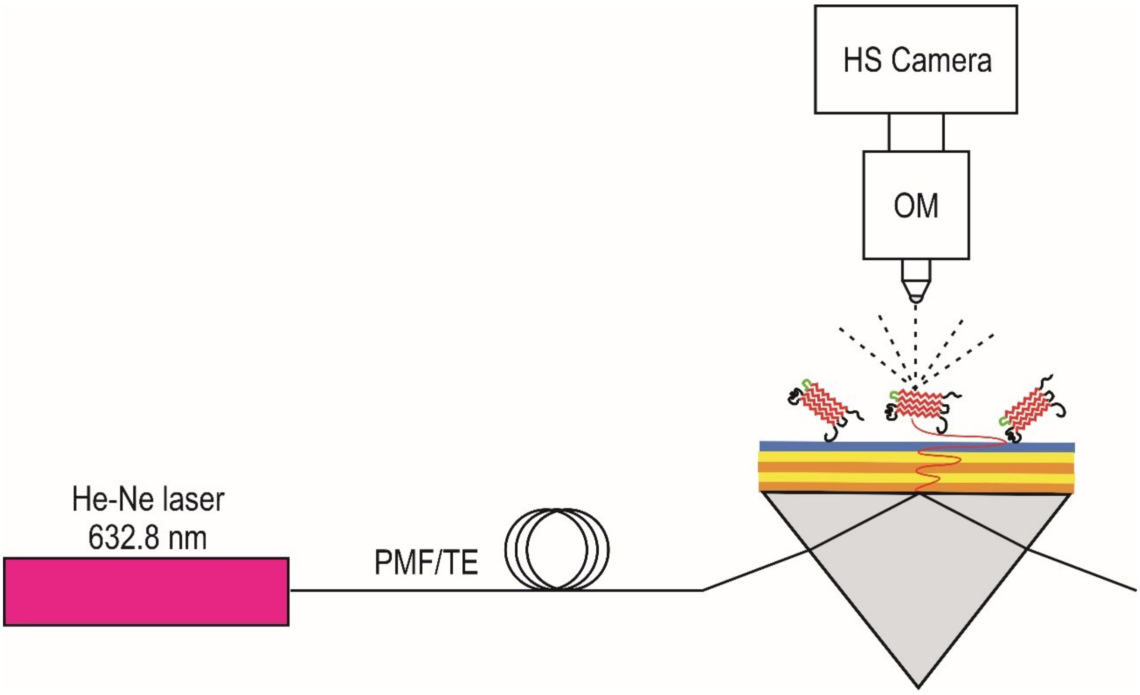

Fig.6.2.3. Schematics of the experimental setup for BILSI. PMF: polarization maintaining fiber; OM: optical microscope; HS: high sensitivity. A 20X microscope objective was used to collect the light. The dashed line symbolizes the light scattering phenomenon. We thank Dr. N. Descharmes from the Optics & Photonics Technology Laboratory, EPFL, for assisting with the setup construction.

The setup consists of an upright optical microscope, used for scattered light collection, provided with a high sensitive camera for light detection and sample imaging. A dielectric multilayer is used in place of a standard glass microscope-slide. For sample illumination, the Kretschman configuration coupling scheme is the same as for the other setups. A He-Ne laser is used to excite the BSW via a right-angle glass prism. However, the multilayer is horizontally positioned and was designed to work in air (Fig.6.2.3). The multilayer was designed as described in Chapter 8 by Dr. Barakat from the Optics & Photonics Technology Laboratory, EPFL. With the goal of performing a proof-of-principle experiment, liquid samples were deposited on the multilayer surface and let dry prior to perform the measurement. The choice of working with a "dry sample" was driven by the will to perform a quick test measurement, otherwise unfeasible in solution for the lack of a properly designed fluidic chamber that could be used with the optical microscope. To verify the scattering induction given by the BSW, the idea was to compare a reflected bright-field imaging under white light to a measurement in BILSI/BEDLS illumination scheme. The investigated sample was therefore the same in both experiments. We deposited a sample of 72 µM Aβ42 peptide in the fibrillar aggregation stage (for sample preparation, see Chapter 8) onto a photonic-crystal multilayer. Upon illumination, the sample under the two different illuminations is presented with the picture in Fig.6.2.4, for the reflected bright-field imaging, and with the micrographs in Figs.6.2.5, 6.2.6, 6.2.7, 6.2.8 for the BSW illumination. From Fig.6.2.5 to Fig.6.2.8 the multilayer sample was sequentially shifted of 2 mm towards the laser illumination spot through the prism. For further details on image acquisition see Chapter 8.

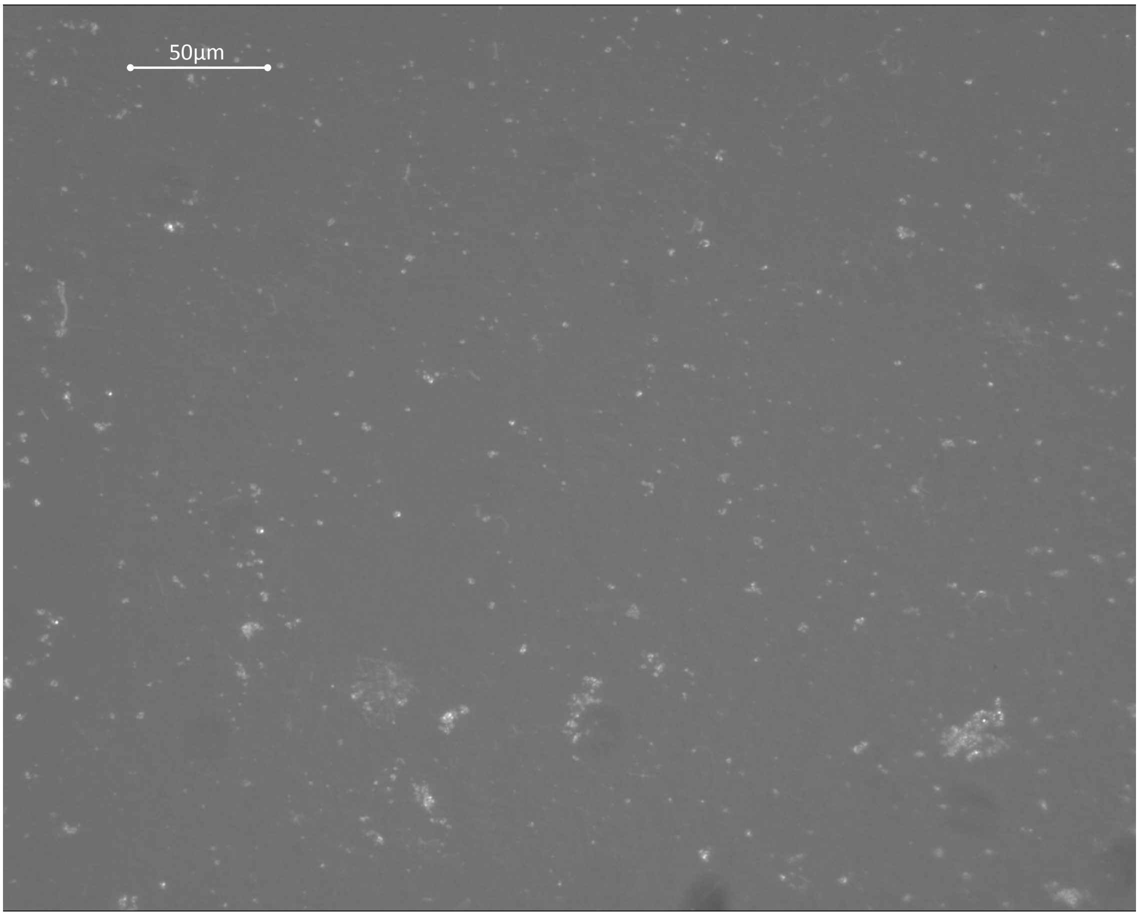

Fig.6.2.4. Reflected bright-field illumination imaging under white light. We thank Dr. E. Barakat from the Optics & Photonics Technology Laboratory, EPFL, for the image.

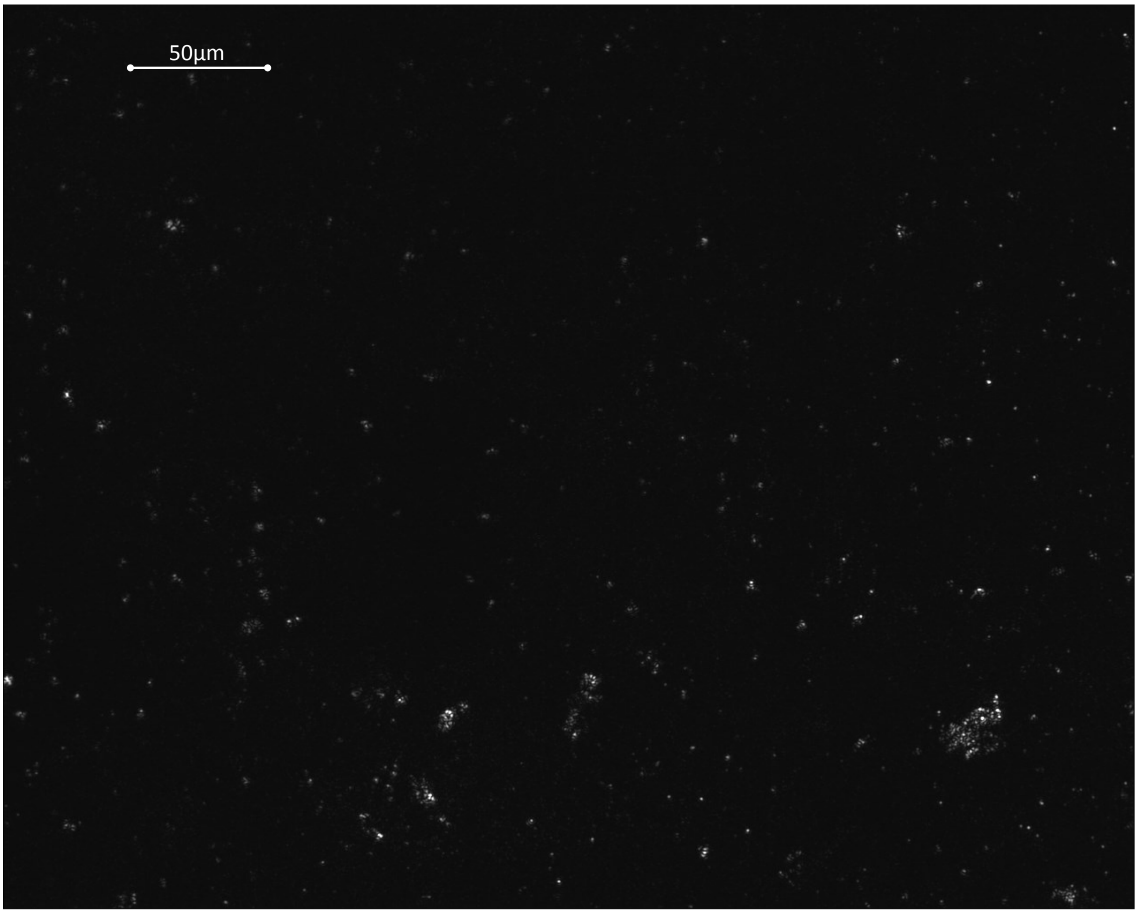

Fig.6.2.5. Micrograph obtained upon BSW illumination. The sample was 8 mm-far from the illumination spot. We thank Dr. E. Barakat from the Optics & Photonics Technology Laboratory, EPFL, for the micrographs.

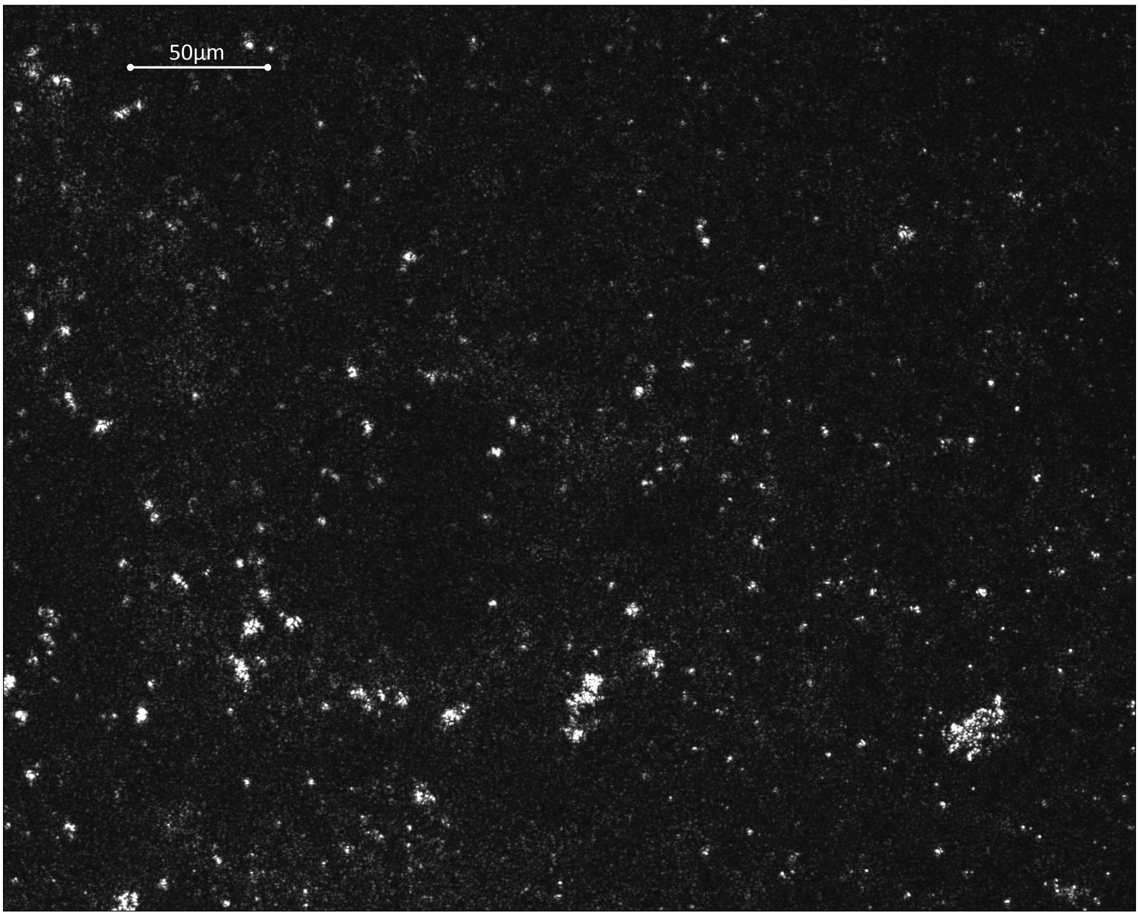

Fig.6.2.6. Micrograph obtained upon BSW illumination. The sample was 6 mm-far from the illumination spot. We thank Dr. E. Barakat from the Optics & Photonics Technology Laboratory, EPFL, for the micrographs.

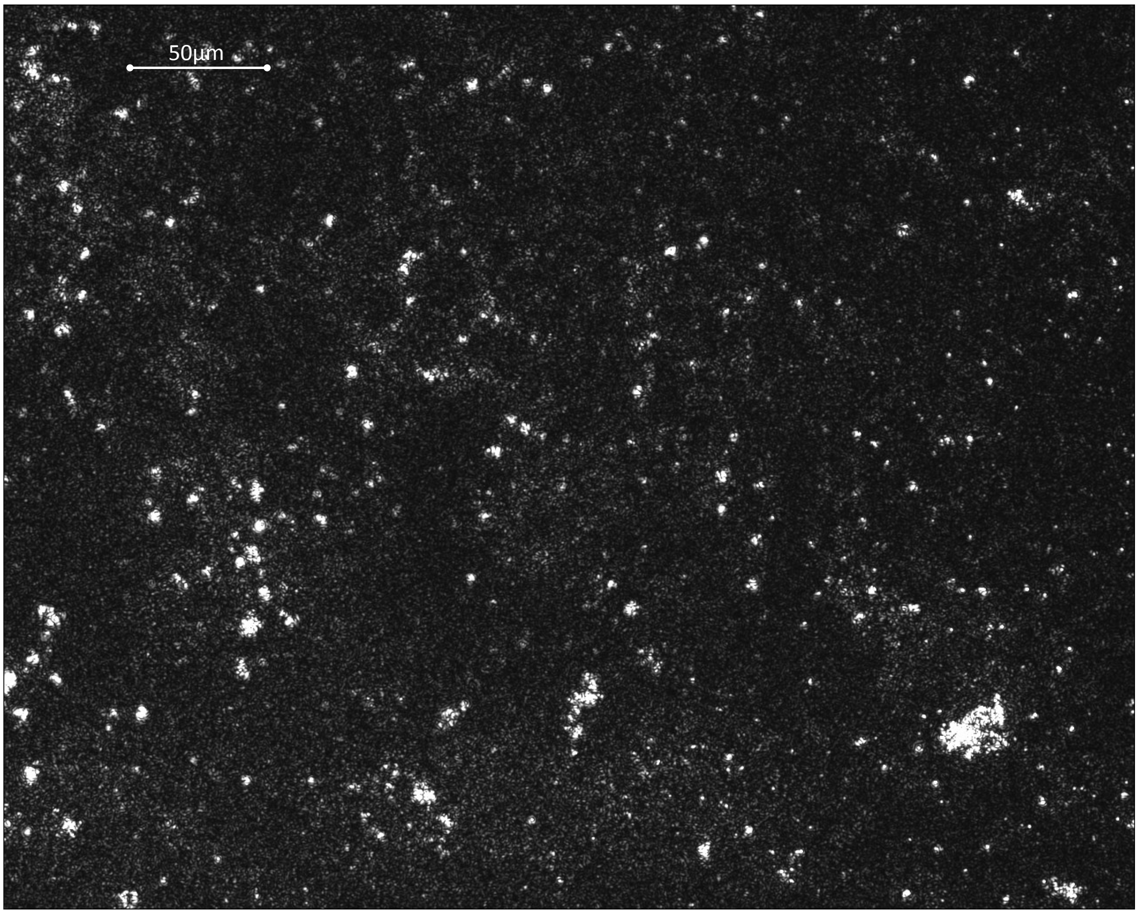

Fig.6.2.7. Micrograph obtained upon BSW illumination. The sample was 4 mm-far from the illumination spot. We thank Dr. E. Barakat from the Optics & Photonics Technology Laboratory, EPFL, for the micrographs.

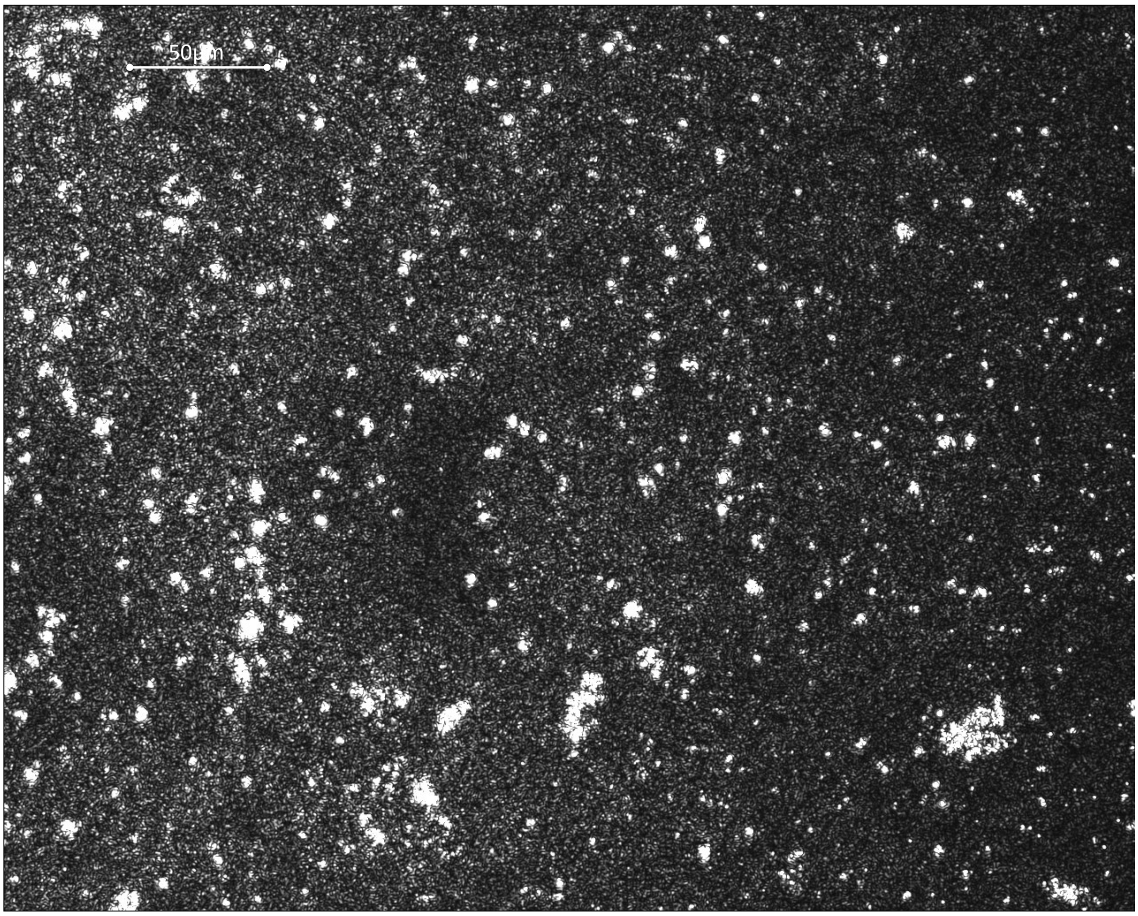

Fig.6.2.8. Micrograph obtained upon BSW illumination. The sample was 4 mm-far from the illumination spot. We thank Dr. E. Barakat from the Optics & Photonics Technology Laboratory, EPFL, for the micrographs.

The purely qualitative analysis of the results reveals a substantial difference in the image and micrographs under the two experimental conditions. In Fig.6.2.4, the light from the sample is mainly reflected, due to the illumination condition. The main difference between the illumination conditions from Fig.6.2.5 to Fig.6.2.8 was the sample proximity to the laser illumination spot through the prism. The BSW propagates on the multilayer surface and the intensity decreases with the propagation distance from the source(20). From a qualitative analysis, the intensity of the light, as imaged onto the HS camera, was increasing with proximity. In Figs.6.2.5, 6.2.6, 6.2.7, and 6.2.8 the light response was different from what exhibited in Fig.6.2.4. Under reflected bright-field illumination, particles under and near the surface were imaged onto the camera. Under BSW-illumination conditions, only the particles at the surface were selectively illuminated, due to the evanescent nature of the BSW. The microscope was thereby not collecting the light from the illumination source. As a consequence, a qualitatively higher contrast is exhibited by the micrographs in Figs.6.2.5, 6.2.6, 6.2.7, and 6.2.8, compared to the image in Fig.6.2.4. We tentatively identified the light from the samples illuminated under the BSW resonance condition with light scattered by the particles deposited onto the multilayer surface. Therefore, we could infer a light scattering induction via BSW illumination. However, due to the size of the analytes deposited onto the multilayer surface, we could not visually discriminate between the buffer salt residues and the Aβ42 fiber morphology. To this purpose, dedicated experiments should be designed.

We are entirely aware that the micrographs in Figs.6.2.5, 6.2.6, 6.2.7, 6.2.8 do not fully validate our BSW-based technique as a means to enhance light scattering. However, these preliminary results are extremely encouraging. With BSW, a field confinement should increase the light scattered by the analyte, thus ameliorating the SNR. We are convinced that our technique is a highly promising concept for a facile combination of two different methods. A BEDLS sensing approach would offer the possibility to perform a refractive index monitoring simultaneously to the DLS measurement, which makes this technique extremely attractive for real-time monitorings of aggregation dynamics.

6.3 Conclusion

This chapter reports on two innovative and original sensing approaches aimed at monitoring the DLS signal given by the aggregation of amyloid peptides. In the first, an attempt to perform a simultaneous DLS and BSW-based monitoring was carried out. This approach did not lead to the expected outcomes in the DLS signal, due to a very low SNR mostly related to the illumination scheme. The use of the MMF as the scattered light collector was also questionable. A MMF is highly sensitive to external perturbations (such as temperature) leading to optical path length fluctuations(22), and thus generating spurious signal variation contributing to additional noise. The choice of a MMF as the light collector has therefore to be avoided in future studies. Finally, introducing a converging lens positioned between the cell back-window and the fiber edge would have improved the light collection. The geometry and size of the fluidic cell imposed constraints that made this improvement impossible: The small back-window was too small to accommodate a lens. The design was limited by the Peltier element hole.

In a second attempt, the methodology was based on the use of a one-dimension photonic crystal capable to generate a BSW, which itself was used as the source for light scattering induction. With a parallelism to REDLS (Resonance-Enhanced Dynamic Light Scattering)(16), where the source for the DLS monitoring are surface plasmons, we introduced the BEDLS (Bloch surface wave-Enhanced Dynamic Light Scattering) technique. Due to time restrictions, we did not accomplish the development of a setup (ideally described in Chapter 7), which could be demonstrated to be fully operational. We implemented a simplified and transitional setup, which allowed for a proof of principle of the feasibility of the proposed sensing scheme. We called this method BILSI (BSW Induced Light Scattering

Imaging), since the scattering enhancement was not experimentally validated, but it is theoretically demonstrated by similar methods(16, 21).

The main advantage of technique described in this chapter should be an improvement of the SNR, due to the high light confinement achievable with the BSW(19). Although we did not explore its full potential, BILSI and BEDLS offer the opportunity to perform a refractive index monitoring simultaneously to the DLS measurement, which makes this technique a valid and attractive alternative to TIRM(12). Moreover, depending on the materials used in the fabrication, the multilayer can be designed to work at–virtually–any desired wavelength and at both polarizations(23-25). Hence, BEDLS appears more versatile even as compared to REDLS. In general, all the benefits achievable with the choice of BSW instead of SPR as a light source for the induction of light scattering are exploitable with BEDLS.

6.4 Bibliography

1. Ahmed M, Davis J, Aucoin D, Sato T, Ahuja S, Aimoto S, Elliott JI, Van Nostrand WE, & Smith SO (2010) Structural conversion of neurotoxic amyloid-beta1-42 oligomers to fibrils. *Nat Struct Mol Biol* 17(5):561-567.

2. Mastrangelo IA, Ahmed M, Sato T, Liu W, Wang C, Hough P, & Smith SO (2006) High-resolution Atomic Force Microscopy of Soluble Aβ42 Oligomers. *Journal of Molecular Biology* 358(1):106-119.

3. Harper JD, Wong SS, Lieber CM, & Lansbury Jr PT (1997) Observation of metastable Aβ amyloid protofibrils by atomic force microscopy. *Chemistry & Biology* 4(2):119-125.

4. Serpell LC (2000) Alzheimer's amyloid fibrils: structure and assembly. *Biochim Biophys Acta* 1502(1):16-30.

5. Xu R (2015) Light scattering: A review of particle characterization applications. *Particuology* 18:11-21.

6. Berne BJ (1976) *Dynamic light scattering : with applications to chemistry, biology, and physics / Bruce J. Berne and Robert Pecora* (Wiley, New York).

7. Li S, Xing D, & Li J (2004) Dynamic Light Scattering Application to Study Protein Interactions in Electrolyte Solutions. *Journal of Biological Physics* 30(4):313-324.

8. Malvern Instruments (2015) Zetasizer: Dynamic Light Scattering DLS for particle size characterization of proteins, polymers and colloidal dispersions. Available at: http://www.malvern.com/en/products/technology/dynamic-light-scattering/ [Accessed March 10, 2016].

9. Militello V, Casarino C, Emanuele A, Giostra A, Pullara F, & Leone M (2004) Aggregation kinetics of bovine serum albumin studied by FTIR spectroscopy and light scattering. *Biophysical chemistry* 107(2):175-187.

10. Pecora R (1985) *Dynamic Light Scattering: Applications of Photon Correlation Spectroscopy* (Springer US, Plenum Press, New York) 1 Ed pp XIV, 420.

11. Prieve DC, Luo F, & Lanni F (1987) Brownian motion of a hydrosol particle in a colloidal force field. *Faraday Discussions of the Chemical Society* 83(0):297-307.

12. Prieve DC & Frej NA (1990) Total internal reflection microscopy: a quantitative tool for the measurement of colloidal forces. *Langmuir* 6(2):396-403.

13. Sigel R (2009) Light scattering near and from interfaces using evanescent wave and ellipsometric light scattering. *Current Opinion in Colloid & Interface Science* 14(6):426-437.

14. Fytas G, Anastasiadis SH, Seghrouchni R, Vlassopoulos D, Li J, Factor BJ, Theobald W, & Toprakcioglu C (1996) Probing Collective Motions of Terminally Anchored Polymers. *Science* 274(5295):2041-2044.

15. Plum MA, Borges Vianna SD, Unger A, Roskamp RF, Butt H-J, Menges B, & Steffen W (2011) Probing dynamics near surfaces: waveguide enhanced dynamic light scattering. *Soft Matter* 7(4):1501-1505.

16. Plum MA, Menges B, Fytas G, Butt H-J, & Steffen W (2011) Resonance enhanced dynamic light scattering. *Review of Scientific Instruments* 82(1):015102.

17. Jan A, Hartley DM, & Lashuel HA (2010) Preparation and characterization of toxic A beta aggregates for structural and functional studies in Alzheimer's disease research. *Nat Protoc* 5(6):1186-1209.

18. Santi S, Musi V, Descrovi E, Paeder V, Di Francesco J, Hvozdara L, van der Wal P, Lashuel HA, Pastore A, Neier R, & Herzig HP (2013) Real-time Amyloid Aggregation Monitoring with a Photonic Crystal-based Approach. *Chemphyschem* 14(15):3476-3482.

19. Yeh P, Yariv A, & Cho AY (1978) Optical surface waves in periodic layered media. *Applied Physics Letters* 32(2):104-105.

20. Yu L, Barakat E, Sfez T, Hvozdara L, Di Francesco J, & Peter Herzig H (2014) Manipulating Bloch surface waves in 2D: a platform concept-based flat lens. *Light Sci Appl* 3:e124.

21. Soboleva IV, Descrovi E, Summonte C, Fedyanin AA, & Giorgis F (2009) Fluorescence emission enhanced by surface electromagnetic waves on one-dimensional photonic crystals. *Appl Phys Lett* 94:231122.

22. Ma L-S, Jungner P, Ye J, & Hall JL (1994) Delivering the same optical frequency at two places: accuratecancellation of phase noise introduced by an optical fiber or other time-varyingpath. *Opt. Lett.* 19(21):1777-1779.

23. Ballarini M, Frascella F, Michelotti F, Digregorio G, Rivolo P, Paeder V, Musi V, Giorgis F, & Descrovi E (2011) Bloch surface waves-controlled emission of organic dyes grafted on a one-dimensional photonic crystal. *Applied Physics Letters* 99(4):043302-043303.

24. Farmer A, Friedli AC, Wright SM, & Robertson WM (2012) Biosensing using surface electromagnetic waves in photonic band gap multilayers. *Sensors and Actuators B: Chemical* 173(0):79-84.

25. Rivolo P, Michelotti F, Frascella F, Digregorio G, Mandracci P, Dominici L, Giorgis F, & Descrovi E (2012) Real time secondary antibody detection by means of silicon-based multilayers sustaining Bloch surface waves. *Sensors and Actuators B: Chemical* 161(1):1046-1052.

7. CONCLUSION AND PERSPECTIVES

7.1 Conclusion

This thesis project has tackled the experimental validation of a Bloch surface wave-based sensing device conceived by the Optics & Photonics Technology laboratory (EPFL, Neuchâtel) for biosensing purposes. It is a novel sensing platform to perform refractive index measurements, reminiscent of SPR-based techniques. The potential of this original sensing approach based on BSWs was exploited by monitoring the toxic early progress of amyloid-beta (Aβ) peptide aggregation. Understanding the process of the complex and still obscure amyloid aggregation is directly linked to the possibility of developing therapies for the fatal and incurable Alzheimer's disease.

The main outcome of this project has been the real-time monitoring of the dynamics of Aβ42 peptide oligomerization, aggregation and fibrils formation. The time frame that we were able to investigate is very often silent through the lens of classical amyloid detection techniques. At present, these conventional techniques, as well as other more sophisticated methods, such as X-ray crystallography and NMR, are often not suitable for studying the early dynamic events in the aggregation process of proteins. While our new biosensing approach provided a tool to monitor the early Aβ42 peptide aggregation dynamics, in parallel we were able to control the progressive formation of the amyloid structures by biochemical and biophysical methods (chromatographic techniques, optical spectroscopies, TEM) classically used for this purpose.

Note that this sensing approach has not to be confused with a diagnosis tool. Our BSW-based sensing method has to be understood more as a helpful tool for fundamental research on amyloid fibrillization. In addition, our optical sensing method could serve as a direct, easy-to-perform screening apparatus for new potential inhibitors of Aβ42 toxic oligomers and early nucleation events, in the context of lead finding and lead optimization for the development of new drugs.

However, questions still remain unresolved, such as what is the nature of the species interacting with the sensing surface and what regulates this adsorption-desorption mechanism. From the hypothesis that this process could be correlated to a conformational transition of the Aβ peptide–presumably of the middle-to-low molecular-weight soluble oligomers–during early aggregation, we conceived experiments aimed at verifying our formulation. Hence, we devised a surface functionalization strategy, specific for silicon oxi-nitride surfaces that decisively contributed to elucidate the process underlying the peptide surface-interaction. Moreover, the results obtained in this context were in good agreement with our proposal for the molecular processes involved in the early events of Aβ42 aggregation. Additionally, we tested known molecular probes interfering with Aβ aggregation dynamics and kinetics to extrapolate details on the nature of the peptidic assembly that showed high affinity for the glass-like multilayer surface. The results we obtained are only in partial agreement with the literature. To acquire complementary information, a NMR-based investigation was carried out using WaterLOGSY experiments. The outcome of this powerful method was in accordance with the conclusion we infer from the BSW-based monitorings, still contradicting some results reported in the literature. Finally, to enhance the performances of the BSW-based sensing device, we implemented a measuring system for simultaneous light scattering experiments.

We designed selective tests to indirectly rule out alternative versions of our hypothesis. This approach was driven by the limitations imposed both by the biological analyte, and by the prototypical nature of the optical setup. As in any field of scientific research, but especially under our working conditions, we were often in lack of valuable references to compare our results. For example, the inherent complexity of the Aβ42 aggregation process led to difficulties in handling the Aβ42 peptide sample. The monomeric Aβ42 peptide is notoriously metastable and rapidly converts into mature aggregates, which prevented us from directly calibrating the sensor with discrete toxic soluble Aβ42 oligomeric species, the target of our study.

This thesis work stemmed for an interdisciplinary project carried out between two laboratories with a very different background, and profited from several valuable external collaborations. The Organic Chemistry group (UniNE) provided support for the surface functionalization chemistry, which I carried out by myself and developed under the supervision of Dr. van der Wal from the Sensors, Actuators and Microsystems Laboratory (EPFL, Neuchâtel). I could profit from the initiation to the handling of the peptidic samples by the Laboratory of Molecular and Chemical Biology of Neurodegeneration (EPFL, Lausanne). From the valuable collaboration with Dr. Descrovi from the Politecnico di Torino (Italy), I was taught the know-how for operating the biosensing platform and achieve the reproducible results presented in this thesis. Dr. Descrovi considerably helped constructing the first optical setup presented in this thesis, which I then improved in terms of resolution and robustness.

Finally, this thesis work is an effort to develop a reliable and powerful real-time sensing approach that could be applied to the investigation not only of the aggregation dynamics of the Aβ peptide, but also to a wider range of aggregating proteins.

7.2 Perspectives

Many supplemental experiments were envisaged, but, due to a lack of time and other technical issues, were not actualized. In the following, a brief list of ideas and outlooks for this thesis project is presented.

7.2.1 BEDLS sensing

Among others, the most compelling follow-up to this project would be the realization of the BEDLS (Bloch surface wave-Enhanced Dynamic Light Scattering) setup, as described in Chapter 6. The aim would be to characterize the change in size of the Aβ42 peptide during aggregation via BSW-enhanced light scattering measurements, in parallel to the BSW-based monitoring. The prospective setup is represented in Fig.7.2.1.

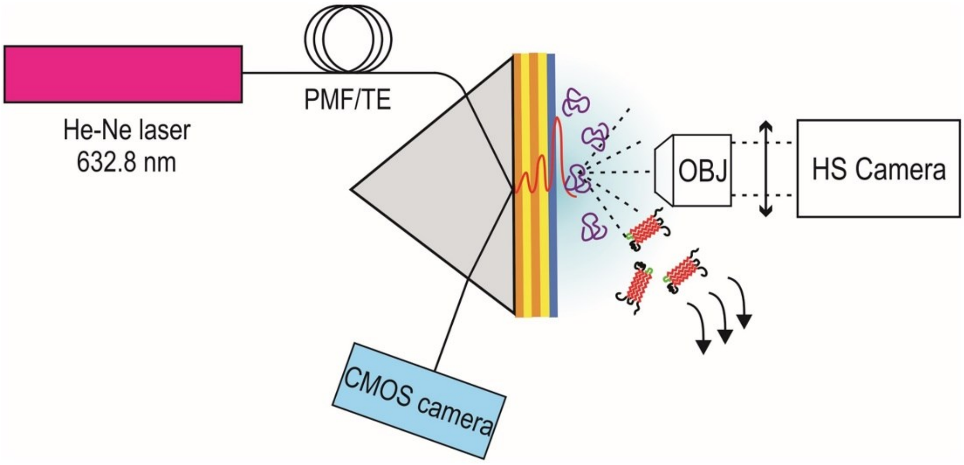

Fig.7.2.1. Top-view schematics of the BEDLS prospective setup. PMF: polarization maintaining fiber; OBJ: microscope objective; HS: high sensitivity.

A PMF guiding the TE polarized laser beam should be used to excite the BSW. The BSW response would be monitored via a CMOS camera tracking the BSW dip displacement in real time, as in the setups previously described in this thesis project. The BSW would act as the source for light scattering induction, which would be then collected by an objective and imaged onto a high sensitivity camera. A 1D or ROI (Region of Interest) integration of the image would follow. The system could be provided with an autocorrelator to extrapolate scattering intensity fluctuation in time.

As a further amelioration, the actual fluidic cell could also be replaced by a microfluidic cell made of PDMS directly deposited onto the photonic crystal, whose features were described in a recent publication by Tonin *et al*(1). In this article, the authors reported on its fabrication and on the possibility to perform high-resolution optical microscopy through it. With this microfluidic cell, the sample volume could be scaled down to few µL. The cell thickness is reported as little as less than 0.2 mm. This condition is most likely to mimic the *in vivo* condition to perform a more accurate kinetic study of the aggregation process. In addition, this upgrade would allow the objective for the collection of scattered light (see Fig.7.2.1) to be oil-contacted onto the cell, thus improving light collection. The numerical aperture of the oil immersion objective could be as high as 1.49.

7.2.2 Surface patterning for spatial selectivity

A modification of the sensor surface to perform an internal-reference measurement was also regarded as a potential improvement of the device.

The sensing surface could be angularly and spatially separated with the periodical deposition of thin-layer stripes of Plasma-Polymerized Styrene (PPST), alternating to a bare multilayer surface (see Fig.7.2.2).

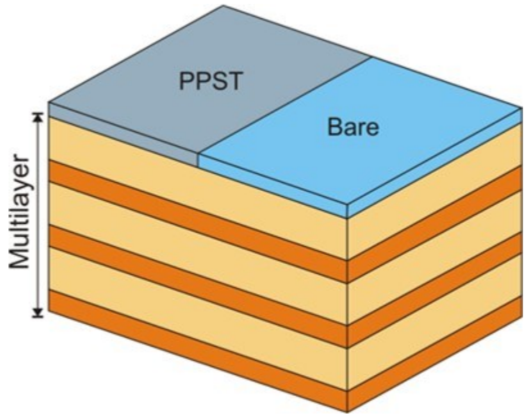

Fig.7.2.2. Scheme of the PPST surface patterning period. The bare surface is Si_3N_4.

This sensing approach is fully described by Ballarini *et al*(2), who have validated an experimental application of this strategy. In their publication, the authors demonstrate that this striped patterning of the multilayer allows for an internal referencing of the measurements: PPST films exhibit a significant hydrophobicity, a chemical inertness towards biomolecule functional groups, and acts as an anti-fouling layer, avoiding non-specific protein adsorption onto the surface. Thus, alternating PPST stripes to a bare multilayer surface a real-time comparison of the contribution to the signal given by the bulk effect and the surface-loading mechanism, respectively, is made possible. This strategy would improve the reproducibility of the measurements. As a further study of the aggregation of amyloid peptides, PPST striping would help identifying the signal revealed by our measurements with the specific conformational stage of the peptide.

PPST supports the BSW phenomenon. However, the coupling conditions should be different from those used for the Si_3N_4 material of the top–bare–layer of the photonic crystal. Working at a fixed wavelength, the two different materials should be illuminated at two different angles. Thus, the BSW on different regions would selectively be excited according to an “on-resonance/off-resonance” illumination condition, depending on the angle of incidence. An adapted camera could be used to detect both the reference and the functionalized optical signal in reflection. A suited Labview program should be developed and adapted for this application.

7.3 Bibliography

1. Tonin M, Descharmes N, & Houdre R (2016) Hybrid PDMS/glass microfluidics for high resolution imaging and application to sub-wavelength particle trapping. *Lab on a Chip* 16(3):465-470.
2. Ballarini M, Frascella F, De Leo N, Ricciardi S, Rivolo P, Mandracci P, Enrico E, Giorgis F, Michelotti F, & Descrovi E (2012) A polymer-based functional pattern on one-dimensional photonic crystals for photon sorting of fluorescence radiation. *Opt Express* 20(6):6703-6711.

8. EXPERIMENTAL MATERIALS AND METHODS

8.1 Biochemical studies

The Aβ42 peptide for the initial experiments was provided by the group of Hilal Lashuel, Laboratory of Molecular and Chemical Biology of Neurodegeneration, EPFL (Lausanne, Switzerland) and synthesized and purified as TFA salts by Elliott, WM Keck Facility, Yale University (New Haven, USA) as described in the literature(1). Aβ42 peptide was also purchased from Bachem AG, Bubendorf, Switzerland, and from PepMic Co, Ltd. (Suzhou, China). We did report no difference between the peptides provided by the three sources under the conditions of our experiments. Buffers and solvents for peptide preparation were purchased from SIGMA Aldrich and Fluka AG (Buchs, Switzerland). We used ultrapure water (Elix 3 water purification system, Merck Millipore, Darmstadt, Germany), unless stated otherwise.

8.1.1 Aβ42 monomer, protofibril and fibril preparation

The procedure for Aβ42 monomer, protofibril and fibril production was carried out according to the protocol developed by Jan *et al*(2).

The preparation of Aβ42 monomers was performed by dissolving the peptide in 6 M Gnd-HCl and purifying it via size exclusion chromatography (SEC). The eluate corresponding to the Aβ42 monomer peak at the maximal absorption intensity was collected, separated in fractions of 200 µL, and immediately stored at 4 °C.

For this purpose, the column Superdex 75 10/300 GL (GE Healthcare, Uppsala, Sweden) was used. It has a separation range for globular proteins of 3000 - 70000 Da, an exclusion limit of 105 Da, and a bed volume of approximately 25 mL. SECs were performed using an

Äkta Purifier 10 system (pumping system P-900) provided with a fraction collector Frac-920 (GE Healthcare, Uppsala, Sweden). Eluent filters ExpressPLUS had a cut-off diameter of 0.22 µm purchased from Millipore Corp. (Billerica, Massachusetts, USA). Buffers and solvents for SEC were purchased from SIGMA Aldrich and Fluka AG (Buchs, Switzerland). All SECs were performed at a flow rate of 0.5 mL/min at 25°C with 10mM Tris HCl elution buffer (pH 7.4). A column calibration with standard proteins was performed prior to its use. The calibration mix (SIGMA Aldrich, Buchs, Switzerland) was composed of 8 mg/mL BSA (MW monomer ~67 KDa; dimer ~130 KDa), 2.5 mg/mL Ovalbumine (MW ~ 43 KDa), 2.5 mg/mL Carbonic Anhydrase (MW ~ 29 KDa), 5 mg/mL RNAse (MW ~ 13.7 KDa), and 0.5 mg/mL Vitamin B12 (MW 1355 Da) in 10 mM Tris HCl buffer at pH 7.4. Prior to injection, the sample mix was centrifuged at 14000 rpm for 5 minutes. To assess the void volume of the column, 1 mg/mL Dextran Blue (MW ~ 2·106Da) in 10 mM Tris HCl buffer at pH 7.4 was used.

Aβ42 protofibril was obtained by dissolving the peptide in 100% DMSO and diluting the solution in ultrapure H_2O, then purifying the obtained solution via SEC, using the chromatographic column described above(2). The final concentration of Aβ42 monomer and protofibril samples in 10 mM Tris HCl was assessed by UV absorption at 280 nm, and calculated using a molar extinction coefficient of 1490 $M^{-1}cm^{-1}$(3).

Aβ42 fibrils were prepared by incubating the monomer sample, obtained as described above, at 37 °C for 48 h without agitation.

8.1.2 Aβ42 sample characterization

UV spectroscopy was used to calculate the purified Aβ42 samples concentration as explained above. Moreover, it was used to monitor the scattering profile of the absorbance spectra of monomer samples ($Abs_{250}/Abs_{280} \leq 0.5$, $Abs_{333} \sim 0$, after baseline correction), to rule out incipient aggregation when the sample was used within 24 h from the preparation. Unreliable Aβ42 samples were discarded.

TEM imaging was performed depositing 2 mL of peptide samples on Formvar/carbon-coated TEM grids negative stained by means of 2% uranyl acetate (2). The preparation of the TEM grids was carried out soon after sample preparation and then after different time lapses (from time 0 to 48 h for the monomer, at time 0 and 24 h for the protofibril, and at time 0 for the fibril) during peptide incubation at 37 °C. Both the grids and the stain were purchased from Electron Microscopy Sciences (Hatfield, USA). Micrographs were acquired on a Philips CM200 Transmission Electron Microscope.

8.1.3 Classical Aβ42 aggregation studies

To monitor the Aβ42 amyloid aggregation, several techniques were used to predict the Aβ42 behavior throughout fibrillization, in parallel to the BSW-based sensing.

All reagents and buffers for ThT-binding fluorescence assays were purchased from SIGMA Aldrich and Fluka AG (Buchs, Switzerland). For the assay, buffers and reagents were freshly prepared according to a protocol developed by Jan *et al*(2). A 100 µM ThT stock solution was prepared dissolving 0.32 mg of ThT in 10mL of ultrapure water. The reagent solution was filtered prior to use and stored at 4 °C protected from light for maximum one month. The reagent was filtered using a Minisart MNL syringe filter with a cut-off membrane of 0.22 µm (Sartorius Stedim, Aubagne Cedex, France). A 500 mM Gly-NaOH stock solution was prepared dissolving 376 mg of Gly in 10 mL of ultrapure water until a clear solution was achieved. The pH was brought to 8.5 by adding 3.75 M NaOH. The solution was filtered prior to use and stored at 4 °C. For fluorescence assays a fresh solution of Aβ42 monomer purified via SEC was used. It was incubated at 37 °C without stirring and 80 µL aliquots were added of 10 µL ThT stock solution and of 10 µL Gly-NaOH stock solution. Spectra detection parameters were selected according to a protocol developed by Nilsson(4). Emission fluorescence spectra were acquired in a wavelength range of 600-450 nm and recorded immediately after sample preparation on a LS50B fluorimeter (Perkin Elmer, Waltham, Massachusetts, USA). We used a fluorescence cell made of quartz SUPRASIL with a light path of 10 mm, and reduced volume of 100 µL purchased from Hellma (Müllheim, Germany). λ_{ex} was 440 nm. To prevent auto-excitation phenomena, λ_{ex} was not the ThT absorption maximum, which is 412 nm. The scan speed was 500 nm/min; the excitation slit was 5.0 nm and the emission slit 10.0 nm; the width was 7.5 nm. Spectra recording was performed with a 2-scan accumulation method. The fluorimeter allowed auto background subtraction. The blank was prepared replacing the peptide with 80 µL of 10 mM Tris HCl, pH 7.4.

All reagents and buffers for the TROL fluorescence quenching assay purchased from SIGMA Aldrich and Fluka AG (Buchs, Switzerland). For the assay, buffers and reagents were freshly prepared according to the literature(5). A reagent stock solution was prepared solubilizing 0.19 mg TROL in 100 µL DMSO and adding 1000 mL of 50 mM Gly-NaOH, pH 8.2. 50 mM Gly-NaOH, pH 8.2, was prepared by dissolving 3.76 g of Gly in 1000 mL ultrapure water and adjusting the pH by adding 3.75 M NaOH. TROL buffered solution final concentration was 10 µM and it was assessed by UV-vis spectroscopy. It was calculated with a molar extinction coefficient of 5690 $M^{-1}cm^{-1}$. The fluorescence assays were performed on a Luminescence Spectrometer LS 55 (Perkin Elmer, Waltham, Massachusetts, USA), using a 96-well black, opaque, flat-bottomed microplate. The Aβ42 peptide was separately incubated at 37 °C without agitation and 10 µL aliquots of the sample were added to 100 µL of 10 µM TROL buffered solution. Measurements were triplicated. Fluorescence intensity was recorded at λ_{em} = 355 nm (λ_{ex} = 280 nm). The excitation slit was 5.0 nm and the emission slit 10.0 nm; the width was 7.5 nm.

For the FTIR assays, HFIP and D_2O were purchased from SIGMA Aldrich (Buchs, Switzerland). To prepare the sample for the ATR-FTIR analysis, 0.15 mg of purchased Aβ42 peptide powder were solubilized in 100 µL of HFIP, as described in the literature(6). Aβ42 peptide samples were then lyophilized using a freeze-dryer Cryodos (TELSTAR Industrial, Terrassa, Spain), working at a temperature of -56 °C and at a pressure of 0.2 mBar, provided with a vacuum pump (Edwards, Munich, Germany). After freeze-drying overnight, the sample was solubilized in 100 µL of D_2O, leading to a peptide concentration of 332 µM. FTIR spectra were registered soon after D_2O solubilization, and after sample incubation at 37 °C without agitation. The monomeric Aβ42 sample for the comparison between β-structure and non-β-structure was obtained solubilizing 0.3 mg of lyophilized Aβ42 in 100 µL of 30% v/v HFIP in D_2O, as described in the literature(7). The final peptide concentration was 665 µM. The IR spectrum was registered after 10 minutes from the solubilization. Samples volume was 20 µL. The experiments were performed on a FTIR spectrometer Vertex 70 provided with an ATR cell holder BioATR II Confocheck (BRUKER Corp., Ettlingen, Germany). Spectra were recorded with the software OPUS version 6 (BRUKER), selecting experimental parameters according to the literature(7, 8). The background spectrum was registered for every new measurement and an automatic subtraction was performed by the software. All the spectra were registered in 32-scan accumulation. The frequency range was 4000-1000 cm^{-1}, and scan velocity was 20 kHz. All spectra were vapor-free (no sharp absorption was observed between 1700 and 1800 cm^{-1}). The beam diameter aperture was 6 mm. Interferograms were multiplied with the Blackman-Harris 3-Term apodisation function. Spectra were recorded at a spectral resolution of 4 cm^{-1}. All measurements were performed at 25 °C. For the second-derivative analysis, spectra in the amide I region were smoothened with a Stavitzky-Golay's 13-point smoothing function.

UV spectroscopy was used to monitor the Aβ42 aggregation by recording absorbance spectra between 240 and 350 nm(2). Monomeric Aβ42 peptide samples were incubated at 37 °C without agitation. Samples were centrifuged at 14000 rpm for 5 minutes. For the real-time UV-absorbance monitoring, the absorbance at 250 nm was measured every 30 seconds. Aβ42 samples were incubated at 37 °C in the spectrometer cell, using the accessorial temperature controller Peltier system ETC-717 (Jasco Corp., Tokio, Japan).

8.1.4 Test of the molecular probes

For the BSW-based measurement with RS-0406 in solution with the Aβ42 peptide, a 16.7 mM RS-0406 stock solution (in 33% DMSO, 66% 10 mM Tris HCl, pH 7.4) was freshly prepared. As an example, to prepare a 150 μL final sample to incubate in the sensing chamber, 1.2 μL of the stock solution were added to 148.8 μL of 13 μM monomeric Aβ42 peptide in 10 mM Tris HCl, pH 7.4. The final sample concentration was 130 μM RS-0406 in 10 mM Tris HCl, pH 7.4, 0.28% DMSO. Volumes were adjusted for the peptide samples at higher concentration. The molar ratio between the molecule and the peptide was 10:1.

For the BSW-based measurement with R548332 in solution with the Aβ42 peptide, a 16.7 mM R548332 stock solution (in 33% DMSO, 66% 10 mM Tris HCl, pH 7.4) was freshly prepared. As an example, to prepare a 200 μL final sample to incubate in the sensing chamber, 1.7 μL of the stock solution were added to 198.3 μL of 13.9 μM monomeric Aβ42 peptide in 10 mM Tris HCl, pH 7.4. The final sample concentration was 139 μM R548332 in 10 mM Tris HCl, pH 7.4, 0.28% DMSO. Volumes were adjusted for the peptide sample at higher concentration. The molar ratio between the molecule and the peptide was 10:1.

8.2 Optical setups

Three different optical setups were implemented in this thesis project. Details on their components, functioning and on data acquisition are presented in this Chapter, as follows: the optical setup for the BSW-based refractive index measurement is detailed in section 8.2.1, the setup for the parallel DLS and BSW-based measurement is described in section 8.2.2, the BILSI setup is discussed in section 8.2.3.

8.2.1 BSW-based optical platform

The light source was a stabilized He-Ne laser ($\lambda = 632.8$ nm), TE polarized via the use of a polarizer filter. An objective (20x), an optical diaphragm and two subsequent lenses (focal lengths 32 mm, reciprocal distance 165 mm) were used to condition the laser beam. The microscope objective was used to obtain a large divergent beam to have a sufficient illumination of the device. The lenses were mostly employed for the fine tuning of the angular range of illumination and to improve the intensity of the beam onto the device. The illumination of the photonic crystal was performed through a right-angle BK7 glass prism (refractive index 1.5149) to couple the light into the multilayer. The photonic-crystal layers were deposited on a BK7 glass substrate with an Oxford Plasmalab 80+ PECVD machine (Oxford, UK).

The fluidic cell was designed by a previous collaborator of the Optics & Photonics Technology laboratory (EPFL), and it is presented in Fig.8.2.1.

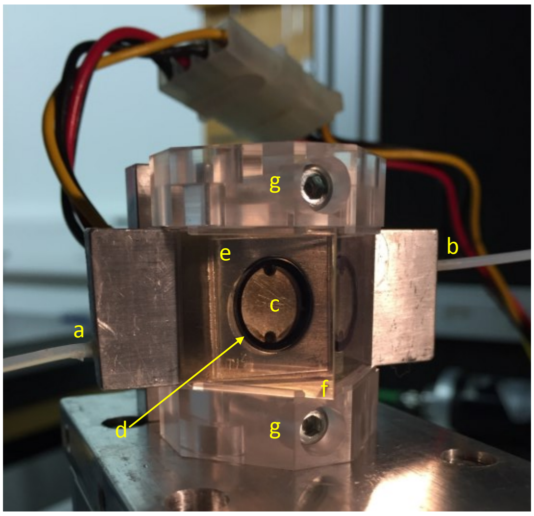

Fig.8.2.1. Picture of the fluidic chamber for BSW-based monitoring. (a) injection tube; (b) extraction tube; (c) incubation chamber; (d) O-ring; (e) multilayer; (f) prism; (g) plastic elements used to hold the chamber and the prism together.

The sample injection is made possible by two small channels inside the aluminum element, to which two Teflon tubes are glued. One tube is used for injection (Fig.8.2.1, a), the other for sample extraction (Fig.8.2.1, b). The two channels are converging into a central open cavity (Fig.8.2.1, c). The cavity is sealed against the multilayer via a plastic O-ring (Fig.8.2.1, d). The multilayer (Fig.8.2.1, e) is oil-contacted onto the prism (Fig.8.2.1, f). These three components are tightened together by two plastic components (Fig.8.2.1, g), which can be properly screwed onto the aluminum element to accommodate the prism. The fluidic cell volume is 200 μL. The incubation of the samples was performed at 37 °C (uncertainty ± 0.1 °C) via the use of a Peltier thermoelectric thermostat system connected to a temperature controller Lightwave ILX (Bozeman, USA). The Peltier element is positioned on the back of the aluminum chamber, opposite to the prism. The data acquisition of the BSW dip resonance position was started 1 min after the injection of the sample solution in the cell, to allow temperature stabilization. The laser beam reflected from the multilayer is directed to the detector, a 1.3 MP Monochrome 8-bit CMOS Camera (Mightex, Toronto, Canada), which allows monitoring the angular shift of the resonance conditions through the camera pixels. The response was therefore reported in numbers of pixels. The software for data collection was developed in collaboration with Dr. Descrovi from the Politecnico di Torino, Italy. The program makes use of a Lorentzian-function fit to interpolate the BSW dip and to track its displacement along the pixels of the camera.

For the results presented in this work, it is important to stress that the zero value in pixel shift corresponds to the BSW resonance position at the beginning of the measurement, and not to the signal of the reference buffer solution (10 mM Tris HCl), unless stated otherwise.

To guarantee identical initial experimental conditions, a new multilayer was used for each measurement.

8.2.2 Parallel DLS and BSW-based-monitoring setup

For the DLS measurement, the original setup was modified using optical fibers to guide the light to the sensing chamber. The optical elements and fibers were purchased from Thorlabs Gmbh, Dachau, Germany. In the optical setup, a laser beam (λ = 632.6 nm) is guided into a SMF via a fiber port (f = 15.4 mm, output waist diameter 0.33 mm). The SMF has a cut-off wavelength of 500-600 nm, a mode field diameter of 3.6-5.3 µm at 633 nm, a cladding diameter of 125 ± 15 µm, and a numerical aperture of 0.10-0.14. The light is then conditioned with a polarizing fiber-bench beamsplitter module. Two PMF collects TE or TM polarized light, respectively. They both have a cut-off wavelength of 570 ± 50 nm, and a numerical aperture of 0.12. The light is then guided to the fluidic cell via two fiber port collimators. For BSW excitement, the beam was slightly divergent. For light scattering induction, the beam was collimated. For light scattering collection, a 2 mm-core MMF is employed. It was polished with a diamond film (mesh 100 nm). It was optically controlled, and it revealed defects size of less than 100 nm.

8.2.3 BILSI setup

The BILSI setup was constructed by adapting a Leika DMR upright optical microscope for reflected bright-field imaging (Leika Microsystems, Heerbrugg, Switzerland). The lens tube size of the microscope is 200 mm. The camera used for the imaging is a Hamamatsu ORCA 100 (Hamamatsu, Japan). It is high sensitive in vis-NIR region and has a high resolution of 1.37 million pixels. The camera pixel size is 6.45 µm. Images and micrographs were recorded with no binning, using a 20X microscope objective. The integration time for image in Fig.6.2.4 was 200 ms, while for the micrographs in Fig.6.2.5, Fig.6.2.6, Fig.6.2.7, and Fig.6.2.8 the integration time was 1 s.

The multilayer used for BSW coupling in air was designed by Dr. Barakat from the Optics & Photonics Technology laboratory (EPFL), according to the scheme:
glass-(H-L)x6-H'-air, where H is silicon nitride and L is silica. Layers thicknesses are: H = 150 nm, L = 230 nm, and H' = 50 nm. For the BSW excitation, the light was guided via a PMF fiber (cut-off wavelength 570 ± 50 nm, numerical aperture 0.12). To couple light inside the multilayer, a right-angle BK7 glass prism was used. The illumination scheme was the same as described in the previous section.

8.3 Surface chemistry

For the multilayer surface chemical treatments, all the reagents and solvents were purchased from SIGMA Aldrich and Fluka AG (Buchs, Switzerland), and Honeywell (Seelze, Germany). d.i. water was obtained with an AquaFine system (CHRIST, Valencia, USA) provided with an UV disinfection system. Each functionalization procedure was carried out for 20 multilayers. The multistep strategy was optimized and partially adapted from the literature(9), as described in the following. For piranha cleaning, multilayers were soaked in a piranha bath (98% H_2SO_4 and 30% H_2O_2 in a volume ratio of 3 to 1) at room temperature for 30 minutes. After this step, multilayers were carefully and extensively washed in d.i. water baths and dried with a gentle N_2 flux. For the amino-silanization, we prepared a stirred bath of 95% toluene at 80 °C, and we added 10% v/v APTES and 0.5% v/v d.i. water. Multilayers were introduced in the bath after 30 minutes from its preparation. This step was important when glassware that could react with APTES was used. After 30 minutes, we assumed that the silanization of the glassware was terminated. The amino-silanization step was carried out by vertically placing the multilayers in a Teflon holder, then in the toluene bath for 2 hours. After this step, multilayers were washed twice in a 99% isopropanol bath, then gently dried with a N_2 flux. When necessary, after this step multilayers were stored in a desiccator. For the linker binding, a room-temperature $CHCl_3$ (HPLC purity grade) bath was prepared by adding 0.5% v/v TEA and 1 mg/mL acetal-NHS. Multilayers were placed at the bottom of the bath, with the dielectric layers oriented upwards for 2 hours. The bath was covered with a watch glass. After this time, the multilayers were washed three times in chloroform baths, and gently dried with N_2 flux. The acetal-NHS linker was deprotected in a 1% m/v citric acid bath at room temperature. The multilayers were incubated for 15 minutes by placing them at the bottom of the bath. Afterward, they were carefully washed three times in d.i. water baths for 5 minutes. For the final step, the ligand attachment, two separate buffer A baths added of 4% of v/v 1 M $NaCNBH_3$ were prepared. Buffer A was 100 mM NaCl, 50 mM NaH_2PO_4, adjusted to pH 7.5 with NaOH. For the preparation of 1 M $NaCNBH_3$, 0.31 g of the substance were added to 5 mL d.i. water. The multilayers were divided into two sets of 10 multilayers each. For PEGylation, one set was positioned at the bottom of the buffered bath solution added of 0.25 mg/mL methoxy polyethylene glycol amine 750. Similarly, for TROL functionalization, the other set was positioned in the buffered bath added of 0.1 mg/mL L-Tryptophanol. The incubation was performed at room temperature for 1 h. After this time, 4% v/v of 1M ethanolamine was added to each bath. After 15 minutes, we assessed the pH neutrality. Then, we removed the multilayers from the reaction bath and washed them three times, for 5 minutes, in PBS baths (150 mM NaCl, 5 mM NaH_2PO_4, adjusted to pH 7.4 by NaOH addition). Multilayers were then extensively washed in d.i. water baths, gently dried with N_2 flux, and stored in a desiccator until use.

The homogeneity of the PEG coating was confirmed using dark-field optical microscopy with a Nikon SMZ1500 stereomicroscope provided with a Nikon Dn100 camera.

8.3.1 BSW-based sensing to assess surface functionalization effectiveness

For the BSW-based monitoring with a PEGylated multilayer surface, BSA protein (SIGMA Aldrich, Buchs, Switzerland) was dissolved in 0.1 M PBS, pH 8.9, without pretreatments. The protein solution was filtered with a Minisart MNL syringe filter with a cut-off membrane of 0.22 μm (Sartorius Stedim, Aubagne Cedex, France). The protein concentration was assessed performing UV-Vis spectroscopy, using a molar extinction factor ε_{280} of 43.824 $m^{-1}cm^{-1}$ and accounting a MW of 66463 Da (ProtParam). 100 mL of 0.1 M PBS was prepared dissolving 1.42 g of Na_2HPO_4 in ultrapure water. The pH was adjusted to 8.9 with 25% v/v HCl. The solution was filtered under vacuum with a cut-off membrane of 0.22 μm. For the BSW-based measurement reported in section 4.2.1, the pixel-shift zero value was corresponding to the BSW dip position while incubating water at the temperature selected for the BSA incubation.

For the BSW-based measurement with TROL in solution with the Aβ42 peptide, a fresh TROL stock solution was prepared before each experiment. 1.8 mg TROL were solubilized in 200 μL DMSO. 5 μL of the TROL stock solution were added to 10 μL of 10 mM Tris HCl, pH 7.4, leading to a final TROL concentration of 16.7 mM in 33% DMSO and 66% 10 mM Tris HCl, pH 7.4. To prepare a 200 μL final sample to incubate in the sensing chamber, 1.7 μL of 16.7 mM TROL were added to 198.3 µL of 13.9 µM monomeric Aβ42 peptide, in 10 mM Tris HCl, pH 7.4. The final sample concentration was 139 µM TROL, 13.9 µM Aβ42 peptide, in 10 mM Tris HCl, pH 7.4, 0.28% DMSO. TROL stock solution concentration was assessed by UV-vis spectroscopy and it was calculated using a molar extinction coefficient of 5690 $M^{-1}cm^{-1}$.

8.4 Bibliography

1. Sato T, Kienlen-Campard P, Ahmed M, Liu W, Li H, Elliott JI, Aimoto S, Constantinescu SN, Octave J-N, & Smith SO (2006) Inhibitors of Amyloid Toxicity Based on β-sheet Packing of Aβ40 and Aβ42. *Biochemistry* 45(17):5503-5516.

2. Jan A, Hartley DM, & Lashuel HA (2010) Preparation and characterization of toxic A beta aggregates for structural and functional studies in Alzheimer's disease research. *Nat Protoc* 5(6):1186-1209.

3. Gill SC & von Hippel PH (1989) Calculation of protein extinction coefficients from amino acid sequence data. *Analytical Biochemistry* 182(2):319-326.

4. Nilsson MR (2004) Techniques to study amyloid fibril formation in vitro. *Methods* 34(1):151-160.

5. Reinke AA, Abulwerdi GA, & Gestwicki JE (2010) Quantifying Prefibrillar Amyloids in vitro by Using a “Thioflavin-Like” Spectroscopic Method. *ChemBioChem* 11(13):1889-1895.

6. Tomaselli S, Esposito V, Vangone P, van Nuland NAJ, Bonvin AMJJ, Guerrini R, Tancredi T, Temussi PA, & Picone D (2006) The α-to-β Conformational Transition of Alzheimer's Aβ-(1–42) Peptide in Aqueous Media is Reversible: A Step by Step Conformational Analysis Suggests the Location of β Conformation Seeding. *ChemBioChem* 7(2):257-267.

7. Juszczyk P, Kołodziejczyk AS, & Grzonka Z (2009) FTIR spectroscopic studies on aggregation process of the β-amyloid 11–28 fragment and its variants. *Journal of Peptide Science* 15(1):23-29.

8. Calero M & Gasset M (2005) Fourier transform infrared and circular dichroism spectroscopies for amyloid studies. *Methods Mol Biol* 299:129-151.

9. Wildling L, Unterauer B, Zhu R, Rupprecht A, Haselgrübler T, Rankl C, Ebner A, Vater D, Pollheimer P, Pohl EE, Hinterdorfer P, & Gruber HJ (2011) Linking of Sensor Molecules with Amino Groups to Amino-Functionalized AFM Tips. *Bioconjugate Chemistry* 22(6):1239-1248.

APPENDIX 1: EXPERIMENTAL BSW RESPONSE CALIBRATION AND SENSOR RESOLUTION DETERMINATION

For the calibration of the multilayer sensitivity, two methods were used. In the first, the angular shift of the BSW resonance dip was obtained varying the temperature of d.i. water (resistivity 13 MΩ/cm). Water refractive indices at different temperatures and at λ = 632.8 nm were extrapolated from discrete values reported in the literature(1), as reported in Fig.A1.1 (a).

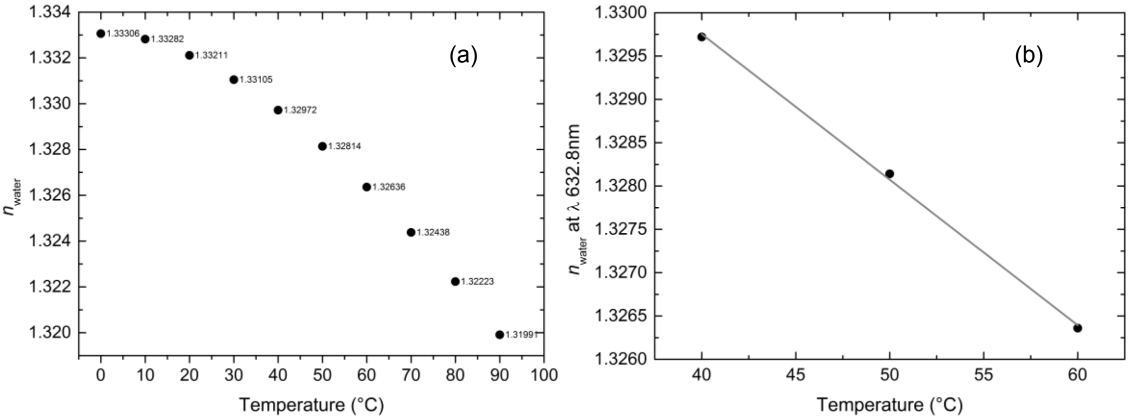

Fig.A1.1. Water refractive index n_{water} at different temperatures: (a) from 0 to 100 °C; (b) from 40 to 60 °C, where the regime is linear(1).

We decided to work in the linear regime of the refractive index variation, which occurs between 40 and 60 °C, as shown in Fig.A1.1 (b). From the linear fit we obtained Eq.(A.1):

$$\Delta n_{water} = 1.33647 - 1.68 \cdot 10^{-4}\, T \qquad \text{(A1.1)}$$

which allowed calculating the refractive index of water at fixed temperatures between 40 and 60 °C.

In the second method, glucose solutions at different concentration C (% m/v) at 25 °C were used (see Tab.A1.1). For the conversion of the refractive index change of glucose solutions in d.i. water at $\lambda = 632.8$ nm we used the formula:

$\Delta n = \beta \cdot C$ (A1.2)

where $\beta = 1.527 \cdot 10^{-3}$ RIU / %(2, 3). This method is fully described by Giorgis *et al*(4), where the refractive indices of different glucose solutions are reported as in Tab.A1.1:

Glucose m/v	**Δn (at 25 °C and λ = 632.8 nm)**
0 % (d.i. water)	0
$5 \cdot 10^{-4}$ %	$7.6 \cdot 10^{-7}$
$1 \cdot 10^{-3}$ %	$1.5 \cdot 10^{-6}$
$5 \cdot 10^{-3}$ %	$7.6 \cdot 10^{-6}$
$1 \cdot 10^{-2}$ %	$1.5 \cdot 10^{-5}$
$5 \cdot 10^{-2}$ %	$7.6 \cdot 10^{-5}$
0.1 %	$1.5 \cdot 10^{-4}$
0.5 %	$7.6 \cdot 10^{-4}$
1.25 %	$1.9 \cdot 10^{-3}$
2.5 %	$3.8 \cdot 10^{-3}$
5 %	$7.6 \cdot 10^{-3}$

Tab.A1.1. Concentration and Δn of different glucose solutions. Glucose concentration is reported in % m/v and the reference for Δn is d.i. water at 25 °C and λ = 632.8 nm(4).

Bibliography

1. Bashkatov AN & Genina EA (2003) Water refractive index in dependence on temperature and wavelength: a simple approximation. pp 393-395.

2. Sinibaldi A, Danz N, Descrovi E, Munzert P, Schulz U, Sonntag F, Dominici L, & Michelotti F (2012) Direct comparison of the performance of Bloch surface wave and surface plasmon polariton sensors. *Sensors and Actuators B: Chemical* 174(0):292-298.

3. Grünewald H (1972) Handbook of Chemistry and Physics. Von R. C. Weast. The Chemical Rubber Co., Cleveland, Ohio/USA 1972. 52. Aufl., XXVII, 2313 S., geb. DM 99.80. *Angewandte Chemie* 84(9):445-446.

4. Giorgis F, Descrovi E, Summonte C, Dominici L, & Michelotti F (2010) Experimental determination of the sensitivity of Bloch surface waves based sensors. *Opt Express* 18(8):8087-8093.

APPENDIX 2: COMPLEMENTARY STUDIES ON THE Aβ42 PEPTIDE AGGREGATION

In this appendix studies on the *in vitro* characterization of the Aβ42 aggregates conformation and kinetics of the process of fibril formation are presented.

The sample purification and identification were carried out using classical biochemistry techniques, such as SEC (size exclusion chromatography) and UV spectroscopy. After the preparation of the monomeric samples their conformational characterization was performed by traditional optical spectroscopies (UV-vis, Fluorescence, and FTIR).

The kinetics of aggregation were monitored under conditions (pH, temperature, and ionic strength) responsible for fibrillation and the evolution of monomers into oligomers and mature fibril was controlled by ThT binding assay, FTIR, and UV spectroscopy.

Aβ42 monomer purification and characterization

Many protocols for preparation, purification and characterization of Aβ42 samples have been proposed(1, 2). In this project we used the one developed by Jan *et* al(3), in which the authors have described the Aβ42 sample preparation via a SEC-based method. SEC is a very commonly used technique to purify proteins exploiting their difference in molecular weight and hydrodynamic volume. The column we used is a Superdex 75 10/300 GL, where the stationary phase is a composite of cross-linked agarose and dextran porose structure with an optimum separation range for globular proteins of 3000 - 70000 Da and an exclusion limit of 10^5 Da.

Firstly, to ensure the functionality and separation properties of the size exclusion chromatographic column we calibrated the column with a mix of known proteins with a well-defined MW. The mix was composed as follows: BSA 8 mg/mL; Ovalbumine 2.5 mg/mL; Carbonic Anhydrase 2.5 mg/mL; RNAse 5 mg/mL; Vitamin B12 0.5g/mL. The elution buffer was 10 mM TRIS HCl, 150 mM NaCl (pH 7.4). It was similar to the one used for the Aβ42 peptide sample preparation. The presence of a high salt concentration was necessary to avoid aspecific interaction between the column and the calibration proteins. The calibration test of the column was successfully performed. To complete the calibration, we estimated the void volume of the column using Dextran Blue at a concentration of 1 mg/mL. We separately performed this assay to prevent the Dextran Blue peak to overlap the BSA peak. The resulting chromatograms are shown in Fig.A2.1.

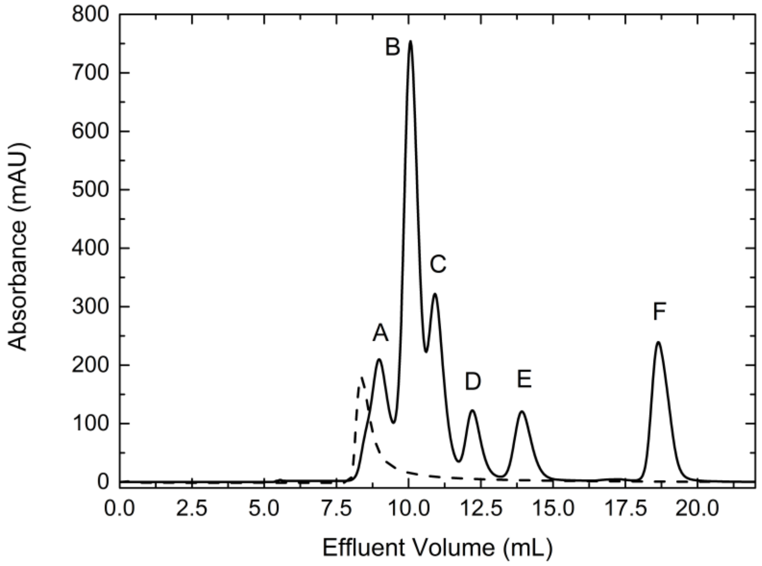

Fig.A2.1. SEC chromatograms for the column calibration. Elution buffer 10 mM Tris HCl, 150 mM NaCl, pH 7.4; flow rate 0.5 mL/min; absorbance recorded at 280 nm. In dashed line the chromatogram of the elution of Dextran Blue. In solid line: (A) BSA dimer; (B) BSA monomer; (C) Ovalbumine; (D) Carbonic Anhydrase; (E) Ribonuclease; (F) Vitamin B12.

As shown in Fig.A2.1.1, each peak is narrow and well defined it was possible to assign unequivocally one peak to one protein in order to estimate the retention volume of each of them. From the chromatographs in Fig.A2.1 we extrapolated the data listed in Tab.A2.1.

Protein	Ve (mL)	MW (Da)	K_d	LogMW
Dextran Blue	8.35	2000000	0	6.30103
BSA dimer	8.98	134000	0.06116	5.12710
BSA monomer	10.07	67000	0.16699	4.82607
Ovalbumine	10.91	43000	0.24854	4.63347
Carbonic Anhydrase	12.21	29000	0.37476	4.46240
RNAse	13.92	13700	0.54078	4.13672
Vit. B_{12}	18.65	1355	1	3.13194

Tab.A2.1. List of the standard proteins used to perform the column calibration. Each standard protein is here reported with its molecular weight, retention volume V_e and diffusion constant K_d.

The coefficient values reported in the table above have been calculated with equation (A2.1):

$$k_d = \frac{V_e - V_o}{V_p} = \frac{V_e - V_o}{V_i - V_o} \qquad \text{(A2.1)}$$

where V_o corresponds to Dextran Blue elution volume V_e (mL) and V_i is Vitamin B_{12} elution volume V_e (mL). It was therefore possible to calibrate the column as shown in Fig.A2.2. The results obtained from this test allowed us to confidently assume the proper functioning of the column, since the relation between logMW and K_d of the selected proteins was linear.

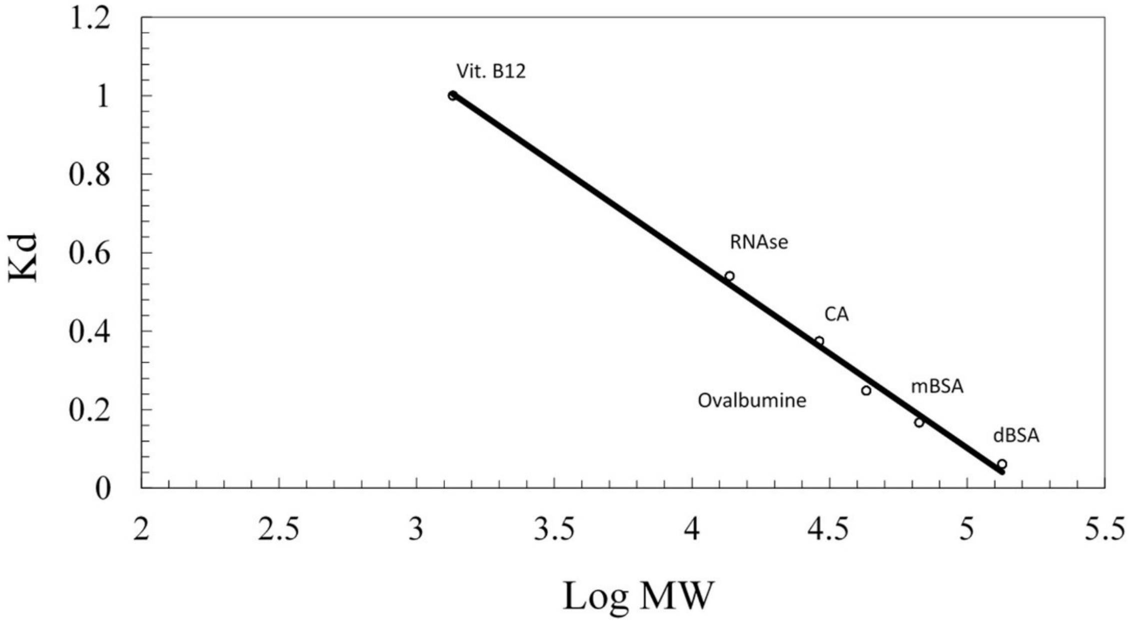

Fig.A2.2. Calibration curve of the Superdex column. A linear relation between the calculated Kd and LogMW is shown.

To prepare the Aβ monomeric samples, we performed SEC separations using as elution buffer 10 mM Tris HCl, without salt added. The chromatograph highlighting the elution volume of the protein is shown in Fig.A2.3.

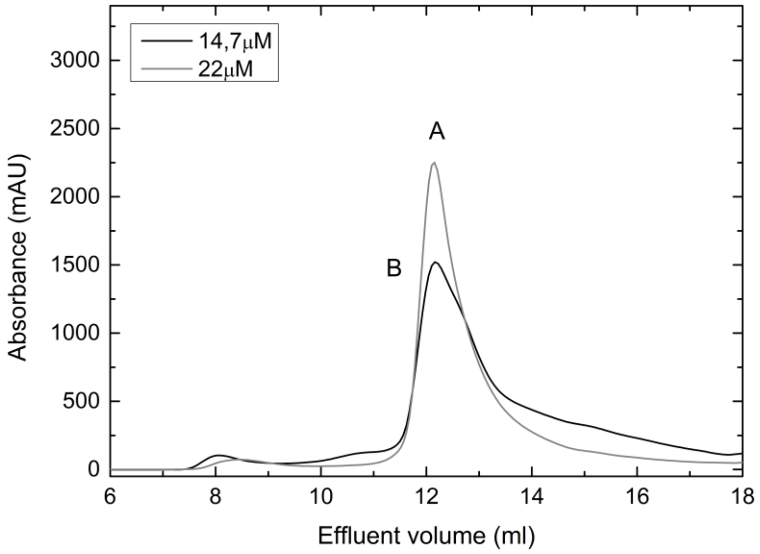

Fig.A2.3. SEC purification of monomeric Aβ42 peptide. In grey and black line runs of Aβ with elution buffer 10 mM Tris HCl at different concentration (V_r Aβ42 oligomer 8.15 mL; V_r Aβ42 monomer 12.53 mL). Flow rate 0.5 mL/min; absorbance recorded at 214 nm. The concentrations reported refer to the final concentration of the monomeric fractions collected.

Lyophilized Aβ42 monomer was solubilized in 6 M Gnd-HCl and insoluble pre-existing aggregates were removed by centrifugation (14000 rpm, 5 min) before injection. The resulting chromatograms showed that the sample solutions contained predominantly monomeric Aβ42(3), as depicted in Fig.A2.3. The peptide eluted as a single peak in the included volume of SEC column (0.45–0.55 CV, elution volume 11-13 mL, Fig.A2.3, peaks A and B). Commonly, ~ 0.25 mg of lyophilized Aβ42 dissolved in 250 μL of Gnd-HCl yielded ~ 1.5 mL of purified monomer at concentrations of ~ 15–25 μM. Repetitions of SEC purifications showed that Aβ predominantly eluted as a monomer with high reproducibility. A low-intensity peak eluting at approximately 8 mL run volume was also reported (Fig.A2.3). The presence of a small amount of LMW oligomers, which exist in rapid equilibrium with the monomer both in Gnd-HCl solution and during the elution, has been suggested by the literature(3). We identified LMW oligomers with the low-intensity peak. However, it was not possible to predict the correct molecular weight of Aβ42 peptides via the linear relation extrapolated from the column calibration test (Fig.A2.2). Aβ42 monomers and oligomers are unfolded or only partially folded. The particular interaction of these highly hydrophobic small proteins with the column bed is not comparable with that of the globular protein used for the calibration(3).

We used SEC fractions to perform quality-control assays of the monomeric Aβ42 samples after 24 h storage at 4 °C (Fig.A2.4). The chromatogram showed two peaks eluting with the expected retention volumes(3). The most intense peak corresponded to the monomeric form of Aβ42 peptide. However, it was impossible to totally inhibit the formation of even a small amount of oligomers (~ 5%) even at 4 °C.

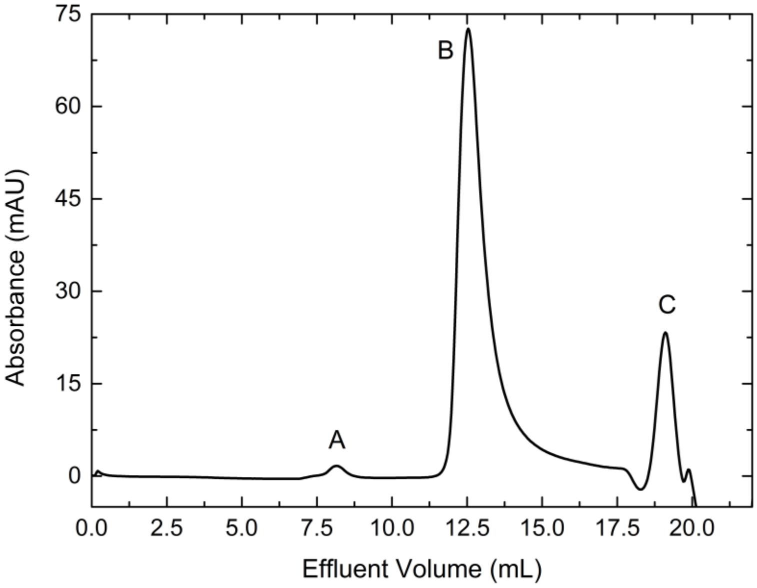

Fig.A2.4. Reinjection of purified monomers into the SEC column. Elution buffer 10 mM Tris HCl; flow rate 0.5 mL/min; absorbance recorded at 214 nm. A→ oligomer; B→ monomer; C→ flow-through.

The SEC-based method ensured the starting material for the aggregation studies experiments to be predominantly monomeric Aβ42 peptide, free from protofibrillar or fibrillar aggregates. To further rule out the presence of fibrillar or protofibrillar aggregates in the SEC purified monomeric samples, aliquots were centrifuged and evaluated by UV spectroscopy (Fig.A2.5.).

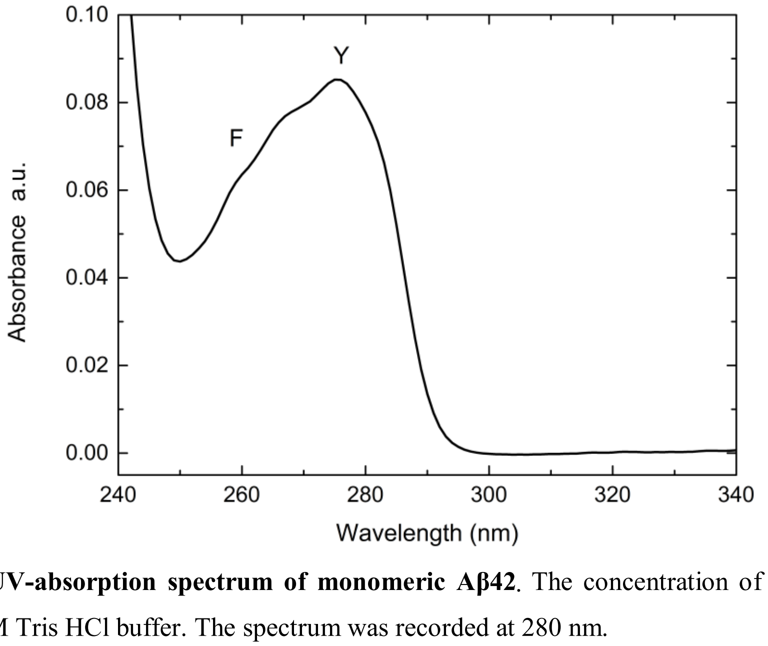

Fig.A2.5. UV-absorption spectrum of monomeric Aβ42. The concentration of the peptide was 51.7 µM in 10mM Tris HCl buffer. The spectrum was recorded at 280 nm.

The shape of the spectrum in Fig.A2.5 is characteristic of soluble proteins or peptides(4). The maximum absorption intensity at 274 nm corresponds to the only Tyrosine (Y) present in the peptide chain. Between 260 and 267 nm two peaks are present due to the absorption contribution of the four Phenylalanines (F) of the Aβ42 peptide. No signal between 320 and 350 nm was reported. This signal is very often correlated to aggregated forms present in the sample(5). UV spectroscopy was also used to carefully estimate the concentration of the SEC-purified Aβ42 fractions, by using a molar extinction coefficient of 1490 M^{-1} cm^{-1} (determined with ProtParam).

Aβ42 aggregation studies

To monitor the Aβ42 peptide aggregation kinetics, several different analysis were routinely carried out. It was crucial to perform these controls before the BSW-based aggregation monitorings. The Aβ42 samples were incubated under specific conditions (pH, temperature, and ionic strength) responsible for protofibril formation, then conformational analyses of samples were carried out by UV-visible spectroscopy and fluorescence spectroscopy via the ThT-binding assay. To determine the content of β-sheet secondary structure during the incubation, FTIR spectroscopy measurements were performed. As a final step, the samples were applied to the BSW device and incubated under the same conditions.

ThT-binding fluorescence assay

The most common technique to identify the presence of amyloid fibrils and to monitor their formation in time is the ThT fluorescence assay. Although ThT fluorescence is not the "definitive" criterion for kinetic studies on amyloid fibrils formation, it is well accepted as a probe of their presence in samples under aggregation conditions. ThT shows a very low fluorescence in the absence of the amyloid aggregates (Fig.A2.6). The assay measures the enhancement in fluorescence intensity of ThT upon binding to amyloid fibrils. The enhanced fluorescence can be observed at 482 nm; the excitation wavelength is 440 nm, a value close to the maximum in absorbance(6), which is 412 nm. The spectroscopic assay was carried out according to the literature(3). Despite this assay is commonly used to monitor fibril formation over time, it is not strictly quantitative.

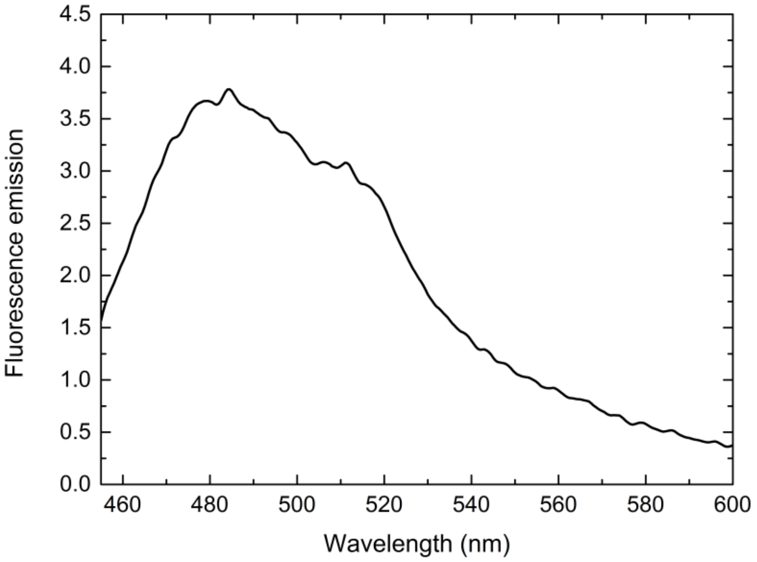

Fig.A2.6. ThT fluorescence emission spectrum. The sample (10 µM in 10 mM Tris HCl, 50mM Gly-NaOH, pH 7.8-8.2) was excited at 440 nm.

In the presence of a freshly purified Aβ42 monomer sample, an almost absent ThT fluorescence increase (see Fig.A2.7, first data point) is the hallmark of the absence of amyloid fibrillar aggregates. After incubation at 37 °C for several hours, a fluorescence enhancement was observed (see Fig.A2.7).

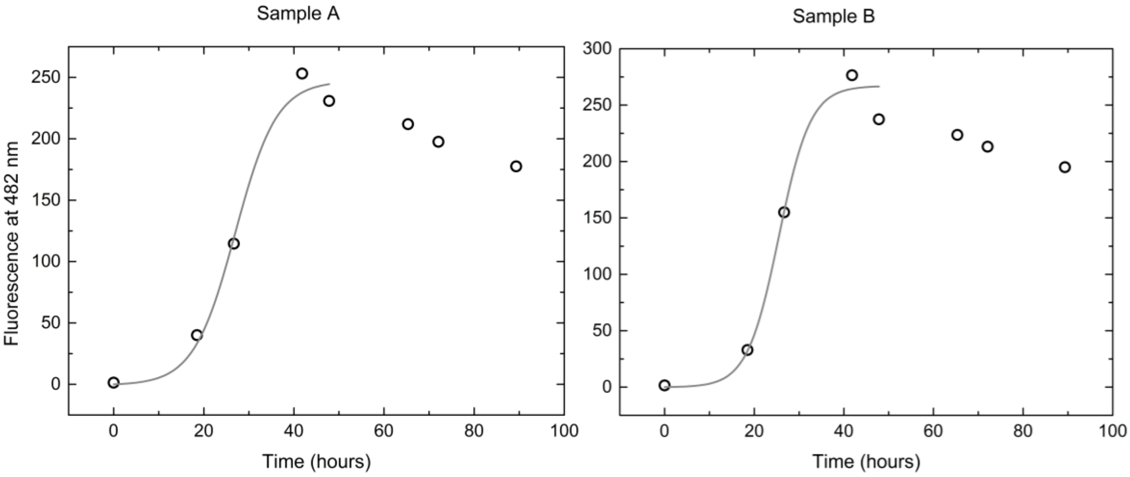

Fig.A2.7. ThT-binding assays. The ThT fluorescence enhancement given by the binding to the peptide during its aggregation at 37 °C is shown. The initial Aβ42 monomer concentration in sample A was 9 µM, and in sample B was 8 µM. Buffer 10 mM Tris-HCl, 50 mM Gly-NaOH, pH 7.8-8.2. ThT was at 10 µM in both experiments.

As highlighted by Fig.A2.7, the ThT fluorescence enhancement was exhibited after several hours of incubation. This is consistent with what reported in the literature(6, 7). After a critical time of incubation, the peptide assembles into β-sheet secondary structure allowing the ThT molecules to insert into the channels made by the long axis of this domain. Thus, the ThT fluorescence intensity is enhanced.

To mathematically analyze the fluorescence data from the ThT-binding assays in Fig.A2.7 according to the nucleation-polymerization kinetic model for protein aggregation, fluorescence data were fitted with Eq.(A2.2):

$$[B]_t = [A]_0 - \frac{\frac{k_1}{k_2} + [A]_0}{1 + \frac{k_1}{k_2[A]_0}\exp(k_1 + k_2[A]_0)\,t} \qquad \text{(A2.2).}$$

It defines a two-steps aggregation mechanism of slow, continuous nucleation followed by typically fast autocatalytic growth. k_1 and k_2 are, respectively, the rate constant for nucleation and the rate constant for growth; $[A]_0$ is the initial monomer peptide concentration and $[B]_t$ is the concentration of the aggregate at the time t. For this specific fitting, $[A]_0$ corresponds to the fluorescence intensity at the end of the reaction, assuming that all the monomer has turned into aggregate; $[B]_t$ is the fluorescence intensity recorded during the incubation(8-10). According to the fitting in Fig.5.2.3, the calculated nucleation rate constant corresponded to 6.18 10^{-4} $h^{-1}\mu M^{-1}$ and 2.04 10^{-4} $h^{-1}\mu M^{-1}$, for sample A and B, respectively. The calculated polymerization rate constants were 8.77^{-4} h^{-1} and 1.06^{-3} h^{-1}, for sample A and B, respectively. These values are consistent with those reported in the literature(11) and describe a slow nucleation, followed by a faster fibril elongation.

The model proposed is described by the two-steps reaction(9):

Nucleation (oligomers formation) $\mathbf{{}_nA \xrightarrow{k_1} B_n}$

Growth (fibrillation) $\mathbf{A + B_n \xrightarrow{k_2} B_{n+1}}$

where *n* is representing the number of the molecules of monomer A that are assembling to form the oligomer B, and k_1 is the rate constant of this nucleation reaction. Then, this nucleus recruits other monomers through the fibrillation reaction, whose constant rate is k_2. The concentration of the monomer determines the velocity of the growing phase, pushing the equilibrium to the formation of the aggregate. This model is consistent with the results we obtained.

FTIR Spectroscopy: a Probe of Secondary Structure Variation

To assess the secondary structure of the Aβ42 peptide throughout aggregation, as reported in the literature(3, 6, 12), we performed FTIR spectroscopy experiments. We concentrated our study on the amide I band absorption that arises from the C=O stretching vibrations of the peptide bond between 1700 and 1600 cm^{-1}. This vibration mode is influenced by the protein backbone conformation. In Fig.A2.8 an IR profile of an initially monomeric Aβ42 peptide is presented. The lyophilized Aβ42 sample was dissolved in D_2O and was subjected to deuteration at 4 °C for 1 hour. We unequivocally identified the amide A (~3300 cm^{-1}), the amide I (1700-1600 cm^{-1}), and the amide II (1500-1400 cm^{-1}) bands. The deep trough in the middle region between 2700 and 2200 cm^{-1} is due to the O-D stretching of D_2O and the dip at 1200 cm^{-1} is due to the O-D bending(13).

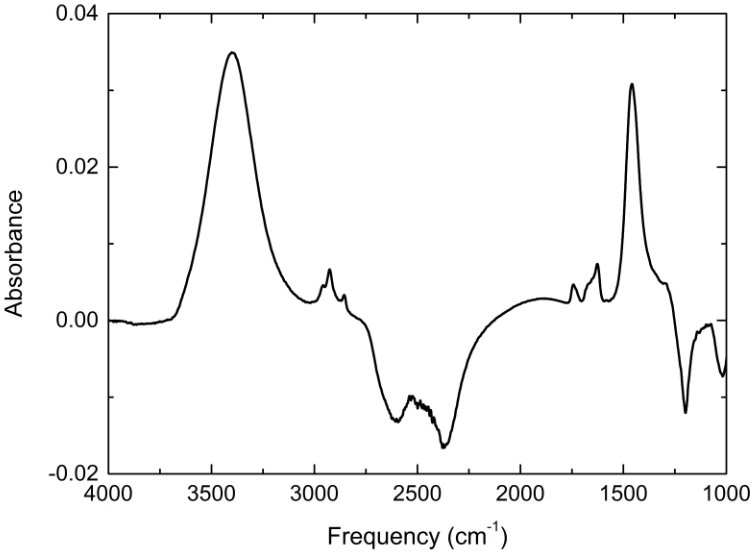

Fig.A2.8. FTIR-ATR spectrum of Aβ42 peptide. The concentration of the protein was 332 μM in D_2O.

The sample was then incubated for two days at 37 °C in D_2O and monitored through FTIR spectroscopy. The overlapping of the IR profiles of the peptide during the aggregation process is reported in Fig.A2.9 (solid lines). Unfortunately, dissolving the Aβ42 peptide in pure D_2O caused an initial formation of oligomers. To assess the structural conformation of the monomer, we prepared the Aβ42 sample by dissolving the lyophilized powder in 30% v/v HFIP and 70% v/v D_2O, which have been reported to be disgregant condition(14). HFIP has been shown to prevent the aggregation of the Aβ42 peptide(14, 15). The FTIR spectrum of the obtained Aβ42 monomeric sample is presented in Fig.A2.9 (dashed line).

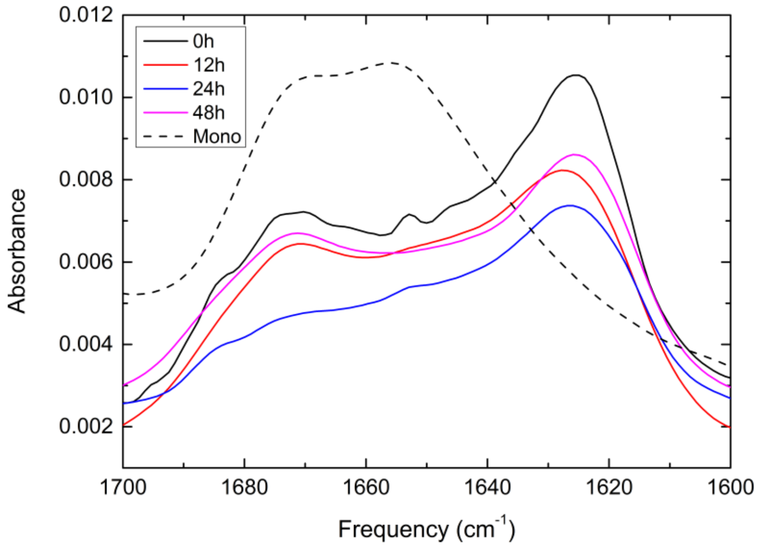

Fig.A2.9. Close-up view of the amide I band region in the FTIR spectrum of the Aβ42 peptide. Solid lines: IR spectra of the Aβ42 peptide before and during incubation at 37 °C (initial monomer concentration 332 µM in D_2O). Dashed line: IR spectrum of a monomeric sample (665 µM) in 30% v/v HFIP, 70% v/v D_2O.

From a first analysis of the spectra in solid lines in Fig.A2.9 it is possible to observe the presence of bands at 1625 cm^{-1} corresponding to a β-sheet structure, but it is not possible to draw more precise results because of a band broadening(12). Several methods for the deconvolution of these broad bands are used; we selected the second-derivative method because of its simplicity in extrapolation and interpretation(14), as presented in Fig.A2.10.

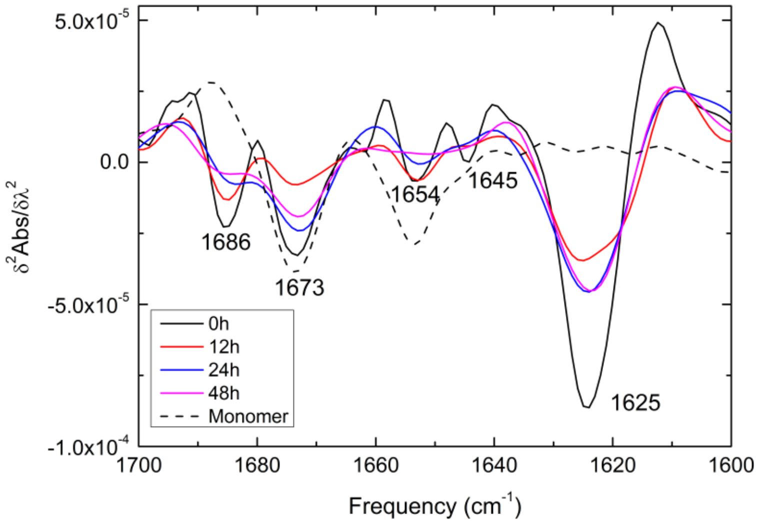

Fig.A2.10. Second-derivative analysis of the ATR-FTIR spectra. The analysis of the Aβ42 peptide spectra in Fig.A2.9 was performed with a 13-smoothing point function.

In the second derivative of the IR spectra of the peptide in the amide I region a trough is shown at 1625 cm^{-1}. This is characteristic of parallel β-sheet. Other three minima are detectable: one at 1654 cm^{-1} that has been assigned to random coil, one at 1673 cm^{-1} assigned to the presence of turns, and one at 1686 cm^{-1}, that has been related to the presence of antiparallel β-sheet and aggregated strands(13, 16). These peaks are especially detectable in FTIR spectrum of the peptide sample that was kept at 4 °C (t = 0, Fig. A2.10). For this sample, a minimum at 1645 cm^{-1} is also detectable. We could not confidently assign this spectroscopic feature to a content in α-helix structure, but authors have suggested this correlation(13).

Over incubation time, the intensity of the peak at 1654 cm^{-1} decreases. This is consistent with aggregates formation concomitant to the disappearance of a random-coil structure, which is typical of non-aggregated peptides. The band at 1625 cm^{-1} decreases over time and this effect may reflect the sample precipitation following aggregation. The persistence of the 1625 cm^{-1} band over incubation time is indicative that a parallel β-sheet conformation is formed even in the early stage of aggregation. The band related to the antiparallel β-sheet (1686 cm^{-1}), whose decrease has been correlated to the formation of more compact aggregates, such as proto fibrils and fibrils(17), is more intense at the beginning of the incubation and this is in agreement with a transition from an oligomeric to a fibrillar state. After an incubation time of 48 h, the most intense band was the one related to a β-sheet structure. Therefore, the Aβ42 peptide, under these experimental conditions, is mostly aggregated into fibrils. This is consistent with results reported in literature(17, 18).

UV Absorption Spectroscopy

To assess the results obtained for the Aβ42 aggregation as monitored with the BSW-based sensing approach, we performed parallel incubations of the peptide at 37 °C and we monitored the UV absorption response of the samples. The Aβ42 sample was incubated under identical conditions compared to the refractive index measurement.

Firstly, the Aβ42 peptide was incubated at 37 °C and centrifuged 14000 rpm for 5 minutes prior to recording the sample absorbance in the UV range between 350 and 240 nm. The results of this investigation are presented in Fig.A2.11.

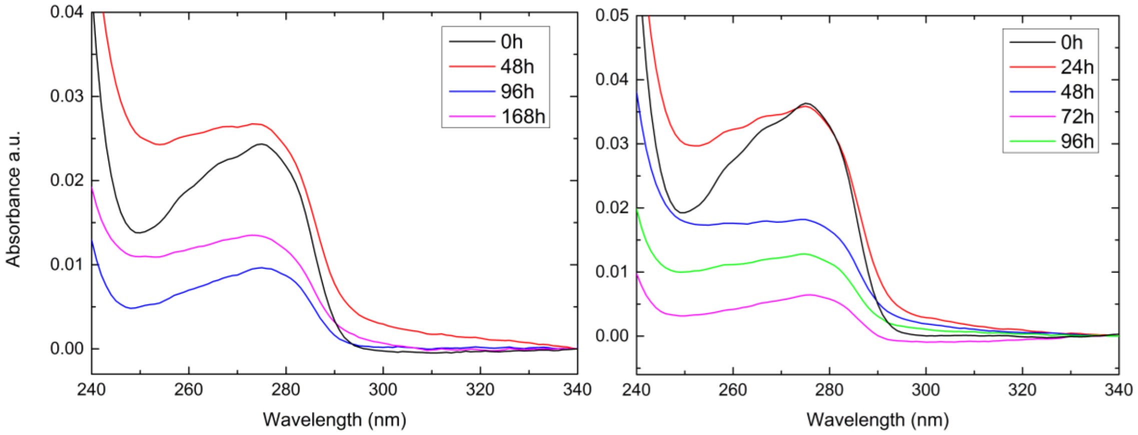

Fig.A2.11. UV spectra of the Aβ42 peptide during incubation. Samples were incubated at 37 °C, in 10 mM Tris HCl, pH 7.4. Left: sample at initial monomer concentration of 14.7 µM. Right: sample at initial monomer concentration of 22 µM. Spectra were not normalized.

From the shape of the spectral profiles, we notice an absorption occurring between 320 and 350 nm. Since this signal is not correlated to any chromophore in the peptide, it has been associated to Rayleigh scattering(5). This contribution to the signal was especially relevant during the first days of incubation (Fig.A2.11, curves in red). We propose that this phenomenon should be due to the formation of small soluble aggregates, such as Aβ42 oligomers. Those aggregates do not precipitate after centrifugation. After several incubation days, the spectra maxima (280 nm) decrease. This event can be safely correlated to the formation of fibrils, which are excluded from the solution via centrifugation. The absorption profiles of the samples after 96 hours of incubation was exhibiting a minor scattering contribution between 320 and 350 nm, related to a decreased amount of soluble aggregates. These results are in accordance with the literature(3).

A real-time absorbance monitoring of the Aβ42 peptide throughout aggregation at 250 nm is presented in Fig.A2.12.

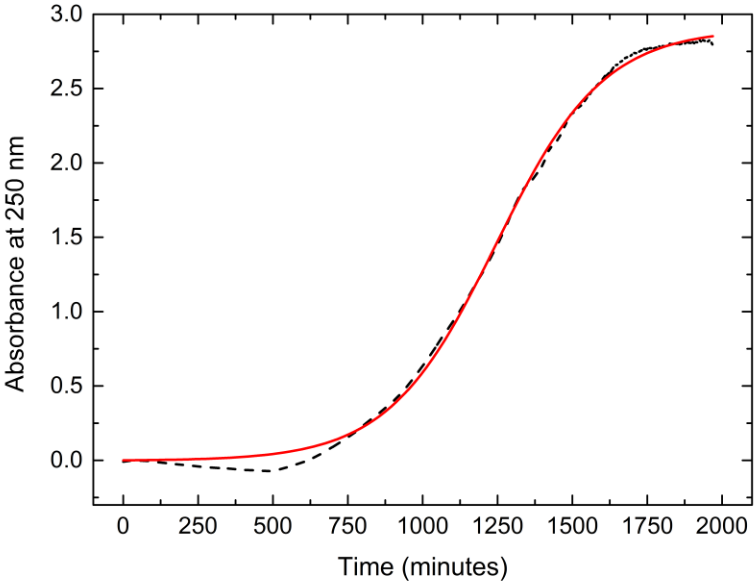

Fig.A2.12. Real-time absorbance change of aggregating Aβ42 peptide. Black: absorbance profile of the Aβ42 peptide at 250 nm during incubation at 37 °C without stirring (in 10 mM Tris HCl, pH 7.4). Initial monomer concentration: 9μM. Red: fitting curve obtained applying Eq. A2.1.

The measurement was performed at the fixed wavelength of 250 nm, where the scattering contribution is directly correlated to the formation of aggregates(19). The peptide solution was incubated at 37 °C for 33 hours, without stirring. The profile in Fig.A2.12 presents an initial absence of signal variation (“lag-phase”), followed by a sharp increase of absorbance. A plateau in the signal is finally reached. The aggregation curve present similarities to the nucleation-polymerization model. From Eq.A2.2, we calculated k_1 and k_2 values, which corresponded to 5.49 10^{-6} h^{-1} and 1.91 10^{-3} $h^{-1}\mu M^{-1}$, respectively. These value are consistent with those reported in the literature(11).

To monitor subtle structural changes in the tertiary protein conformation during the incubation(20), we investigated the changes in the phenylalanine peak ratio via a second-derivative analysis of the spectra in Fig.A2.11. The variations are directly correlated to changes in the microenvironment around the aromatic amino acid. This study is presented in Fig.A2.13.

The second-derivative analysis of the absorbance spectral profile aimed at studying the environment of the peptide phenylalanines residues during aggregation. This investigation is carried out observing the intensity variation of the troughs between 250 and 274 nm. It has been demonstrated that the positions of phenylalanine minima do not change upon microenvironment variations. This method is frequently used to detect protein aggregation or denaturation, since the intensity variation of minima is due to changes of the solvent exposition of aromatic amino acids(21).

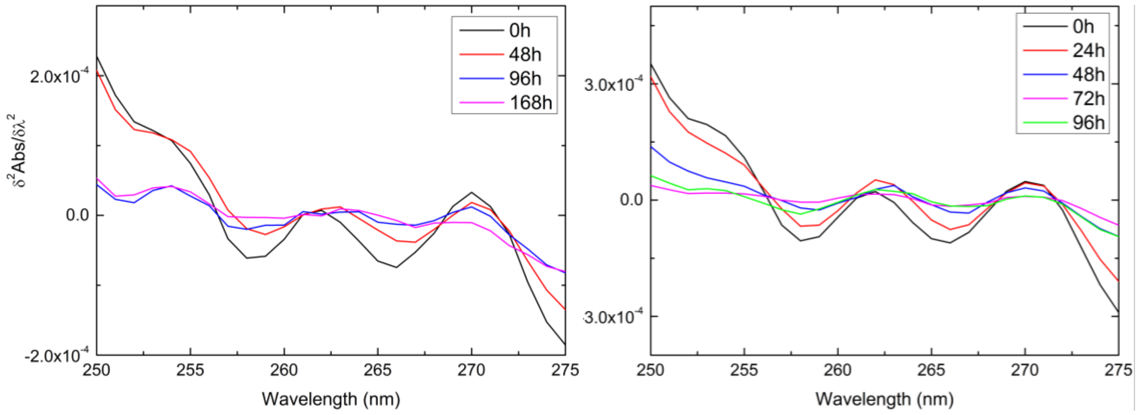

Fig.A2.13. Second-derivative analysis of the UV spectra of the Aβ42 peptide during incubation. Original spectra are reported in Fig.A2.11.

From the observation of the results presented in Fig.A2.13, one notices that the fine structure of the spectra disappears during the incubation (from 0 to 168 hours, on the left, and to 96 hours, on the righ). At long incubation times valleys disappear. This phenomen has been correlated to the "hiding" of the aromatic AA in the core of the structure, evidence of an aggregated conformational state of the peptide(21).

Bibliography

1. Teplow DB (2006) Preparation of Amyloid-Beta Protein for Structural and Functional Studies. *Methods in Enzymology*, eds Indu K & Ronald W (Academic Press), Vol Volume 413, pp 20-33.

2. Wiberg H, Ek P, Ekholm Pettersson F, Lannfelt L, Emmer Å, & Roeraade J (2010) Separation and characterization of aggregated species of amyloid-beta peptides. *Analytical and Bioanalytical Chemistry* 397(6):2357-2366.

3. Jan A, Hartley DM, & Lashuel HA (2010) Preparation and characterization of toxic A beta aggregates for structural and functional studies in Alzheimer's disease research. *Nat Protoc* 5(6):1186-1209.

4. Gill SC & von Hippel PH (1989) Calculation of protein extinction coefficients from amino acid sequence data. *Analytical Biochemistry* 182(2):319-326.

5. Raynal B, Lenormand P, Baron B, Hoos S, & England P (2014) Quality assessment and optimization of purified protein samples: why and how? *Microbial Cell Factories* 13(1):1-10.

6. Nilsson MR (2004) Techniques to study amyloid fibril formation in vitro. *Methods* 34(1):151-160.

7. Levine H (1993) Thioflavine T interaction with synthetic Alzheimer's disease β-amyloid peptides: Detection of amyloid aggregation in solution. *Protein Science* 2(3):404-410.

8. Watzky MA, Morris AM, Ross ED, & Finke RG (2008) Fitting yeast and mammalian prion aggregation kinetic data with the Finke-Watzky two-step model of nucleation and autocatalytic growth. *Biochemistry* 47(40):10790-10800.

9. Watzky MA & Finke RG (1997) Transition Metal Nanocluster Formation Kinetic and Mechanistic Studies. A New Mechanism When Hydrogen Is the Reductant: Slow, Continuous Nucleation and Fast Autocatalytic Surface Growth. *Journal of the American Chemical Society* 119(43):10382-10400.

10. Morris AM, Watzky MA, & Finke RG (2009) Protein aggregation kinetics, mechanism, and curve-fitting: a review of the literature. *Biochim Biophys Acta* 1794(3):375-397.

11. Morris AM, Watzky MA, Agar JN, & Finke RG (2008) Fitting Neurological Protein Aggregation Kinetic Data via a 2-Step, Minimal/"Ockham's Razor" Model: The Finke−Watzky Mechanism of Nucleation Followed by Autocatalytic Surface Growth†. *Biochemistry* 47(8):2413-2427.

12. Zandomeneghi G, Krebs MR, McCammon MG, & Fandrich M (2004) FTIR reveals structural differences between native beta-sheet proteins and amyloid fibrils. *Protein Sci* 13(12):3314-3321.

13. Calero M & Gasset M (2005) Fourier transform infrared and circular dichroism spectroscopies for amyloid studies. *Methods Mol Biol* 299:129-151.

14. Juszczyk P, Kołodziejczyk AS, & Grzonka Z (2009) FTIR spectroscopic studies on aggregation process of the β-amyloid 11–28 fragment and its variants. *Journal of Peptide Science* 15(1):23-29.

15. Tomaselli S, Esposito V, Vangone P, van Nuland NAJ, Bonvin AMJJ, Guerrini R, Tancredi T, Temussi PA, & Picone D (2006) The α-to-β Conformational Transition of Alzheimer's Aβ-(1–42) Peptide in Aqueous Media is Reversible: A Step by Step Conformational Analysis Suggests the Location of β Conformation Seeding. *ChemBioChem* 7(2):257-267.

16. Barth A (2007) Infrared spectroscopy of proteins. *Biochim Biophys Acta* 1767(9):1073-1101.

17. Cerf E, Sarroukh R, Tamamizu-Kato S, Breydo L, Derclaye S, Dufrene YF, Narayanaswami V, Goormaghtigh E, Ruysschaert JM, & Raussens V (2009) Antiparallel beta-sheet: a signature structure of the oligomeric amyloid beta-peptide. *Biochem J* 421(3):415-423.

18. Ahmed M, Davis J, Aucoin D, Sato T, Ahuja S, Aimoto S, Elliott JI, Van Nostrand WE, & Smith SO (2010) Structural conversion of neurotoxic amyloid-beta1-42 oligomers to fibrils. *Nat Struct Mol Biol* 17(5):561-567.

19. Lehninger AL, Nelson DL, & Cox MM (1999) *Principles of biochemistry* (Worth Publishers).

20. Mach H, Thomson JA, Middaugh CR, & Lewis RV (1991) Examination of phenylalanine microenvironments in proteins by second-derivative absorption spectroscopy. *Archives of Biochemistry and Biophysics* 287(1):33-40.

21. Ichikawa T & Terada H (1979) Estimation of state and amount of phenylalanine residues in proteins by second derivative spectrophotometry. *Biochimica et Biophysica Acta (BBA) - Protein Structure* 580(1):120-128.

Sara SANTI

Nationality: Italian

Date of Birth: September 23, 1986

Work Address: EPFL IMT OPT, Microcity, rue de la Maladiere 71b, CH-2000 Neuchâtel

Private Address: Ch. Du Vieux-Moulin 4, CH-2088 Cressier NE

+41 76 728 70 90

sara.santi23@gmail.com

CURRENT POSITION

06.2012 – 06.2016	Laboratory of Organic Chemistry, Prof. R. Neier Institute of Chemistry, Université de Neuchâtel *and* Optics & Photonics Technology Laboratory, Prof. H.-P. Herzig Institute of Microengineering (IMT) - EPFL **PhD Student**	**Neuchâtel, CH**

PROFESSIONAL EXPERIENCE

2013 – 2015	Laboratory of Analytical Chemistry - “Travaux Pratiques” for 2nd-year Biology students Laboratory of Chemistry of Natural Products - “Travaux Pratiques” for Biology Master-students Institute of Chemistry, Université de Neuchâtel **Laboratory Assistant**	**Neuchâtel, CH**
05.2011 – 04.2012	Optics & Photonics Technology Laboratory, Prof. H.-P. Herzig and Laboratory of Molecular and Chemical Biology of Neurodegeneration, Prof. H. Lashuel Brain Mind Institute, EPFL **Scientific Assistant**	**Lausanne, CH**

EDUCATION

09.2005 – 03.2011	Università degli Studi di Padova **BSc and MSc in Pharmaceutical Chemistry and Technology** Final-thesis Supervisor: Prof. V. De Filippis, Final thesis title: “Investigation of the Mechanisms of Aβ42 Peptide Fibrillation by Optical Spectroscopy and Bloch Surface Waves: Potential Implication in the Diagnosis Of Alzheimer’s Disease”. Grade 110/110	**Padua, IT**
09.2010 – 02.2011	Optics & Photonics Technology Laboratory, Prof. H.-P. Herzig Institute of Microengineering (IMT) - EPFL **Master Thesis Project** Supervisors: Prof. H.-P. Herzig and Dr. V. Musi	**Neuchâtel, CH**
1999 – 2005	Liceo Scientifico Tecnologico “Diploma Scientifico” (equivalent to A level or Swiss Matura)	**M.belluna, IT**

RESEARCH EXPERIENCE

Biophysics and Biophotonics on the molecular dynamics of protein misfolding and aggregation

- Aβ1-42 peptide aggregates conformational studies by means of classical optical spectroscopies, electron microscopy, and analytical biochemical techniques
- *In vitro* study of the dynamics of β-amyloid peptide early events of aggregation *via* a novel label-free optical platform based on Bloch Surface Wave (BSW)
- *In vitro* study of Bovine Serum Albumin (BSA) protein aggregation dynamics

RESEARCH SKILLS

Protein Chemistry	• Chromatographic techniques (reverse-phase HPLC, SEC, gel filtration, ion-exchange, affinity chromatography) • Electrophoretic methods (SDS-PAGE, agarose gel electrophoresis) • Mass Spectrometry techniques (ESI-TOF, LC-MS)
Molecular Biology	• Basic techniques for expression and purification of recombinant proteins
Optical Spectroscopy	• UV-vis absorption spectroscopy • Fluorescence spectroscopy • Fourier Transformed Infra-Red (FTIR) spectroscopy and ATR-FTIR
Optics	• Basics on micro and nano-technologies for optics and photonics applications • Surface Plasmon Resonance sensing and Bloch Surface Wave sensing • Optical-fibers alignment and applications
Microscopy	• Basic techniques of Transmission Electron Microscopy (TEM) imaging for proteins • Basics on Scanning Electron Microscopy (SEM) imaging
Surface Chemistry	• Silicon Nitride/Oxide surface chemical functionalization

PUBLICATION LIST

S. Santi, V. Musi, E. Descrovi, V. Paeder, J. Di Francesco, L. Hvozdara, P. van der Wal, H. A. Lashuel, A. Pastore, R. Neier and H.-P. Herzig (2013) Real-time Amyloid Aggregation Monitoring with a Photonic Crystal-based Approach. *ChemPhysChem*, *14*, 3476-3482.

S. Santi, E. Barakat, R. Neier, H. P. Herzig (2015) Real-time protein aggregation monitoring based on a simultaneous light scattering investigation and a Bloch surface wave-based approach. *Proc. SPIE 9550*, Biosensing and Nanomedicine VIII, San Diego, CA, 95500V-95500V-95503.

S. Santi, E. Barakat, E. Descrovi, R. Neier and H. P. Herzig (2014) Real-time Protein Aggregation Monitoring with a Bloch Surface Wave-based Approach. *Proc SPIE*, Biophotonics: Photonic Solutions for Better Health Care (Conference 9129), Brussels, Belgium.

H. P. Herzig, R. Neier, **S. Santi** and E. Barakat. Bloch meets Alzheimer, in SPG Mitteilungen, vol. Januar 2014, num. 42, p. 11-14, 2014.

V. Paeder, **S. Santi**, V. Musi, and H. P. Herzig (2011) Investigation of protein aggregation dynamics with a Bloch surface wave sensor. *Proc SPIE*, Novel Biophotonic Techniques and Applications, *8090*, 80900C.

OTHER SKILLS/AWARDS

Geographically flexible, sociable, flexible team worker, excellent in interpersonal relations, excellent skills with Microsoft Office, proficiency in grant proposal writing.

Interests: travelling, sailing, learning new languages, reading.

Language skills: native Italian speaker; fluent in English (level C2), both written and oral; fluent in French (level C1), both written and oral.

Best Poster Award – EPFL Photonics Day 2013 – 18th November 2013 – Lausanne (Switzerland).

Jürg Engi Prix – Faculté des Sciences, Université de Neuchâtel – June 2015 – Neuchâtel (Switzerland).

REFERENCES

Prof. Hans Peter Herzig	Institute of Microtechniques (IMT) - Optics & Photonics Technology Laboratory - EPFL - Switzerland	hanspeter.herzig@epfl.ch +41 21 69 54270
Prof. Reinhard Neier	Institut de Chimie – Laboratoire de Chimie Organique - Université de Neuchâtel - Switzerland	reinhard.neier@unine.ch